NASA-CR-164695
19810022530

The Telecommunications and Data Acquisition Progress Report 42-64

May and June 1981

N. A. Renzetti
Editor

August 15, 1981

National Aeronautics and
Space Administration

Jet Propulsion Laboratory
California Institute of Technology
Pasadena, California

JET PROPULSION LABORATORY *California Institute of Technology • 4800 Oak Grove Drive, Pasadena, California 91103*

August 15, 1981

Recipients of TDA Progress Report 42-63

SUBJECT: Erratum

Please note the following correction to JPL TDA Progress Report 42-63, March and April 1981:

Page 154, second column, last line:

"...sponsored and managed by the Department of Energy."

should read:

"...sponsored and managed by The Gas Research Institute."

Very truly yours,

John Kempton, Manager
Documentation Section

Telephone (213) 354-4321 *Twx 910-588-3269* *Twx 910-588-3294*

The Telecommunications and Data Acquisition Progress Report 42-64

May and June 1981

N. A. Renzetti
Editor

August 15, 1981

National Aeronautics and
Space Administration

Jet Propulsion Laboratory
California Institute of Technology
Pasadena, California

The research described in this publication was carried out by the Jet Propulsion Laboratory, California Institute of Technology, under contract with the National Aeronautics and Space Administration.

Preface

This publication was formerly entitled *The Deep Space Network Progress Report*. Although the practice of reporting progress in the development and operations of the Deep Space Network continues, the report has been expanded to include developments in Earth-based radio technology as applied to other research programs. These programs are:

(1) Geodynamics: For several years, the laboratory has been developing radio interferometry at microwave frequencies for application to geodetic measurements. This branch of telecommunications technology is now being applied to the study of geodynamics.

(2) Astrophysics: The deep space stations, individually and in pairs as an interferometer, have been used by radio astronomers for astrophysics research by direct observations of radio sources.

(3) An activity closely related to radio astronomy's use of the deep space stations is NASA's continuing program of radio search for extraterrestrial intelligence in the microwave region of the electromagnetic spectrum.

Each succeeding issue of this report will present material in some, but not all, of the following categories:

Radio Astronomy
Search for Extraterrestrial Intelligence
Radio Interferometry at Microwave Frequencies

- Geodetic Techniques Development
- Spacecraft Navigation
- Orbiting Very Long Baseline Interferometry

Deep Space Network

- Description
- Program Planning
- Planetary and Interplanetary Mission Support
- Advanced Systems
- Network and Facility Engineering and Implementation
- Operations
- Spacecraft Radio Science
- Planetary Radar
- Energy

In each issue, there will be a report on the current configuration of one of the seven DSN systems (Tracking, Telemetry, Command, Monitor and Control, Test Support, Radio Science, and Very Long Baseline Interferometry).

The work described in this report series is either performed or managed by the Telecommunications and Data Acquisition organization of JPL.

This Page Intentionally Left Blank

Contents

PLANETARY AND INTERPLANETARY MISSION SUPPORT

Planetary Flight Projects

Advanced Flight Projects

ADVANCED SYSTEMS

Tracking and Ground-Based Navigation

Communications

Network Data Processing and Productivity

NETWORK AND FACILITY ENGINEERING AND IMPLEMENTATION

Network

OPERATIONS

Network Operations

ENERGY

This Page Intentionally Left Blank

Radio Astronomy

P. R. Wolken and R. D. Shaffer
Control Center Operations Section

M. V. Gorenstein
Massachusetts Institute of Technology

This article reports on the activities of the Deep Space Network in support of Radio Astronomy Operations during April and May 1981. Work in progress in support of an experiment selected for use of the DSN by the Radio Astronomy Experiment Selection Panel, Twin Quasi-Stellar Object VLBI, is reported.

I. Introduction

Deep Space Network (DSN) 26-, 34- and 64-meter antenna stations are utilized in support of three categories: NASA Office of Space Science (OSS), Radio Astronomy Experiment Selection (RAES), and Host Country.

II. Radio Astronomy Operations

A. NASA OSS Category

During this period, 94 hours and 35 minutes of DSN station support was given for Pulsar Rotation Constancy and 77 hours and 45 minutes of support for Planetary Radio Astronomy.

B. RAES Panel Category

1. **RA 175 (SS-433).** On 17 and 18 May 1981, the Goldstone 64-meter station supported very long baseline interferometry (VLBI) observations of the source SS-433 (1909+04) for a total of 28 hours and 15 minutes. Continuing support of this experiment is expected to produce further resolution of the angular radio structure of this unusual object along with the possible origin of it as reported in *TDA Progress Report 42-62, January and February 1981.*

2. **RA 176 (Twin Qusai-Stellar Object (QSO) VLBI, 0957+561 A, B and 1038+528 A, B;** see ***TDA Progress Report 42-63, March and April 1981***). The pair of quasars 0957+561 A, B, separated by 6 arc-sec (redshift of 1.4) almost certainly arise from a single quasar whose light has been gravitationally deflected by a foreground galaxy. The optical spectra of the quasars are essentially identical, and a foreground galaxy with an associated cluster has been found that can explain the image doubling via the gravitational lens hypothesis. A second pair of physically unrelated quasars, 1038+528 A, B separated by 33 arc-sec (redshifts of 0.678 and 2.296 respectively) are close enough to be observed simultaneously in the same antenna beamwidth. One quasar can then provide an independent reference frame, with respect to which possible superluminal motions of components in the other quasar can be detected. We have conducted observations at two epochs that have yielded or promise to yield significant return on these pairs of sources.

Observations of 25-26 February 1980. Three stations (DSS 14 at Goldstone, Calif., DSS 63 in Madrid, Spain, and the 100-m antenna at Effelsberg, Germany) conducted observations of 0957+561 A, B. The data from these observations have been reduced to show that the quasars have elliptically

shaped radio cores at S-band of 1 milli-arc-sec extent with similar axis ratios and position angles on the sky. The data place a 3% upper limit on flux density of a predicted third quasar image compared to the flux density from the core of the B image. We are currently constructing a model of the bending due to the cluster that will account for these results. We have also measured the separation of the quasar cores with an rms error of ±50 micro-arc-sec using differenced phase-delay measurements. We will submit an article containing these results by mid-September 1981.

Observations of 15-16, 17-18 March 1981. Seven stations (DSS 63, DSS 14, Onsala, Effelsberg, the National Radio Astronomy Observatory (NRAO) 40-m antenna in Greenbank, W. Va., Haystack Observatory 38-m antenna in Westford, Mass., and Owens Valley Radio Observatory (OVRO) 39-m antenna at Big Pine, Calif.) observed 1038+528 A, B at S- and X-band (17-18 March), and all stations but Haystack observed 0957+562 A, B at S-band only (15-16 March). Observations were carried out successfully at all sites; about 90% of the scheduled scans produced satisfactory recordings. We have detected (found fringes on) the sources on baselines to all stations for both epochs of observation. Correlation of the data is now underway at the Haystack Observatory's Mark III correlator. (Mark III recording terminals were used at all sites.) As of mid-June 1981 about half the data has been correlated for both pairs of sources. We expect that processing will be finished by late July, with preliminary maps of both source pairs made by the end of the summer.

C. Host Country

Many astronomically interesting objects were observed under the auspices of Host Country activities in Australia in April 1980. These observations were carried out as part of a southern hemisphere interferometer consisting of Tidbinbilla (either DSS 42 or DSS 43), Parkes, and Hartebeesthoek. A number of significant results are expected shortly.

The 64-meter antenna in Madrid (DSS 63) devoted 7 hours and 15 minutes of support to Host Country activities for an interplanetary scintillations experiment.

The SETI Program Plan and Instrument Development Status

A. L. Berman
TDA Mission Support Office

R. B. Crow
Communications Systems Research Section

The SETI (Search for Extraterrestrial Intelligence) Program is a NASA Supporting Research and Technology Program with primary thrust to search the microwave region of the spectrum for signals of extraterrestrial intelligent origin. During the next several years, the foremost SETI Program goal is the development of a SETI Breadboard Instrument. This article describes the SETI Program Plan and current SETI Breadboard Instrument development activities.

I. Introduction

Serious scientific concern with the possibility of detecting extraterrestrial intelligence dates back at least to 1959, when Cocconi and Morrison published (Ref. 1) a paper entitled "Search for Interstellar Communications." Additional scientific papers on this subject were published during the 1960s. In the 1970s, more intensive and formal studies of the subject were conducted. Notable during this time frame were study efforts which are documented in "Project Cyclops: A Design Study of a System for Detection of Extraterrestrial Life" (Ref. 2) and "The Search for Extraterrestrial Intelligence (SETI)" (Ref. 3). During the late 1970s, intensive effort was undertaken at the Jet Propulsion Laboratory (JPL) and Ames Research Center (ARC) to obtain the initiation of a formal SETI (Search for Extraterrestrial Intelligence) Program under NASA sponsorship. Starting in fiscal (FY) 1980, such a program has come into existence. The NASA SETI Program is a Supporting Research and Technology (SR&T) effort with primary thrust to search the microwave region of the spectrum for signals of extraterrestrial intelligent origin. The SETI Program is managed by the Life Sciences Division of NASA's Office of Space Sciences, and within the Life Sciences Division, is an element of the Life in the Universe Program.

Initially, the foremost goal of the SETI SR&T Program is the development of a SETI Breadboard Instrument. Beyond the SR&T effort, the goal of the SETI Program will be the exploration of a well-defined volume of multidimensional microwave search space using large existing radio telescopes and a new technologically sophisticated data acquisition and analysis system (Berman, Ref. 4, Gulkis et al., Ref. 5). The approach of this SETI search includes two major components – a "target survey," which will observe at high sensitivity

all attractive star candidates within 25 parsecs of the sun, and a "sky survey," which will observe the entire celestial sphere at a somewhat lower sensitivity. The sky survey will cover all frequencies between 1 and 10 GHz, while the target survey will cover the frequency range 1 to 3 GHz.

II. The SETI SR&T Program

The SETI SR&T Program mode is expected to operate for approximately 5 years. During this time period, the specific goals of the SETI SR&T Program are:

(1) Develop a fully functional SETI Breadboard Instrument.

(2) Evaluate the SETI Breadboard Instrument field experience to determine the most cost-effective method to implement a Microwave Observing Program (MOP).

(3) Carry out limited but significant SETI observations.

The SETI Breadboard Instrument will be operated primarily with radio telescopes at DSS 13 and Arecibo, Puerto Rico, with some considerably smaller usage on the DSN 64- and/or 34-m radio telescopes. The SETI Breadboard Instrument will initially be 74K channels single polarization, and during the SR&T Program will be upgraded in four phases to 500K channels dual polarization. Although only a single breadboard instrument is being developed, it will, during the various phases of development, contain functional capabilities pertaining to both sky survey and target survey modes. In particular, Phase III will emphasize the sky survey mode, while Phase IV will support the target survey mode.

High-level functional requirements for the SETI Breadboard Instrument during the planned 4 phases of development during the SR&T Program are as follows:

(1) Phase I Breadboard Instrument
   (a) 74-kHz bandwidth/1-Hz resolution
   (b) 1024-Hz, 32-Hz, 1-Hz outputs
   (c) Single polarization

(2) Phase II Breadboard Instrument
   (a) 74-kHz bandwidth/1-Hz resolution
   (b) 1024-Hz, 32-Hz, 1-Hz outputs
   (c) Dual polarization

(3) Phase III Breadboard Instrument
   (a) 4-MHz bandwidth/32-Hz resolution
   (b) 74-kHz/1-Hz resolution
   (c) 1024-Hz, 32-Hz, 1-Hz outputs
   (d) Dual polarization

(4) Phase IV Breadboard Instrument
   (a) 4-MHz bandwidth/32-Hz resolution
   (b) 500-kHz bandwidth/1-Hz resolution
   (c) 1024-Hz, 32-Hz, 1-Hz outputs
   (d) Dual polarization

III. SETI Breadboard Instrument Development

A. SETI Breadboard Instrument – System Development

The goals of the SETI Breadboard Instrument system development are described as follows:

(1) The rapid development of a SETI Breadboard Instrument and subsequent integration with Deep Space Station equipment, thus allowing the timely acquisition of SETI field experience in an operational environment.

(2) The carrying out of limited but significant SETI observations.

In seeking to accomplish the above goals, the SETI Breadboard Instrument system will be implemented according to the following precepts:

(1) Utilization to the highest degree of existing Deep Space Station equipment.

(2) Allocation of the majority of SETI resources to the development of the Multichannel Spectrum Analyzer and Signal Processor – the SETI areas which require development of new technology.

Figure 1 presents a simplified block diagram of the SETI Breadboard Instrument system at DSS 13. As is seen, the front end, including antenna mechanical, antenna microwave, Block III receiver, and noise adding radiometer, are existing DSS 13 equipment. The portion of the SETI Breadboard Instrument system (i.e., the "SETI Breadboard Instrument") currently under development includes the SETI downconverter, the analog-to-digital converter (ADC), the Multichannel Spectrum Analyzer (MCSA), and the SETI Signal Processor (initially the "SETI Computer").

The development of the SETI signal processing functions will be started by using the breadboard equipment to generate and store real-time data. Non-real-time test algorithms will

evaluate this data and be utilized to determine the most efficient approach to the signal processing tasks. Once a signal processing task (e.g., developing a baseline for the data that removes instrument gain variation, applying threshold tests to the data, dedrifting CW signals, etc.) has been successfully tested, a hardware version will be developed. As the Signal Processor's special hardware is developed, the SETI Computer will move toward real-time data analysis, instead of the "snapshotting" of data and subsequent processing.

The phased SETI Breadboard Instrument development will provide the total experience necessary to design a technically capable and cost-effective operational SETI Instrument. In particular, new advances anticipated in the area of very large scale integration (VLSI) can be expected to play a significant role in the operational SETI Instrument.

B. SETI Breadboard Instrument Phased Development

1. Phase I. The Phase I SETI Breadboard Instrument will have a 74-kHz passband, single polarization, with 1024-, 32-, and 1-Hz outputs. Signal identification will be accomplished via software using the SETI Computer. This breadboard configuration represents a narrow profile in the frequency domain of either a sky survey or target survey type instrument. Figure 2 presents a functional block diagram of the Phase I configuration.

2. Phase II. Phase II augments the SETI Breadboard Instrument in two significant ways, as follows:

(a) Baseline and threshold algorithms will be implemented in high-speed, special-purpose hardware that is capable of operating at the data rates envisioned for the fully operational SETI Instrument.

(b) A second channel will be added to allow dual polarization signals for usage in the evaluation of SETI identification algorithms.

Figure 3 presents a functional block diagram for the Phase II SETI Breadboard Instrument.

3. Phase III. In Phase III, the 1024- and 32-Hz resolution outputs are increased from 74 kHz to 4 MHz, thus allowing the first significant sky survey observations. In addition, the Signal Processor development of Phase II is continued by the addition of a pulse detector module. Figure 4 presents the functional block diagram of the Phase III SETI Breadboard Instrument.

4. Phase IV. Phase IV completes the SETI Breadboard Instrument by adding a module to dedrift CW signals and expanding the passband capability of the 1-Hz output resolution from 74 kHz to 500 kHz, thereby providing the ability to make the first significant target survey observations, as well as performing all signal identification in special-purpose signal processing hardware. Figure 5 presents a functional block diagram of the Phase IV SETI Breadboard Instrument.

C. SETI Breadboard Instrument Development Status

The SETI Breadboard Instrument development was begun in mid-1980, and has been previously reported on by Crow (Ref. 6). Delivery of the completed SETI Phase I Breadboard Instrument is scheduled for mid-1982. The SETI-peculiar equipment that is currently under development is the SETI downconverter, analog-to-digital converter (ADC), Multichannel Spectrum Analyzer (MCSA) and the SETI Computer.

The SETI Computer (a PDP 11/44) has been received and is currently being installed. Remote operating terminals will be provided to allow the SETI Science Team to utilize the SETI Computer from remote locations both at JPL and ARC. The SETI downconverter and analog-to-digital converter have been fabricated and are currently undergoing subsystem testing. The Multichannel Spectrum Analyzer development is currently in the module fabrication phase and is scheduled for shipment to JPL in early 1982.

Acknowledgement

The authors would like to thank Dr. M. J. Klein for many excellent suggestions and comments.

References

1. Cocconi, G., and Morrison, P., "Searching for Interstellar Communications," *Nature*, Vol. 184, pp. 844, 1959.
2. Oliver, B.M., and Billingham, J., Project Cyclops, NASA Document CR114445, 1973.
3. Morrison, P., Billingham, J., and Wolfe, J., *The Search for Extraterrestrial Intelligence SETI*, NASA Publication SP-419, 1977.
4. Berman, A. L., "The SETI Observational Plan," in *The TDA Progress Report 42-57*, Jet Propulsion Laboratory, Pasadena, California, 15 June 1980, pp. 9-15.
5. Gulkis, S., Olsen, E. T., and Tarter, J., "A Bimodal Search Strategy for SETI," in *The TDA Progress Report 42-59*, Jet Propulsion Laboratory, Pasadena, California, 15 October 1980, pp. 23-32.
6. Crow, B., "The SETI Instrument Development Plan," in *The TDA Progress Report 42-59*, Jet Propulsion Laboratory, Pasadena, California, 15 October 1980, pp. 15-22.

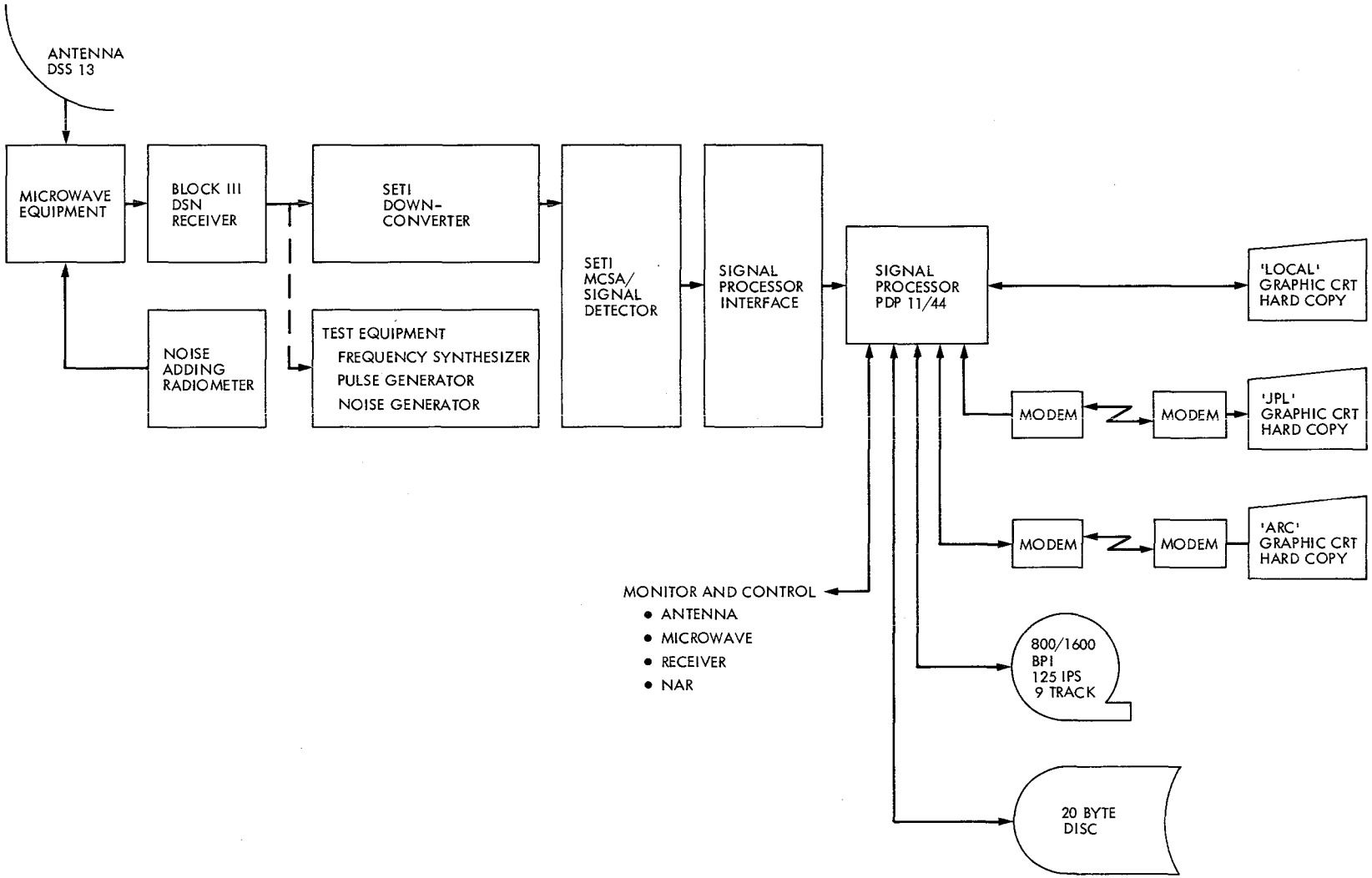

Fig. 1. SETI Breadboard Instrument system functional block diagram

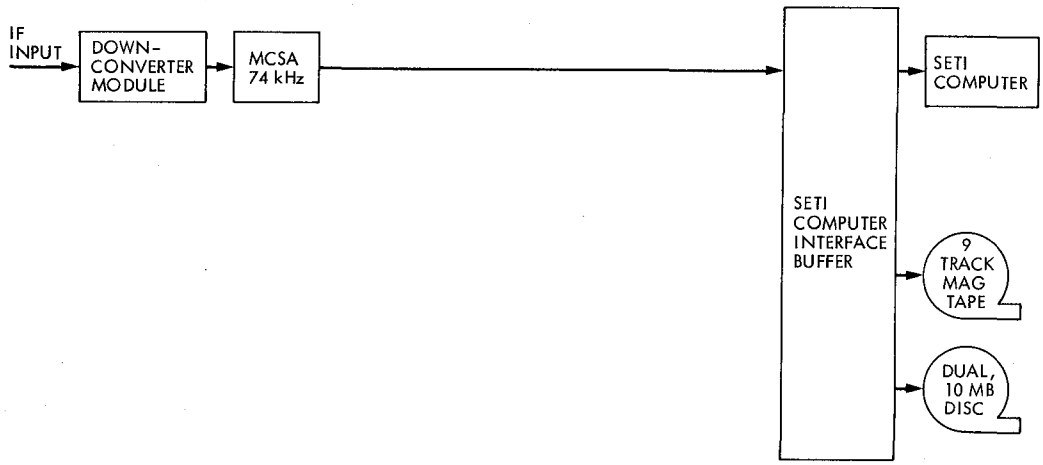

DATA TYPE	BW	RESOLUTION
POWER	74 kHz	74 kHz, 1024 Hz, 32 Hz, 1 Hz
COMPLEX VOLTAGE	74 kHz	1024 Hz, 32 hz, 1 Hz
ACCUMULATION POWER	74 kHz	1024 Hz, 32 Hz, 1 Hz

Fig. 2. Phase I SETI Breadboard Instrument functional block diagram

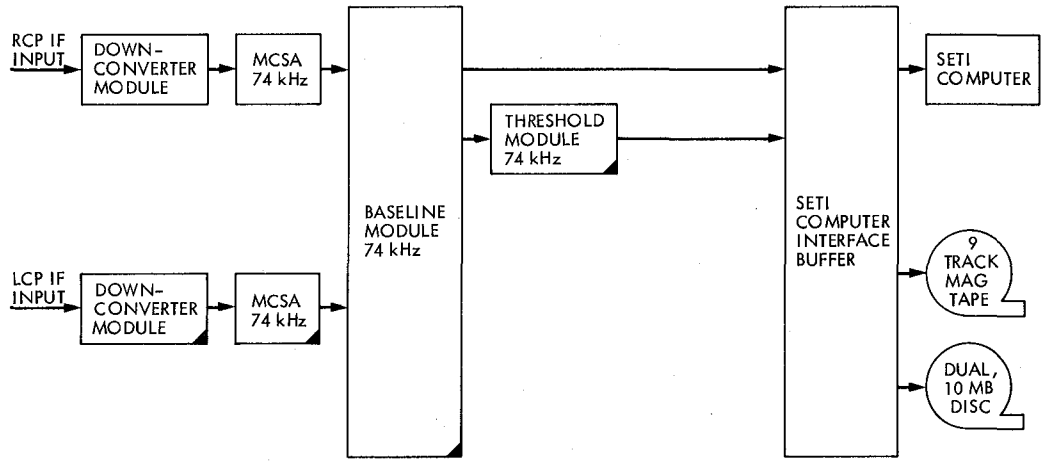

DATA TYPE	BW	RESOLUTION
POWER	74 kHz	74 kHz, 1024 Hz, 32 Hz, 1 Hz
COMPLEX VOLTAGE	74 kHz	1024 Hz, 32 Hz, 1 Hz
ACCUMULATION POWER	74 kHz	1024 Hz, 32 Hz, 1 Hz

= PHASE II UPGRADE

Fig. 3. Phase II SETI Breadboard Instrument functional block diagram

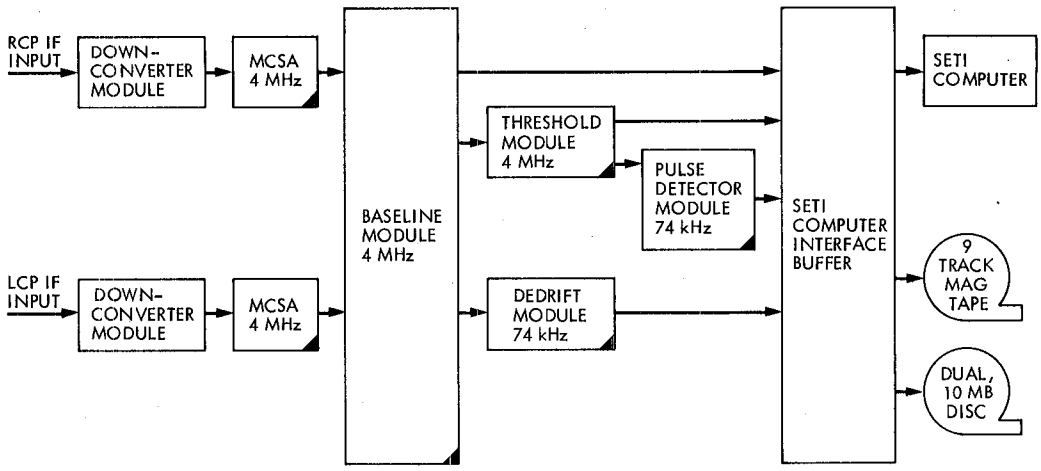

DATA TYPE	BW	RESOLUTION
POWER	4 MHz 74 kHz	74 kHz, 1024 Hz, 32 Hz 1 Hz
COMPLEX VOLTAGE	4 MHz 74 kHz	1024 Hz, 32 Hz 1 Hz
ACCUMULATION POWER	4 MHz 74 kHz	1024 Hz, 32 Hz 1 Hz

◢ = PHASE III UPGRADE

Fig. 4. Phase III SETI Breadboard Instrument functional block diagram

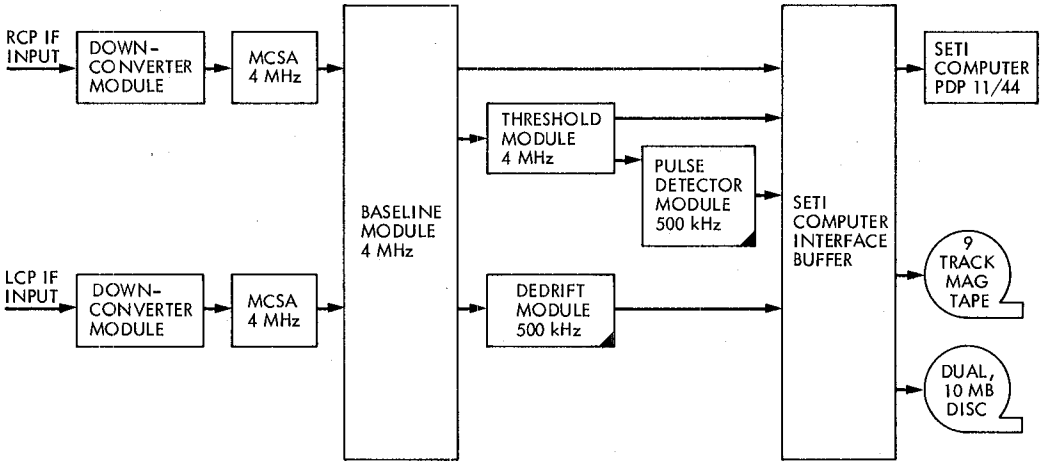

DATA TYPE	BW	RESOLUTION
POWER	4 MHz 500 kHz	74 kHz, 1024 Hz, 32 Hz 1 Hz
COMPLEX VOLTAGE	4 MHz 500 kHz	1024 Hz, 32 Hz 1 Hz
ACCUMULATION POWER	4 MHz 500 kHz	1024 Hz, 32 Hz 1 Hz

◢ = PHASE IV UPGRADE

Fig. 5. Phase IV SETI Breadboard Instrument functional block diagram

Project ORION Microwave Subsystem Design

D. L. Gannon
Spacecraft Telecommunications Equipment Section

The proposed design for the Microwave Subsystem of Project ORION is presented. Performance characteristics and subsystem capabilities are discussed. Functional requirements and key performance parameters are stated for the subsystem as well as a proposed schedule of events.

I. Introduction

The ORION (Operational Radio Interferometry Observing Network) mobile system is being implemented in support of the NASA Crustal Dynamics Project. The purpose of the system is to provide a means for measurement of length and orientation of vectors between sites located in areas of geophysical interest. This is accomplished by using Very Long Baseline Interferometry (VLBI) techniques operating at microwave frequencies using extragalactic radio sources. For an overview of the functional requirements and system capabilities of the entire ORION system the reader should refer to *TDA Progress Report 42-60,* pages 6 through 32.

The Microwave Subsystem (MWS) of ORION is one of nine subsystems that make up the mobile unit. The functional requirements of the MWS are as follows:

(1) Receive and amplify S- and X-band signals from the Antenna Subsystem (AS).

(2) Provide coupling for the S- and X-band phase calibration tones.

(3) Provide performance monitoring information to the Monitor and Control Subsystem (MCS).

The MWS consists of the S- and X-band feeds, S- and X-band low noise amplifiers (LNA), a frequency selective subreflector (FSS), and cooling assemblies. A block diagram of the MWS is shown in Figure 1.

II. Performance Parameters

Table 1 lists the performance parameters of the MWS as stated by the ORION Mobile Station Functional Requirements Document (1700-2).

III. Design Requirements

In order to meet or exceed the performance specified for the MWS, the following design requirements became necessary. To allow adequate description of the entire design the MWS was divided into the following subassemblies:

(1) X-band LNA

(2) S-band LNA

(3) Cryogenic cooling system

(4) Thermoelectric cooling system

(5) S- and X-band feeds

(6) Frequency selective subreflector

(7) Microwave transmission components

Figure 2 shows each assembly and its relationship to the Antenna Subsystem (AS).

A. X-Band LNA

To meet the performance requirement of 110 K zenith system noise temperature for X-band it is required that the X-band LNA have an equivalent noise temperature of approximately 60 K. This value of noise may only be reached by cryogenically cooling a GaAs FET amplifier to a physical temperature of 20 K if the large bandwidth requirement is also to be met. Standard off-the-shelf GaAs FET LNA's cannot be cooled to the physical temperature of 20 K as proposed in this design. The LNA must therefore be specially built to withstand this low temperature. The detailed design steps taken to achieve this are beyond the scope of this report, but Table 2 lists the basic LNA specifications for this application. Minimum mass and power dissipation are also important to the design to have the lowest possible load on the cryogenic refrigerator.

B. S-Band LNA

In order to meet the performance requirement of 160 K zenith system noise temperature for S-band, the S-band LNA must have an equivalent noise temperature of approximately 75 K. This noise temperature is not as difficult to achieve as in the case of X-band, but physical cooling of a GaAs FET is required. The noise temperature specification can be met by cooling the LNA to -50°C. This is done using thermoelectric cooling devices arranged in multiple stages. This design will be discussed in a later section. Table 3 lists the basic LNA specifications for S-band. As with X-band, the S-band LNA must also have minimum mass and low power dissipation.

C. Cryogenic Refrigeration System

Figure 3 can be referred to in the following description of the Cryogenic Refrigeration System. The system is a basic closed-cycle helium refrigeration unit consisting of a compressor, a refrigerator, and a roughing (evacuation) pump. The refrigerator has two stages which produce a temperature of 20 K at one cold station and 77 K at the other. The X-band LNA is located at the 20 K station. The cold stations and LNA are contained in an evacuated dewar to minimize the ambient heat loss. The dewar is evacuated using the roughing pump and a solenoid-controlled vacuum valve. Locations of the 3 parts of this system are shown in Fig. 4.

D. Thermoelectric Cooling System

A block diagram of a thermoelectric cooling system can be found in Fig. 3. It consists of a cold plate, a multistage thermoelectric heat pump, a heat sink/fan, and a temperature control unit. The S-band LNA is attached to the cold plate by a method that assures good thermal conduction. DC current is then applied to the thermoelectric module, which is also attached to the cold plate. The thermoelectric module draws heat from the LNA and deposits that heat to the heat sink on the opposite side. The fan dissipates heat from the heat sink. A temperature control unit can maintain a temperature of 50 $\pm 0.3^{\circ}$C for the LNA by changing the current supplied to the cooling module. The LNA is enclosed in foam insulation to minimize the ambient heat load. The location of the S-band LNA and thermoelectric control unit can be seen in Figs. 2 and 4.

E. S- and X-Band Feeds

The feed configuration implemented for ORION is a dual-frequency, Cassegrain X-band, focal point S-band design with a dichroic hyperbolic subreflector. The subreflector design will be discussed in the next section. Figure 2 shows the locations and dimensions of the two feeds. The X-band feed assembly includes a transformer which extracts right-hand circularly polarized (RHCP) energy from the incoming energy and has an output compatible to WR112 waveguide. The energy is then channeled to the refrigerator through WR112 waveguide and then transformed to coax cable for amplification by the X-band LNA. The S-band feed is located within the subreflector assembly as shown in Fig. 2. It also gives an output of RHCP for transmission to the S-band LNA located beside it, as shown. Both the S- and X-band feed are designs derived from the Voyager project.

F. Frequency Selective Subreflector (FSS)

The primary purpose of the FSS is to reflect X-band energy and pass S-band energy. The subreflector is an unshaped hyperboloid of dimensions given in Fig. 2. The front skin of the FSS is Mylar with etched aluminum dipoles that reflect X-band. The X-band reflective loss is approximately 0.1 dB while the S-band transmission loss is 0.28 dB for a single layer FSS. Double layers can be used to lower the S-band loss, if required. The FSS assembly will support the S-band feed and the S-band LNA including the thermoelectric cooling assembly. These items will be enclosed in a plastic cover for weatherproofing purposes, as shown in Fig. 2.

G. Microwave Transmission Components

These components of the MWS were chosen on the basis of low loss, high durability, and the interface requirements of the MWS with other subsystems.

1. **Coax cable.** Three types of coax cable are used in the MWS. Each cable has 50-ohm characteristic impedance and a foam dielectric. Coax cable of 0.141-in.-diameter is used within the thermoelectric enclosure. This cable is made of stainless steel for low thermal conductivity. Copper 0.358-cm (0.141-in.) coax cable is used from the input transition of the X-band LNA to the LNA itself. This is implemented for high

thermal conductivity. The third cable used in the MWS is 1.27-cm (0.5-in.) diameter coax cable with a copper-clad center conductor, an aluminum outer conductor, and a plastic covering on the outside for weatherproofing purposes. This cable runs from both LNA's to the receiver, as shown in Fig. 1.

2. **Waveguide.** Solid copper WR112 waveguide is used from the OMT to the X-band input at the refrigerator. This waveguide offers the lowest possible X-band loss.

3. **Phase calibration inputs.** Phase calibration inputs are provided at the inputs and the outputs of the two LNA's. At the input of the X-band LNA a 30-dB crossguide coupler with an "N" type input is implemented for signal insertion purposes. At the output of the X-band LNA a 30-dB coaxial directional coupler is used for signal insertion. Coaxial directional couplers of the same value (30 dB) are also implemented for S-band at the input and output of the LNA.

4. **Coaxial switches.** Coaxial switches are provided for S- and X-band to enable the phase calibration signal to be input either before or after the respective LNA's.

IV. Noise Budget

Table 4 summarizes the estimated noise for the MWS at zenith. According to these estimates both the S- and X-band noise requirements can be met.

V. Monitor and Control Interface

Table 5 summarizes the proposed monitor and control points for the MWS. Interface between the MWS and the MCS will be via RS-232 under a format provided by the MCS. The MCS will provide automatic operation of all parts of the MWS and will monitor the subsystem status of operation.

VI. Subsystem Startup

The following is an MWS startup procedure. The sequence of events will remain the same but times between events will change depending on the weather and the operating condition of the subsystem components.

(1) Arrive at the site

(2) AC and DC power available

(3) X-band cool-down:

  (a) Roughing pump ON for 30 seconds

  (b) Open vacuum valve

  (c) Pump dewar to 50 microns vacuum

  (d) Turn on compressor

  (e) Turn on refrigerator

  (f) Close vacuum valve at 10 microns, shut off roughing pump

  (g) Allow LNA to reach 20 K

  (h) Turn on LNA

  (i) Monitor performance

(4) S-band cooldown (simultaneous to X-band)

  (a) Turn on thermoelectric control unit

  (b) Allow LNA to reach -50°C

  (c) Turn on LNA

  (d) Monitor performance

VII. Schedule of Events

Figure 5 is a proposed time schedule for implementing the MWS. It is designed to conform with the Work Breakdown Schedule for the subsystem and will allow integration of the MWS with the entire system on schedule.

VIII. Conclusion

The proposed design of the Microwave Subsystem for ORION meets the functional requirements previously set forth. The zenith system noise temperature at X-band is estimated to be close to the functional requirement of 110 K, so this requirement may have to be relaxed at some future date. The S-band requirement of 160 K at zenith should be met. Details such as weatherproofing and operation at low outdoor temperatures are now being considered to complete the design of the subsystem.

Table 1. Microwave Subsystem performance parameters

Performance requirements	Requirement
Input frequencies	8180 to 8600 MHz (–3 dB) 2220 to 2320 MHz (–3 dB)
Antenna efficiency	
S-band	⩾0.40
X-band	⩾0.50
Polarization	RCP (right circular polarization)
Zenith system noise temperature	
S-band	⩽160 K
X-band	⩽ 110 K
Low noise amplifier gain	33 +3, –0 dB
Interfaces	
Signal output	–105 to –65 dBm (33 dB LNA)
Phase calibration output	–30 dBm
Monitor and control	RS 232C
Power requirements	105 to 130 VAC 1ϕ, 1736 W avg, 2276 peak

Table 2. X-band low noise amplifier

Frequency	8180 to 8600 MHz (3 dB BW)
Gain	33 dB minimum at 77 K (LN_2 temperature)
Flatness	±0.50 dB
Gain stability	±0.50 dB per 8 hours
Noise temperature (All noise figures at 77 K cooling)	50 K (design goal) 60 K (expected) 85 K (maximum
1-dB compression	+3 dBm (output power minimum)
Input and output impedance	50 ohms
Connectors	Power: solder turrets RF: SMA female
Input VSWR	⩽1.5:1
Output VSWR	⩽1.5:1
Power dissipation	0.5 watts (maximum)
Maximum overall dimensions	10.16 cm (4.0 in.) L 3.81 cm (1.5 in.) W 1.778 cm (0.7 in.) H (excluding connectors)

Table 3. S-band low noise amplifier

Frequency	2220 to 2320 MHz (3 dB BW)
Gain	33 dB minimum
Flatness	±0.50 dB
Gain stability	±0.50 dB for 8 hours
Noise temperature	40 K (design goal at –50°C) 60 K (max at –50°C) 75 K (at 25°C)
Cooling	4-stage thermoelectric to (–50°C)
1-dB compression	+3 dBm (output power minimum)
Imput and output impedance	50 ohms
Input/output VSWR	⩽1.5:1
Connectors	Power: solder turrets RF: SMA female
Power dissipation	0.5 watts (maximum for amp only)
Maximum dimensions	10.16 cm (4.0 in.) L 3.81 cm (1.5 in.) W 1.778 cm (0.7 in.) H

Table 4. Estimated noise

		Contribution
(1) X-band (Cassegrain):		
Estimated antenna noise w/struts	=	10 K
FSS blockage	=	6 K
FSS reflective loss	=	6.7 K
Orthomode transducer	=	1 K
WR112 waveguide to LNA	=	4 K
Pressure window and input trans.	=	3 K
Low noise amplifier	=	60 K (expected)
Directional couplers	=	3 K
Cable from LNA to receiver	=	1 K
Estimated system temperature		95 K
(2) S-band (LNA at focus):		
Estimated antenna noise w/struts	=	27 K
FSS blockage/dissipation	=	25 K
Cable from feed to LNA	=	9 K
Low noise amplifier	=	60 K
Directional couplers	=	14 K
Cable from LNA to receiver	=	1 K
Estimated system temperature	=	136 K

Table 5. Monitor and control points

Monitor points	Control points
(1) Dewar vacuum	(1) Refrigerator on/off
(2) LNA temperatures (2)	(2) Compressor on/off
(3) Helium supply pressure	(3) X-band LNA on/off
(4) Helium return pressure	(4) S-band LNA on/off
(5) Helium tank pressure	(5) Evacuation valve open/close
(6) LNA current (2)	(6) X-band coax switch
(7) Compressor temperature	(7) S-band coax switch
(8) Instrumentation power supply	(8) Roughing pump on/off
	(9) Thermoelectric cooling on/off

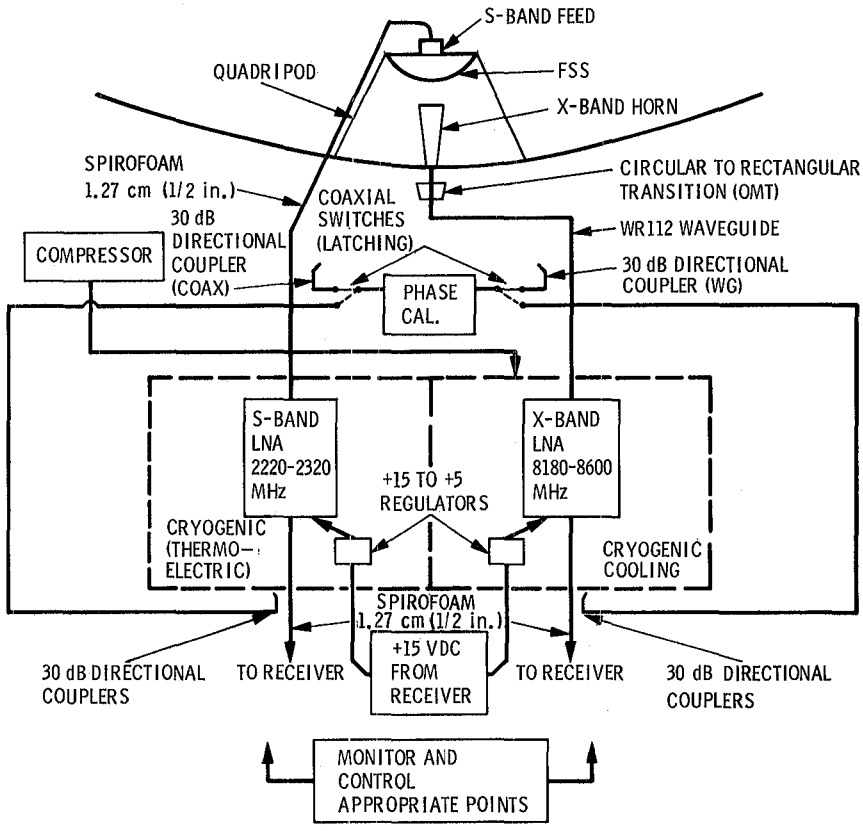

Fig. 1. Microwave Subsystem block diagram

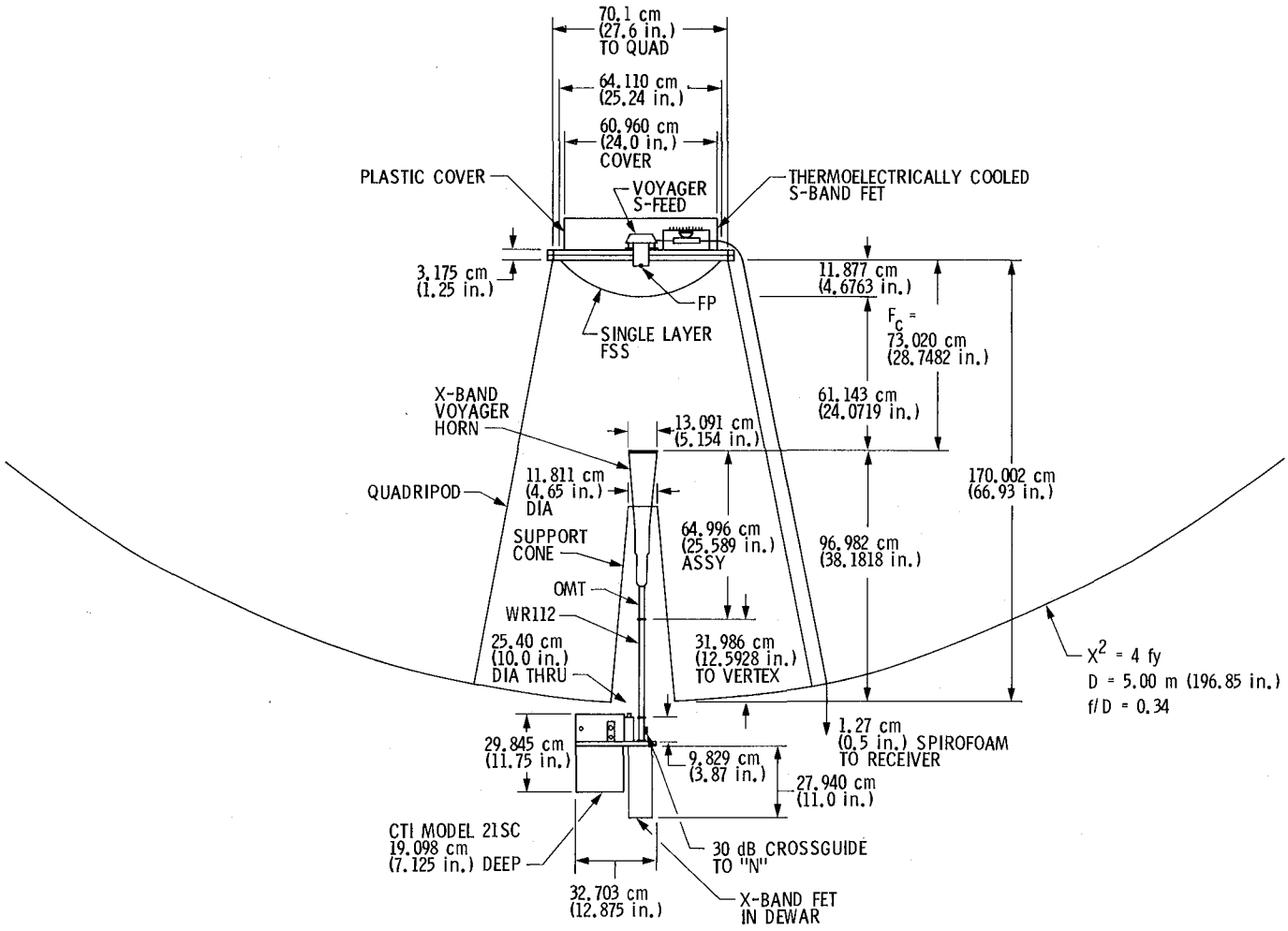

Fig. 2. Project ORION antenna layout

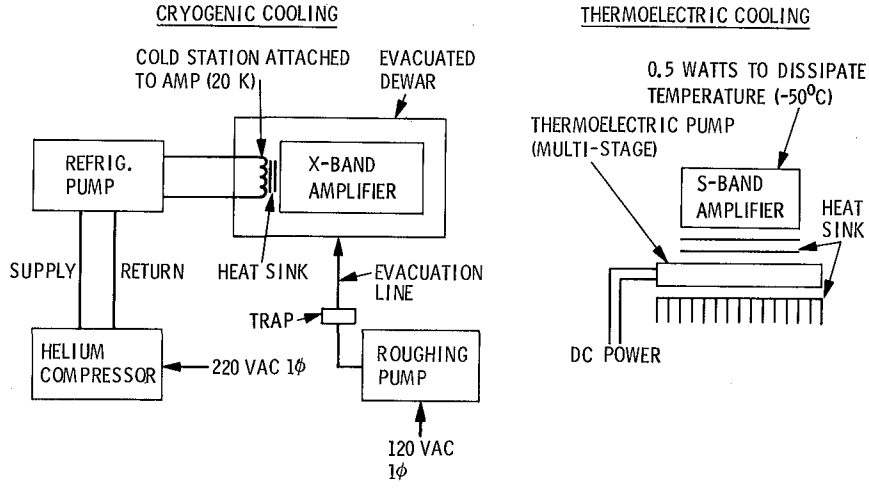

Fig. 3. Refrigerator block diagrams

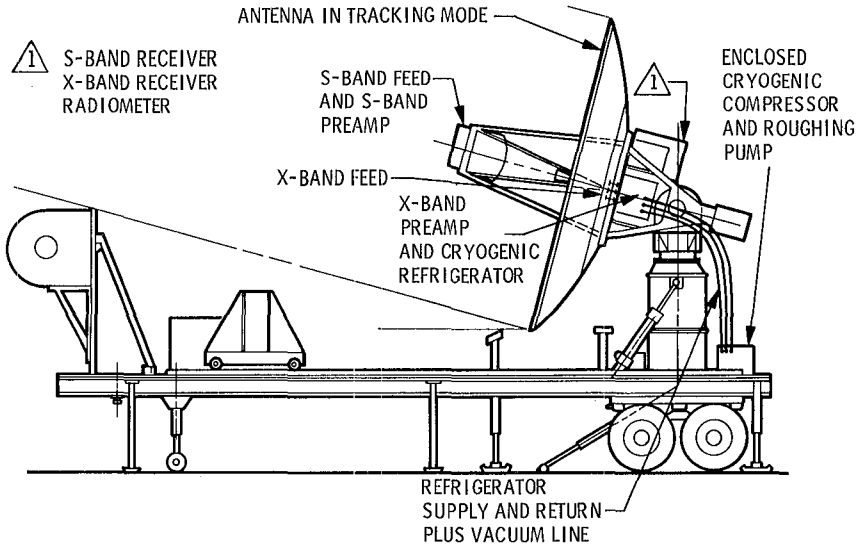

Fig. 4. Microwave Subsystem layout on transporter

	MILESTONES	1981 J	F	M	A	M	J	J	A	S	O	N	D	1982 J	F	M	A	M	J	J	A	S	O	N	D
1	SUBSYSTEM REVIEW				▲																				
2	PRELIMINARY SPECIFICATIONS					▲																			
3	LNA's CONTRACT/DELIVERY					△	▬	▬	▬	▬	▬	▬	▬	▬	▬	△									
4	CRYOGENIC CONTRACT/DELIVERY						△	▬	▬	▬	▬	△													
5	CRYOGENIC ON-LAB INTEGRATION											△	▬	▬	△										
6	FSS CONTRACT/DELIVERY							△	▬	▬	▬	▬	▬	▬	▬	△									
7	MWS CABLE FABRICATION							△	▬	▬	▬	▬	▬	▬	▬	△									
8	S-AND X-BAND FEED FABRICATION/RECEIVED							△	▬	▬	▬	▬	▬	▬	▬	△									
9	INTEGRATION READINESS																△								
10	ANTENNA TEST START/COMPLETE																			△	▬	▬	△		
11	FINAL SPECIFICATIONS/DRAWINGS																			△					
12	FINAL O&M/TEST PROCEDURE																			△					
13																									
14																									
15																									
16																									
17																									
18																									
19																									
20																									
21																									

△ SCHEDULED COMPLETION
▲ COMPLETED ON SCHEDULE
▬ FABRICATION/INTEGRATION

JPL 1470-S 8/73

Fig. 5. Schedule of events

Narrow Channel Bandwidth Receiver for VLBI

E. N. Sosa, T. Sato, and D. A. Tyner
Radio Frequency and Microwave Subsystems Section

An introduction to the Phase 4 Receiver Subsystem to be implemented into the DSN for VLBI applications is presented. The key design areas are discussed along with the design approach. Preliminary evaluation data indicate that a feasible, straightforward design may be obtained.

I. Introduction

Navigation techniques utilizing very long baseline interferometry (VLBI) were successfully demonstrated in 1979 using the Voyager spacecraft near Jupiter encounter. Since this demonstration, which essentially used existing receiving and processing equipment, a series of improvement phases have been in progress to arrive at a major phase (Phase 4) that will implement the receiver described below. The configurations of phases 1, 2, and 3 were unchanged with respect to the receiver and the principal changes were related to the Network Operational Control Center and VLBI Processing Area. The Phase 4 receivers operate at both S- and X-band and will replace the DSS Block IV receivers for this application.

The Phase 4 receiver being developed employs double conversion and narrowband filtering to permit the utilization of tape recording and/or data transmission lines that operate in the audio and video frequency range. The first downconverter takes the RF signals down to IF, and the second downconverter converts the IF signals to video frequencies. The problem with the above scheme is that image noise foldover becomes an important consideration. To overcome this problem, a single sideband (SSB) down-conversion technique is used, but the complete IF-to-video down conversion is comprised of analog and digital techniques. This combination provides good spectrum rejection to prevent image noise foldover and also provides low-amplitude ripple and phase ripple, which are necessary to meet system requirements. The receiver subsystem is required to furnish only the analog portion of the IF-to-video downconverter, i.e., two video signals in quadrature, 0 and -90 deg, to the Radio Science Subsystem (DRS). In turn, DRS will use digital techniques to generate the second -90-deg phase lag and summation to accomplish the image rejection and the low phase ripple. Another significant feature of this new receiver is its low phase noise and small phase dispersion contributions to the down-converted signal. This is necessary to limit the group delay error to the desired signals.

A general description of this receiver is given below along with more detailed description of its principal components.

II. Design

The open-loop receiver under development for Phase 4 is characterized by double conversion, high phase stability, and output channels in quadrature. In addition, the receiver will be

operable from a central facility for controlling and monitoring, and will be capable of unattended operation. The receiver subsystem comprises two independent receivers for simultaneous S- and X-band reception. Each of these receivers has independent IF-to-video downconverters. Within a span bandwidth of 100 MHz and 40 MHz for the X- and S-band, respectively, eight narrowband data channels will be available for X-band and four for S-band. An important characteristic of the analog portion of the IF-to-video downconverter is the use of 12 digitally controlled local oscillators. This design maintains continuous operation of the individual oscillators and ensures that signal phase continuity of the individual channels is preserved as they are multiplexed during observations of either radio star or spacecraft signals. A simplified block diagram illustrating the principal components of the receiver is shown in Fig. 1, and the receiver subsystem design parameters are given in Table 1. Of these, the critical ones are the quadrature channel balance (which relates to image rejection and low phase ripple) and the phase stability.

To meet the design goals of the receiver subsystem, the initial approach is to modify the existing front end of the multimission receiver (MMR) and to generate a new design for the analog portion of the IF-to-video downconverter. A significant part of IF-to-video downconverter task comprises the selection of the synthesizers that serve as local oscillators. Because there are 12 synthesizers per X- and S-band IF-to-video downconverter, a total of 36 synthesizers plus spares will be required for three 64-m station sites. Therefore, the design approach had to include an evaluation program to arrive at a cost-effective synthesizer. The evaluation of the synthesizers is currently in progress and will be completed in August.

While the IF-to-video downconverter is primarily concerned with the phase quadrature and amplitude imbalance requirements, the local oscillators and mixers are the main concern with respect to the phase stability. Simplified models of the receiver subsystem have been generated (Refs. 1 and 2), and these have been discussed in terms of phase-error contributions. The phase error as a parameter is of interest because it is involved directly in the VLBI application. Unfortunately, phase error as a function of integration time is not a criterion used in the industry with respect to specifying mixer and local oscillator performance. Single sideband spectral density in the frequency domain and frequency deviation in the time domain are widely used as performance criteria by industry. Fractional-frequency deviation measurements are presently being used to measure the stability of receiver components and these measurements can be directly related to the stability of the hydrogen maser. Therefore, a frequency stability technique is desired for the measurement of receiver subsystem stability. Attempts to generate a sufficiently accurate frequency-to-phase transformation are in progress. Success in generating the transform will permit verification that the frequency stability of the receiver subsystem is in keeping with the phase error required in the VLBI application.

Using a simplified model of the receiver subsystem (as in Refs. 1 and 2) a fractional-frequency deviation analysis has been made to generate stability criteria for the synthesizers and to relate the frequency stability of the subsystem to a phase error as a function of time. This analysis is given in the Appendix. A simple frequency-to-phase transformation was used, and the results indicated the receiver subsystem was close to the range of the desired phase stability. While more refinement is still in progress with respect to relating the frequency deviation and the phase error, the analysis has given sufficient confidence for going forward toward the building of breadboard assemblies that would support the design goals given in Table 1.

The other components of the receiver subsystem are considered to be straightforward in design and will not be described in this report. However, the initial design of the receiver subsystem including all the components is shown in Fig. 2.

A. IF-to-Video Downconverter

The analog section of the IF-to-video downconverter is a four-port assembly consisting of two inputs and two outputs. One input is the IF signal and the other is the LO signal from the Synthesizer Subassembly. The outputs are two identical video frequency signals possessing a phase shift of approximately 90 deg between them and having nearly equal amplitudes. These outputs are subsequently delivered to the digital subsystem. The block diagram of the analog portion of the downconverter is shown in Fig. 3 and the key design goals of the analog section are given in Table 2. To limit the noise contribution of the suppressed sideband to the desired signal, a system requirement of 23-dB image rejection ratio has been imposed. The method of implementing the IF-to-video downconverter function is described by Weaver (Ref. 3) and image rejection ratio and phase ripple characteristics of the outputs are dependent on the amplitude and phase balance of the components comprising the converter. The image rejection ratio, I, in terms of amplitude and quadrature imbalance components, is given by

$$I = 10 \log \left(\frac{A_1^2 + A_2^2 + 2 A_1 A_2 \cos \delta}{A_1^2 + A_2^2 - 2 A_1 A_2 \cos \delta} \right) \qquad (1)$$

in which A_1 and A_2 are the amplitudes of the two signals in quadrature and δ denotes their phase difference. The analog portion of the phase and amplitude imbalance is given in Table 2.

To investigate the manner in which the respective imbalance of each component contributes to the overall performance, a partial model of the analog section was assembled using available parts. The antialiasing filters and video amplifiers were not included due to the unavailability of suitable filters with a cutoff frequency of 300 kHz. Figure 4 is the block diagram of the test assembly used for initial design parameter measurements. Low-pass filters with 150-MHz cutoff frequency were used to eliminate the upper sideband from the inputs to the gain-phase meter.

Amplitude and phase data were measured by setting the signal levels for maximum beat note amplitude. In Fig. 5 are shown the measured relative phase shift and the amplitude ratio of the 250-kHz beat note output from the test assembly.

The amplitude imbalance is 0.1 dB over the band 265 MHz to 400 MHz. The observed differential phase shift is within 90 ±2 deg. Maximum image rejection is obtained when the differential phase shift is 90 deg assuming the digital subsystem processes the signal ideally. Data were taken also across small (0.2-MHz) frequency increments over selected portions of the band. These data indicate both amplitude and phase characteristics were free of rapidly varying ripples. The experimental data generated with the test assembly are expected to degrade somewhat when the low-pass filter and video amplifiers are included. However, the experimental data taken with the test assembly indicate that with the use of components selected for closer tolerance, the present design objectives of 90 ±4 deg, ±0.4 dB, and ±0.75 deg for phase shift, amplitude balance, and phase ripple respectively, can be achieved.

B. Synthesizer Subassembly

The technique of bandwidth synthesis (BWS), used in determining group delay in narrow channel bandwidth VLBI, requires a controlled selection of stable signal sources, used as local oscillators, into the IF-to-video downconverter. A block diagram depicting the control and use of the synthesizers is shown in Fig. 6. A digital control interface to the receiver controller provides the controlling and monitoring functions to this subassembly. Time tagged predicts from the control computer will be sequenced to provide BWS channels. The stability of the synthesizer signals is derived from the highly phase-stable reference provided by the hydrogen maser through the FTS.

While the function of the subassembly is straightforward, the primary concern is the procurement specification of the synthesizers. It was previously mentioned that a total of 36 synthesizers plus spares are required for the three station sites. Thus, there is a tremendous cost leverage that prompted an evaluation program to obtain a cost-effective synthesizer. The prices of commercially available synthesizers range from $6K to $30K and their performances are also widely varied. In addition, the digitally controlled synthesizer (DCS) used in the Mark III System is also considered a prime candidate because of its previous use and because of the possibility of lower costs due to its single-purpose function (the commercially available synthesizers all have multipurpose functions). The performance parameters the synthesizers must meet to support the overall performance of the receiver subsystem are given in Table 3.

The plan for the synthesizer selection centers about the evaluation of some commercial synthesizers and the Mark III type DCS with respect to the parameters delineated in Table 3. From the spectral-purity and frequency stability requirements, the number of synthesizer candidates was narrowed to four: Hewlett-Packard Model HP8662, Ailtech Model 460, John Fluke Model 6071, and the Mark III type DCS (also called the Haystack DCS). These units meet all the requirements except that of phase stability, which is still under study. However, the key performance parameter measured has been the fractional-frequency deviation, which relates directly the synthesizers' stability to that of the hydrogen maser.

To obtain the most meaningful and precise stability measurements, the synthesizers were locked to a hydrogen maser. A block diagram depicting the method used to measure the stability of the various synthesizers is found in Fig. 7. Fractional-frequency data were taken over a range of integration times up to 1000 s. The results of three units are shown in Fig. 8. The data indicate that a JPL-built Haystack DCS and the Fluke 6071 exhibit essentially the same stability. The HP8662 synthesizer is far superior in performance at integration times below 100 s and about the same as the other two synthesizers in the 100- to 1000-s integration times. The JPL-built Haystack DCS used in this measurement is one of three units especially fabricated for evaluation for use in the Phase 4 receiver.

The Ailtech Model 460 synthesizer does not have the frequency setting resolution of the other synthesizers tested. Therefore, its frequency stability was measured with a larger offset frequency, ν_b. For example, the data shown in Fig. 8 were taken with ν_b equal to 1 Hz while the Ailtech was measured with ν_b equal to 10 kHz. For consistent comparison with the other synthesizers, data were also obtained with the other synthesizers for ν_b equal to 10 kHz. The data are shown in Fig. 9. An apparent loss of stability is observed when a much larger offset and measurement bandwidth are used; these data can be normalized to the 1-Hz offset, if desired. The key point, however, is that the relative merit of the synthesizers is fairly obvious. The HP8662 exhibits the best performance. The JPL-built DCS and Fluke 6071 are about a factor of 5 less

stable than the HP8662 at $\tau \leqslant 10$ s and have comparable stability with the HP8662 at integration times 100 to 1000 s. The Ailtech Model 460 exhibited the lowest stability and is marginal with respect to the VLBI application.

Other measurements, e.g., single sideband phase noise and rms phase jitter at short integration times (<10 s), have been performed on the synthesizers. In addition, initial temperature effects on phase drift have been measured on the JPL-built DCSs. The continued refinement of these measurements and those described in this report, in conjunction with cost analysis, will be used to make the final selection in August 1981.

III. Future Plans

To support the VLBI plans, the receiver subsystem must be designed, fabricated, and tested as a breadboard model by March 1982. This is a key milestone and signifies the earlier completion of experimental and analytical investigations with respect to the analog portion of the IF-to-video downconverter, including the synthesizers. Additional significance to this milestone is that it is the start of the procurement cycle for six complete receivers plus spares. This procurement is expected to take about 22 months for completion by January 1984.

While trade-offs among the various parameters will still occur until all the system and subsystem designs are consolidated, the design parameters given in Table 1 are presently the targets for the receiver breadboard model. Based on the data acquired thus far and on the planned modifications to the front end, the indications are that a receiver subsystem breadboard model capable of meeting the design parameters delineated in this report can be achieved.

References

1. Ham, N. C., "Frequency Down-Converters as Applied to VLBI," *DSN Progress Report 42-53*, pp. 74-82, Jet Propulsion Laboratory, Pasadena, Calif., July 1979.
2. Ham, N. C., "VLBI Receiver Phase Stability Specification," Interoffice Memo NCH:3300-80-214, Jet Propulsion Laboratory, Pasadena, Calif., November 1980. (JPL internal document.)
3. Weaver, D. K., "A Third Method of Generation of Single Sideband Signals," *Proc. IRE*, pp. 1703-1705, December 1956.

Table 1. VLBI, Phase 4 Receiver Subsystem design parameters

Performance parameters	Values	
	X-band	S-band
Input		
Frequency range, MHz	8400 to 8500	2265 to 2305
Span bandwidth, MHz	100	40
Sinusoid input power, dBm	−67 to −114	−65 to −124
Noise input power, dBm/Hz	−131 to −173	−132 to −162
Output		
Number of data channels	8	4
Bandwidth of data channels, kHz	360	360
Channel tuning resolution, kHz	$\leqslant 10$	$\leqslant 10$
Channel time multiplexing, s	0.2	0.2
Output signal level, V	±5	±5
Quadrature channel balance		
Amplitude, dB	$\leqslant \pm 0.4$	$\leqslant \pm 0.4$
Phase, deg	90 ±4 deg	90 ±4 deg
Data channel phase ripple, deg	±0.75	±0.75
Phase stability		
Nonrandom, deg peak ($\Delta t \leqslant 30$ s)	$\leqslant 1$	$\leqslant 1$
Phase jitter, deg rms ($\tau < 10$ s) 1 Hz $< f_{offset} <$ 250 kHz	6	6
Random error, deg rms		
1 s $< \tau <$ 10 s	4	4
10 s $< \tau <$ 25 s	0.4 τ	0.4 τ
25 s $< \tau <$ 600 s	10	10

Table 2. Design goals for analog section IF-video downconverter

Parameter	Value
Input frequency range	265 to 400 MHz
Input, signal level, sinusoid	−3 dBm max
Output signal level (5000 Ω)	±5 V max
Output frequency range	10 to 250 kHz
Mixer synthesizer drive	+7 dBm
Differential phase of output	90 ±4 deg
Output amplitude balance	±0.4 dB
Output phase ripple	±0.75 deg

Table 3. Digitally controlled synthesizer performance parameters

Parameters	Value
Frequency range	265 to 400 MHz
Frequency resolution	$\leqslant$10 kHz
Frequency stability	4×10^{-13} at 30 s
Output power over frequency range	$\geqslant$0 dBM ±1 dB
Spectral purity	
Harmonics	<−25 dBc
Spurious	<−40 dBc
Power line related	<−60 dBc
Remote programming	IEEE-488 [GPIB]
Frequency selection	<5 s
Status monitor	–
Leakage/susceptibility	<10 μV
Operating temperature range	20 to 30°C

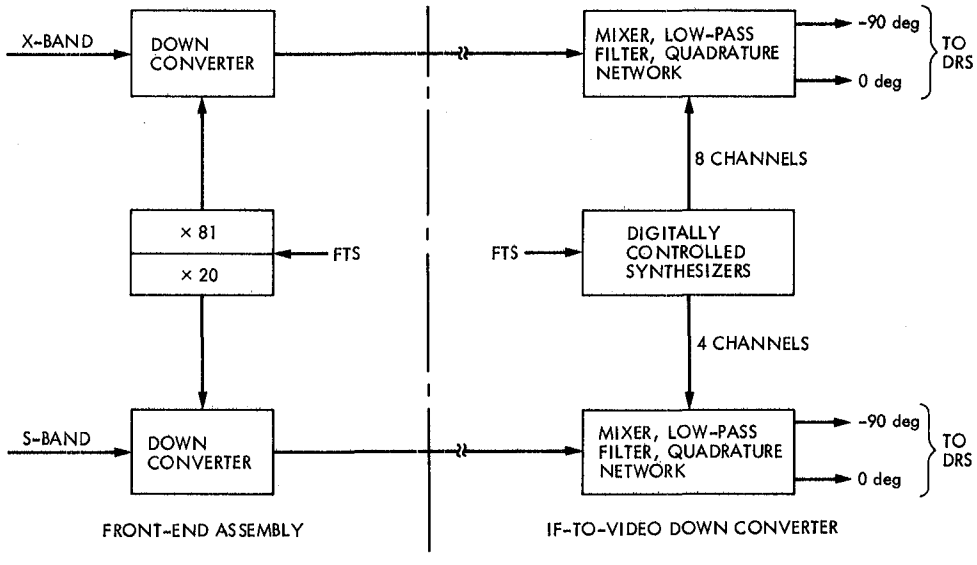

Fig. 1. Simplified block diagram of Phase 4 receiver

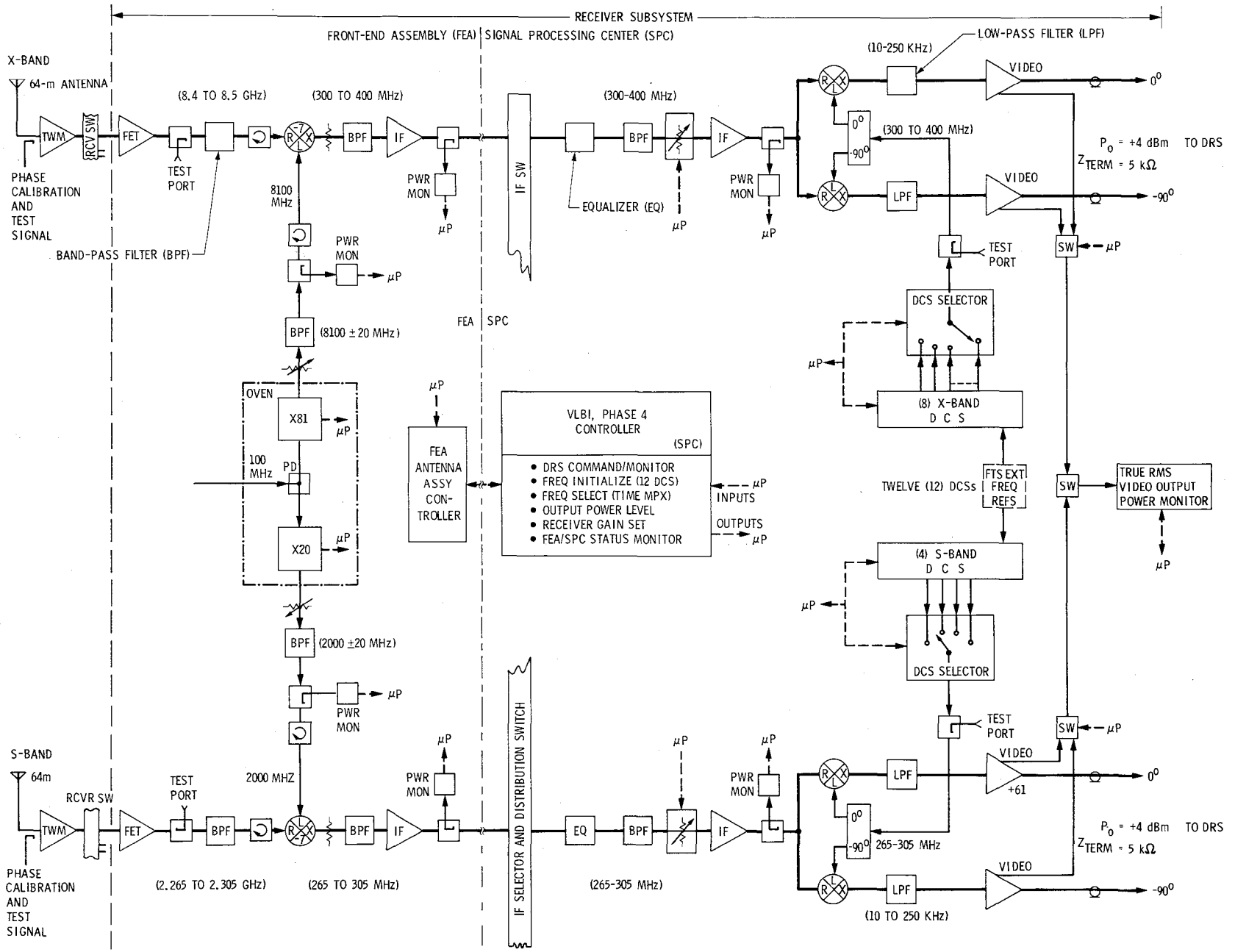

Fig. 2. Initial design of the Phase 4 Receiver Subsystem

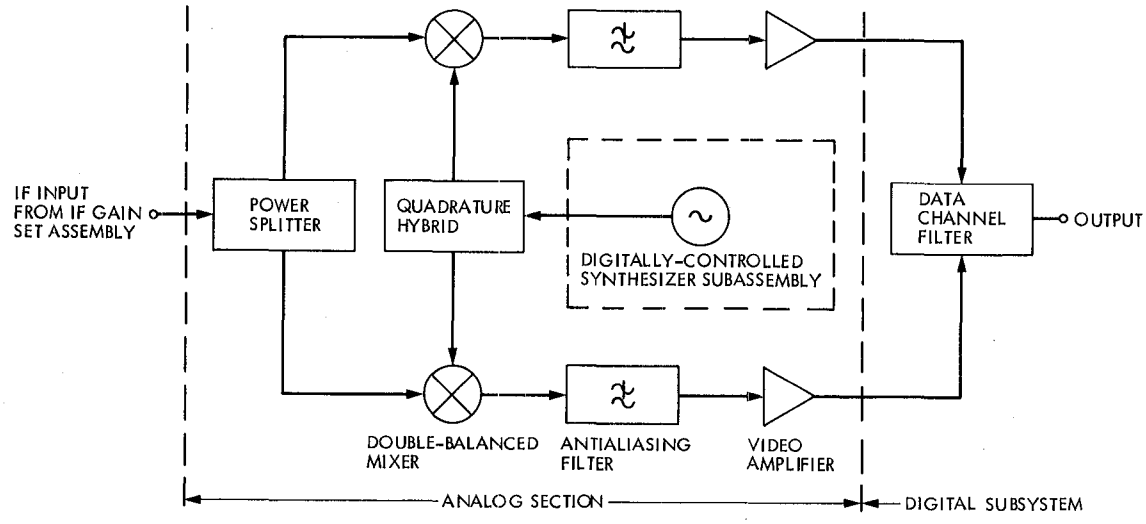

Fig. 3 IF-to-video downconverter

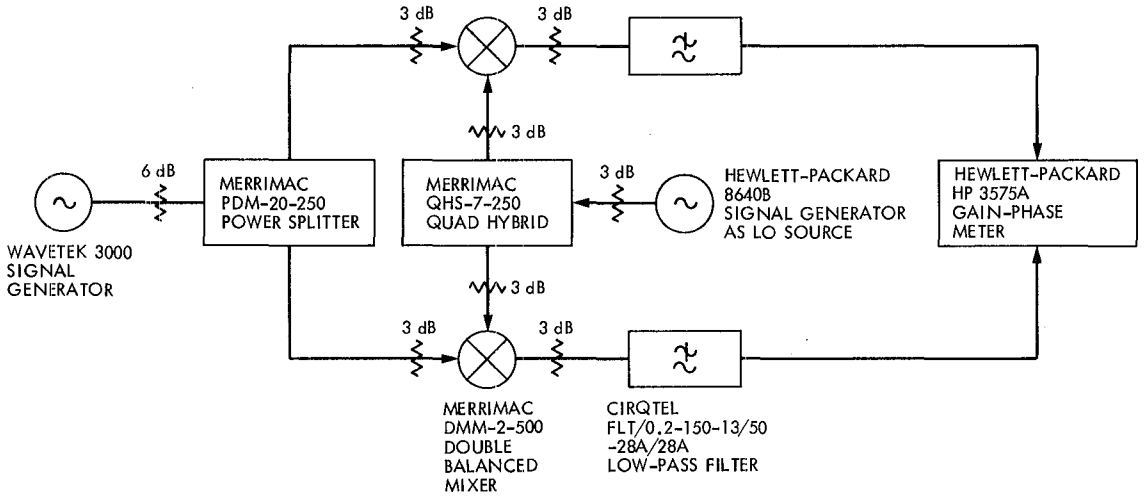

Fig. 4. IF-to-video downconverter, analog section test assembly

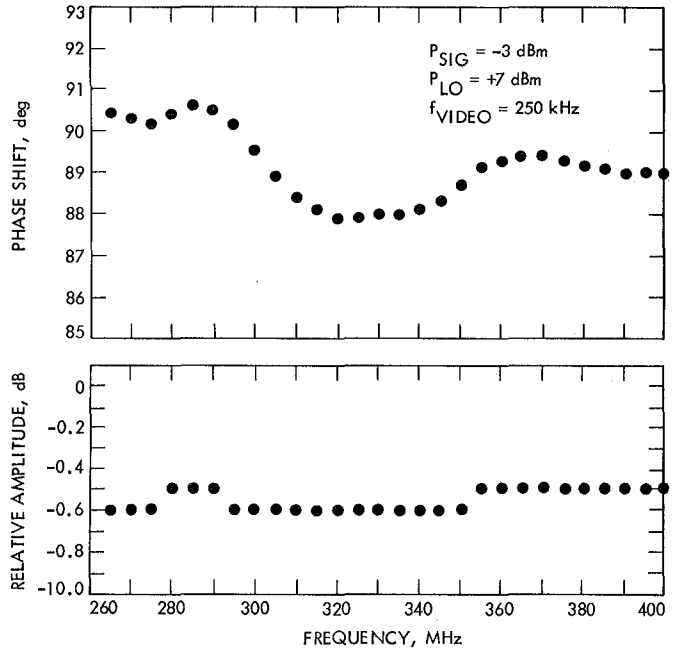

Fig. 5. Test assembly relative phase and amplitude ratio at 250-kHz output frequency

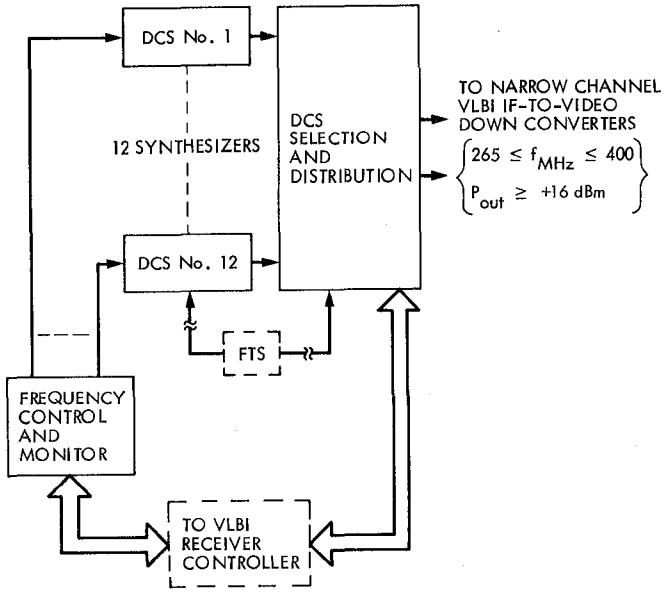

Fig. 6. Synthesizer subassembly

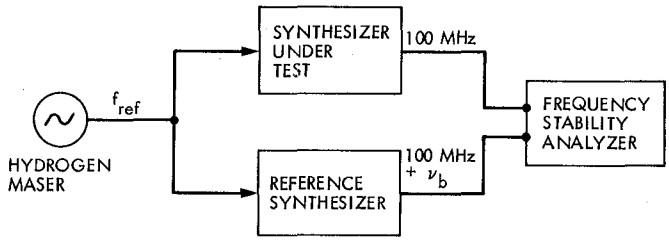

Fig. 7. Measurement method for synthesizer comparison

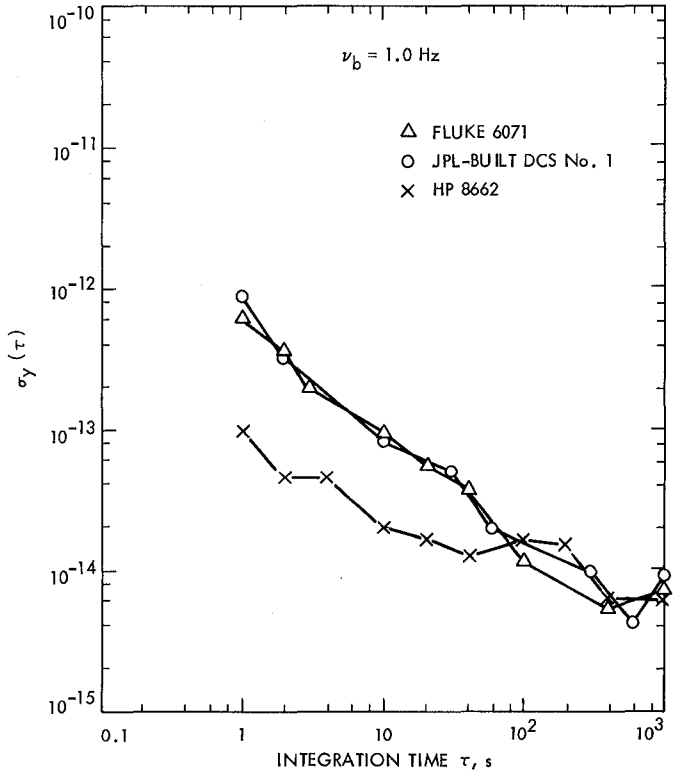

Fig. 8. Fractional frequency deviation of Fluke 6071, HP8662, and JPL-built DCSs

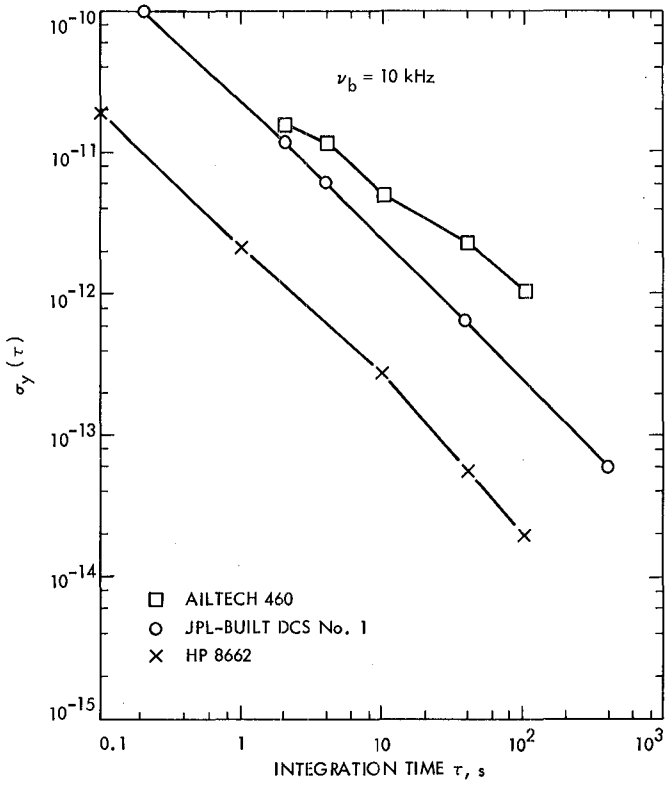

Fig. 9. Fractional frequency deviation of Ailtech 460, HP8662 and JPL-built DCSs

Appendix
Frequency Stability Model

To obtain an idea of the frequency stability expected at the receiver's output for a double down-conversion process, a simplified receiver model is generated below. The principal components of this model are shown in Fig. A-1. In this model, σ's denote the fractional-frequency deviation as a function of integration time and the frequencies, f's, pertain to the different ranges, e.g., microwave, IF, and video.

The relationship of the inputs to a mixer and its output in terms of fractional frequency deviation is

$$\sigma_{mixer\ out} = \sqrt{\left(\frac{f_{input}}{f_{mixer\ out}}\ \sigma_{input}\right)^2 + \left(\frac{f_{LO}}{f_{mixer\ out}}\sigma_{LO}\right)^2} \qquad (1)$$

For our particular case, the above equation is applied twice; once for the first downconverter, and again for the IF-to-video downconverter. The net result of the operation gives a working equation, which is

$$\sigma_{out} = \sqrt{\frac{f_{in}^2}{f_{out}^2}\ \sigma_{in}^2 + \frac{f_{LO}^2}{f_{out}^2}\ \sigma_{LO}^2 + \frac{f_{DCS}^2}{f_{out}^2}\ \sigma_{DCS}^2} \qquad (2)$$

By ascribing some practical values to the variables of Eq. (2), one can see the dependence of σ_{out} on σ_{DCS} i.e., on the stability of the synthesizer. For example, if we let $\sigma_{in} \cong \sigma_M \cong 6 \times 10^{-15}$, f_{in} = 8500 MHz, f_{LO} = 8100 MHz, f_{DCS} = 400 MHz, f_{out} = 10 kHz, and $\sigma_{LO} \cong 7.5 \times 10^{-15}$, for an integration time of 30 s and a measurement bandwidth of 1 Hz we obtain the graph shown in Fig. A-2. The graph indicates that the DCS stability can be as large as 10^{-13} before it starts affecting the output signal's frequency stability of 7.6×10^{-9}. Using 4×10^{-13} as the value for minimum frequency stability for the synthesizer gives a fractional-frequency deviation, σ_{out}, of 1.8×10^{-8} for the output signal. One obtains a phase jitter equivalent by using

$$\Delta\phi = \sigma_{out}\ f_{out}\ \tau\ 360 \qquad (3)$$

where $\Delta\phi$ is the phase jitter, f_{out} is the output signal at 10 kHz, and τ is the integration time (30 s). Substitution of the aforementioned values yields, $\Delta\phi \approx 2$ deg.

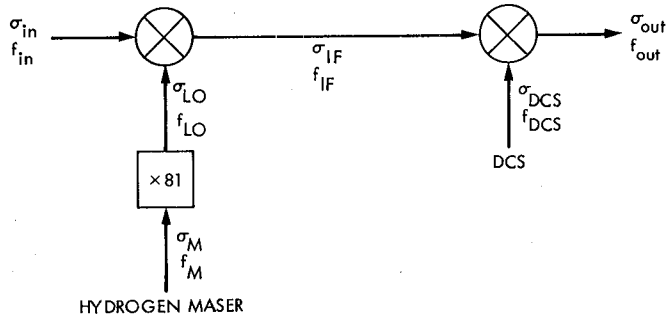

Fig. A-1. Double conversion model

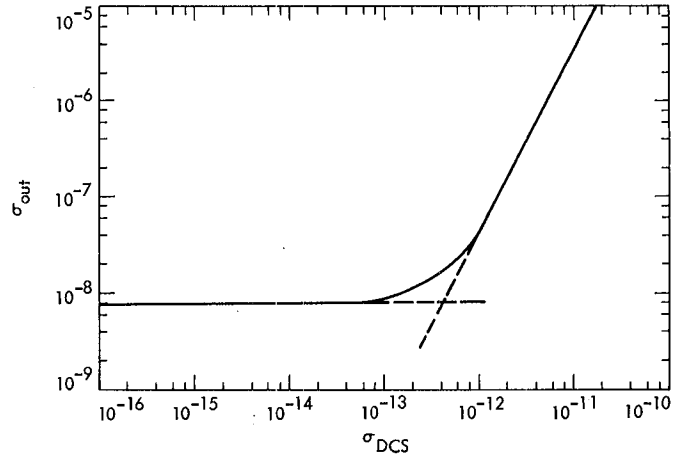

Fig. A-2. Fractional frequency stability of the output signal as a function of synthesizer stability

Developing New Architectures for the Block II VLBI Correlator System

J. C. Peterson
DSN Data Systems Section

This article focuses on the overall LSI (large-scale integrated circuits) architecture design and current status of the VLBI (very long baseline interferometry) Block II correlator. The VLBI correlator algorithms demand a computing system that provides a throughput of hundreds of millions of instructions per second to perform cross-correlation detection for six baselines. LSI technology lights the way for the computation of complex parallel process and is raising the upper bound of computerization.

I. Introduction

The Block II VLBI (very long baseline interferometry) correlator can best be understood by reference to Fig. 1, which shows a simplified block diagram for the acquisition and processing of VLBI data. The data acquisition facility consists of an antenna pointed at the signal and low-noise microwave amplifiers and receivers for receiving the signal. Analog-to-digital (A-D) converters convert the data to digital form for recording. This recording requires large volumes of data so the data are recorded on a digital instrumentation recorder, the digital recorder assembly (DRA). These tapes are then shipped to the data processing facility, which employs special-purpose hardware for computer-controlled correlation. The correlation algorithms demand a special-purpose computing system that provides a throughput of hundreds of millions of instructions per second.

The input data rate for a 6-station VLBI correlator, as shown in Fig. 1, is 1344 million bits per second. The fast Fourier transform (FFT) algorithm, which is only one of many algorithms in the system, requires 12 million instructions per second to adequately handle data reduction. Systems with such unprecedented throughputs have been named "super-systems."

Advances in LSI (large-scale integrated circuits) technology have significantly reduced the cost and enhanced the reliability of computer components. It is now feasible to design reliable modular computing systems containing more hardware resources than ever before, resulting in a sharp increase in the number of instruction and data streams that may be computed by a parallel system. LSI technology has provided powerful means of improving throughput, such as architectural adaptation and increased parallel computation.

Since existing systems have failed to provide such enormous throughputs, let us look at the potential of adaptable data flow architectures, which are now feasible with the advent of LSI and promise to be the architectures of future super-

systems. This article describes a complex parallel system equipped with the architecture for creating this exceptional throughput. The design work is for a 28-channel, 3-station VLBI correlator system with transfer of hardware to operations scheduled for April 1982. The expansion to a 28-channel, 6-station system is possible shortly after this date. The system design must be characterized by allowing an increase in system complexity.

II. Problems of System Complexity

The VLBI correlator requires a system capable of computing 168 (28 channels × 6 stations) parallel streams, each of which may have rates in the range of 1 to 8 million bits per second. A system operating at this speed must also maintain a high reliability since the cost of failure will create a backlog of data and thereby other associated problems.

Research on supersystems has shown that these extreme throughputs have been difficult to obtain by merging existing complex computers into a system (Refs. 1 and 2). Let us consider the question associated with this system merger.

Since including a very large number of computers in a single supersystem leads to enormous complexity, the supersystem is thereby degraded by worsening reliability. It then becomes unsuitable for computing many complex real-time algorithms that require high reliability.

In addition, complex real-time algorithms are characterized by an increase in the number of data streams involved. The supersystem then has to respond by an increase in the number of computers it incorporates. This then leads to an increase in delay or adds complexity by introducing interconnecting logic. This complexity is shown with a VLBI correlator system; a N-station, 28-channel correlator will require $28N(N\text{-}1)/2$ copies of a module for simultaneous, all-baseline cross-correlation. As the data streams increase ($28N$), the complexity of the system involved increases by $(N^2\text{-}N)/2$.

To reduce the number of interconnections required or the delay between connecting modules, a new type of architecture has to be developed to offset the problem. The new architecture has to be capable of performing a dynamic adaptation to the computational requirements of the algorithms being processed. This will allow the system to increase throughput with the same resources, but without changing the system's complexity. In this way, supersystems will become suitable for new algorithms requiring higher throughput and reliability. In adaptable architectures, this purpose is accomplished by microprogrammable, reconfigurable, and dynamic adaptations to algorithms.

Another new type of architecture, data flow architecture, increases the efficiency of computation by the architecture's ability to conform to the computational flow graph of the executing algorithm. Both of these architectural principles require distributing the processing among multiple processors, memory, and input/output (I/O) units connected via one of the interconnection networks.

III. New Architectures

Making new architectures feasible requires the effective distribution of the algorithm among multiple resources. The problem is, given the multiple resources as individual modules, one has to allocate processor and memory resources to them in a way that minimizes time and system complexity.

Real-time algorithms provide a processor architect with clues as to what types of adaptations must be performed. These algorithms are characterized by a variable number of both data and instruction streams. In the VLBI correlator, the system is designed to process variable-number lengths of concurrent data streams. Since each module unit requires its own process, it is characterized by a variable lag length for the different data streams. This lag length, characterized by its own instruction and data streams, is able to adapt so that it may redistribute the available lags into another cross-correlation module unit. For example, a VLBI correlator incorporating 420 8-lag cross-correlators must be capable of a software-controlled reconfiguration into 240 16-lag, 120 32-lag, 60 56-lag, 30 112-lag or 15 224-lag cross-correlators. To meet these reconfigurations, the FFT algorithm also has to match the redistributed cross-correlator and process 240 16-point FFT, 120 32-point FFT, etc. As a result, the VLBI correlator increases its throughput while maintaining the same resource complexity, thus preserving its level of reliability.

Distributed processing enhances system performance by employing many processors to handle the processing load. A representation of the VLBI correlator distributed processing system is shown in Fig. 2. The key elements in this system are a set of modules assigned to the same processor.

Only three unique processors are necessary in this distributed system: station, correlation and FFT processors. These processors are distributed in the system as needed, depending on the number of station streams to be processed. Each station data stream input requires a station processor and sharing of correlation and FFT processors, which can handle up to 3 baselines of data. The network of processors for a 6-station, 28-channel system then assigns 6 station processors and 5 correlation and FFT processors to a VLBI correlator system. By employing these distributed processors in the

VLBI system, the processing load is contained in the correlator hardware and not in the controlling computer. It is expected that the FFT processor, for example, will yield performance superior to that of a general-purpose computer on FFT operations. The FFT algorithm requires 20 million instructions per second for a 6-station processor. The algorithm load is distributed into 5 FFT processors, each requiring 4 million instructions per second. The performance of a Digital Equipment Corporation VAX 11/780 computer, for example, is capable of about one million FFT-type instructions per second. A speedup of 20 times is achieved by going to specialized distributed processors for just this algorithm, which is one of many in the system.

These processors in the network are homogeneous; they are fully connected by control entry points and the effect of precedence relationships among modules can be ignored. This assigning or grouping of modules with high intermodule communication can be used for module allocation, subject to real-time and memory constraints. This clustering of modules to a processor is called fusion. In an algorithm, after finding a group of modules, we check to see whether this fusion satisfies the real-time and memory constraints, the fusion of which will eliminate the greatest amount of interprocessor communication. That module group is then represented by a module cluster for the next iteration. This fusing process continues until all eligible modules are allocated. The goal is to balance the load among the set of processors, yielding high throughput and faster response time.

The 28 modules fused to the station processor (Fig. 2) are tailored to the real-time constraints. Each module is actually a group of subcircuit-modules assigned to one channel of data. The module load is divided up into these different, well-defined subcircuits. They make up the bit and frame synchronizer, buffer delay and calibration tone detector. The main real-time burden in the station hardware falls on these subcircuits. This is true also in the correlator hardware, but here the modules make up the cross-correlator and time domain integration.

The task allocation problem is important in the initial design phase of a distributed processing system, in the normal operational mode, and in the reconfiguration phase of a dynamic reallocation environment.

During the design phase, it is necessary to evaluate competing design configurations including network topology, channel bandwidth, and number of processors. Task allocation allows determination of the value of these parameters to achieve a desired level of performance.

In the normal operational mode of the VLBI correlator, it is important to assign modules to processors to meet critical timing constraints. It should not be assumed that all processors are ready and available at task allocation time. Task allocation is also important during reconfiguration due to changing operating environment. These changes may be a result of changes in task input rate, processing and channel capacity.

Because of the computational complexity of the correlator system, a need has arisen for a simplified approach to the task allocation problem. This is generally a heuristic approach where one balances the loading constraints with real-time constraints. Figure 3 shows the task and communication allocation assigned to the three different processors. The processors in this environment communicate among themselves via an interconnection mechanism. This communication is essential for overall system throughput. All the modules and processors are related by two interrupts: the frame rate interrupt (FRI) and correlator output interrupt (COI). Every 20,000 data stream bits a FRI is generated, and every 100,000 data stream bits a COI is generated. Assigning these two interrupts to all modules and processors speeds up the overall processing time by establishing a mutual relationship among all elements.

IV. Lengthening the Life Cycle with New Architectures

Many complex real-time algorithms may require an increased number of data and instruction streams. In the VLBI correlator, for instance, some algorithms face an increased number of lags and an increased level of each FFT that must be handled in real-time. To be adequate, a supersystem must be able to increase its throughput by integrating new resource units into the existing system. Such an increase in complexity, however, may lead to a deterioration in reliability. Thus, its life cycle for the application may be shortened since the supersystem may become incapable of providing highly reliable computations within a specified time limit.

The architecture adapts to an increase in lags and FFT via dynamic redistribution of the available resources, and it will augment the concurrent computer resources that will be needed with the system hardware. This additional processing power is gained without adding equipment, and the associated increase in complexity, to the supersystem. Consequently, the VLBI correlator system is capable of maintaining the same level of reliability that existed before. Its life cycle thus lengthens since its computational adequacy is sustained in spite of the increased processing requirements encountered in the algorithms. It should be noted here that this dynamic redistribution is not just designed into the cross-correlator modules and FFT processor but into some of the other modules and processors as well. Only in the cross-correlator modules and FFT processor is the life cycle lengthened so remark-

ably because most of the hardware encountered is in this area of the system. This is shown in the following examples.

The VLBI cross-correlator module is designed for an application in which the data requires a lag length of either 28 channels – 8 lag points, 14 channels – 16 lag points, 7 channels – 32 lag points, 4 channels – 56 lag points, 2 channels – 112 lag points or 1 channel – 224 lag points. The system is capable of adapting its cross-correlator resources on instruction to any of the above modes. This adapting is handled by a recursive feedback design between cross-correlator modules. Its total complexity of lag resources is equivalent to 28 X 8 = 224 lag.

Now let us find the complexity of a VLBI correlator system that computes the same algorithms but performs no adaptations for cross-correlator lags. Since it must handle the same required lag length, it must have 1 channel – 224 lag points, 1 channel – 112 lag points, 2 channels – 56 lag points, 3 channels – 32 lag points, 7 channels – 16 lag points and 14 channels – 8 lag points. Thus, the overall channels are still 28 but the resources complexity of lag has increased to 96 – 8 lag cross-correlator. Its total complexity is equivalent to 96 X 8 = 768 lag.

Consequently, to maintain the same level of concurrency, the system with conventional architecture must increase its complexity of lag resources to 3.43 times that of a system which can perform adaptations on parallelism. An 8-lag cross-correlator module requires about 25 integrated circuits (ICs). To realize the level of hardware required for a 6-station by 28-channel adaptable cross-correlator, one must have 25 ICs X 28 channels X 15 baselines = 10,500 ICs. A cross-correlator with no adaptations is 3.43 times this amount or 36,015 ICs. Since new adaptable cross-correlator modules must communicate with each other, new connecting elements must also be added, their number depending on which recursive feedback design is utilized. This addition is very small compared to the overall cross-correlator module hardware.

V. Detailed Design Summary and Status

This section summarizes the detailed design and implementation work now proceeding for the high-speed digital cross-correlator. For the following discussion, reference to Fig. 4 should be made. This diagram shows the overall data flow for one station/correlator baseline. The input data, at the left, enters from magnetic tape with 28 data streams per station and at rates up to 8 million bits per second per stream.

A. Emitter-Coupled Logic (ECL), Frame Sync and Delay Buffer Circuits

1. **ECL.** The data from tape head line drivers first enters the ECL circuit board. This board has 30 28-to-1 ECL multiplexers, one for each of the 28 channels and two for self-test. Any tape track may therefore be routed into any data channel for processing. The data then enters a digital bit-synchronizer circuit which generates a clock reference from data. Data and clock for all channels are converted to TTL (transistor-transistor logic) level before leaving the board.

Total ICs for this board 450

Total power required . . . . . 160 W

Design and check-out of ECL prototype is complete.

2. **Frame Sync.** The data stream first enters FIFO (first in/first out) memory, which removes the effects of recorder jitter and synchronizes the data to an internal clock. A sync word is decoded from the data stream to locate frame boundaries and generates a BOF (buffer output frame) timing interrupt. This decode circuit uses only two Programmable Array Logic (PAL) ICs. Loss of frame synchronization is detected when the decoder finds a sync word at the wrong bit count. Resynchronization is then started, a frame error generated and counted.

3. **Delay Buffer.** Buffering of the data streams, for correct alignment before cross-correlation, is implemented with 16 X 1 dynamics RAMs (random access memory). 8-RAM ICs are used for data delay or a total of 0.131 million bits of delay. Three additional RAM ICs are added for parity delay and delaying the BOF/FRI (frame read interval) timing interrupts. FRI is a master interrupt generated by the hardware every frame period. The delayed time difference between BOF and FRI is a delay correction made to the delay buffer by the station's phase processor. A delay update is made every 5k bits. This buffer circuit is upward compatible to 64k X 1 or 256k X 1 dynamic RAMs (2.097 million bits of delay), when it becomes cost effective to do so.

Additional FIFO memory is added for storing time labels, auxiliary data words, 12-bit cycle redundancy check character and frame error counts.

Total ICs for 15 modules (one board) 600

Total power per board . . . . . 250 W

Design and checkout of FRAME SYNC/ DELAY BUFFER is complete.

B. Calibration Tone Detectors

The data at the output of the delay buffer is converted back to a serial data stream for mixing and cross-correlation. The cal-tone is also extracted at the buffer's output. The

serial data is mixed with 8 bits of phase from the station's phase processor. This gives 127 levels to the sine and cosine waveforms. The fringe rate generator word length is 24 bits and is updated every 5k data bits. The output of the mixing is then accumulated in 16-bit counters before transfer to the station phase processor for additional processing.

Total ICs for 28 modules (one board) 620

Total power per board . . . . . 275 W

Design is complete.

Additional board slots are provided so that up to 4 cal-tones per channel may be tracked simultaneously.

C. Station Process Controller

The station process controller is designed to handle all of the high intermodule communication between the tailor data modules and data processor. These data modules, i.e., frame sync, buffer and cal-tone detectors, are assigned to a controller so that all the real-time constraints are off-loaded from the data processor. This clustering of modules to a processor is called fusion. All frame sync, buffer and cal-tone detectors are fused to the station process controller for communication I/O at the data stream bit rate. The design of the controller throughput has to be 8 million instructions per second for a data stream rate of 8 million bits per second. To provide that kind of throughput, special microprogrammable hardware was designed. The hardware's microword length is 96 bits by 512 words. Built into the firmware are also fault detection and diagnosis, capable of fault isolating down to subcircuits within a data module.

Total ICs required 60

Power required . . . . . 25 W

Design and checkout of prototype is complete.

The hardware for this process controller is identical with the correlator process controller, with about 80% of the firmware transferable.

D. Station Phase Processor

The station phase processor will compute the calibration fringe rate for all cal-tone modules and compute the buffer delay for all channels. Calculation is based on a 64-bit-word-length algorithm which is completed every 100k data bits. Typical cal-tone accumulation dumps also occur every 100k data bits. From this data the phase processor computes the phase (arctan i/r) for four tones per channel. The computed phase is than transmitted to the cal-interface for transfer to the cross-correlator. Here the phase is applied as a correction to the cross-correlated output every 100k data bits. New model updates to the station phase processor from the computer are typically made every 25 seconds. The data word length of the processor is 32 bits and is capable of doing a 32-bit by 32-bit multiply in 333 nanoseconds. Throughput is six million instructions per second.

Total estimated ICs 175

Total estimated power . . . . . 75 W

Design is 80% complete.

The hardware design for the phase processor and the design for the corralator phase processor are identical, with about 60% of the firmware transferable.

E. Station Rack

The number and type of boards in the station racks are one ECL board, two frame sync-buffer boards, one cal-tone detector board and one control/processor board. A total of 11 boards may be housed in the station rack along with the Honeywell recorder electronics.

F. Digital Interfaces

1. **Data Interface.** Data stream interfaces between the station racks and correlator rack are made of twisted-pair flat cable, 14 data and 14 invalid plus clock twisted-pairs per cable. All interfaces are designed for digital transmission over balanced differential lines. Data speeds are less than 10 million bits per second per data stream pair.

2. **Calibration interface.** The calibration interface transfers cal-phase between station racks and correlator rack, also using twisted-pair flat cable. This interface transfers 16-bit data words over a common interface. Each station rack sends 120 words every 100k data bit times. The data rate is about 1 million bytes per second.

G. Cross-Correlator

After both data streams are buffered by a programmable delay in the station racks, the data is sent to the correlator for cross-correlation. One stream is multiplied by 3-level approximations of the sine and cosine functions, then cross-correlated with the other data stream. The cross-correlator has 8 lags per channel and 16-bit accumulation. After cross-correlation the correlator process controller dumps the correlated data to the correlation signal processor. The fringe rate generator word length is 24 bits and is updated every 5k data bits.

The cross-correlator is designed to process a variable-number correlated length of concurrent data streams. So different numbers of data streams processed by the cross-correlators will be characterized by variable lag lengths. The cross-correlator may be reconfigured into 1 channel – 224 lags, 2 channels – 112 lags, 4 channels – 56 lags, 7 channels – 32 lags, 14 channels – 16 lags or 28 channels – 8 lags. The algorithms in the digital signal processor will also have to match this redistribution in processing the data.

The cross-correlator has been designed without the use of custom LSI chips. The design uses a number of the programmable array logic family ICs for reducing package count.

Total ICs for 14 modules (one board) 400

Total power per board . . . . . 175 W

Design and checkout of prototype is complete.

H. Correlator Process Controller

The correlator process controller, like the station controller, is designed to handle all of the high intermodule communication between the tailor data modules and data processors. The design of the controller throughput has to be 8 million instructions per second for control of data stream rate up to 8 million bits per second. One controller can handle up to 3 baselines – 28 channels and can also fault detect with fault isolating hardware down to subcircuits within a cross-correlator module.

Total ICs required 60

Power required . . . . . 25 W

Design and checkout of prototype is complete.

The hardware for this process controller and the hardware for the station process controller are identical, with about 80% of the firmware transferable.

I. Correlator Phase Processor

The correlator phase processor will compute the fringe rate for all 3-baseline, 28-channel cross-correlator modules. Calculation is based on a 64-bit-word-length algorithm, which is completed every 100k data bits, as in the station phase processor design. The processor also calculates the fractional bit correction for each cross-correlator. The output of the fractional bit correction algorithm is a phase value which is added to the cal-phase values every 100k data bit times. These added phase values are then passed along to the correlation signal processor for data correction. The values are sent over the cal-correction interface between phase processor and correlation signal processor. New model updates to the correlator phase processor from the computer are typically made every 25 seconds. The data word length of the processor is 32 bits. The processor is capable of doing a 32-bit by 32-bit multiply in 333 nanoseconds. Throughput is six million instructions per second.

Total estimated ICs 175

Total estimated power . . . . . 75 W

Design is 80% complete.

The hardware design for the phase processor and that of the correlator phase processor are identical, with about 60% of the firmware transferable.

J. Correlation Signal Processor

The correlation signal processor uses an FFT directly to compute estimates of the cross-correlation function for lags/channel, where lags/channels are the size and sequence of the transform used. Using an N-point FFT, the power density spectrum may be estimated at N uniformly spaced frequencies around the unit circle. In order to improve the estimate at the finite set of frequencies, a correction window must be used to reduce the effects of fraction bit and oscillator phase uncertainty. This correction window is supplied by the correlator phase processor as phase values, and is updated every 100k data bit times. The windowed FFT output is then boxcar-filtered (integration) for typically one second before outputing to the computer or tensor processor.

It is advantageous to reduce the output to the computer as much as possible so that storage and arithmetic operations can be minimized in the computer. Sample rate reduction can be performed with no loss in sensitivity by passing the data through a digital low-pass filter. Then only every N samples will be retained for output. The filter will be a IIR (infinite impulse response) recursive design type with a selectable reduction ratio. The reduction is independent for each group of three baselines processed by the correlation signal processor. The filter will operate on the 32-bit boxcar-filtered data.

The data word length of the processor is 16 bits, and it will do a 16-bit by 16-bit multiply in 166 nanoseconds. Throughput is six million instructions per second.

Total estimated ICs 175

Total estimated power . . . . . 75 W

Design is complete.

K. Tensor Processor

The tensor processor has previously been called 'phasor' and has been renamed to prevent confusion with the Mark 2 / Block O phasor software program.

The output of the correlation signal processor may be routed to the tensor processor for additional processing in the hardware. The additional processing requires filling a bandpass buffer holding 2048 complex points. Points in the buffer which are not loaded with data are set to zero. The bandpass buffer will be Fourier transformed from frequency domain to time domain. If a priori information allows one to estimate delay, one can select a delay window that defines the delay range and keep that data for further processing. Mutiple windows may be defined. This windowed data then fills a programmable delay buffer. When full, a Fourier transform is performed on the columns of the delay buffer. After the transform, the array contains visibilities on a grid of synthesized delay and fringe rate. Data in the array may be output to the computer on a selective basis. This is according to the delay window already selected and according to a priori fringe rate information. The tensor processor reduces overall I/O data rates between the computer and hardware correlator, for normal processing, by 1000 to 1 plus facilitating storage economics in the computer. The tensor processor implementation is planned to handle three baselines.

In the design of the correlation signal and tensor processor it was attempted to include sufficient flexibility to support all the known observational requirements. In the extreme case, it will be possible to bypass all the functions described here, and dump the 'raw' cross-correlated data directly to the computer.

Total estimated ICs 400

Total estimated power . . . . . 160 W

The design is preliminary at this time.

L. Correlator Rack

A 3-baseline, 28-channel cross-correlator requires 6 boards; two additional boards are required for control and processing. A total of 28 boards can be housed in one correlator rack. The rack is a VAX 11/780 double-wide CPU (central processing unit) cabinet.

M. I/C Summary

For one station, ICs total 2505, plus an additional 200 for recorder control and interface, or

ICs 2705

Power . . . . . 1135 W

For one three-baseline correlator system, ICs total 3210, plus an additional 100 for interfaces or

ICs 3310

Power . . . . . 1485 W

The JPL/CIT hardware design for a 4-station 6-baseline correlator system uses 17,440 ICs and consumes 7510 watts of power.

The Haystack Mark III processor design is based on a straightforward modular concept of one module per baseline per track. Thus, 28 (350 ICs) modules are required per baseline. The Haystack hardware design for a 4-station 6-baseline correlator system uses 58,800 ICs and consumes 6470 watts of power. The Haystack hardware design is an existing VLBI cross-correlator design using mostly SSI technology ICs and designed without new data-flow architectures.

VI. Conclusions

We have shown that to increase throughput and lengthen the life cycle of supersystems, new architectures must perform distribution and adaptation to algorithms not implemented in traditional systems. The proliferation of both types of architectures was encouraged by advances in large-scale integrated circuits (LSI) technology that significantly reduce the cost and enhance the reliability of processor components. These advances in LSI technology have made distributed processing a practical system design approach. The modularity, flexibility, and reliability of distributed processing make it attractive to many types of users.

The VLBI correlator system has been designed without the use of custom LSI chips. In the near future the advantages provided by this custom LSI technology will allow even faster and less expensive computations for processor systems. This technology will become part of the accepted processing repertoire of future system designers.

We must assume that, in the end, system resources are limited. That is, the number of available processors, processor speed, memory capacity, and number of modules are fixed and limited by available system resources. In real-time applications, allowed elapsed time is also a limited resource. In any case, system design methodology should strive for simplicity balanced by a need for being fast enough to meet system performance requirements.

References

1. Wittle, L.D., "Efficient Message Routing in Mega-Microcomputer Networks," *Proc. Third Annual Symp. Computer Architecture,* 1976, pp. 136-140.
2. Vick, C. R., "Research and Development in Computer Technology, How Do We Follow the Last Act?" *Proc. 1978 International Conference on Parallel Processing*, August 22-25, 1978, pp. 1-5.
3. Kurtashev, S. P., and Kartashev, S. I., "Adaptable Pipeline System with Dynamic Architecture," *Proc. 1979 International Conference on Parallel Processing*, pp. 222-230.
4. Peterson, J. C., and Dillon, J. W., "Implementation of the DSN VLBI Correlator," *The DSN Progress Report 42-50*, Jet Propulsion Laboratory, Pasadena, Calif., January 1979, pp. 226-236.

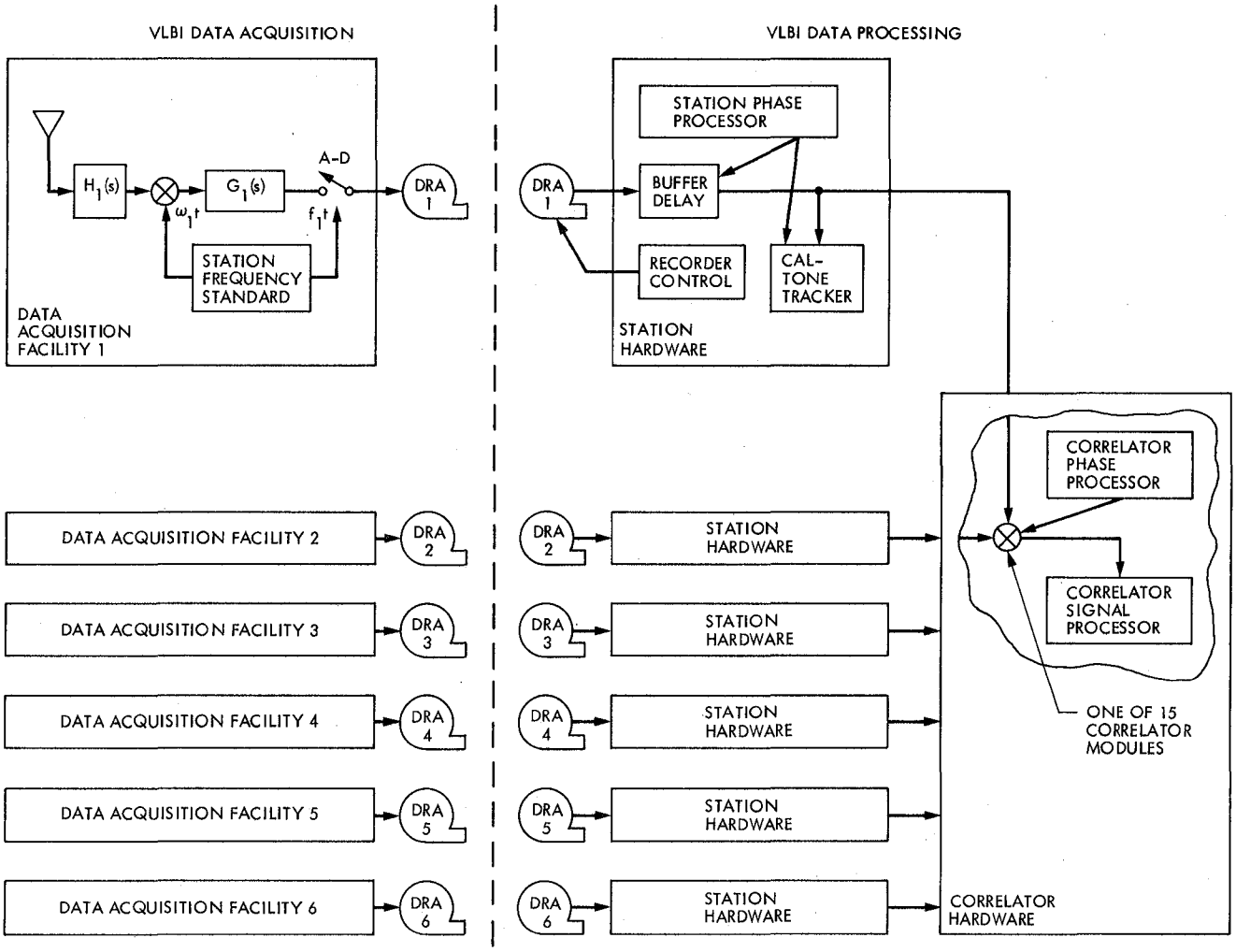

Fig. 1. VLBI data acquisition and processing

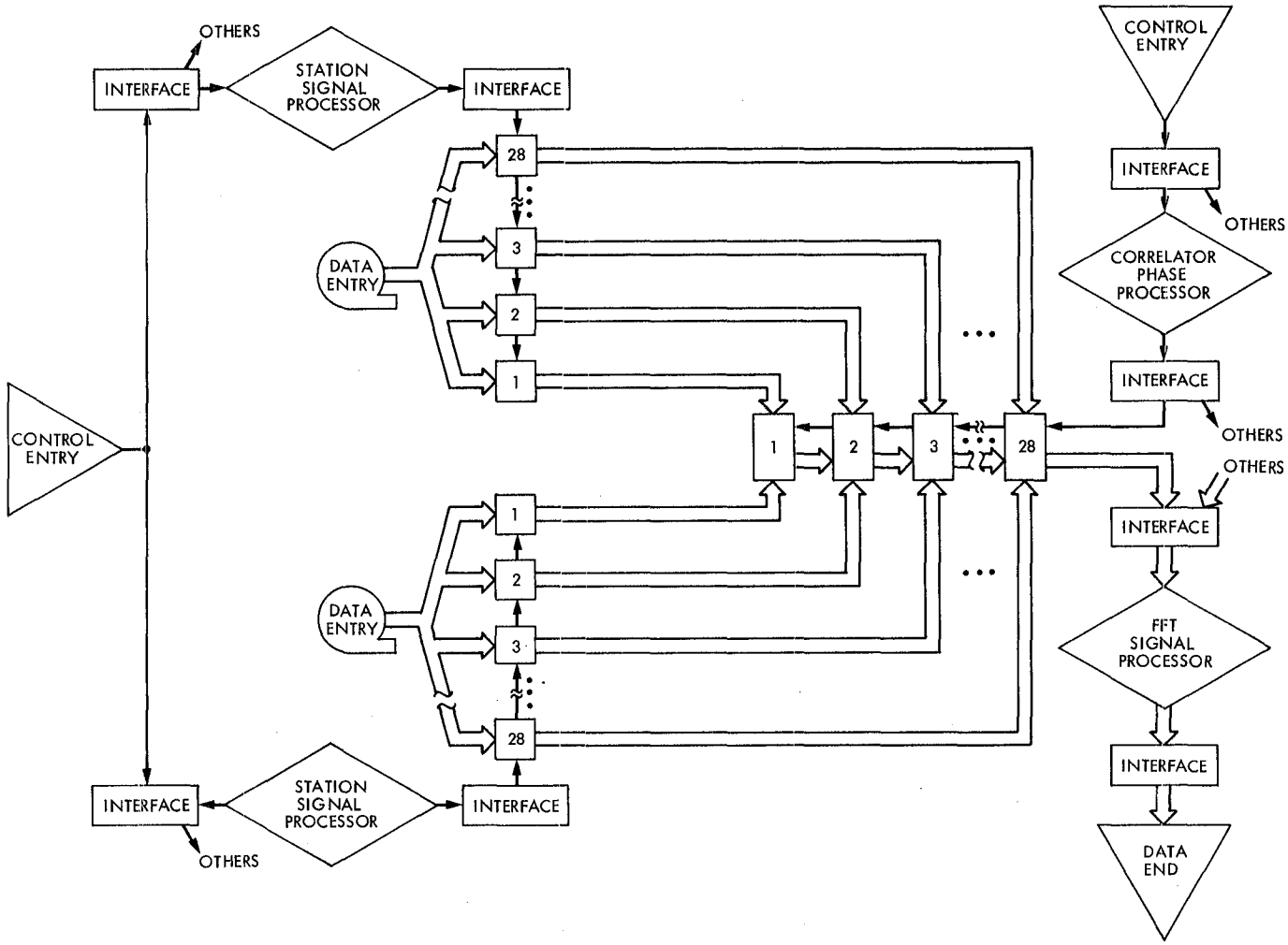

Fig. 2. VLBI distributed correlator system, 2-stations/28 channels

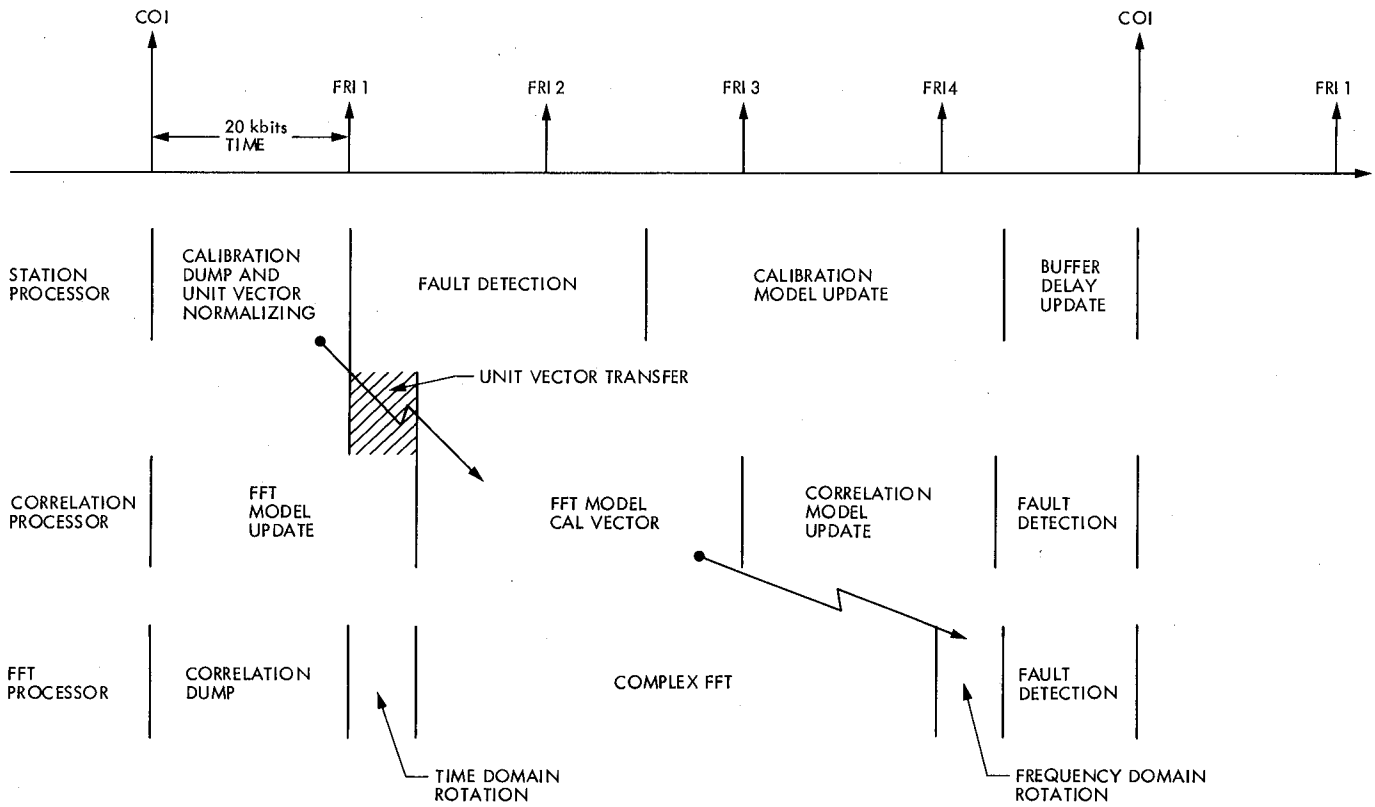

Fig. 3. VLBI correlator system, task and communication allocation

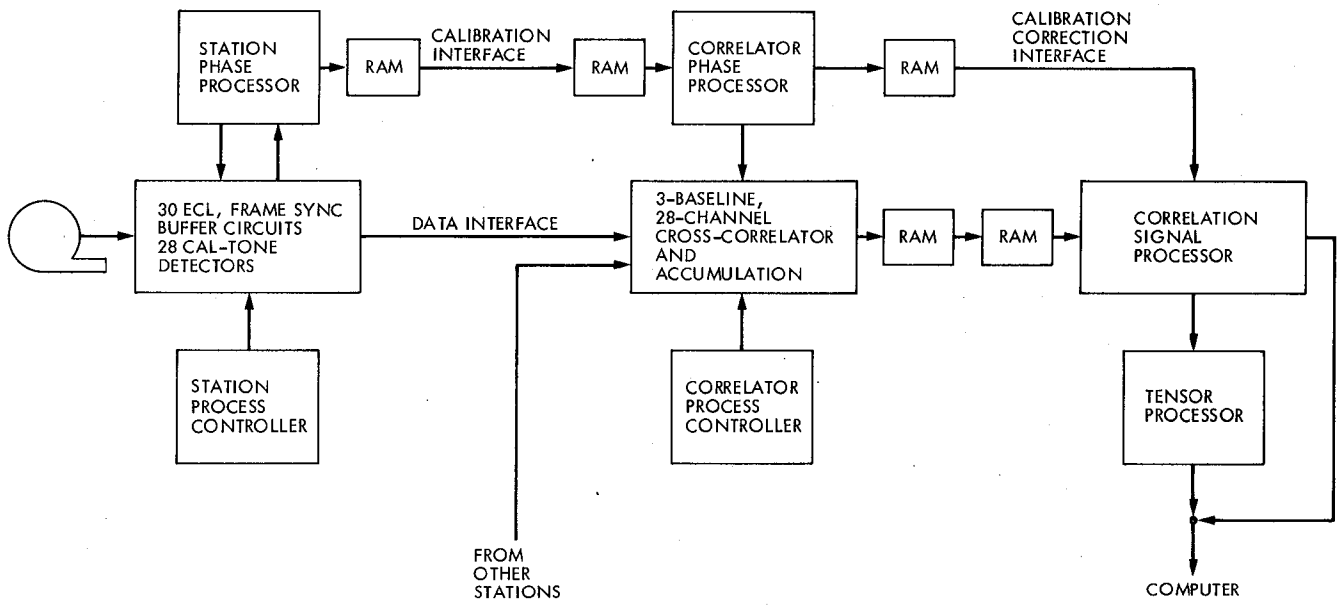

Fig. 4. Block VLBI correlator data flow block diagram

DSN Frequency and Timing System Mark III-81

J. B. Curtright
TDA Engineering Office

The DSN Frequency and Timing System configuration and functions are described. The text is historical in nature, ending with the current system design and performance.

I. Introduction

Frequency and timing requirements in the DSN have, in the past 20 years, approached state-of-the-art technology. In the frequency domain, we have evolved from high-quality crystal oscillators, having accuracies of parts in 10^6, to today's technology of hydrogen masers having stabilities to parts in 10^{15}. Intermediate technology provided rubidium vapor standards and cesium beam standards which are still very much a part of the DSN.

The time domain capabilities have followed the advances of frequency standards along the evolutionary path. Timing accuracies have advanced from milliseconds to nanoseconds, in support of spacecraft navigation requirements. The Frequency and Timing Subsystems are now the hub of DSN requirements, providing all subsystems with fast, accurate and reliable frequency and timing references.

The following is a discussion of the current timing system in the DSN, with some background on how it evolved to be the most accurate and reliable global system in the world.

II. Background

As early as 1965, it became evident that deep space probes would require very accurate time and frequency synchronization between Deep Space Stations in order to achieve the required navigational performance. Until this time, time ticks broadcast by the National Bureau of Standards (NBS) radio stations WWV and WWVH were adequate. Time could be synchronized to within one millisecond of NBS time in the United States and about five milliseconds at the overseas Deep Space Stations. Several very low frequency (VLF) stations began broadcasting about the same period, making it possible to establish and track frequency offsets for the then used rubidium vapor standards. This method allowed detection of a few parts in 10^{10} and later parts in 10^{11} frequency offset or change. The result of this double-spoked process allowed time synchronization to within one millisecond and determined offset in time from that initial point forward. A few microseconds per day change, plus or minus, was not abnormal.

The digital timing equipment consisted of very early transistorized decade dividers, which provided the various pulse rates for the user subsystems. A commercial time code generator was used for serial and binary-coded decimal codes for recoding purposes as well as displays. Commercially available frequency distribution amplifiers were used to distribute 100 kHz, 1 MHz and 5 MHz to users. Phase coherency and pulse to phase relationships were poor by today's standards, but very adequate for that period in the Deep Space Network.

Redundancy in this equipment was not available. However, a battery backup mode was provided to power oscillators and

divider circuits in case of firm power outages. Frequency counters, oscilloscopes, and amplifiers were excluded from power backup due to high alternating current requirements.

In the late 1960's, a new digital Frequency & Timing Subsystem was designed with a special highly reliable collection of circuit boards and components. The equipment, known as FTS-II, is the equipment now used in the Deep Space Stations. It was installed in all Deep Space Stations in 1969-1971. The subsystem design featured a triple redundant clock with majority voting, allowing measurement of the output of all three clocks to 1 microsecond. If the outputs did not agree to within 1 microsecond, the erroneous clock was flagged as bad, still leaving two clocks available. The bad clock was negated from providing user outputs if selected.

Another feature provided by the present system is an uninterruptable power system, which provides alternating current to the subsystem in case of firm power outages. This reduced hardware and special circuit design for selected modules that had to be powered to preserve frequency stability and time synchronization. Figure 1 depicts the current Frequency and Timing Subsystems at the Deep Space Stations.

In the early 1970's a system was introduced into the Deep Space Network which successfully and accurately accomplished network time synchronization. Commonly known as "Moon Bounce," the system consisted of an X-band transmitter at Goldstone (DSS 13), the moon as a reflector body, and a receiver at the Deep Space Stations. A psuedorandom code was transmitted to the moon and reflected to the stations with a mutual view. The receiving station had a receiver with a similar code generator, and a correlator for aligning the codes. This technique provided time synchronization and transfer in the 10-microsecond range throughout the network. The system provided time synchronization for the network for nearly a decade before being abandoned in 1980 for more sophisticated reliable methods, such as very long baseline interferometry.

By the mid-1970's, hydrogen masers had come to the forefront as the frequency reference of the future. Units were built and purchased to supply 64-meter stations with oscillator stabilities to 1 part in 10^{15}. Reliability of the units was uncertain, although while operating, the performance was superb. Further design analysis and modification provided units with much higher reliability, and today's units now function very well up to three years before major maintenance is required.

With this background and history, we have set the stage for a truly accurate and reliable network-wide system to meet the sophisticated and rigorous requirements of deep space flight projects. We have reliable and redundant timing subsystems, very accurate and reliable frequency standards driving the clocks and the technology to provide microsecond timing accuracies with frequency accuracies to parts in 10^{14}.

Through the span of 20 years the DSN has progressed in the frequency and timing disciplines 5 orders of magnitude in an operational environment. That is progress!

III. DSN Frequency and Timing System Description – Mark III-81

The "System" consists of several major components as depicted in the block diagram (Fig. 2). The National Timing Standard block (upper center of Fig. 2) is the reference for the DSN. Through agreements and cooperation with several international agencies, time and frequency are provided to the three Deep Space Communications Complexes.

The United States Naval Observatory (USNO) and the National Bureau of Standards (NBS) are the references for the Deep Space Network (DSN). Although they are independent agencies, they cooperate totally in establishing this country's Time and Frequency Standards. They are aware of their differences and publish notes to any user identifying the differences by the day. This portion of the block diagram is not a controlled part of the Frequency and Timing System, only a reference, and is discussed to describe continuity of the DSN as the reference.

A close examination of the National Timing Standard (Fig. 3) shows the relationship between all the complexes and the signal source (or traceability) of time and frequency. As can be seen, a traveling clock is the correspondent between the USNO and NBS, and is the key to maintaining their relationship. Comparisons are made both in frequency and time at regular intervals.

To service Australia, portable clock trips are made to the Australian National Mapping Services at least twice per year by the USNO. The Mapping Service then serves as the Australian distributor of time to users. Occasionally, clock trips are made to the Canberra Complex for comparison with clock performance measured by Australian TV synchronization pulse techniques.

The Spanish Complex is serviced by the Long Range Navigation system (LORAN) network, which provides timing signals via radio waves. On occasions the USNO travels to Europe, and when convenient pays a visit to the Madrid Complex for comparison. With the LORAN network and occasional clock trips, the Spanish Complex is synchronized to USNO, and therefore synchronized to a known offset to the Australian Complex (Fig. 4).

The Goldstone Complex is serviced similarly to the other complexes by traveling clock, but at more frequent intervals. The Goldstone Reference Standards Laboratory (RSL) maintains an ensemble of cesium oscillator clocks which, as discussed later, are the Network Master Clocks. Historically, the master clock has maintained time to within 50 nanoseconds of the NBS/USNO, and is often referred to as the best clock ensemble on the U.S. West Coast.

As described, the three complexes are serviced by the NBS/USNO entity, tying the complexes to one reference. The subsystems at the complexes assume the role of local standards for the generation and distribution of time and frequency to the users. A typical subsystem is described below (Refer to Fig. 5).

In Fig. 5, which depicts the Australian Complex, there are three major functions: The Frequency and Timing Subsystem and its users in the 64-m and 34-m configuration; the stand alone 34-m Frequency & Timing Subsystem; and the Communication Facility.

The 64-m/34-m conjoint station is considered the Complex Master Clock. The clock consists of one hydrogen maser as the primary oscillator, two cesium oscillators as backup, a coherent frequency distribution assembly and a triple redundant clock. Typically, the hydrogen maser maintains its stability to several parts in 10^{14} and is specified to support 3×10^{13} for 10 days. Translated into time, this relates to approximately 26 nanoseconds, which is considered very stable. The cesium oscillators are specified about 1 order of magnitude less than the masers.

Referring again to Fig. 5, frequencies are generated and distributed to the various users. Sinusoidal waves of 0.1 MHz to 100 MHz are derived, synthesized and distributed by the coherent reference generator. Constant amplitude and phase relationships are maintained. A 1-p/s pulse train is also supplied to the outlying stations via a microwave link. The delay time between the two clocks is measured to the submicrosecond level so that the clock at the outlying station can be accurately synchronized.

Again, note that although the complex is remote from other complexes, constant vigilance of the NBS/USNO and complex frequency and timing relationship is maintained. Television time synchronization is observed, calculated and used at the complex as well as the remote station. Weekly reports are made to JPL by teletype message, identifying relationships of all the oscillators and clocks. It is not uncommon for a complex to know its time relationship to NBS/USNO to within ±5 microseconds at any given time.

Figure 6 describes the Goldstone Complex, which can be seen as somewhat more diversified. The major difference is, of course, the Reference Standards Laboratory, which is the home of the DSN Master Clock. The Deep Space Network Master Clock is an ensemble of several cesium oscillators and a hydrogen maser. Although the hydrogen maser is currently remote from the bank of cesiums, its frequency is used, along with the cesium, to establish the Deep Space Network Standard. Similarly, Goldstone distributes time synchronization to the outlying Deep Space Stations by microwave and, again, the Deep Space Stations are typically within ±3 microseconds of the NBS/USNO reference. Each Deep Space Station generates and distributes frequencies and time to its particular users.

As a system check, independent from the NBS/USNO, a very long baseline interferometer technique has been utilized. By this technique, all three 64-m Deep Space Stations are scheduled to observe the same radio star source within 24 hours twice per week. The data are sent to JPL for reduction and establishment of the Deep Space Station offset to the Deep Space Network Master clock. This method is a near-real-time technique, and with historical data can very precisely determine each complex's frequency and time offset. It can be seen that with hydrogen-maser-driven clocks, continuous checks by TV and LORAN, and the VLBI, the Deep Space Network very precisely keeps track of itself.

Figure 2 describes the total global systems, pointing out time and frequency distribution, both on a global and local level. One can readily see the NBS/USNO relationship, the reporting process and how the complexes are tied together.

IV. Frequency and Timing Subsystem Description

The Frequency and Timing Subsystem generates and distributes sinusoidal reference frequencies, timing pulses, and epoch time codes for other subsystems within each Deep Space Communications Complex (DSCC). The primary frequency standard and epoch time are maintained within prescribed tolerance throughout the entire DSN and relative to the selected National Standards Agency.

The foundation of the DSCC Frequency and Timing Subsystems is the oscillator selected for use. The 64-m network (Deep Space Stations 14, 43, and 63) is equipped with hydrogen masers. The 64-m network requires hydrogen masers because of intricate navigation of the deep space probes. These are the stations that are ultimately used to gather VLBI data and radio metric data for orbit determination and navigation. The smaller aperture Deep Space Stations are equipped

with cesium oscillators, which are nearly as stable as the hydrogen masers.

The masers are kept in an environmentally controlled area, away from vibration and fluctuating magnetic fields. The area is designed for temperatures of 21 to 26°C, at 50% humidity. At these specifications, the maser stability is specified as follows, in terms of Allan Variance (see Appendix A):

1×10^{-12} for 1 second	1×10^{-14} for 12 hours
1×10^{-14} for 10^4 seconds	1×10^{-13} for 10 days

As seen in Fig. 7, the outputs of the three oscillators are connected to a switching network that selects the frequency standard desired. Three inputs are necessary, i.e., 0.1, 1 and 5 MHz, which are input to the coherent reference generator. The switch is semiautomatic in that it will switch to another oscillator if the primary standard fails. This switching takes place in less than 1 microsecond.

Due to the complexity of the Deep Space Stations supported by the Frequency and Timing Subsystem, the coherent reference generator must synthesize and distribute several frequencies. The coherent reference generator provides sinusoidal signals at frequencies of 0.1, 1, 5, 10, 10.1, 45, 50, and 55 MHz at 11.5 ±1.5 dBm. All frequencies maintain a constant phase relationship.

The triple redundant clock receives 1 MHz from the coherent reference generator for pulse shaping, pulse train generators and time code generators. The three clocks are identical and act upon the 1-MHz reference in the same manner, providing pulses and time codes. Controls are available on the front panel of the equipment to allow adjustment of the three clocks. The majority vote circuitry determines, at the microsecond level, if the three clocks are in synchronization, and permits timing signals to be distributed if at least two clocks are synchronized to within 1 microsecond.

The rationale for triple redundant majority voted clocks is to ensure that at least two clocks are operating correctly to obtain outputs. If all three clocks are not synchronized, no output is available. The assumption here is that it is better to have no time output than to have an output that may be erroneous. The majority vote circuitry cannot switch clock outputs, only detect if an output is incorrect. A manual switch is provided for clock selection.

Pulse trains are generated in the clocks in decade steps from 1 million pulses per second to 1 pulse per minute. Except for selected pulses that are treated independently, all pulse trains have 10 percent duty cycles. Rise and fall times are typically 250 nanoseconds from the 10 to 90 percent amplitude levels. Parallel and serial time codes are generated and distributed in 30-bit parallel binary-coded decimal, 30-bit parallel binary and 36-bit serial (NASA time code). Provision is also made for time displays throughout the control rooms, displaying day of year, hour, minutes and seconds of day adjusted to Greenwich Mean Time (GMT). (All clocks at all complexes are adjusted to GMT.)

An auxiliary reference divider is utilized to generate an independent 1 pulse per second derived from the secondary oscillator. Provided one knows the offset of the primary oscillator, by comparing the 1-pulse-per-second signals from the clocks and the auxiliary divider, an offset of the secondary or backup oscillator can be determined. In fact, this process is routinely recorded and long-term frequency offsets are determined for any and all backup oscillators at all Deep Space Stations.

To determine the offset of the primary oscillator, a portable clock measurement is made. Measurements are made on a weekly basis by determining the time difference between portable clock and the station clock on a nanosecond resolution counter (Goldstone only). As described earlier, the portable clock is referenced similarly to NBS/USNO. Therefore, the offset and rate of offset of the station clocks and oscillators can be accurately determined, traceable to the NBS/USNO references. In the case of overseas Deep Space Stations, as implied in Figs. 3 and 4, offsets are determined by LORAN or television signals. The tie is again via portable clock to NBS/USNO, periodically.

A reporting scheme from all Deep Space Stations, on a weekly basis, provides data to the Deep Space Network Operations Analysis Group, which determines how well the DSN is synchronized and what the precise offsets are. This data is provided all users, such as projects and experimenters.

To negate the possibility of a power failure rendering the equipment useless, endangering the record analysis credibility, a backup power system is utilized. Basically, it is a large converter system that is powered by a bank of batteries, converting the direct current to 115 volts alternating current. The unit is on line continuously, able to switch from firm power to its batteries for a power source. This scheme has proven satisfactory in the past several years, having had only one minor and inconsequential failure.

V. DSN Frequency and Timing System Performance

Performance of the frequency and timing equipment is measured in availability, accuracy and stability. Although

accuracy and stability are represented by minute numbers, availability is represented by a large number, displaying the engineering that was applied to the subsystem design, with redundancy designed into the clock, oscillators and power. The subsystem boasts of availability of better than 99.8%. In terms of hours per year this implies the equipment was available for support all but 17.5 hours. Unlike most subsystems, Frequency and Timing is operating 24 hours per day supporting missions, testing and experiments.

Accuracy in this discipline is measured both in time and frequency. In regard to time, during the period of Voyager 1 encounter of Saturn to this writing, clock accuracies between complexes, i.e., Madrid, Canberra and Goldstone, were kept to within 20 microseconds and the accuracy between USNO and any complex was within 20 microseconds. During the 130-day encounter phase, accuracies were within 10 microseconds.

In the frequency domain, the masers have performed at better than 3 parts in 10^{13} for the same period, or less than 26 nanoseconds clock change per day. The stability of the masers, hence the clocks, performed at better than 2×10^{13} long term, i.e., up to 10 days, in terms of Allan Variance.

The above performance was measured by the "System" over a period of one year. Portable clocks, LORAN, TV time synchronization, VLBI and the data analysts contributed to the impressive results.

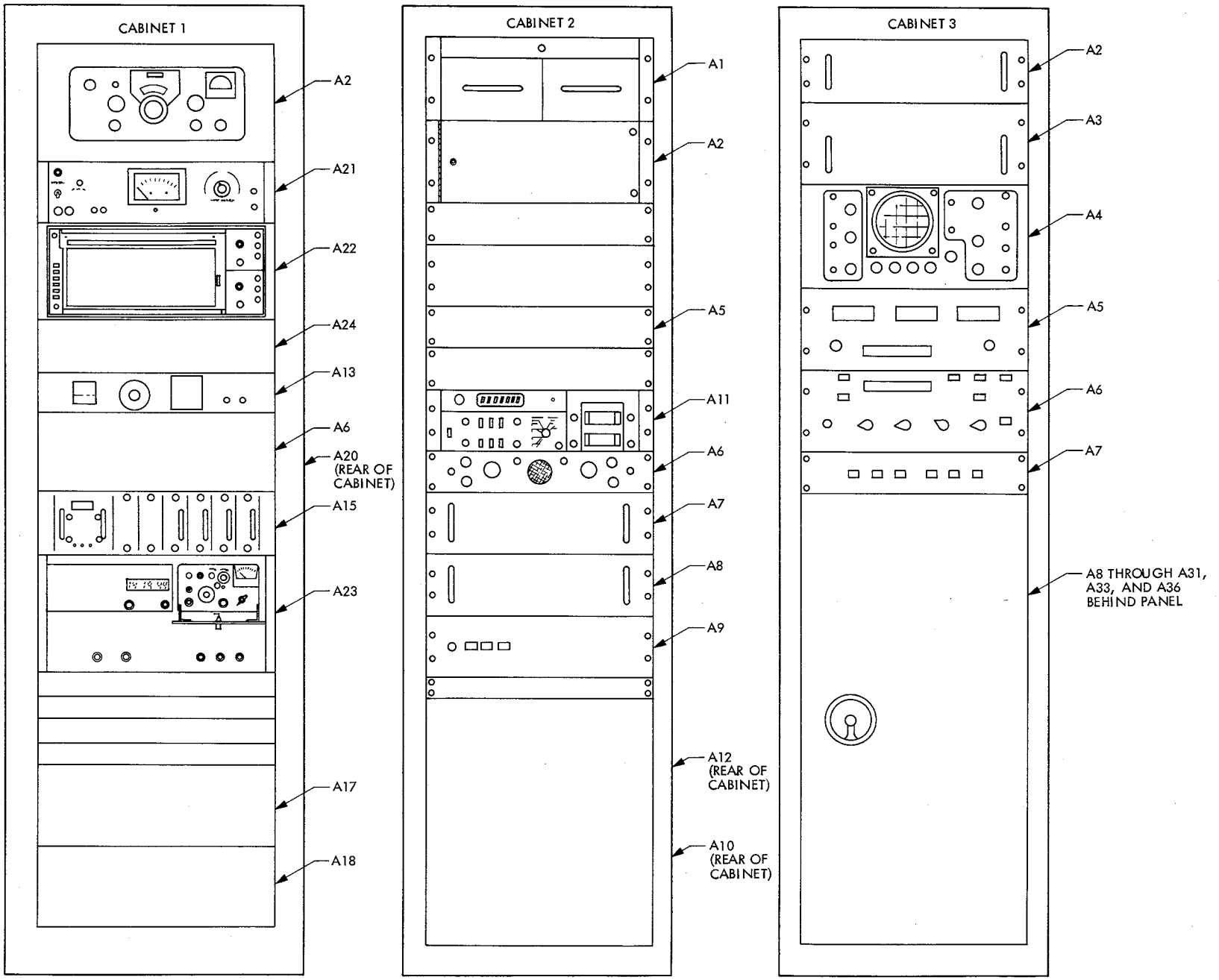

Fig. 1. DSN Frequency and Timing Subsystem—major cabinet assemblies components

COMPONENT REFERENCE DESIGNATION	NOMENCLATURE	COMMON NAME
1-2		
1986/FTS-1	CABINET ASSEMBLY NO. 1	CABINET 1
A2	COMMUNICATION RECEIVER	WWV-WWVH RECEIVER
A3	PHASE COMPARATOR AND RECORDER ASSEMBLY	PHASE COMPARATOR AND RECORDER
A3A1, A3A2	SECONDARY FREQUENCY STANDARD ASSEMBLY	SECONDARY FREQUENCY STANDARD (CRYSTAL)
A4	VLF TRACKING RECEIVER SERIES 599	VLF RECEIVER
A6	FREQUENCY SOURCE SELECTOR ASSEMBLY	SOURCE SELECTOR
A8	RUBIDIUM FREQUENCY STANDARD R20	RUBIDIUM NO. 2
A9	RUBIDIUM VAPOR FREQUENCY STANDARD HP 5065A	RUBIDIUM NO. 1
A10	RUBIDIUM RUNNING TIME PANEL	TIME PANEL
A11	RUBIDIUM V-4760 POWER SUPPLY	RUBIDIUM POWER SUPPLY
A13	FREQUENCY DISTRIBUTION AMPLIFIER	5 MHz DISTRIBUTION AMPLIFIER
A14	FREQUENCY DISTRIBUTION AMPLIFIER	1 MHz DISTRIBUTION AMPLIFIER
A15	WIDE BAND FREQUENCY DISTRIBUTION AMPLIFIER	WIDE BAND DISTRIBUTION AMPLIFIER
A17	ISOLATION AMPLIFIER POWER SUPPLY ASSEMBLY	PULSE AMPLIFIER POWER SUPPLY
A18	PULSE ISOLATION AMPLIFIER	PULSE AMPLIFIER
A20	BCD TIME PANEL	BCD DISTRIBUTION PANEL
A21	PHASE COMPARATOR	PHASE COMPARATOR
A22	CHART RECORDER ASSEMBLY	CHART RECORDER
A23	CESIUM FREQUENCY STANDARD	CESIUM STANDARD
A24	CESIUM SWITCH PANEL ASSEMBLY	CESIUM SWITCH PANEL
1-3		
1987/FTS-2	CABINET ASSEMBLY NO. 2	CABINET 2
A1	ISOLATION AMPLIFIER POWER SUPPLY ASSEMBLY	PULSE AMPLIFIER POWER SUPPLY
A2	PULSE ISOLATION AMPLIFIER	PULSE AMPLIFIER
A5	DECIMAL LAMP DRIVERS ASSEMBLY	LAMP DRIVER
A6	COMMUNICATION PANEL	COMMUNICATION PANEL
A7	TRANSFORMER PANEL ASSEMBLY	TRANSFORMER PANEL
A8	POWER SUPPLY ASSEMBLY	POWER SUPPLY
A9	AUXILIARY REFERENCE DIVIDER CONTROL ASSEMBLY	DIVIDER CONTROL
A10	JUNCTION MODULE ASSEMBLY	JUNCTION MODULE
A11	COUNTER	COUNTER
A12	AUXILIARY LOGIC DRAWER ASSEMBLY	AUXILIARY LOGIC DRAWER
1-4		
1988/FTS-3	CABINET ASSEMBLY NO. 3	CABINET 3
A2	POWER SUPPLY ASSEMBLY	POSITIVE POWER SUPPLY
A3	POWER SUPPLY ASSEMBLY	POSITIVE-NEGATIVE POWER SUPPLY

COMPONENT REFERENCE DESIGNATION	NOMENCLATURE	COMMON NAME
A4	OSCILLOSCOPE	OSCILLOSCOPE
A5	STATION CLOCK MONITOR CONTROL ASSEMBLY	CONTROL NO. 2
A6	SUBSYSTEM MONITOR CONTROL ASSEMBLY	CONTROL NO. 1
A7	MISCELLANEOUS DECODER CARD FILE ASSEMBLY	ERROR DETECTOR
A8	REFERENCE TIMING PULSE GENERATOR CARD FILE ASSEMBLY	REFERENCE DIVIDER
A9	TIME CODE GENERATOR CARD FILE ASSEMBLY	NASA 36-BIT GENERATOR
A10	TIME CODE GENERATOR CARD FILE ASSEMBLY	NASA 28-BIT GENERATOR
A11	TIME CODE GENERATOR CARD FILE ASSEMBLY	NASA 20-BIT GENERATOR
A12	FILTER MODULATION CARD FILE ASSEMBLY	FILTER MODULATOR
A13	JUNCTION BOX CARD FILE ASSEMBLY	JUNCTION BOX NO. 3
A14	BCD TO DEC CONVERTER CARD FILE ASSEMBLY	BCD TO DEC
A15	JUNCTION BOX CARD FILE ASSEMBLY	JUNCTION BOX NO. 2
A16	BCD TO DEC CONVERTER CARD FILE ASSEMBLY	BCD TO DEC CONVERTER
A17	JUNCTION BOX CARD FILE ASSEMBLY	JUNCTION BOX NO. 1
A18	AUXILIARY REFERENCE TIMING PULSE GENERATOR	AUXILIARY TIMING PULSE GENERATOR
A19	AUXILIARY PULSE AMPLIFIER CARD FILE ASSEMBLY	PULSE AMPLIFIER
A20	BCD TIME SELECTOR CARD FILE ASSEMBLY	30-GATE FILE A
A21	BCD TIME SELECTOR CARD FILE ASSEMBLY	SIMULATOR 30-GATE FILE
A22	BCD TIME SELECTOR CARD FILE ASSEMBLY	30-GATE FILE B
A23	JUNCTION BOX CARD FILE FILE ASSEMBLY	JUNCTION BOX NO. 4
A24	BCD TIME SELECTOR CARD FILE ASSEMBLY	30-GATE FILE C
A25	TIMING PULSE GENERATOR CARD FILE ASSEMBLY	DATA DIVIDER A
A26	CLOCK CARD FILE ASSEMBLY	CLOCK A
A27	TIMING PULSE GENERATOR CARD FILE ASSEMBLY	DATA DIVIDER B
A28	CLOCK CARD FILE ASSEMBLY	CLOCK B
A29	TIME PULSE GENERATOR CARD FILE ASSEMBLY	DATA DIVIDER C
A30	CLOCK CARD FILE ASSEMBLY	CLOCK C
A31	POWER DISTRIBUTION AND MONITOR ASSEMBLY	POWER DISTRIBUTION AND MONITOR
A33	INTERCONNECT BOX	INTERCONNECT BOX
A36	INTERCONNECT BOX	INTERCONNECT BOX

Fig. 1 (contd)

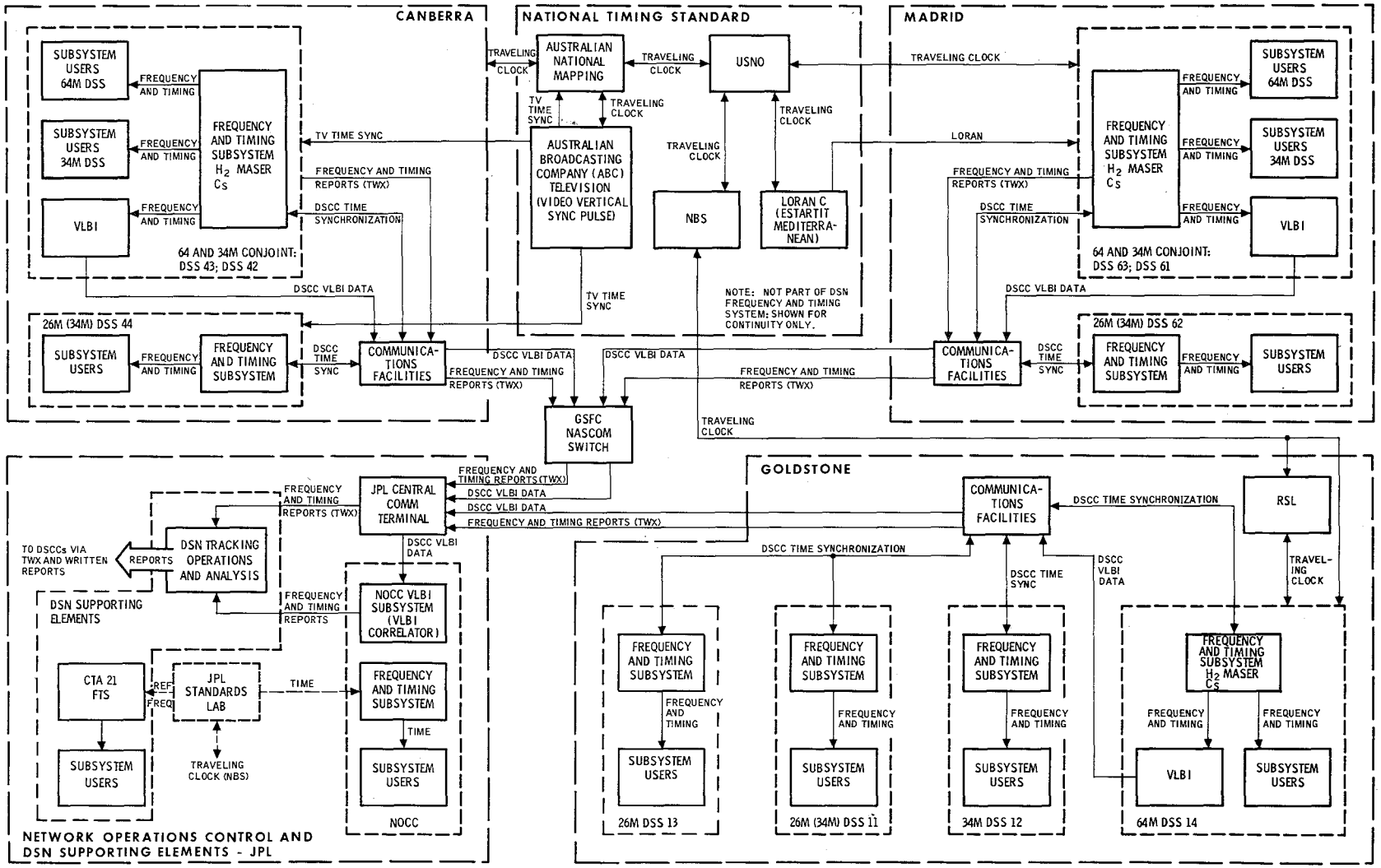

Fig. 2. DSN Frequency and Timing System block diagram

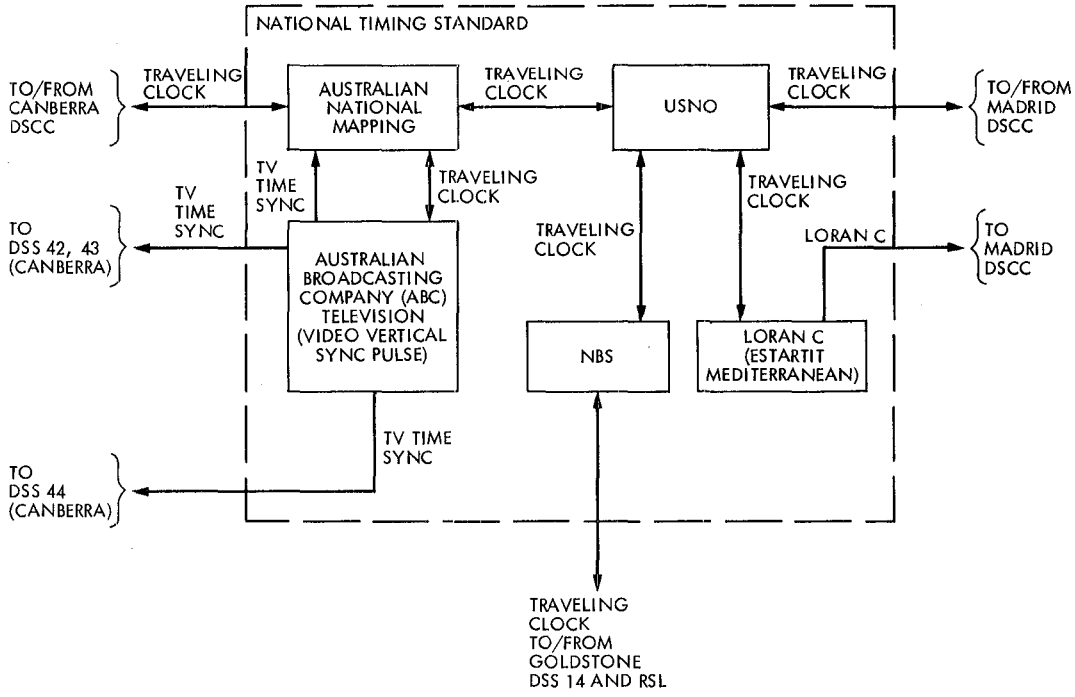

Fig. 3. National Timing Standard data flow

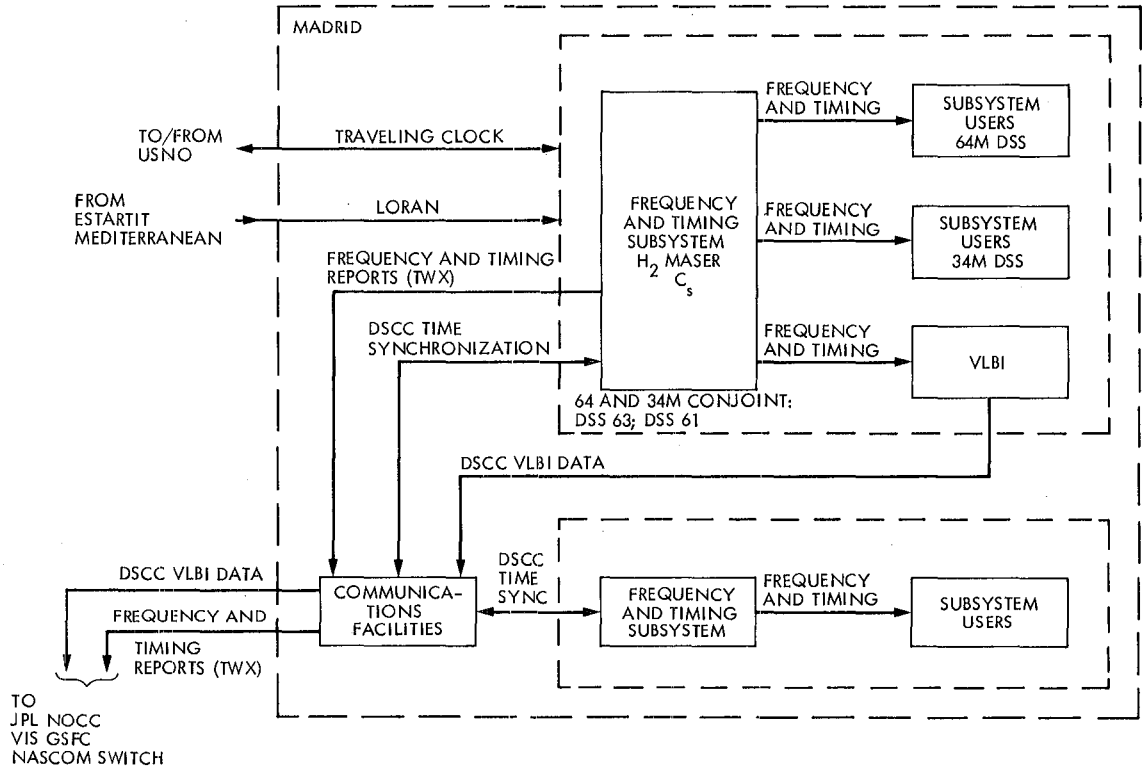

Fig. 4. Frequency and Timing Subsystem (Madrid, Spain)

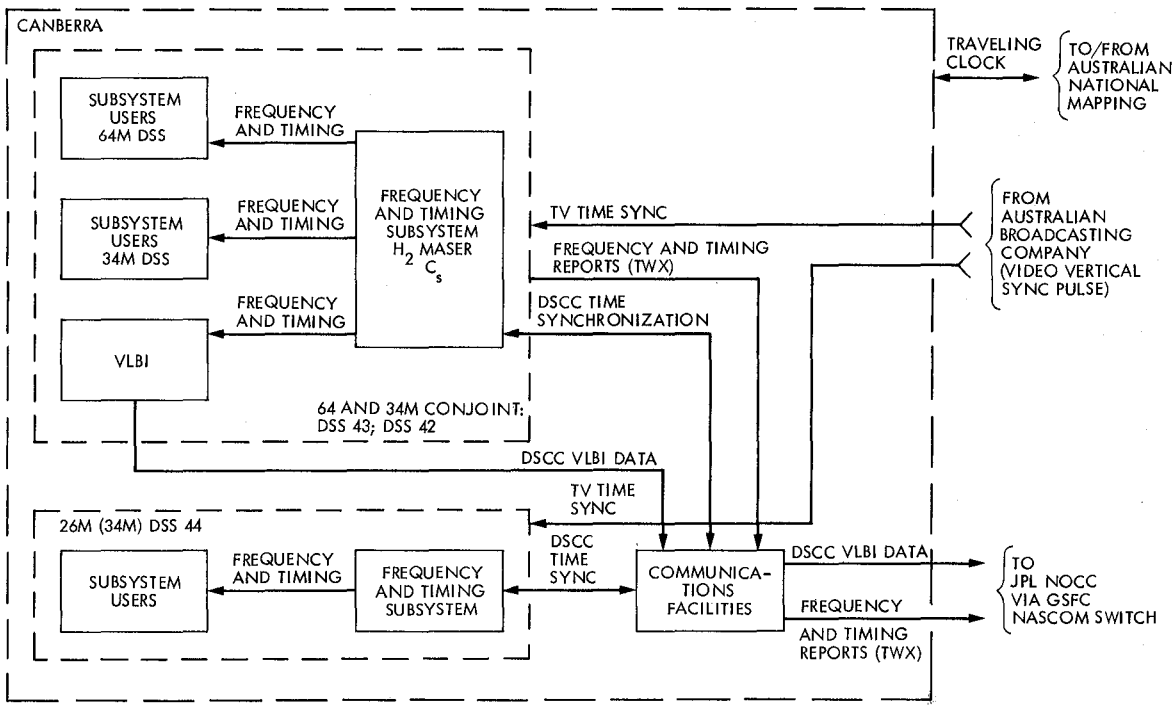

Fig. 5. Frequency and Timing Subsystem (Canberra, Australia)

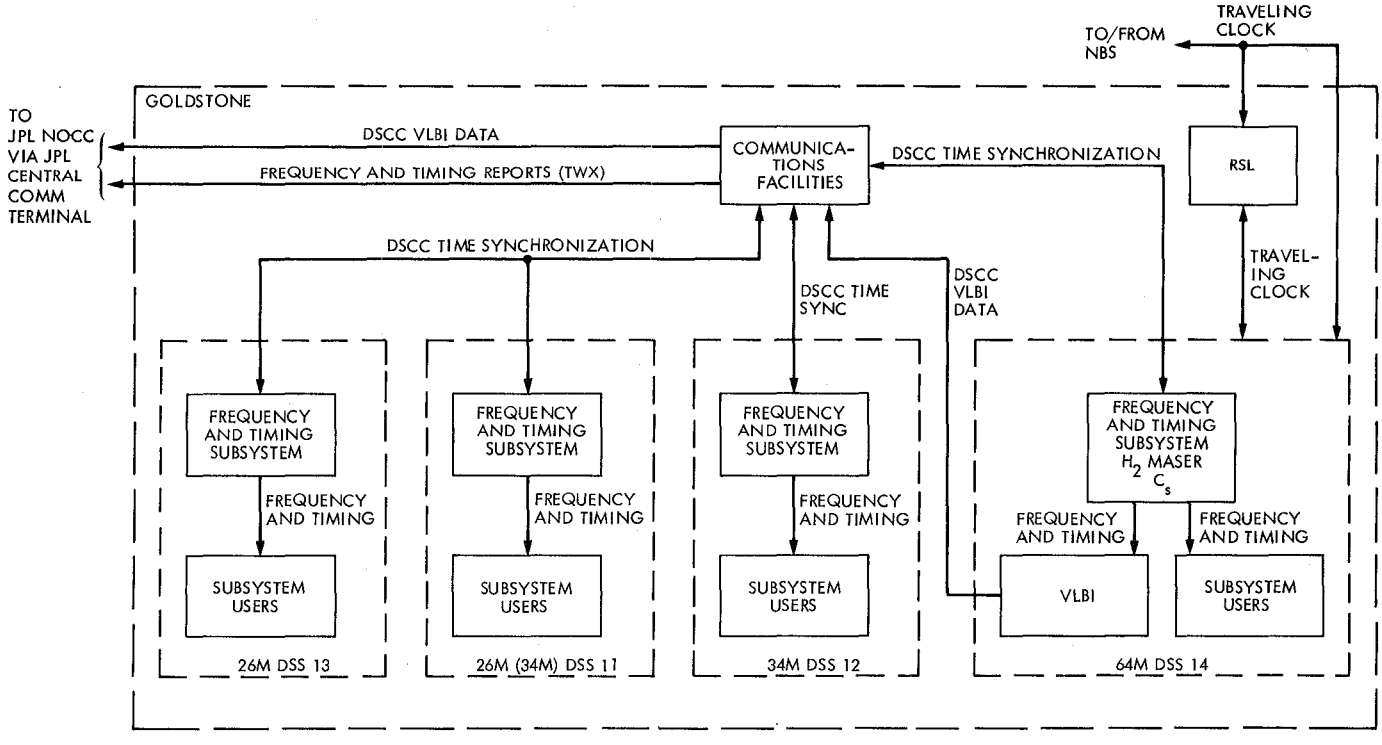

Fig. 6. Frequency and Timing Subsystem (Goldstone, California)

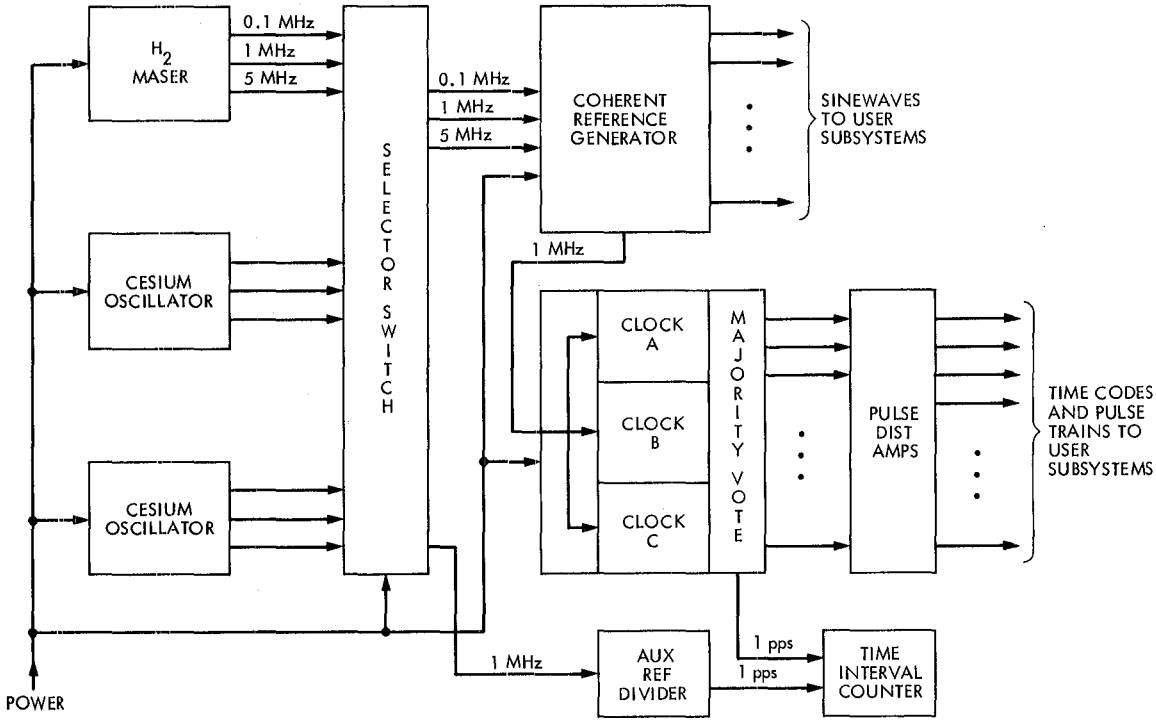

Fig. 7. Frequency and Timing Subsystem block diagram

Appendix A

Allen Variance Definition

A measure of the average fractional frequency deviation of a frequency source is defined as follows: Let the instantaneous phase of the source be $2\pi\nu_0 t + \phi(t)$, where ν_0 is the nominal frequency, and 0(t) is the instantaneous phase deviation. The instantaneous fractional frequency deviation y(t) is

$$y(t) = \frac{1}{2\pi\nu_0} \frac{d\phi(t)}{dt} .$$

Fix an averaging time τ, and consider successive time intervals $(k\tau, (k + 1)\tau)$, $k = 0, 1, 2, \ldots$. The average of y(t) over the k^{th} interval is

$$\bar{y}_k = \frac{1}{\tau} \int_{k\tau}^{(k+1)\tau} y(t)\, dt = \frac{\phi((k + 1)\tau) - \phi(k\tau)}{2\pi\nu_0\tau} .$$

By definition, the Allan variance is the quantity

$$\sigma_y^2(\tau) = \frac{1}{2} < (\bar{y}_{k+1} - \bar{y}_k)^2 >,$$

where $< >$ means infinite time average over k.

In practice, where only a finite number m of differences $\bar{y}_{k+1} - \bar{y}_k$ are available, the Allan variance is estimated by

$$\hat{\sigma}_y^2(\tau) = \frac{1}{m} \sum_{k=0}^{m-1} \frac{1}{2} (\bar{y}_{k+1} - \bar{y}_k)^2 .$$

Since $\sigma_y^2(\tau)$ does vary with τ, each specification of deviation ($\sqrt{\text{variance}}$) should include the averaging time, which gives the time scale over which the deviation specification applies. The specification should also mention the number of samples and the noise bandwidth of the measuring system.

DSN Command System

H. C. Thorman
TDA Engineering Office

Modification of the currently operational DSN Command System MK III-80 in 1981 consisted of improvement of the uplink carrier frequency tuning capability to satisfy Voyager 2 requirements. Upgrading of Command System monitoring functions in the Network Operations Control Center is scheduled for 1982. DSN Command System requirements and functional design are described for the Mark IVA Network, which is planned for 1984-1985 implementation.

I. DSN Command System Mark III-80

The Mark III-80 configuration of the DSN Command System, which was described in Ref. 1, is the currently operational configuration. In early 1981 the uplink digitally controlled oscillator (DCO) hardware was modified to correct a performance anomaly, and the metric data assembly (MDA) software was modified to provide satisfactory control of the DCO for Voyager 2 uplink carrier frequency tuning. No other major modifications were required in the Command System.

The command processor assembly (CPA) software upgrade previously planned for 1981 has been rescheduled to late 1983 to coincide with the Mark IV-84 configuration implementation. Network Operations Control Center (NOCC) Command Subsystem software modifications, to provide computer-controlled prepass data transfer and validation tests and revised displays, are scheduled for mid-1982 as part of a general upgrade of the Network Operations Control Area (NOCA) to reduce operations costs.

II. DSN Command System Mark IV-85

A. Introduction

Functional requirements and functional design have been established for the Command System of the Mark IVA Network. The network functional design provides one Signal Processing Center (SPC) at each Deep Space Communications Complex (DSCC). The Ground Communications Facility (GCF) will provide communications between JPL and each SPC.

The Networks Consolidation Program (NCP) requires the Mark IVA Network to support high-apogee earth-orbital missions in addition to the deep space and planetary missions.

A simplified block diagram of the DSN Command System Mark IV-85 is shown in Fig. 1. Each of the three complexes (Goldstone, Tidbinbilla, and Madrid) will have a 64-meter antenna with deep space uplink, a 34-meter antenna with both deep space and earth orbiter uplinks, and a 9-meter antenna

with earth orbiter uplink. (Each complex will also have additional 34-meter antennas, for downlink only.)

B. Implementation Schedule

The Mark IVA Network implementation plan calls for an interim configuration to be installed at all three complexes in early 1984, a final configuration at Goldstone by February 1985, and at Tidbinbilla and Madrid by August 1985. The interim configuration will include new command equipment for 34-meter antenna support of high earth orbit and deep space missions, while retaining portions of the present Mark III configuration. The final configuration at each complex will include the 9-meter antenna and associated front end equipment, a total of four strings of DSCC command subsystem equipment, and the new DSCC Monitor and Control Subsystem, as shown in Fig. 1.

C. Mission Set

The Mark IVA Network baseline design is required to provide capabilities to support the flight missions listed below:

(1) Current deep space missions:
   (a) Pioneer 6 through 12
   (b) Viking Lander
   (c) Helios
   (d) Voyager 1 and 2

(2) Planned deep space missions:
   (a) Galileo
   (b) International Solar Polar Mission (ISPM); 2 spacecraft

(3) Current high elliptical earth orbital missions:
   (a) International Sun-Earth Explorer No. 3 (ISEE-3)

(4) Future high elliptical earth orbital missions:
   (a) Active Magnetospheric Particle Tracing Explorer (AMPTE); 3 spacecraft
   (b) Origin of the Plasma in the Earth's Neighborhood (OPEN); 4 spacecraft

D. Performance Requirements

Support of the Mark IVA mission set will require Command System performance characteristics compatible with the NASA standard transponder to be used on future spacecraft and also compatible with current in-flight spacecraft and certain planned spacecraft that do not use the standard transponder. Some of the required capabilities are listed below:

(1) Data rates. Data rates from 1 bit/sec to 2000 bits/sec will be provided.

(2) Subcarrier frequencies. Sine wave and square wave subcarriers will be generated at frequencies of 100 Hz to 16 kHz.

(3) Subcarrier data modulation. Selection will be provided for phase-shift-keyed (PSK) or frequency-shift-keyed (FSK) modulation of the subcarrier by the pulse-code-modulated (PCM) command symbol stream. An option for amplitude modulation (AM) of the FSK subcarrier will also be provided.

(4) Carrier modulation. The command-modulated subcarrier will be phase-modulated on an S-band carrier for radiation to the spacecraft. Control of modulation index angle will be provided over a range from 0.1 to 1.8 radians.

(5) Carrier frequencies. Generation of the uplink carrier at S-band frequencies assigned for deep space missions will be provided at the 64-meter and 34-meter antennas. S-band frequencies assigned for earth orbit missions will be provided at the 34-meter and 9-meter antennas.

III. System Functional Description

As discussed in Ref. 2, many of the spacecraft supported by the DSN have onboard storage and sequencing capabilities that permit command sequences to be sent well in advance of the actions to be taken by the spacecraft. Thus, fewer direct-action (real-time) commands are needed. Ground system capabilities providing massive storage of spacecraft commands, multimission operating functions, and standardized protocol were incorporated in the DSN Command System in 1978 (Ref. 3). These capabilities will be continued in the Mark IV-85 system configuration.

A. Operational Functions

End-to-end spacecraft command operations are represented functionally in Fig. 2. Command sequences for one or more spacecraft are generated and stored at a Mission Operations Center (MOC). Commands for a particular spacecraft are selected from the command files, formatted into messages, and stored for transmittal to a specified link of a DSCC. Command data are extracted from the message received and are stored until radiated. Finally, the commands arrive at the spacecraft and are either executed immediately, or stored onboard for later execution.

The functions of the DSN Command System in this process include the following:

(1) Establishing the DSCC configuration for the specified spacecraft.

(2) Receiving and storing command data at the DSCC.

(3) Queuing command data to be radiated to the spacecraft.

(4) Radiating the command data to the spacecraft.

(5) Monitoring and reporting system status and events.

B. Operational Procedure

On-site configuration inputs to the DSCC Command (DCD) Subsystem specify the flight project name and the spacecraft identification number. These inputs cause the Command Processor Assembly (CPA) software to transfer a specified configuration and standards and limits table from disk storage to memory, and to configure the DCD Subsystem according to the table. Changes may later be made by high-speed data messages from NOCC (or by keyboard entries at the Link Monitor and Control Console).

Prior to the beginning of the scheduled spacecraft track, the control of the DSCC command functions is transferred to the NOCC. Configuration standards and alarm/abort limits are updated by transmission of high-speed data messages from the NOCC Command Subsystem (NCD) real-time monitor processor. The standards and limits are derived from files maintained in the NOCC Support Subsystem. Spacecraft-dependent parameters, such as symbol period, subcarrier frequency, alarm limits, and abort limits, are established via these messages. After the proper configuration standards and limits have been established, test commands are transmitted through the system to ensure that the system can accept spacecraft commands via high-speed data messages, temporarily store the commands, and confirm radiation. After the network operations control team has established that the system is operating properly, the system control is transferred to the flight project's MOC for loading of actual spacecraft command sequences to be radiated to the spacecraft during the track period.

At the time for radiation of each command element, the subsystem advances to the active mode (see Fig. 3 for description of the various modes) and command data are transferred to the Command Modulator Assembly (CMA) for immediate radiation via the Receiver-Exciter, Transmitter, Microwave, and Antenna Subsystems.

C. Command Data Handling

The DCD Subsystem design allows mission operations to prepare large files of spacecraft commands in advance and then to forward several files to the DSCC link at the beginning of a spacecraft track.

1. Command files. Each file may consist of up to 256 high-speed data blocks. The content of each data block is a file *element*. The first block in a file contains the *header element* and each remaining block contains a *command element*. Each command element may consist of up to 800 bits of spacecraft command data. Up to 8 files for a given mission can be stored by the CPA. Thus, the available storage is over 1.6 million command bits.

The header element contains file identification information, file processing instructions, and a file checksum. The file processing instructions include optional file radiation *open* and *close window times*, and an optional file *bit 1 radiation time*. File open and close window times specify the time interval during which command elements in the file may begin radiation (i.e., a mission sequence may demand that specific commands not be sent before or after a certain time). The bit 1 radiation time allows the project to specify the exact time at which the file is to begin radiation to the spacecraft. The file checksum provides end-to-end error protection for the ground command system. It is created at the time of file generation and is passed intact to the DSS. It adds reliability to insure that no data were dropped or altered in the transfer from one facility to another.

The command elements each contain command bits, file identification, element number, element size, and an optional "delay time" (interval from start of previous element). If delay time is not specified, the element will start radiating immediately after the end of the previous element.

2. Receiving and storing command data at a DSCC. Normally, the files of commands to be radiated to the spacecraft will be sent from the MOC to the specified DSCC link at the beginning of a spacecraft track period. However, files may be sent to the DSCC link at any time during the spacecraft track period. The first step in receiving and storing command data at a DSCC is the process of opening a file area on the CPA disk. The MOC accomplishes this by sending a header element, which serves as a *file-open* directive. After the CPA acknowledges receipt of the header element, the MOC sends the remainder of the file (up to 255 command elements) and follows it with a *file-close* directive. The CPA acknowledges the file-close instruction and indicates whether the file loading was successful or unsuccessful. If the file loading was unsucessful, the acknowledge message contains the reason for the failure and from what point in the file the command elements are to be retransmitted. When the file is successfully closed, the MOC may proceed to send additional files, up to a total of eight.

3. Queuing the command data for radiation. After the files are stored at the CPA, the MOC sends one or more *file-attach* directives to place up to five file names in the radiation *queue*. The Mission Control Team determines in which order the files

are to be attached. The order in which they are attached determines the sequence in which they will be radiated: that is, first attached, first to radiate to the spacecraft.

4. Command radiation to the spacecraft. The first command element in the top (prime) file in the queue begins radiation to the spacecraft immediately after attachment or as soon as all optional file instructions (such as bit 1 radiation time) are satisfied. The prime file status is defined to be *active* when the first command element begins radiation. Upon completion of radiation of the first command element, the second command element begins radiation either immediately or when the optional delay time has been satisfied. The process continues until all command elements in the file have been radiated. After the first file completes radiation, the second file in the queue automatically becomes the prime file and the command radiation process is repeated. After the second file completes radiation, the third file becomes prime, etc. This process is repeated until all files in the queue are exhausted. The MOC can attach new files to the queue whenever space is available.

Confirmations of command element radiation are reported in *event messages* to the MOC and NOCC once per minute, or after five elements have been radiated, whichever occurs first. If a command element is aborted, or if an alarm occurs, an event message is sent immediately.

5. Additional data processing. The foregoing descriptions of the DSCC functions of storing the command files, attaching the files to the queue, and radiating the commands to the spacecraft assume nominal-standard operation. Additional data processing functions are provided for worst-case conditions, nonnominal operations, and failure recovery. Control of these functions is normally exercised remotely from the MOC. However, emergency control is also available at the Link Monitor and Control Console.

a. File erase. A file can be deleted from storage at the CPA by means of a *file erase* directive, if the file is not attached to the radiation queue.

b. Clearing the queue. As previously stated, the order of file radiation to the spacecraft is dependent on the order of files in the queue. To rearrange the order, a *clear-queue* directive must be sent, followed by file-attach directives in the desired order.

c. Suspend radiation. If the Mission Control Team desires to stop command radiation, a *suspend* message can be sent to the CPA. This message stops command radiation to the spacecraft upon completion of the current element. The file status then changes from active to suspended.

d. Resume command radiation. To restart radiation of a suspended file (either suspended intentionally or from an abort), a message can be sent to *resume* radiation *at* a specified unradiated element in the file. The suspend and resume-at directives can be used for skipping elements of the prime file, if desired.

e. Command abort. As each command bit is radiated to the spacecraft, numerous checks are made to insure validity of the command data. If a failure is detected during the radiation, the command element is automatically aborted, the prime file status is changed from active to suspended, and radiation is terminated until a resume directive is received.

In addition to the automatic abort function there is provision for the MOC to send an *abort and suspend* directive to terminate command radiation immediately without waiting for completion of an element.

f. Close window time override. If a close-window time is specified in a file header element, and the Mission Operations Team later decides to extend the permissible time for radiation of that file, an *override* message can be sent (after the file becomes prime) which instructs the CPA to ignore the close-window time.

D. Data Records

All high-speed data blocks received by the CPA and all blocks sent from the CPA are to be logged at the DSCC on the Original Data Record (ODR). In addition, the CPA has the capability to record a temporary ODR on disk if the ODR is disabled.

High-speed data blocks from all complexes are recorded at the GCF central communications terminal (CCT). Command system high-speed data blocks from a Mission Operation Center to a DSCC are also recorded at the CCT.

The DSCC original data records and the CCT recording provide information for fault isolation in case problems occur in the Command System operation.

IV. Subsystems Configurations for Mark IV-85 System

Planned modifications and reconfiguration of subsystems for the DSN Command System Mark IV-85 (and Mark IV-84) are summarized below.

A. Antenna Mechanical Subsystem

At Tidbinbilla and Madrid all antennas will be located in the vicinity of the SPC. At Goldstone, the 64-meter antenna

and the 9-meter antenna will be located near the SPC. The Goldstone 34-meter transmit-receive antenna will remain at the present DSS 12 (Echo Station) site, but control will reside at the SPC.

B. Antenna Microwave Subsystem

For the 9-meter antenna, the microwave subsystem will provide uplink signal feed at S-band frequencies assigned for earth orbital missions (2025-2110 MHz). For one 34-meter antenna at each complex, the microwave subsystem will be required to handle S-band uplinks over the range of earth orbital and deep space missions (2025-2120 MHz). For the 64-meter antenna the microwave subsystem uplink capability will be unchanged (S-band 2110-2120 MHz).

The 9-meter and 34-meter antenna microwave subsystems provide selection of right or left circular polarization. The 64-meter antenna microwave subsystem provides selection of linear polarization or right or left circular polarization.

C. Transmitter Subsystem

The 9-meter antenna will have a 10-kW transmitter operating in the earth orbital mission S-band frequency range. A 34-meter antenna will have a 20-kW transmitter operating over the range of earth orbital and deep space mission S-band frequencies. The 64-meter antenna will have 20-kW and 100-kW transmitters for the deep space mission S-band frequency range, as now.

D. Receiver-Exciter Subsystem

An S-band exciter will be acquired with each 9-meter antenna from the Ground Spaceflight Tracking and Data Network (GSTDN). The DSN exciter for the 34-meter antenna will be upgraded to cover earth orbital and deep space mission S-band frequencies. The present DSN S-band exciter will be retained in the 64-meter antenna link.

Functions of the exciter include receiving the command-modulated subcarrier signal from the DSCC Command (DCD) Subsystem, phase-modulating that signal on the uplink carrier, returning a demodulated signal to the DCD subsystem for confirmation, and sending modulation on or off indications to the DCD subsystem.

E. DSCC Command Subsystem

In the final Mark IVA Network configuration (in 1985), the DCD Subsystem in the SPC at each complex will be implemented as shown in Fig. 1. A new Command Switch Assembly (CSA) will permit any of three exciters to be connected to any of four Command Modulator Assemblies (CMA) under control of the Complex Monitor and Control console. New CMA's will be implemented to accommodate the Mark IVA mission support requirements. The Command Processor Assemblies (CPA) will use existing Modcomp II-25 computers with core memory increased to maximum capacity. CPA software will be upgraded to satisfy new mission support requirements, to modify the CMA interface functions, and to provide required functions for interfacing with the new DSCC Monitor and Control Subsystems.

For the interim configuration (in 1984), two of the new CMA's (one prime, one backup) will be provided at each complex, to provide required command capability for the 34-meter antenna subnetwork. An interim software program will be implemented in the CPA to operate with the new CMA.

F. DSCC Monitor and Control Subsystem

New equipment will be implemented for the DSCC Monitor and Control (DMC) Subsystem at each complex in the final Mark IVA Network configuration. Assignment of command equipment (antenna, transmitter, exciter, and command modulator-processor combinations) to a given "link," for each scheduled spacecraft pass or for a scheduled test, will be accomplished by the DMC Subsystem along with telemetry and tracking equipment assignments. Prepass countdown will be controlled by inputs at the Link Monitor and Control Console.

The DMC Subsystem will receive antenna pointing and uplink frequency predictions and will relay them to the appropriate subsystems. The DMC Subsystem will send link status information to the CPA, and the CPA will send Command Subsystem status information to the DMC Subsystem for link console displays and for incorporation into the monitor data that the DMC Subsystem sends to the NOCC.

In the interim configuration, the Monitor and Control Subsystem will be limited to the existing Data System Terminal (DST) and Digital Information Subsystem (DIS) functions.

G. GCF Subsystems

In the final Mark IVA Network configuration, the GCF Digital Communication (GDC) Subsystem will replace the present GCF High Speed and GCF Wideband Subsystems. All command data blocks will be communicated at a line rate of 56 kb/s, instead of the present 7.2 kb/s rate, between the Central Communications Terminal at JPL and the Area of Routing Assembly at each DSCC.

At the Goldstone DSCC the GCF Intersite Communication Subsystem will communicate the CMA output signal from the

SPC to the DSS 12 exciter and the confirmation signal from the exciter to the SPC.

H. NOCC Command Subsystem

The NOCC Command (NCD) Subsystem Real-Time Monitor (RTM) software will be upgraded to accommodate new destination codes, spacecraft identifiers, standards and limits tables and test command tables for the interim and final configurations. The NOCC Support Subsystem will be expanded to provide capability for command system performance records and analysis and additional capacity for test command tables.

References

1. Thorman, H. C., "DSN Command System Mark III-80," in *The Telecommunications and Data Acquisition Progress Report 42-57*, pp. 35-42, Jet Propulsion Laboratory, Pasadena, California, June 15, 1980.
2. Stinnett, W. G., "DSN Command System Mark III-78," in *The Deep Space Network Progress Report 42-43*, pp. 4-8, Jet Propulsion Laboratory, Pasadena, California, February 15, 1978.
3. Thorman, H. C., "DSN Command System Mark III-78," in *The Deep Space Network Progress Report 42-49*, pp. 11-18, Jet Propulsion Laboratory, Pasadena, California, February 15, 1979.

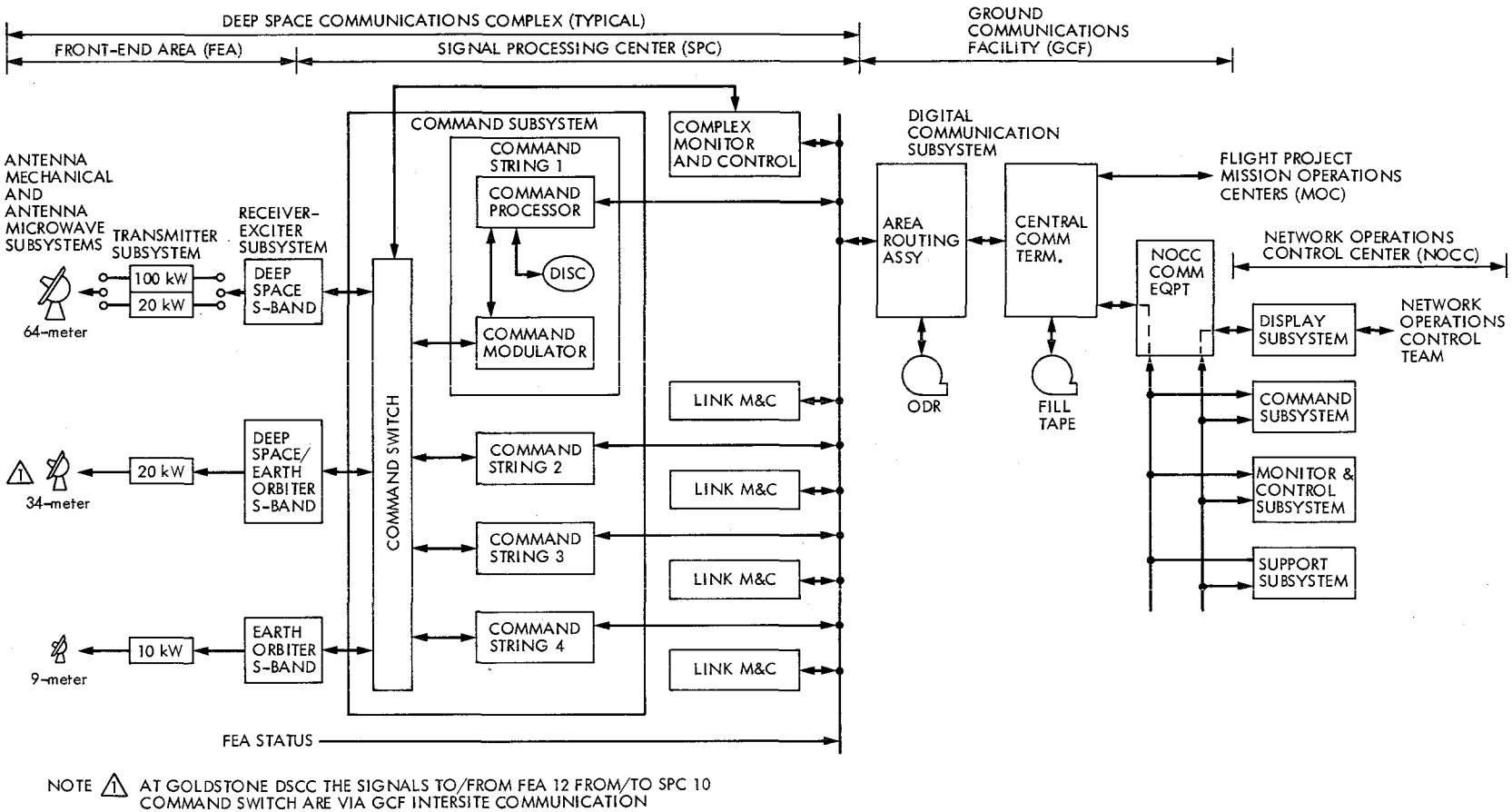

NOTE ⚠1 AT GOLDSTONE DSCC THE SIGNALS TO/FROM FEA 12 FROM/TO SPC 10 COMMAND SWITCH ARE VIA GCF INTERSITE COMMUNICATION

Fig. 1. DSN Command System Mark IV-85 block diagram

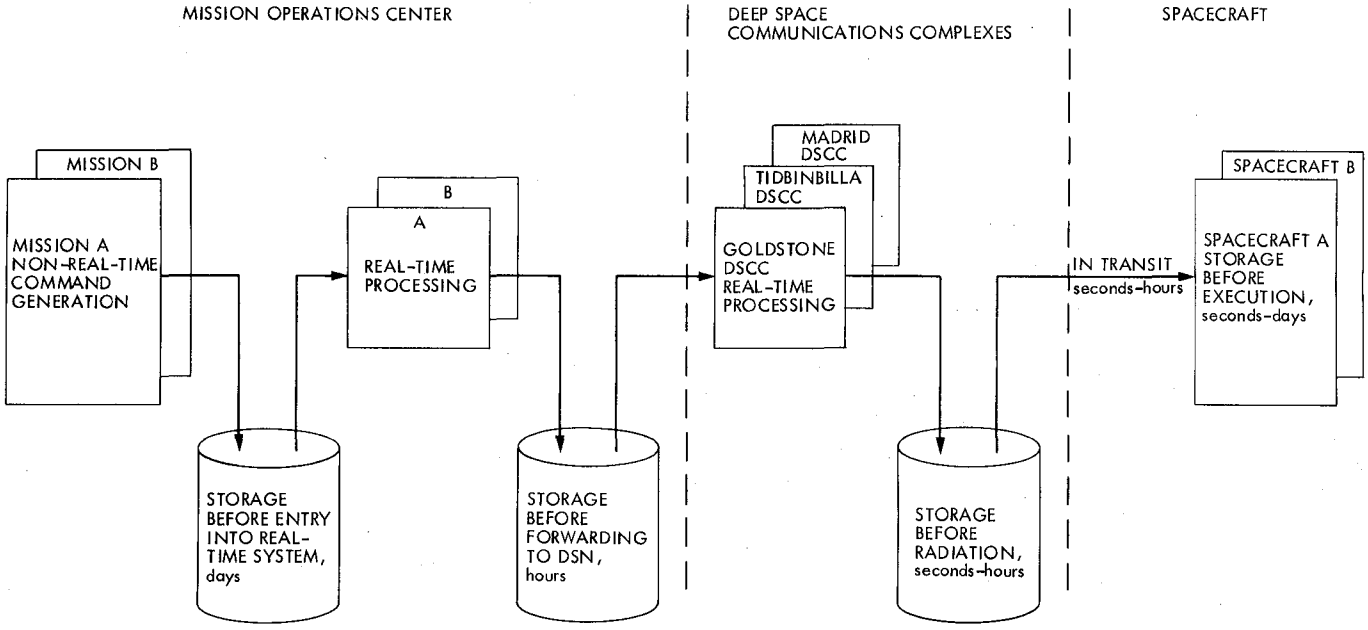

Fig. 2. End-to-end command data flow – typical storage times

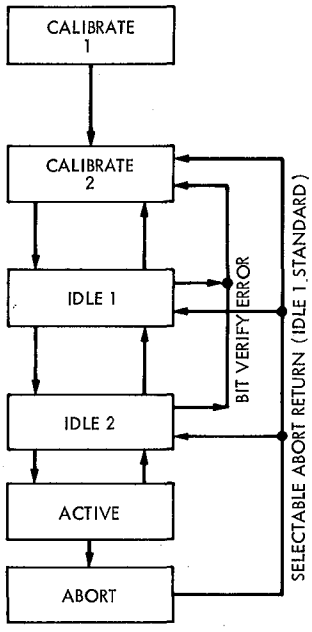

SUBSYSTEM MODE	PRIME PURPOSE	DATA ACCEPTED VIA HIGH SPEED	COMMENTS
CALIBRATE 1	ALLOWS DSS OPS PERSONNEL TO PERFORM INITIALIZATION TASKS	CONFIGURATION, STANDARDS AND LIMITS, MODE CONTROL, RECALL	UPON RECEIPT OF A STANDARDS AND LIMITS AND CONFIGURATION HSD BLOCK, THE CALIBRATE 2 MODE WILL BE ENTERED
CALIBRATE 2	STANDARD MODE FOR UPDATING STANDARDS AND LIMITS AND CONFIGURATION DATA VIA HIGH SPEED PRIOR TO SPACECRAFT ACQUISITION	CONFIGURATION, STANDARDS AND LIMITS, MODE CONTROL, RECALL	MULTIMISSION STANDARD PROCEDURES SHOULD STATE THAT THIS MODE IS TO BE ENTERED FOR CHANGING SUBCARRIER FREQUENCY, BIT RATE
IDLE 1	SAFE MODE - CANNOT COMMAND. PROVISION FOR IDLE/ACQUISITION SEQUENCE. ALLOWS CONFIGURATION AND STANDARDS AND LIMITS TO BE CHANGED	CONFIGURATION, STANDARDS AND LIMITS, MODE CONTROL, RECALL	ALL STANDARDS AND LIMITS AND CONFIGURATION DATA PARAMETERS WILL TAKE IMMEDIATE EFFECT IN THIS MODE
IDLE 2	ALLOWS ENTRY INTO ACTIVE MODE. PROVIDES IDLE/ACQUISITION SEQUENCE DURING COMMAND PERIODS	RECALL AND MODE CONTROL DATA ONLY	MODE CONTROL DATA CONTAINED IN THE COMMAND ELEMENT BLOCK
ACTIVE	COMMAND TRANSMISSION	RECALL AND MODE CONTROL DATA ONLY	
ABORT	PROVIDES ABORT INSTRUCTION TO CMA	RECALL AND MODE CONTROL DATA ONLY	

NOTES: 1. COMMAND DATA MESSAGES WILL BE ACCEPTED IN ALL MODES
2. ALARM MESSAGES/ALARM DATA WILL BE TRANSMITTED TO THE MOC IN ALL MODES EXCEPT ABORT

Fig. 3. DSCC Command Subsystem modes

The DSN VLBI System Mark IV-85

W. D. Chaney
TDA Engineering Office

The DSN VLBI System was established as a Network system in 1978. This article describes the evolution of the VLBI System from Mark I-79 to Mark IV-85 and discusses the system functional requirements for Mark IV-85.

I. Introduction

Very long baseline interferometry (VLBI) is a capability implemented in the Network to support flight project navigation requirements and provide station frequency standard stability measurements to validate the hydrogen maser frequency standard performance.

To manage this new major implementation, a DSN VLBI Program was established and led by a program manager from the TDA Office and a task manager from the implementing divisions. The initial functional requirements were reviewed in February 1978. The phases of implementation are described in Ref. 1.

This article updates the functional description and requirements given in Ref. 1 and defines the levels of implementation that constitute the Mark I-79, Mark II-81, Mark III-83, and Mark IV-85 VLBI Systems.

II. Definition

Very long baseline interferometry is a method of measuring the time of arrival of a radio signal at two locations very distant from each other on the Earth's surface. From the measurement of difference in time of arrival, the position of the radio source and/or several other parameters of the problem can be determined. These other parameters include Universal Time One (UT1) (the instantaneous rotational angle of the Earth), polar motion, the relative position of the two stations, and the time offset and rate of change of the clocks at the two stations.

The levels of implementation are defined as Mark I-79, Mark II-81, Mark III-83, and Mark IV-85 VLBI Systems.

The Mark I-79 VLBI System, implemented in 1979, provides time offset, rate of change of the clocks at the two stations, Universal Time One (UT1), and polar motion to the following performance:

Time offset: < 20 nanoseconds

Clock rate of change: < 3 parts in 10^{13}

Universal Time One: < 1.25 milliseconds

Polar motion: < 50 centimeters

The Mark II-81 VLBI System adds delta differential one-way range (ΔDOR) capability for use by flight projects' navigation in determining the angle between the spacecraft and a reference extragalactic radio source (EGRS). The differential

time delay between the spacecraft and EGRS is measured by the DSN to < 30 centimeters.

The Mark III-83 VLBI System improves the accuracy and operability of the Mark I-79 and Mark II-81. The accuracies available are:

Time offset: < 10 nanoseconds

Clock rate of change: < 7 parts in 10^{14}

Universal Time One: < 0.75 milliseconds

Polar motion: < 30 centimeters

All equipment used for determining the above parameters are operational and calibration data for troposphere, ionosphere, and the VLBI instrument are available. Improved hydrogen masers with a stability of $\approx$ 7 parts in 10^{15} will be implemented for fully operational capability.

The Mark IV-85 VLBI System adds the wide channel bandwidth (WCB) for operational support of radio source catalog update and maintenance and two-station baseline measurements. The accuracies are as follows:

Absolute radio source location: < 5 microradians

Relative radio source location: < 50 nanoradians

Two station baseline: < 3 centimeters

III. Mark IV-85 VLBI System Description

A. Introduction

The Narrow Channel Bandwidth (NCB) and Wide Channel Bandwidth (WCB) VLBI System will be implemented at the 64-meter antenna and the 34-meter listen-only (X-Y mount) antenna. Data acquisition, formatting, and recording are performed by the common equipment in the Signal Processing Center (SPC). A simplified block diagram indicating switching capability of the 64-meter and 34-meter antennas is shown in Fig. 1. The NCB VLBI System data are recorded at each DSS and transmitted via GCF wideband data lines at the GCF line rate. Ancillary data such as angles, angle residuals, weather data, predicts, and control data are routed via GCF wideband data lines to the Network Operations Control Center (NOCC) VLBI Processor Subsystem (VPS) where they are used to control and calibrate the VLBI data being correlated. The correlated output is used to compute: (1) time and time-rate offset, (2) polar motion and Universal Time, and (3) delta differential one-way range for spacecraft navigation.

The WCB VLBI System records data at 4 to 112 megabits/second rates (in the Haystack Observatory Mark III compatible format) for wideband correlator processing. WCB VLBI data tapes generated at the DSS are mailed to the JPL/CIT correlator for processing. The ancillary data are the same for both the NCB and WCB systems.

VLBI predictions are generated by the Predict Program in the NOCC Support Subsystem and transmitted to each DSS for antenna pointing and frequency control. Control messages of DSS assemblies used for VLBI are generated by the NOCC Support Subsystem and transmitted to the DSS Monitor and Control Subsystem. Monitor of DSS assemblies used for VLBI data acquisition is performed by the assemblies and collected by the DSS Link Monitor and Control Subsystem. These data are forwarded to NOCC via high-speed data lines (HSDL) for display and analysis of the DSN VLBI System.

Both NCB and a sample of WCB VLBI are correlated in near-real time by the NOCC correlator. Validation of the correlation results are displayed for the analysts for the Network Operations Control Team (NOCT) and are transmitted to the DSS for display and analysis.

B. Key Characteristics

The key characteristics of the NCB and WCB VLBI systems are given in Table 1.

C. Functions and Interface

1. Narrow Channel Bandwidth (NCB) VLBI. To determine intercomplex time and time-rate offsets, and universal time and polar motion, narrow band VLBI acquisition of at least 10 radio sources at S- and X-band frequencies must be accomplished. For precision measurements, Coherent Comb Generators Assemblies must be used to calibrate the RF downlink. The determination of these parameters utilizes the functions and interfaces as shown in Fig. 2. VLBI data acquisition is obtained by rapidly switching a pair of 64-meter DSS between radio sources.

The NCB VLBI System is also used to acquire differenced time delay data for Delta Differential One-Way Range (ΔDOR). In the acquisition of these data, the antenna pairs are rapidly switched between a spacecraft and a nearby natural radio source.

NCB VLBI data are correlated in the NOCC VLBI Processing Subsystem (VPS) to obtain intercomplex time and time rate offset, universal time, polar motion, and data for ΔDOR. An accurate radio source catalog is required to measure these parameters.

Interfaces to the NCB VLBI System are natural radio sources, spacecraft signals, predicts, configuration and control data, frequencies, and timing pulses and epoch time.

Interfaces from the NCB VLBI System are time and time rate offset; Universal time and Polar motion, and spacecraft and radio source delay data.

2. Wide Channel Bandwidth (WCB) VLBI System. The purpose of WCB VLBI (Fig. 3) is to provide accurate radio source catalog and intercomplex baseline data for station locations. The inputs are X- and S-band signals from natural radio sources, predicts, control, frequencies, timing pulses, and epoch time. Outputs are the updated radio source catalog and intercomplex baselines.

Wide Channel Bandwidth (WCB) VLBI is used as backup to NCB for ΔDOR data reliability. It is also used for ΔDOR where the natural radio source signal-to-noise ratio is not sufficient for NCB VLBI data acquisition and correlation.

IV. System Functional Requirements and Performance

A. General

This section defines the DSN VLBI System functional requirements to support Project VLBI requirements for spacecraft navigation. It defines the DSN VLBI functional requirements imposed on the DSS, Ground Communications Facility (GCF), and NOCC. Figures 1 and 2 present the DSN VLBI System functions and interface for NCB and WCB VLBI respectively. A block diagram of functions and data flow for the Mark IV-85 VLBI System is shown in Fig. 5.

B. Project Requirements

Project requirements (Table 2) are derived from Project Requirements and DSN Support Plan for the following missions:

(1) Voyager II

(2) Galileo

(3) VOIR

C. DSS Functions and Performance Requirements

This paragraph presents the performance requirements imposed on the DSS by the DSN VLBI System. DSS functions, subsystems and interfaces are given in Fig. 5.

VLBI predictions, system configuration, and data mode messages stored by the DSS Link Monitor and Control Subsystem are used to configure and control the DSS subsystems for VLBI data acquisition. The DSS Link Monitor and Control is controlled and monitored by the DSS Complex Monitor and Control.

Antenna pointing control of the DSS antenna is given in Table 3. A pointing error matrix is used to provide position offsets to maintain pointing accuracy.

A description of the acquisition of VLBI signals follows.

1. Narrow Channel Bandwidth (NCB) VLBI. The frequency span bandwidths are 40 MHz at S-band and 100 MHz at X-band. Therefore, frequency range shall be 2265 to 2305 MHz at S-band and 8400 to 8500 MHz at X-band. Therefore, operating system temperature is < 27 K at S-band and < 24 K at X-band. Polarization shall be right-hand circular polarized (RCP). Phase stability is < 14 deg rms at S-band and < 50 deg rms at X-band.

Up to 12 selectable VLBI downconverted radio frequency channels are provided (four at S-band and eight at X-band). Up to three calibration tones shall be provided for each IF – video converted channel.

2. Wide Channel Bandwidth (WCB) VLBI. RF frequency span bandwidth is 100 MHz at S-band and 400 MHz at X-band, which will require user supplied microwave equipment. Frequency range is 2235 to 2335 MHz at S-band and 8100 to 8580 MHz at X-band. System operating temperature shall be < 120 K at S-band and < 100 K at X-band. Phase stability is < 14 deg rms at S-band and < 50 deg rms at X-band.

3. 40/100 MHz Bandwidth. Frequency bandwidth is 40 MHz at S-band and 100 MHz at X-band. Frequency range is 2265 to 2305 MHz at S-band and 8400 to 8500 MHz at X-band. System operating temperature is < 27 K at S-band and 22 K at X-band. Phase stability is < 100 deg (0.1 to 30 sec) at S- and X-band frequencies.

There are eight RF downconverted channels selectable within the bandwidth of the received frequency bandwidth. Up to three calibration tones are supplied for each frequency channel.

4. Coherent Comb Generator. A coherent reference frequency is to be transmitted from the DSS primary frequency reference to the Configuration Control Group (CCG) where coherent tones are generated and inserted into the S- and X-band RF receiving channels. The tones generated by the CCG are used to calibrate the VLBI data acquisition system for phase instabilities in the VLBI instrument. The tones have hydrogen maser stability as specified in Fig. 6.

Sampling and recording of VLBI data channels are now described.

1. Narrow channel bandwidth. VLBI data sampling of up to 12 video band channels is provided with time multiplexing of channels. Sampling and recording rates of 500, 250, 125, and 62.5 kilobits/second are provided.

2. Wide channel bandwidth. Simultaneous VLBI data sampling of eight video band channels is provided with expansion to 28 video band channels. Sampling and Recording rates of 4, 2, 1, 0.5 and 0.25 megabits/second are provided for each channel. The tape format is compatible with the Haystack Observatory Mark III VLBI data tapes.

Ancillary data are sampled and recorded with the VLBI data. The ancillary data consists of such data as follows:

(1) VLBI predicts.

(2) Subsystem configuration, status, and data mode.

(3) Angles and angle residuals.

(4) Recorder status.

(5) Ground weather data.

(6) Water vapor radiometer data.

(7) Ionosphere data.

(8) Other.

Configuration, status performance, and data mode are transferred from the relevant subsystem to the Occultation Data Assembly (ODA) for inclusion with the ancillary data. Monitor data are also be routed to the DSN Maintenance Center (DMC) for DSS operations display together with other ancillary data.

NCB ancillary and VLBI data are transmitted at the maximum wide-band data line (WBDL) rate to the NOCC for validation of two-station VLBI data and for near-real-time VLBI correlation and parameter estimation. WCB data tape of ancillary and VLBI data is mailed to JPL. A portion of WCB VLBI data and ancillary data is transmitted via WBDL for VLBI validation.

Monitor data from ODA is transmitted via HSDL to the Radio Science Real Time Monitor Assembly for evaluation and display to the Network Operations Control Team. This monitor data is the VLBI related subsystem parameters and a subset or all of the ancillary data.

D. GCF Functional Requirements

The functions, subsystems, and interfaces of the GCF use for VLBI are given in Fig. 7.

The WBDL is used to transmit NCB ancillary and VLBI data from the DSS to the NOCC VLBI Processor Subsystem (VPS) in near-real time. NCB VLBI maximum data acquisition rate is 500 kilobits/second. This amounts to 5×10^8 bits or 10,000 seconds of GCF wide band data transmission for each narrow band VLBI observation. WBDL data throughput should be $> 95\%$ for time offset, and rate and earth platform parameter observations, and $> 98\%$ of data for ΔDOR observations. Selective recall will be available to fill in data outages. Though WBD is routed directly to the NOCC VLBI Processor Subsystem, a capability of generating IDRs is provided.

The HSDL provides transmission of VLBI predicts, configuration, data mode, and replay requests from the NOCC to the DSS. HSDL throughput shall be $> 99.8\%$ of these data with no detected errors. End-to-end verification of data sent versus data received is performed by the sending and receiving subsystems. Replay requests are initiated by the receiving subsystem to the transmitting subsystem for retransmission.

The HSDL provides transmission of VLBI monitor and ancillary data and replay requests from the DSS to the NOCC. HSDL throughput will be $> 98\%$ with no detected errors. Replay requests are issued by the receiving subsystem to the transmitting subsystem for retransmission.

E. NOCC Functional Requirements

The functions, subsystems, and interfaces of the NOCC used for VLBI are given in Fig. 8.

VLBI predictions are to be generated from a natural radio source catalog that is generated and maintained by the WCB VLBI data system. Spacecraft predictions for ΔDOR are computed from a project supplied trajectory tape. The NOCC provides a file of predictions for each observation (assume a maximum of 10 observations).

The NOCC verifies that the DSS system configuration and mode corresponds to that planned for the VLBI observation sessions. Alarms are generated for all mismatches. Displays are made of the system configuration, and data mode alarms. System status and alarms are transmitted to the DSS Monitor and Control System. Also the VPS shall correlate VLBI data from two stations to determine quality. Reports of VLBI quality are supplied to NOCT displays and transmitted to DSS Monitor and Control System for DSS operations display.

The following parameters are determined from NCB VLBI data:

Mark I-79:

(1) Interstation time offset and rate < 20 nanoseconds and $< 1 \times 10^{-13}$, respectively.

(2) Universal time and polar motion < 1.25 milliseconds and < 50 centimeters, respectively.

(3) Differential spacecraft and quasar time delay < 30 centimeters.

Mark III-83:

(1) Interstation time offset and rate < 10 nanoseconds and 7 parts in 10^{14}, respectively.

(2) Universal Time One and polar motion < 0.75 millisecond and 30 centimeters, respectively.

(3) Differential spacecraft and quasar time delay < 10 centimeters.

VLBI Processing Subsystem performs the following NCB functions:

(1) The VLBI and ancillary data are received via WBDL or from a VLBI IDR. An accountability record is made and automatic replay request messages generated to provide the required data.

The ancillary data is used with the accountability data to edit the VLBI data for cross correlation.

(2) The NOCC VPS will be a twelve-channel, two-station, one-baseline processor dedicated to DSN applications. During NCB VLBI observations, the twelve bandwidth-synthesis channels will be time multiplexed.

(3) The correlation rate is selected to ensure that the correlation process can handle the data acquisition without backlog. It is highly desirable to have the correlation process run equal to or faster than WBDL rates.

(4) To calibrate the VLBI data, a known signal of constant frequency is injected at the receiver during a VLBI observation. During correlation, the Correlator Assembly will generate (with a local model) this same frequency and calibrate for phase changes due to drifts in the microwave and receiver.

(5) The correlation software generates the geometric delay and phase and sends the data to the hardware correlator. Due to quantization and round-off, the hardware may not exactly track the software. However, the error shall be less than 10^{-4} cycles of fringe.

(6) Given a set of parameters, the software model shall calculate the phase to within 10^{-5} cycles of fringe. Also, a record of the calculations along with their results will be kept with a precision of 10^{-5} cycles of fringe.

(7) The software model constantly updates its computation of the required geometric delay lag due to the earth's rotation. Eight instantaneous lags (four preceding and four following the nominal geometric delay) shall be provided to determine the actual geometric delay. The maximum equivalent error of the VPS in tracking the model delay (the error in keeping constant the point of maximum correlation) shall be 0.01 lag.

(8) The postcorrelation functional requirements for delta DOR are as follows:

(a) Receive spacecraft predicts tape from project navigation.

(b) Compute quasar and spacecraft phase.

(c) Compute VLBI time delay for the quasar and spacecraft.

(d) Provide quasar and spacecraft delay tape to project navigation.

(9) The postcorrelation functional requirements for time and time rate, UTI, and polar motion are as follows:

(a) Compute quasar and tone phase.

(b) Calibrate quasar phase for station instrument errors.

(c) Compute calibrated quasar delay.

(d) Resolve cycle ambiguities.

(e) Compute preliminary clock parameters.

(f) Calibrate for transmission media effects.

(g) Solve for time and time rate, UTI, and polar motion.

(h) Provide solved-for parameters to project navigation after validation.

Functional requirements for the WCB VLBI processor subsystem are given below:

(1) The WCB VLBI Processor must be capable of simultaneously correlating VLBI data from three stations, with expansion to seven stations. It must also be able to correlate, in parallel, 28 frequency channels per station.

(2) To calibrate the VLBI data, known time signals of constant frequency shall be injected in the microwave subsystem during a VLBI observation. During correlation, the Correlator Assembly will generate (with a local model) this same frequency and measure its phase change due to phase instabilities in the microwave and receiver subsystems.

(3) The correlation software generates the geometric time delay and phase and sends the data to the hardware correlator. Due to quantization and round-off, the hardware may not exactly track the software. However, the error shall be less than 10^{-4} cycles of fringe.

(4) Given a set of parameters, the software model shall calculate the phase to with 10^{-5} cycles of fringe. Also, a record of the calculations along with their results will be kept with a precision of 10^{-5} cycles of fringe. Output should be available in both delay and frequency domain.

(5) The software model constantly updates its computation of the required geometric delay lag due to the earth's rotation. Eight instantaneous lags (four preceding and four following the nominal geometric delay) shall be provided to determine the actual geometric delay. The maximum equivalent error of the JPL/CIT VLBI Processor tracking the model delay (the error in keeping constant the point of maximum correlation) shall be 0.01 lag.

(6) The JPL/CIT VLBI Processor subsystem shall be able to process data collected and recorded by GSFC/Haystack Mark III VLBI System.

(7) Postcorrelation functional requirements are as follows:

(a) Compute quasar amd tone phase.

(b) Calibrate quasar phase for station instrument error.

(c) Compute calibrated quasar delay.

(d) Resolve cycle ambiguities.

(e) Calibrate for transmission media effects.

(f) Solve for quasar locations and baseline.

(g) Update radio source catalog and baselines.

Reference

1. Chaney, W. D., and Ham, N. C., "DSN VLBI System Mark I-80," in *The Deep Space Network Progress Report 42-56, January and February 1980.* Jet Propulsion Laboratory, Pasadena, Calif., April 15, 1980.

Table 1. VLBI system key characteristics

Narrow Channel Bandwidth (NCB)
Near-real-time interstation time and frequency measurements
Universal time and polar motion determination
Delta differential one-way range
NCB VLBI capability at one 64-meter and one 34-meter antenna, each complex (with shared SPC equipment)
Centralized monitor and control of system by NOCC
Data rates of 62.5, 125, 250 and 500 kbits/second
On-site recording of NCB signals with near-real-time playback through GCF at prevailing GCF wideband rates
Correlation and postcorrelation processing performed in NOCC
Near-real-time "quick-look" processing for system validation
VLBI validation feedback from VPS to DSS
Moderate RF span bandwidths
Wide Channel Bandwidth (WCB) VLBI
Radio source catalog maintenance
Intercomplex distance determination
WCB VLBI capability at one 64-meter and one 34-meter antenna, each complex (with shared SPC equipment)
Centralized monitor and control of system by NOCC
Data rate up to 112 megabits/second (compatible with Haystack Mark III VLBI data acquisition system)
On-site recording of wide-band signals on tape. Tape shipped to corelation processing facility
Correlation and postcorrelation processing performed at Caltech
Near-real-time "quick-look" processing using the NOCC VPS
VLBI validation feedback from VPS to DSS
Moderate and wide RF span bandwidth

Table 2. VLBI System functional project requirements

Voyager
Calibration of Intercomplex time rate to 3×10^{-13} (1×10^{-13} desired)
Calibration of UT-1 and polar motion to < 50 centimeters (desired)
Use of differential time delay for ΔDOR to validate two-station ranging (Voyager II demonstration)
ΔDOR for Voyager II Saturn-to-Uranus navigation (accuracy equivalent to two-station differenced range)
Galileo
Differential time delay for ΔDOR to < 30 centimeters
Calibration of intercomplex time rate to 3×10^{-13} (1×10^{-13} desired)
Calibration of universal time and polar motion to < 50 centimeters (desired)
Voir
Narrowband ΔDOR to 10 centimeters

Table 3. Antenna pointing control

Parameter	64-meter DSS	34-meter DSS
Pointing accuracy	0.002 deg	0.005 deg
Tracking rate (HA/dec)	0 to 0.004 deg/s	0 to 0.004 deg/s
Maximum slew rate (HA/Dec)	0.25 deg/s	0.70 deg/s
Visibility: elevation	7 to 90 deg	7 to 90 deg
azimuth	±180 deg	±180 deg

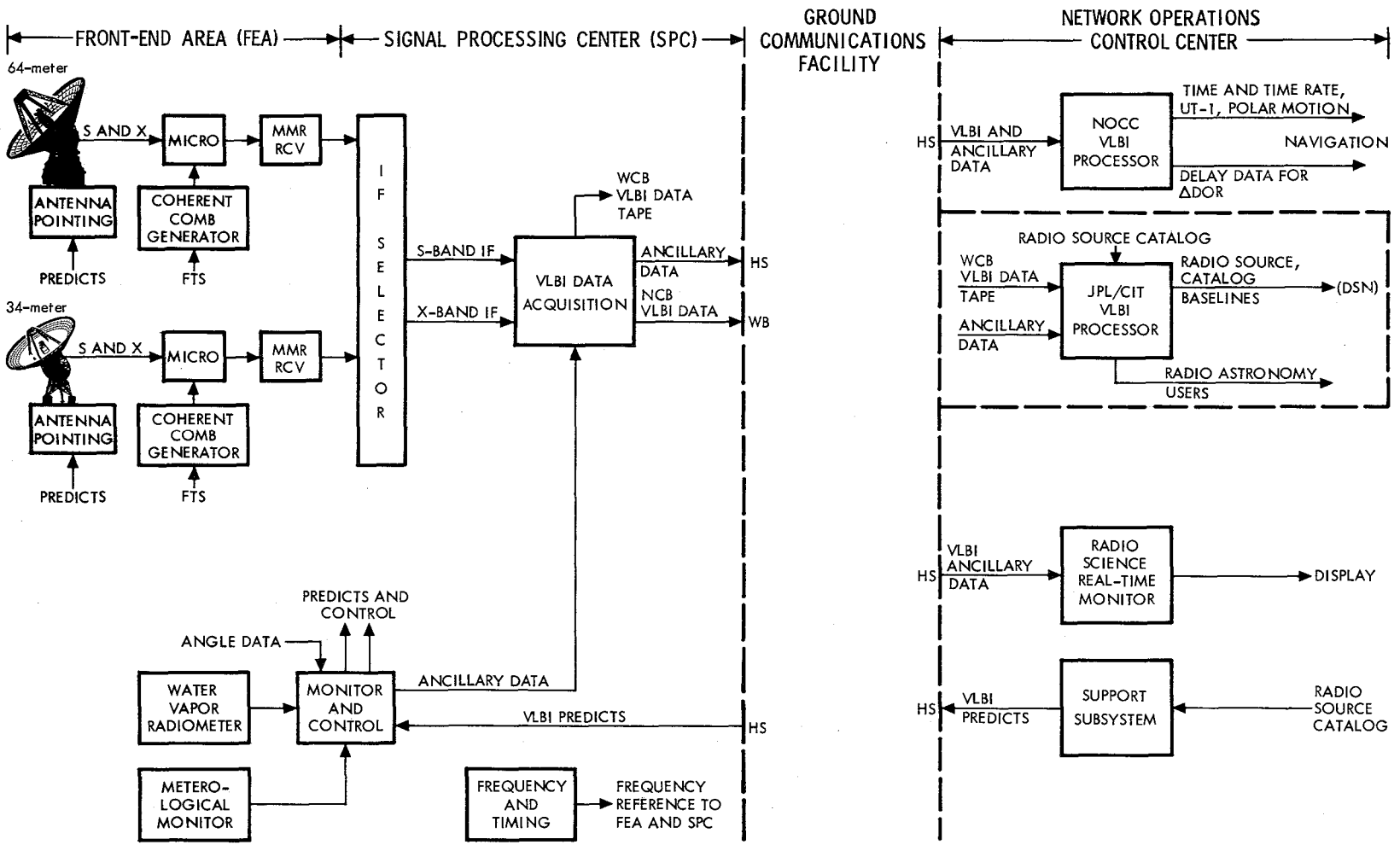

Fig. 1. VLBI System block diagram

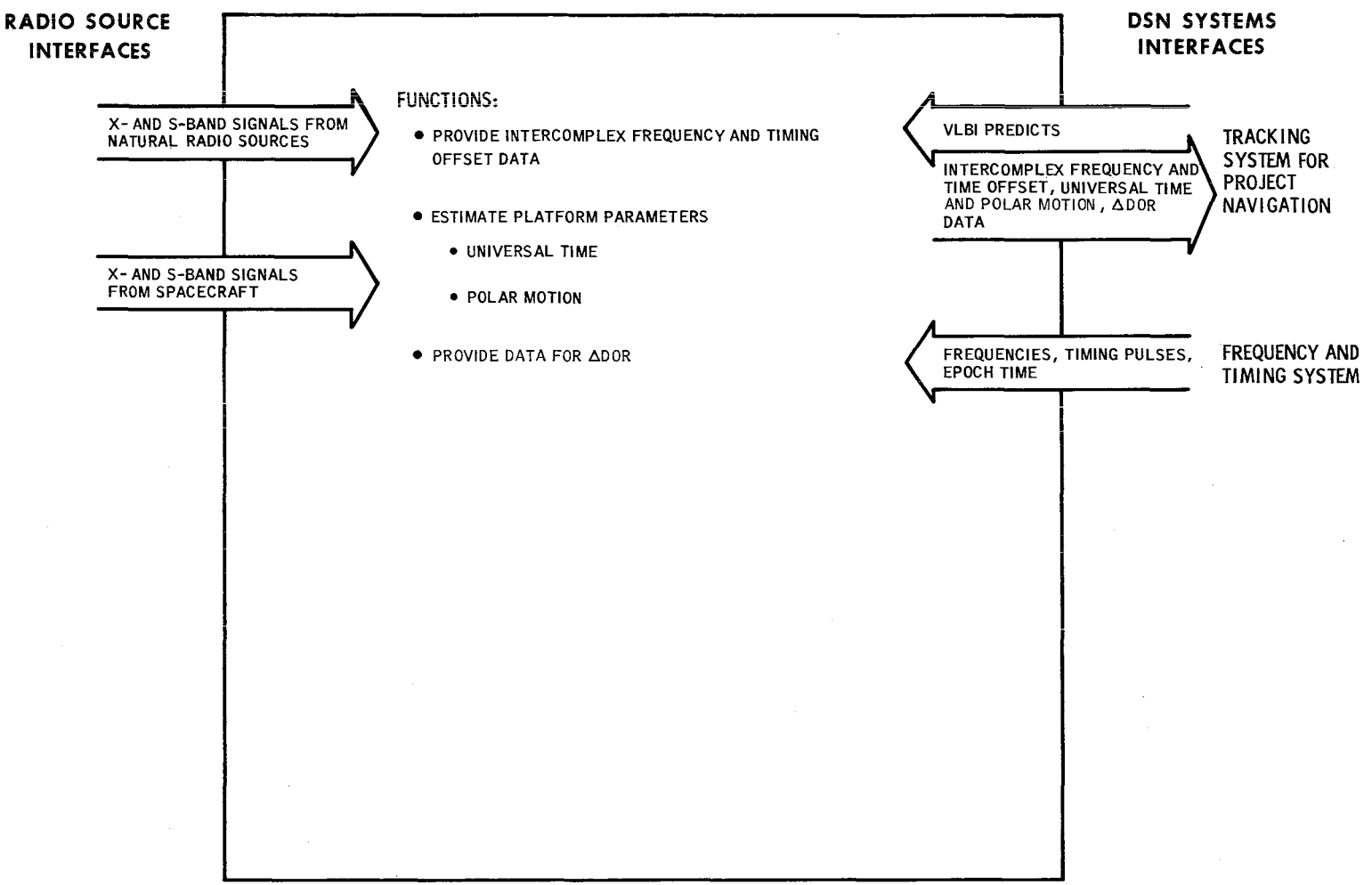

Fig. 2. VLBI System narrow channel bandwidth functions and interfaces

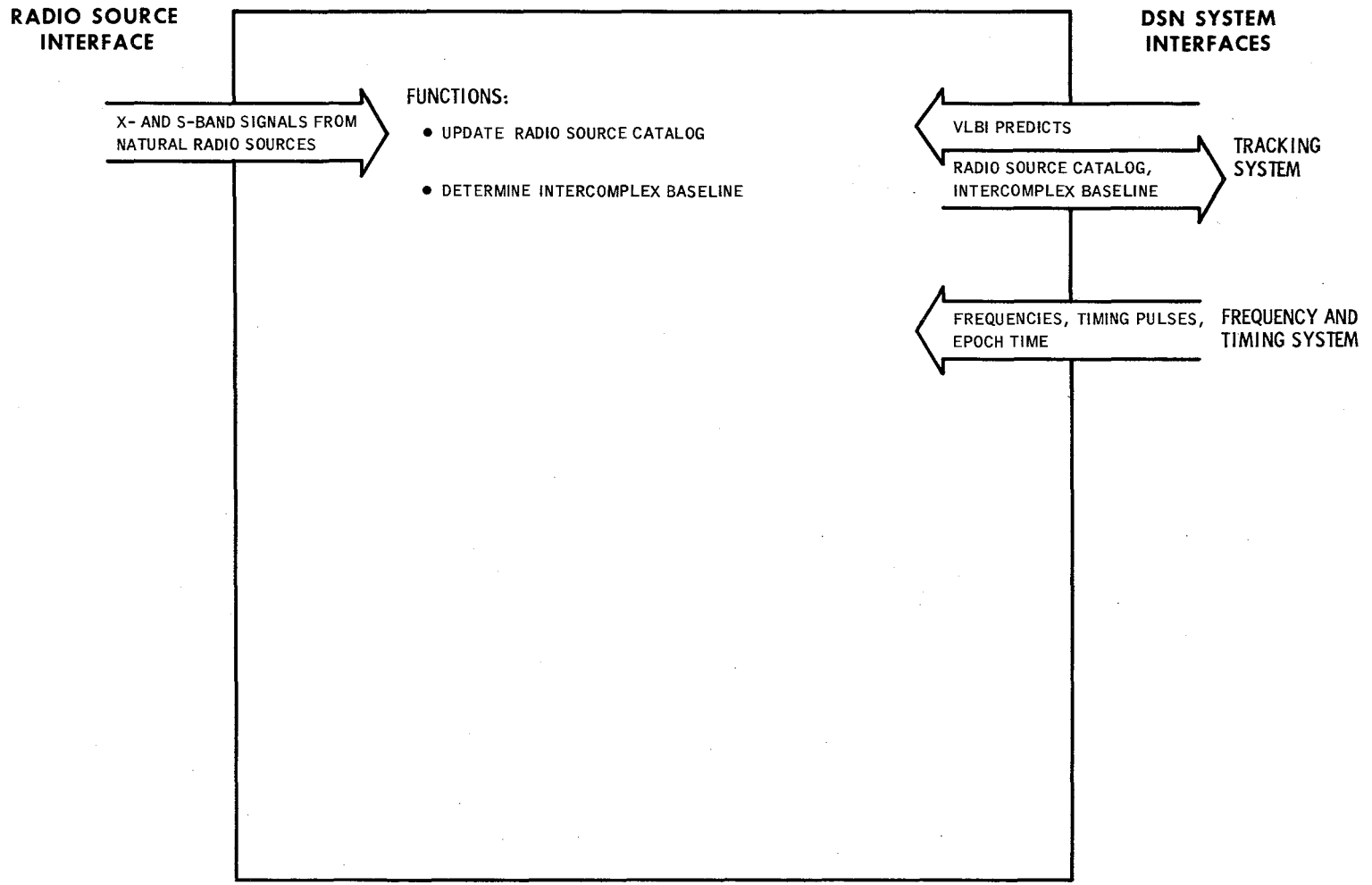

Fig. 3. VLBI System wide channel bandwidth functions and interfaces

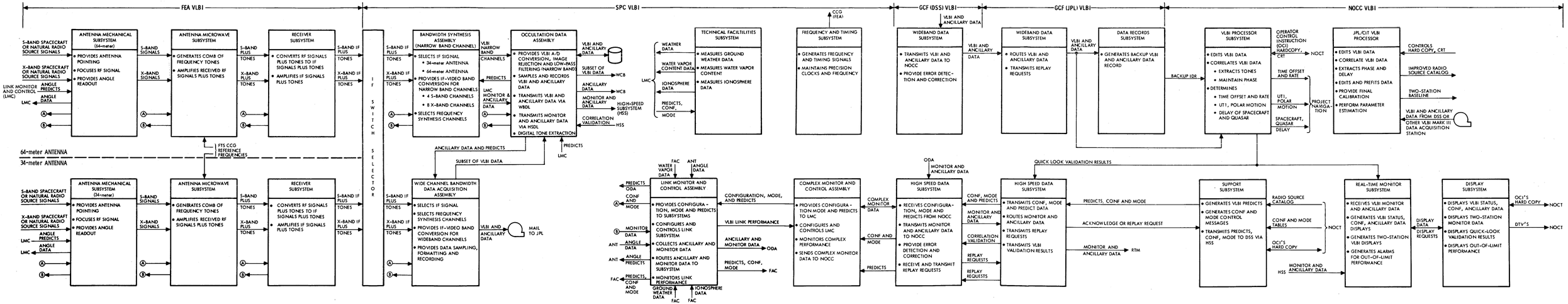

Fig. 4. Functions and data flow DSN VLBI System, Mark IVA-85

This Page Intentionally Left Blank

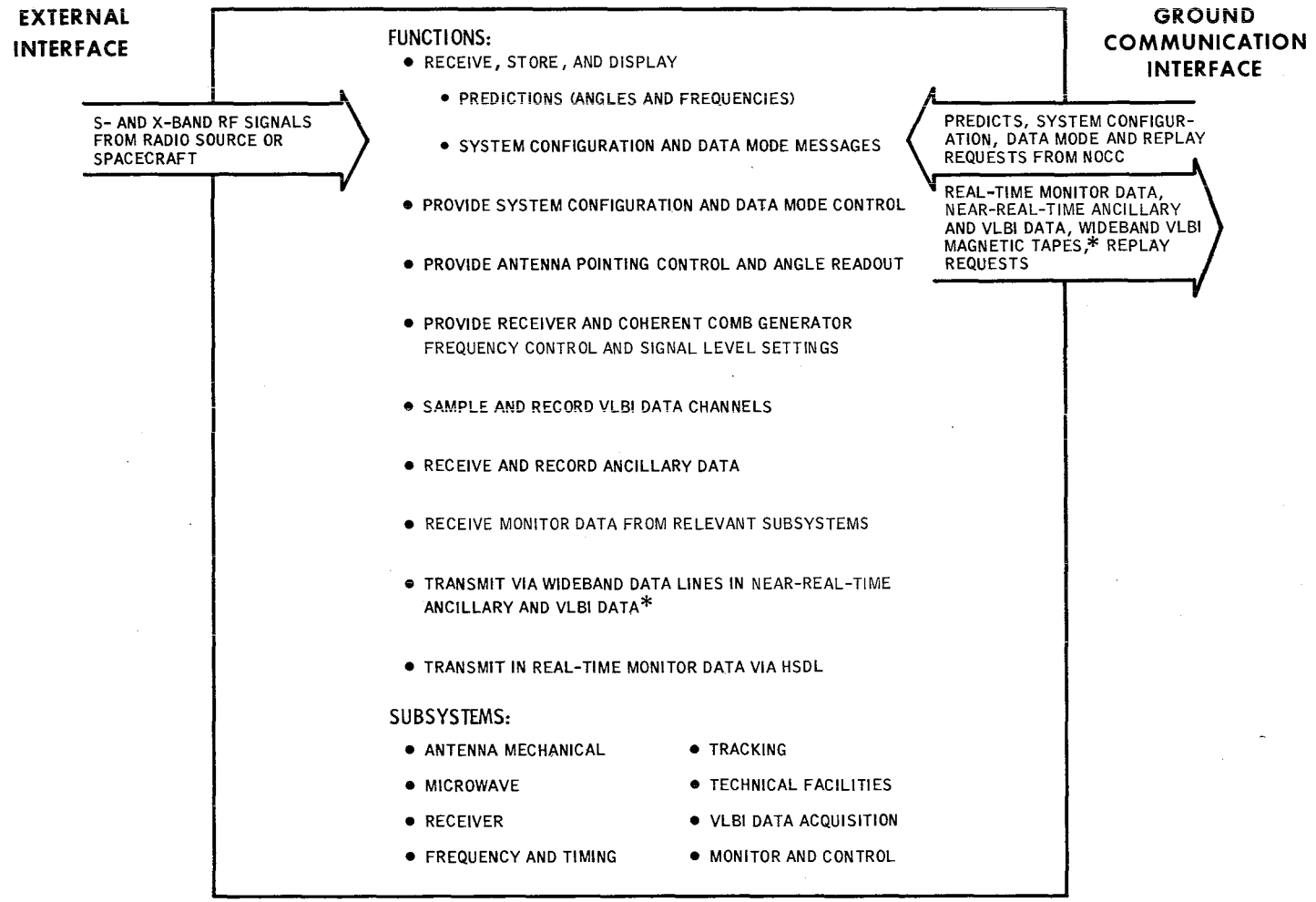

Fig. 5. DSS VLBI System functions, subsystems and interfaces

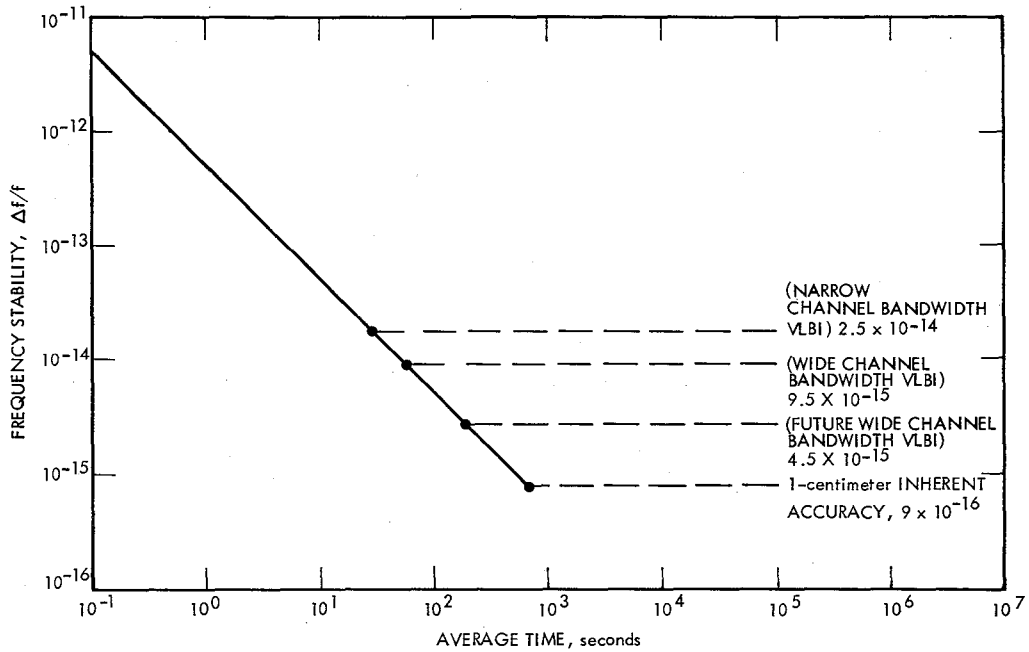

Fig. 6. VLBI frequency stability requirements

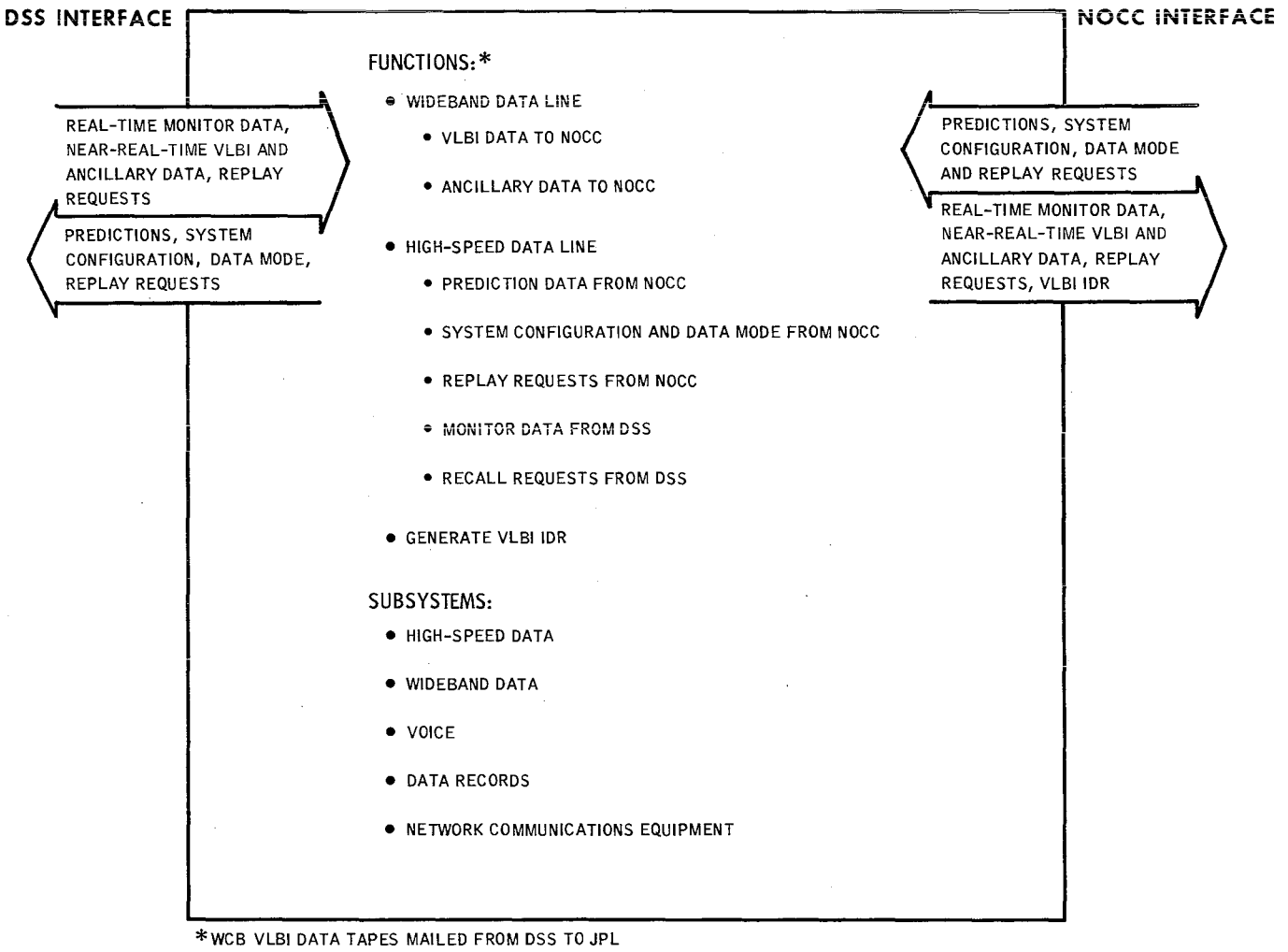

Fig. 7. GCF VLBI System functions, subsystem and interfaces

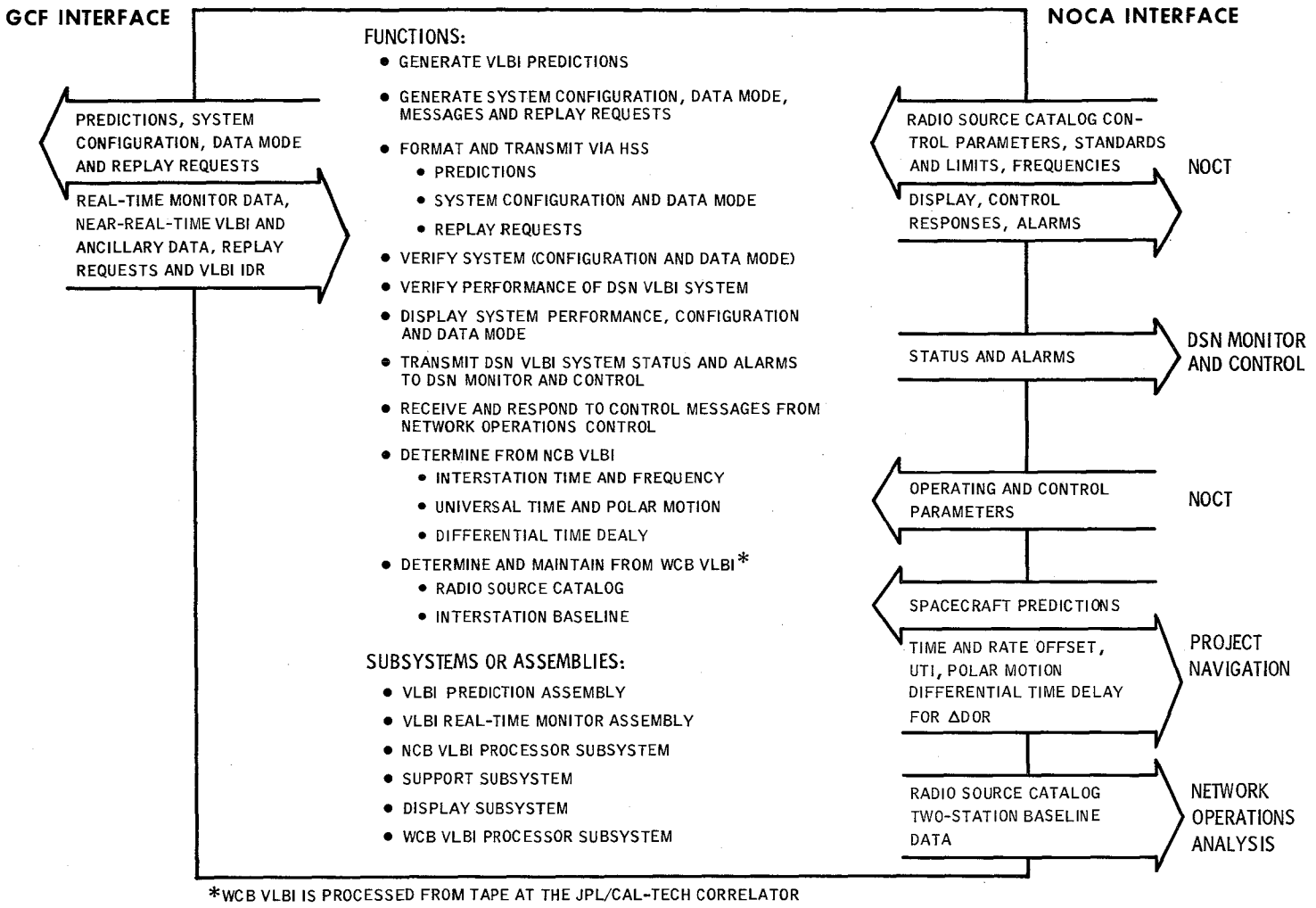

Fig. 8. NOCC VLBI System functions, subsystems and interfaces

Voyager Mission Support

N. Fanelli and H. Nance
Control Center Operations

This is a continuation of the Deep Space Network report on tracking and data acquisition for Project Voyager. This article covers the period of April through June 1981.

I. Introduction

During this reporting period (April through June 1981), Voyager 1 was in the extended mission phase of operations. Voyager 2 completed the cruise phase of its operations and on 5 June entered the Observatory Phase of the Saturn Encounter operations.

II. DSN Support

A. Voyager 1

With the completion of the prime mission phase of Voyager 1 in December 1980, the emphasis was shifted to Voyager 2 and preparation for its Saturn Encounter. A reduced tracking support schedule was implemented. However, navigation cycles, command detector unit/signal noise ratio (CDU/SNR), periodic engineering and science calibration (PESCAL), Radio Frequency Subsystem/automatic gain control (RFS/AGC), tracking loop capacitor (TLC), high-gain antenna and sun sensor calibration (ASCAL) and ultrastable oscillator (USO) activities were routinely scheduled to maintain a check on the spacecraft's health.

On 13-14 May, a special cruise science maneuver was exercised by the spacecraft. The purpose of the maneuver was to allow a full-sky survey by the body-fixed instruments. The maneuver consisted of 10 complete yaw revolutions and 25 roll turns. During the maneuver, the spacecraft antenna was off earth-point for 18 hours and 47 minutes with no downlink for this period of time. DSS 63 (Madrid) successfully supported the activity at the start of the maneuver and the next day for the scheduled re-establishment of the downlink.

On 19 May the spacecraft was used for a dual uplink command test supported by DSS 12 (Goldstone) and 63 (Madrid). The uplink command capability for Voyager 1, using a single 64-meter-diameter antenna station with an output power level of 80 kW into the spacecraft low gain antenna, will be lost in mid-1982. A concept was developed to use dual uplink commanding via two 64-meter stations.

The concept consists of two 64-m simultaneous uplinks. The first part of the test has one 64-meter station uplink as a single sideband sine wave subcarrier. This is accomplished by off-setting the carrier by 512 Hz at S-band. For test purposes, the uplink was modulated plus/minus 90 degrees with a 16-Hz square wave to simulate command bits. During the second part of the test, the uplink was set to the same frequency at both 64-meter stations. The one uplink was modulated plus/minus 90 degrees with a 512-Hz square wave subcarrier to produce a double sideband suppressed carrier command signal. High precision ramps are required by both stations, with a maximum

allowable frequency error of 0.1 Hz at S-band to ensure acceptable operation. The test was not completely successful. However, the Project assessment of the test was that uncorrected frequency variation between the two stations precludes the use of the noncoherent single-sideband sine wave subcarrier technique. The technique of combining two uplinks at the same frequency with one signal suppressed 20 dB with command modulation looks promising. Laboratory tests to determine the spacecraft threshold using this technique will be proposed on the next step.

B. Voyager 2

Preparations for the Voyager 2 Saturn encounter became the primary DSN support activity. The first general activity was to revalidate the array configuration of the 34-meter/64-meter stations and to provide training for the station personnel. A series of array tests began on 1 April for DSS 42/43 (Australia) and DSS 61/63 (Madrid) and continued periodically throughout the period. The DSS 12/14 (Goldstone) tests were scheduled to begin on 20 April. The tests went comparatively smoothly, with equipment operation well within the desired performance range and personnel quickly displaying operational proficiency.

The Radio Science Operational Verification Test (OVT) at DSS 43 (Australia), started in March, continued periodically throughout the period. Several equipment and procedural problems were identified during the tests. The precalibration and configuration requirements were a matter of concern and took close coordination to ensure understanding by both the station and the Radio Science personnel. The main equipment problem appears to have been in the recorders and malfunction of the recorder bypass switch; the reproduce selection switch caused early concern until the problem was resolved. The recordings continued to be evaluated to ensure that the Intermediate Data Records (IDRs) reproduced from the recorded data were complete and processable by the user. This process continued throughout the period. The activity will reach a milestone on 1 July with the system being exercised during the Radio Science Operational Readiness Test (ORT) No. 2 by the Voyager Project Radio Science Team.

The Voyager Ground Data System Engineer was required to validate telemetry, monitor, and command data end-to-end system operation with the updated software prior to encounter operation. The facilities of CTA-21 (Compatibility Test Area, JPL) were used on 1 and 6 April to perform the initial validation. The tests were successfully completed. A long-loop Ground Data System (GDS) test was scheduled with DSS 43 (Australia) on 13 April. Although DSS 43 had a coded multiplexer/demultiplexer/simulation conversion assembly (CMD/SCA) interface problem that made it necessary to loop back the simulated high rate data at the CMD input jack panel, the test conductor considered the test as successful and further testing not required.

The adaptive tracking procedure (whereby the uplink frequency is changed in real-time based on current estimates of the receive frequency) was exercised three times during the reporting period. The first time was on 13 April and was supported by DSS 14 (Goldstone) and 63 (Madrid). The activity occurred after spacecraft activity that had caused a temperature change and corresponding receiver VCO frequency changes. DSS 63 (Madrid) performed the best-lock frequency (BLF) determination ramping and the initial adaptive tracking frequency offsets, with DSS 14 (Goldstone) continuing the offsets. The second period occurred during a target maneuver with the BLF determineation ramping by DSS 63 (Madrid) starting prior to the reacquisition of the downlink and subsequent to the ground receipt of the ramping results shortly after the reacquisition of the spacecraft. Adaptive tracking offsets were performed by DSS 63 and DSS 11 (Goldstone. The last period occurred on 17 April with the BLF determination ramping again being performed by DSS 63 and the adaptive tracking offsets performed by DSS 63 and 14. The tests were successfully completed and valuable training accomplished by station personnel.

The target maneuver mentioned above was performed by Voyager 2 on 15 April. The spacecraft performed a negative yaw turn followed by a positive roll turn in order to position the photometric calibration plate to be illuminated by the sun with a 30-degree angle of incidence. The return-to-earth point was accomplished by a negative roll unwind followed by a negative yaw turn. The spacecraft was off earth-point with no downlink for 3 hours and 31 minutes. DSS 63 supported the entire maneuver during a tracking pass, including the adaptive tracking activity. DSS 63 used the spectral signal indicator (SSI) capability to assist in the search for the return-to-earth point and reacquired the spacecraft downlink signal on time.

On 21-22 April, DSS 61 (Madrid) and DSS 12 (Goldstone) supported another dual spacecraft, dual station, differenced range exercise with the Voyager 1 and 2 spacecraft to provide additional data on the technique. Again both stations tracked both spacecraft during their view period. DSS 61 started the procedure by tracking Voyager 2. After DSS 12 rise, a transfer was performed from DSS 61. DSS 61 then made a turnaround to Voyager 1. DSS 62 was tracking at the time and made a transfer to DSS 61. DSS 12, after tracking Voyager 2 for the specified period of time, turned around to Voyager 1 and received the spacecraft from DSS 61. The passes went smoothly and the data are being evaluated along with the data provided by previous tests. Results are indicated as being promising.

On 28-29 May, a Cruise Science Maneuver was performed by Voyager 2. The maneuver consisted of 10 negative yaw rotations followed by 25 negative roll rotations, which allowed a full-sky survey by the spacecraft body-fixed instruments. During the maneuver the spacecraft was off earth-point for 18 hours and 53 minutes, during which there was no scheduled downlink from the spacecraft. DSS 63 supported the start of the maneuver, which included the real-time command to enable the maneuver and the loss of the downlink at the start of the yaw turns. The next day, during the DSS 63 tracking pass, the spacecraft completed its roll sequence and returned to earth-point. DSS 63 reacquired the downlink at the predicted time. The playback of the recorded maneuver data started about two hours later and was received by DSS 63 at the start and completed during the subsequent DSS 14 pass.

On 5 June the Observation Phase of the Saturn Encounter began. The first activity was the movie sequence, which started over DSS 61/63 and was concluded on 7 June over DSS 42/43. During the movie phase the arrayed (34-meter/64-meter) configuration was used at all complexes to enhance the received imaging telemetry data. During the movie sequence severe thunderstorms over Spain while DSS 63 was tracking caused a real-time data reception outage via the wideband data line. In spite of this, with data replay no images were lost for the entire period. Preliminary evaluation of results showed that the arraying was well within tolerance and the picture quality was excellent.

On 7 June, after the movie was completed, Voyager 2 entered the preliminary observation routine of performing cyclic periods of ultraviolet system scan in real-time, recording Saturn zoom imaging for spectral and dynamics study during the view periods of Australia and Goldstone, and playing back the recorded data during the view period of Spain. Also, over Spain, interspersed multicolor imaging for long-time base spectral and dynamics study sequences was executed, with real-time data being received. This activity continued throughout the remainder of June.

III. DSN Capabilities

DSS 12 completed antenna upgrade work ahead of schedule and returned to operational status on 20 April. A demonstration Voyager pass was conducted on that day to verify operational status. DSS 12 antenna gain improvements of about 0.7 dB were measured. The DSS 14/DSS 12 array system performance gain improved also as expected.

Space Shuttle Launch Era Spacecraft Injection Errors and DSN Initial Acquisition

A. R. Khatib
Mission Design Section

A. L. Berman
TDA Mission Support Office

J. A. Wackley
TDA Engineering Office

The initial acquisition of a spacecraft by the Deep Space Network (DSN) is a critical mission event. This results from the importance of rapidly evaluating the health and trajectory of a spacecraft in the event that immediate corrective action might be required. Further, the DSN initial acquisition is always complicated by the most extreme tracking rates of the mission. DSN initial acquisition characteristics will change considerably in the upcoming Space Shuttle launch era. This article describes the method being developed for evaluating the impact of spacecraft injection errors on DSN initial acquisitions during the Space Shuttle launch era.

I. Introduction

The initial acquisition of a spacecraft by the Deep Space Network (DSN) is a critical mission event. This results from the importance of rapidly evaluating the health and trajectory of a spacecraft in the event that immediate corrective action might be required. Further, the DSN initial acquisition is always complicated by the most extreme tracking rates of the mission. DSN initial acquisition characteristics will change considerably in the upcoming Space Shuttle launch era. Therefore, it is desirable to understand how given injection errors at spacecraft separation from the upper stage launch vehicle (carried into orbit by the Space Shuttle) impact the DSN initial acquisition, and how this information can be factored into injection accuracy requirements to be levied on the Space Transportation System (STS). The approach developed in this article begins with the DSN initial acquisition parameters, generates a covariance matrix, and maps this covariance matrix backward to the spacecraft injection, thereby greatly simplifying the task of levying accuracy requirements on the STS, by providing such requirements in a format both familiar and convenient to STS.

Section II of the article describes the Space Transporation System, while Section III describes the method developed to map DSN initial acquisition accuracy requirements back to a STS formatted spacecraft injection covariance matrix.

II. The Space Transportation System (STS)

The basic elements of the STS are the Space Shuttle, which will carry its payload to a nominal 275-kilometer (150-nautical-mile) circular orbit, and the payload, which for deep space missions will consist of the spacecraft mated to a staging vehicle. The staging vehicles currently under consideration are the Boeing Inertial Upper Stage (IUS) with or without a spinning kick stage (e.g., Star 48), the General Dynamics modified single-stage liquid Centaur, or the Martin hypergolic Transtage. Basic tracking support for STS is handled by the Tracking and Data Relay Satellite System (TDRSS), with Ground Spaceflight Tracking and Data Network (GSTDN) (and in approximately 1985, the Consolidated DSN) as a backup, and launch support and control provided by Johnson Space Center (JSC). It is assumed that formal handover to JPL mission control occurs at the initial acquisition of the spacecraft by a DSN station.

It is of interest to note the differences between initial acquisitions in the expendable launch vehicle era and those in the STS era. In the expendables' era, initial acquisition generally occurred over the same Deep Space Station (DSS) regardless of launch date or time. Trajectory dispersions were relatively small due to the precise control of the launch vehicle cryogenic propellant flow rate, and the shortness of flight time to injection, which minimized guidance system errors. In the Shuttle era, the initial acquisition DSS can change from day to day, and possibly from one Shuttle orbit revolution to the next. Additionally, larger trajectory dispersions are likely because of the possible usage of solid fuel upper stages and longer elapsed times from launch to injection (dependent on the guidance scheme used), with a correspondingly larger effect through guidance system hardware inaccuracies.

A. Spacecraft Injection Errors

Spacecraft injection errors are normally specified in the form of a covariance matrix (Λ_0) representing dispersions of the nominal state (i.e., position, velocity, and time). These dispersions reflect uncertainty in attitude, propellant and dry mass of the stages, thrust and specific impulses, thrust vector control response, control limit cycles (dead bands), on-board software bias errors, timing errors, modeling errors, and initial parking orbit uncertainities. Because of the large number of parameters representing both performance and hardware, and the various guidance strategies involved, such as a ground update of the parking orbit state, or attitude update of the inertial measuring unit (IMU) utilizing star scanners, the injection covariance matrix (Λ_0) is usually generated by Monte Carlo simulation techniques (Ref. 1).

B. Figure of Merit

The figure of merit (FOM) has been adopted as a means of defining the spacecraft propellant requirements for the post-injection trajectory correction maneuvers required to null injection errors. Thus the FOM allows the spacecraft designers to determine the required propellant mass, and serves as a key parameter for evaluating launch errors from all sources. This results in a launch phase optimization of guidance, navigation, and control subsystems. A mapping matrix (U) from injection to a nominal first maneuver time (e.g., 10 days for outer planet missions) is generated. This 3×6 mapping matrix relates injection errors to elements of the maneuver Δv, namely, $\Delta\dot{x}$, $\Delta\dot{y}$, and $\Delta\dot{z}$, at the destination (i.e., target planet). Let:

$$\Lambda_{\Delta v} = U \Lambda_0 U^T$$

$$FOM \triangleq (\text{trace } \Lambda_{\Delta v})^{1/2}$$

Thus, the FOM is not actually the one sigma maneuver, but is somewhat greater. The statistical significance of the FOM will not be discussed here (Ref. 1); nevertheless, injection accuracy requirements via this process have been simplified to a scalar number and a mapping matrix.

In a fashion similar to the FOM, it is the intent here to simplify the DSN initial acquisition accuracy requirement interface to the STS.

C. DSN Initial Acquisition Requirements on STS

The DSN initial acquisition prediction requirements are based on hardware configurations and capabilities. The primary concern is to ensure a two-way acquisition within ten minutes of the earliest opportunity (i.e., spacecraft rise). This ensures that potent tracking data for navigation, especially in the event of nonstandard spacecraft configurations or trajectories, will be generated during the initial tracking pass. At a minimum, the angular dispersions should be less than the acquisition aid antenna beamwidth for angular searches, and frequency dispersions should be less than both the uplink spacecraft frequency prediction uncertainty (~2000 Hz) and the downlink spacecraft frequency prediction uncertainty (~3000 Hz) for frequency searches. The configuration of the initial acquisition DSS includes a 34-m antenna with a 0.27-deg beamwidth, and Block III receivers with tracking loop bandwidths of 152 Hz or less. The 9-meter antenna, which will provide the angular error signals for the 34-m antenna, has a 1-deg beamwidth with a 10-deg beamwidth acquisition aid antenna and wide bandwidth multifunction receivers. An angular error greater than 5-deg and a radial velocity error greater than 130 m/s (2000 Hz) (assuming that the one-way

spacecraft frequency prediction uncertainty is 2000 Hz) could adversely affect the acquisition of the downlink and the uplink. Thus to achieve the initial acquisition within 10 minutes of spacecraft rise, the angular and velocity accuracies are required to be:

3σ angular uncertainty $\leqslant 5$ deg

3σ radial velocity uncertainty $\leqslant 130$ m/s

III. Translation of DSN Initial Acquisition Requirements to a Spacecraft Injection Covariance Matrix

Normally, the covariance matrix Λ_0 is mapped forward to initial DSS rise utilizing the state transition matrix. The error ellipsoid is then rotated locally to station coordinates (e.g., azimuth-elevation (az-el), hour angle-declination (HA-dec), or NASA X-Y), and the 1σ errors are evaluated in comparison to DSN initial acquisition requirements. The angular rates of the nominal trajectory are used to obtain timing errors on the events (e.g., rise and maximum elevation). A more effective method is to utilize the DSN requirements to generate a covariance matrix at DSS initial rise, map this covariance matrix backward to injection, and then rotate the matrix locally (at injection time) to the coordinate system type and units the STS uses. This results in a covariance matrix Λ_c expressing DSN initial acquisition constraints. Expressing DSN constraints in this form simplifies the interface in a way similar to the FOM specification. The STS has only to evaluate the constraint covariance matrix by simple mathematical tools described in the remainder of this section.

Given the injection covariance matrix Λ_0 generated by the STS, and the DSN constraint covariance matrix at injection Λ_c as supplied by the flight projects, the problem is reduced to an eigenvalue solution of the following equation:

$$X^T_{max} (\Lambda_0 - \Lambda_c) X_{max} \leqslant 0$$

where X^T_{max} is the normalized eigenvector associated with the largest eigenvalue of the symmetric matrix $(\Lambda_0 - \Lambda_c)$. Violation of the above equation (positive eigenvalues) implies possible DSN acquisition constraint violations.

For positive eigenvalues $(\lambda_i\ (max))$, the probability that DSN constraints will be violated can be computed as follows:

$$\sigma^2_{0i} = X^T_{max} \Lambda_0 X_{max}$$

$$\sigma^2_{ci} = X^T_{max} \Lambda_c X_{max}$$

Assuming a Gaussian distribution, and by utilizing asymptotic theorems (i.e., De Moivre-Laplace), the probability that random variable X_i lies between σ_{ci} and σ_{0i} is:

$$\text{probability}\ (\sigma_{ci} \leqslant X_i \leqslant \sigma_{0i}) = 2\left[\text{erf}(1) - \text{erf}\left(\frac{\sigma_{ci}}{\sigma_{0i}}\right)\right]$$

$$= 0.68268 - 2\,\text{erf}\left(\frac{\sigma_{ci}}{\sigma_{0i}}\right)$$

where

$$\text{erf}(-\alpha) = -\,\text{erf}(\alpha);\quad \text{erf}(\infty) = 1/2$$

The above process is currently being incorporated in a computer program called SSTATS (for Station Statistics). The program will be able to handle the various error coordinate systems, and the various DSS antenna types (i.e., az-el, HA-dec, and NASA X-Y), in addition to the Tracking and Data Relay Satellite (TDRS) coverage.

In a subsequent TDA Progress Report, numerical examples of this method using the SSTATS Program with characteristic Space Shuttle trajectories, will be provided.

IV. Conclusions

A method of reconciling DSN initial acquisition prediction accuracy requirements with injection accuracy requirements has been developed. This method involves the comparison of the spacecraft injection covariance matrix with a backward generated covariance matrix based upon DSN initial acquisition requirements.

Use of this method will allow a simplified interface to be developed between the DSN, the flight projects, and the STS.

Reference

1. Khatib, A. R., and Deaton, A. W., "Shuttle/IUS Trajectory Design for Planetary Missions," AIAA Paper No. 78-1433, August 7, 1978.

Tracking and Data Relay Satellite System (TDRSS) Navigation With DSN Radio Metric Data

J. Ellis
Navigation Systems Section

This study explores the use of DSN radio metric data for enhancing the orbit determination capability for TDRS. Results of a formal covariance analysis are presented which establish the nominal TDRS navigation performance and assess the performance improvement based on augmenting the nominal TDRS data strategy with radio metric data from DSN sites.

I. Introduction

In the mid 1980's NASA will support low-altitude Earth-orbiting spacecraft missions with a Tracking and Data Relay Satellite System (TDRSS). Two geosynchronous relay satellites spaced 130° apart will serve as primary communication links and sources of metric data for low Earth orbiters. A dedicated ground tracking system will be constructed for TDRS navigation. This article explores the use of DSN radio metric data for enhancing the orbit determination (OD) of the relay satellites and for serving as a backup for the proposed TDRS ground tracking system.

The study describes the current baseline plans for TDRS navigation support and evaluates the navigation performance based on augmenting the nominal TDRS metric data with DSN-generated radio metric data. In addition, the potential role of data from a proposed fourth DSN terminal is explored in relation to TDRS navigation. Justification for this terminal is based on the relay-satellite ground station viewing constraints, and the necessity to track each TDRS with two widely separated sites. The rationale for this fourth terminal for deep space missions is also briefly reviewed.

Results of a formal covariance analysis are presented which establish the nominal TDRS orbit determination capability and assess the navigation performance with data from DSN sites. Strategies using DSN range and interferometric data in conjunction with the baseline TDRS metric data are evaluated.

Study objectives are restricted to the orbit determination for the individual relay satellites. The effect of TDRS navigation errors on the ability to recover orbits of user satellites is not examined. However, studies conducted by the Goddard Space Flight Center (GSFC) (Ref. 1) have demonstrated that the relay satellite navigation error is a dominant error source for user satellite orbit determinations. A second issue which is not addressed is the compatibility between the DSN Tracking System and the TDRS.

II. Fourth Terminal Rationale

Navigation of future deep space missions is expected to rely on precise dual-station radio metric data types such as nearly simultaneous range and ΔVLBI. Data acquisition depends on the mutual visibility of the probe from two widely separated

sites with the information content of the data dependent on the interstation baseline length. With the existing three-site network, dual-station tracking opportunities typically range from 2 to 5.5 hours for spacecraft at declinations between ±20°. Hence, tracking opportunities for data generation are limited and loss of any site for a prolonged period can significantly degrade the navigation performance. For this reason an appropriately located fourth site is an attractive option for navigation support.

The Navigation Network Project (Ref. 2) studied the potential utility of a fourth DSN terminal in Hawaii to support navigation. Because of the short baselines, it was concluded that dual-station data from this site would not serve as a backup for existing sites. The project did recommend that the fourth terminal study continue with the focus on other potential sites. Based on geometric considerations, a more desirable site location would be Santiago, Chile. This site provides north-south and east-west baseline components comparable with the current DSN sites. Furthermore, GSTDN maintains a 9-meter (receive/transmit) and a 12-meter (receive only) S-band antenna at this site (Ref. 3) at this time, although they are scheduled to be decommissioned when TDRSS becomes operational.

In addition to navigation benefits, other factors must be evaluated in developing a case for a fourth terminal. The impact of this terminal on telemetry, command, operations, radio science and geodynamics must also be assessed. For example, the DSN faces a heavy loading problem during the mid 80's due to the number of probes at negative declinations and the added responsibility of supporting highly elliptic Earth orbiter missions. A fourth terminal at Santiago will provide an additional 12 hours of communication capability for negative declination probes. The following sections assess the role of this Santiago terminal for supporting TDRS navigation. A follow on study will evaluate the application of radio metric data generated at a Santiago site for highly elliptic Earth orbiter missions.

III. Baseline System for TDRS OD

The Tracking and Data Relay Satellite System (TDRSS) (Ref. 4) consists of three geosynchronous satellites and a ground terminal near White Sands, New Mexico. Two of the satellites, TDRS-East at 41°W and TDRS-West at 171°W longitude, operate as orbiting stations to provide telemetry, command and navigation support for low altitude orbiting Earth satellites. The third, TDRS-Spare at 99°W longitude, serves as an in-orbit spare for rapid deployment in the event of a satellite failure.

To provide navigation support for the user satellites, it is necessary to precisely determine the locations of the TDRS satellites. Current plans (Ref. 4) specify daily estimation of a definitive orbit for each TDRS using metric data acquired from pairs of Bilateration Ranging Transponders (BRT) located at selected ground sites. The BRT is essentially a user transponder with a 2-foot parabolic antenna that operates in a completely automated mode. The BRT continuously receives a signal from the TDRS, but transmits only when commanded from White Sands via the TDRS. Transmission time is anticipated to be for five minutes every hour. Figure 1 illustrates the observed metric data flow, which consists of a K-band uplink from White Sands to the spacecraft, an S-band downlink and uplink between TDRS and the BRT, and a K-band downlink return to White Sands. Table 1 lists the proposed ground sites for the automated BRTs supporting each TDRS, and the corresponding DSN sites (including a Santiago terminal) which can also view the spacecraft.

Metric data from at least two widely separated sites are required for TDRS OD. For the DSN, the inclusion of a Santiago site results in visibility of each TDRS by two DSN sites.

IV. TDRS Navigation With DSN Radio Metric Data

There are two motivations for analyzing the use of DSN metric data for TDRS navigation support:

(1) As a backup for the TDRS-BRT automated ground system.

(2) To determine if the navigation accuracy for TDRS can be improved by the addition of DSN radio metric data.

To assess the role of DSN data, the study has focused mainly on the performance of the TDRS-East. Loss from Ascension Island data would significantly degrade its navigation accuracy with the position error increasing from 140 meters to 39 km. Unlike TDRS-West, there is no third BRT site to support navigation, and hence the DSN Madrid terminal and the proposed Santiago terminal are the only alternatives. Since the White Sands BRT is located in the vicinity of TDRS ground terminal, it is assumed that prolonged loss of this facility is less likely.

A linearized covariance analysis was used to evaluate the TDRS navigation performance for several tracking configurations. The nominal or baseline TDRS system performance was defined based on a BRT range data acquisition strategy and dynamics and measurement error model assumptions consistent with those used in previous TDRS OD studies at GSFC (Ref. 1). For this nominal strategy, BRT range data were

acquired from two sites at a sampling rate of 1 observation per minute for 5-minute passes every hour. The performance criterion for comparing data strategies was the current state position error after 24 hours of tracking. Effects of velocity errors were evaluated by comparing the predicted state after a one-day mapping.

To supplement the BRT ranging data, it was assumed the DSN would provide either conventional two-way range or Very Long Baseline Interferometric (VLBI) data. The latter would either be in the form of differenced one-way range (DOR) or a quasar relative variant (ΔDOR). Sampling rate for the DSN range data was assumed to be the same as for the BRT system, i.e., 5-minute samples hourly. For the VLBI data types, one observation every 12 hours was sampled. Table 2 summarizes the measurement system error models for the four data types. The DOR errors are equivalent to a 3-nanosecond random component and a 10-nanosecond clock offset error. For the DSN sites the effects of station location, UT1 and media errors are reduced to equivalent station location errors. Independent ΔVLBI calibration techniques are assumed to be employed to maintain the station location errors at this 1.0-meter level.

The baseline TDRS study performed by GSFC treated solar pressure, spherical harmonics, Earth gravitational constant, BRT range bias and station location errors as systematic consider error sources. Such parameters are not modeled by the filter, but their a priori uncertainty is included in the computation of the statistics of the spacecraft state estimate. Two filtering modes were used in this study. The baseline filtering model which treats the BRT range bias as a consider parameter was the initial strategy. A second strategy which attempts to estimate the BRT range bias proved more advantageous for certain data combinations. For both filtering modes, the DSN range bias and the DOR clock offset error were considered as unmodeled parameters. Tables 2 and 3 summarize the measurement and dynamics error models.

A. TDRS-East

Figure 2 displays the current state East relay satellite OD errors for the baseline BRT range data strategy (sites at White Sands and Ascension Island) and for strategies in which the data are augmented with conventional DSN range. The filter mode for Fig. 2 (as well as Figs. 3 and 4) treats BRT range bias as a consider parameter. Individual contributions of major error sources – Earth GM, BRT range bias and stations locations – are plotted along with the total OD error. The nominal BRT system performance after one day of tracking is 140 meters. Augmenting this schedule with range from either Santiago or Madrid reduces the total error to 90 and 120 meters respectively. Including range from both DSN sites results in a 70-meter OD error. However, for this configuration the OD error is virtually insensitive to the presence of BRT range data. Effectively, this reflects more accurate DSN ranging data and the more stringent station location calibrations.

Figure 3 explores the use of DSN ranging data as a backup to the BRT system in the event of a loss of data from the Ascension Island site. Tracking from White Sands only results in a position error of 39,000 meters. The addition of ranging from either Madrid or Santiago combined with White Sands BRT data maintains the error below 240 meters. However, the performance in either case is not on a par with the baseline strategy, even with the more accurate DSN ranging. This is due to the sensitivity of the OD estimates to ground site geometry. The most desirable configuration results from simultaneously maximizing east-west and north-south separations of the tracking sites. Only the White Sands-Ascension Island or Madrid-Santiago combinations satisfy this criterion.

Figure 4 examines the effectiveness of augmenting the BRT data with either ΔDOR or DOR data. This strategy has the distinct advantage of using a receive-only antenna at the Santiago site. A data schedule of only one DOR or ΔDOR measurement every 12 hours is assumed for this phase. The results demonstrate significant improvements in position determination with ΔDOR data, and only a modest reduction with DOR data.

The availability of independent data from the DSN sites suggests the possibility of modifying the nominal filter strategy to attempt to estimate the BRT range bias parameters. Figure 5 displays the navigation performance for this revised filter model. For the baseline case, estimation of the bias degrades the performance, with the OD error increasing to 170 meters. Consequently, considering the BRT range bias is a preferred filter model for the baseline system. The bias estimation filter also fails to improve the performance for data strategies which use range from BRT and DSN sites. However, significant OD improvements are realized for options which utilize VLBI data types. In this case position errors are reduced to 20 meters with ΔDOR and 30 meters with DOR. This improvement is due to the decreased sensitivity to the unmodeled error sources such as GM which are absorbed by the estimated BRT range bias parameters.

Predicted estimates based on a one-day mapping of the state are plotted in Fig. 6 for the nominal BRT range, two site DSN range, and VLBI data strategies. The current and predicted position errors and the corresponding velocity errors for the four configurations are displayed. The addition of VLBI data significantly improves velocity estimates and limits

the growth of predicted position errors. Velocity errors are reduced from 1-2 cm/sec to less than 0.25 cm/sec and predicted position errors from 200-270 meters to less than 40 meters.

B. TDRS-West

The navigation performance for TDRS-West was briefly studied assuming BRT ranging data from the Orroral-White Sands sites are augmented with data from DSN sites at Goldstone and Canberra. Since the BRT and DSN baselines are nearly equivalent, the addition of DSN data does not provide additional geometric information. The principal advantage is the increased accuracy of the DSN data types. Figure 7 displays the results of this study.

The baseline BRT system determines the spacecraft position with an accuracy of 120 meters. The addition of DSN range from both sites results in a factor of 2 improvement. However, when the baseline BRT range is augmented with either ΔDOR or DOR data the errors are reduced to the 20- to 25-meter level. The latter strategy estimates the BRT range bias parameters.

V. Conclusions

The objectives of this study were to explore the use of DSN radio metric data for supporting and enhancing TDRS navigation. DSN range data from a single site results in a modest improvement in performance for the baseline strategy. However, in the event of the loss of a BRT site such data can maintain the OD error at an acceptable level. Range data from two DSN sites reduces the OD error by a factor of 2 and essentially obviates the need for the BRT data. However, the most significant improvement results when either DSN ΔDOR or DOR data augments the BRT range. Typically, current and predicted position errors are reduced by a factor of 6 to 8 or, based on a VLBI observation, every 12 hours. This configuration also yields a tenfold improvement in estimating velocities.

The capability of the DSN to support TDRS navigaion is considerably improved by the availability of a fourth DSN site at Santiago. Both the Spare and the East relay satellites can be tracked from this site. Furthermore, the favorable geometry of Madrid-Santiago baseline enables us to generate metric data which significantly enhances the TDRS-East navigation capability.

Acknowledgment

The author would like to acknowledge the contribution of L. R. Stavert and N. Hamata in providing computational support and the assistance of C. E. Hildebrand in discussions regarding the treatment of bias parameters.

References

1. Argentiero, P., and Loveless, F., "Orbit Determination with the Tracking Data Relay Satellite System," NASA/GSFC TM-X-71280, Feb. 1977.
2. Navigation Network Study Phase B Study Report, 890-116, Jet Propulsion Laboratory, Pasadena, Calif., Oct. 1980 (an internal document).
3. Ground Spaceflight Tracking and Data Network User's Guide (GSTDN) Rev. 2, STDN No. 101.3, June 1980.
4. Salzberg, I. M., "TDRSS Program Review – Bilateration Tracking," presented to NASA, Dec. 1979.

Table 1. BRT and DSN candidate tracking sites

TDRS	BRT sites	DSN sites
West	Orroral, White Sands (Samoa)	Canberra (CAN), Goldstone (GLD)
East	Ascension, White Sands	Madrid (MAD), Santiago (AGO)
Spare	Samoa, White Sands	Goldstone, Santiago

Table 2. TDRS dynamic error model assumptions

Error source	Magnitude
GM	1×10^{-6} of nominal value
Solar radiation	10% of nominal
Spherical harmonics	Full difference between APL and SAO models

Table 3. Measurement error model assumptions

	BRT	DSN		
Error source	Range	Range	ΔDOR	DOR
Random error M	2.0	0.3	0.3	0.9
Bias M	10.0	2.0	–	3.0
Station location M (all components)	10.0	1.0	1.0	1.0

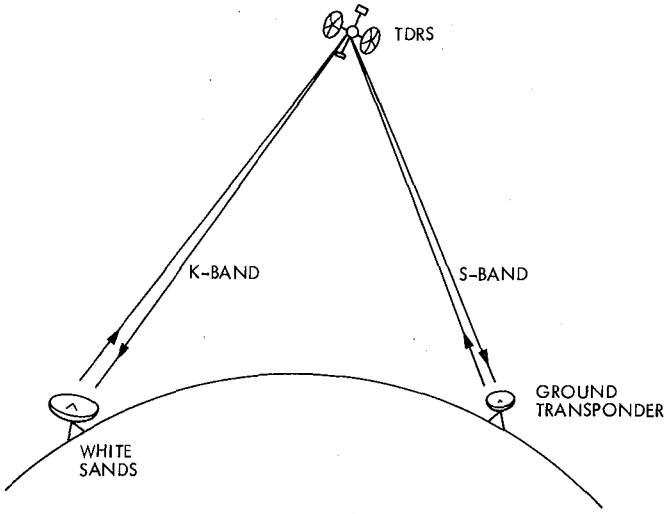

Fig. 1. Bilateration tracking of TDRS

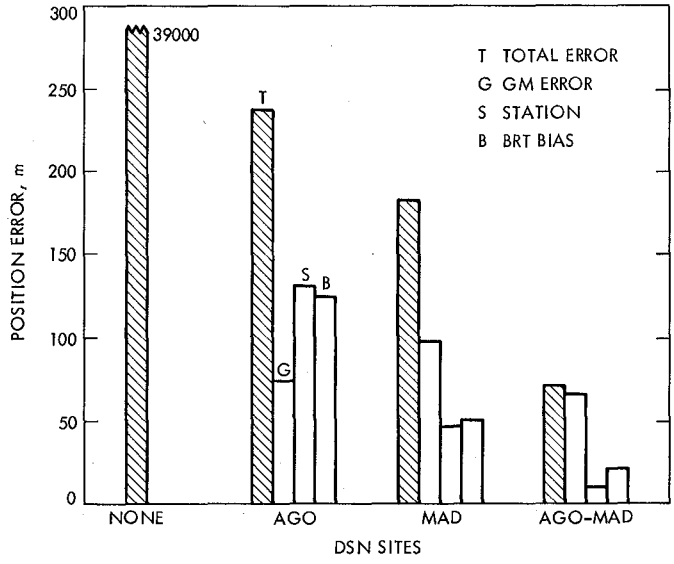

Fig. 3. White Sands BRT with DSN range

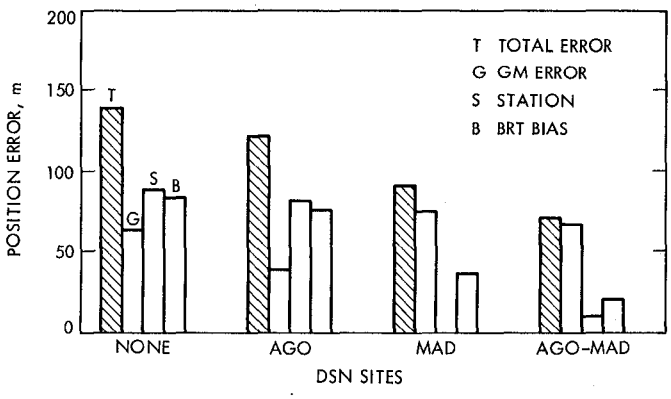

Fig. 2. TDRS-East OD with DSN and BRT range

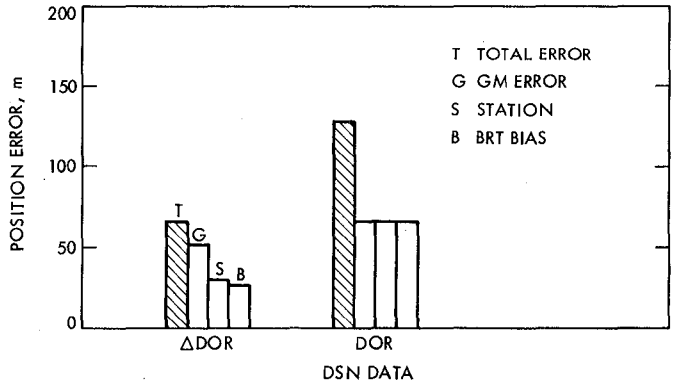

Fig. 4. TDRS OD with DSN VLBI

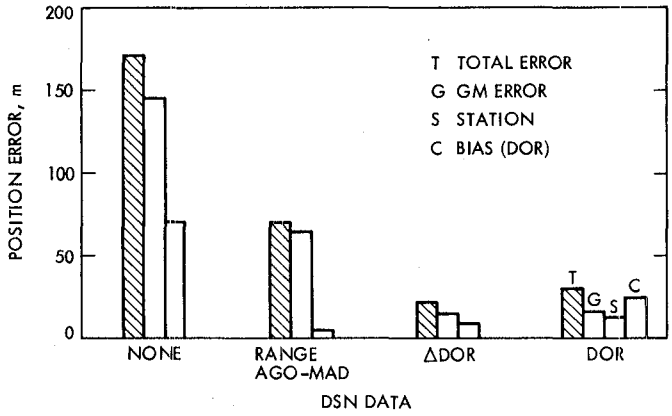

Fig. 5. TDRS OD with bias estimation filter

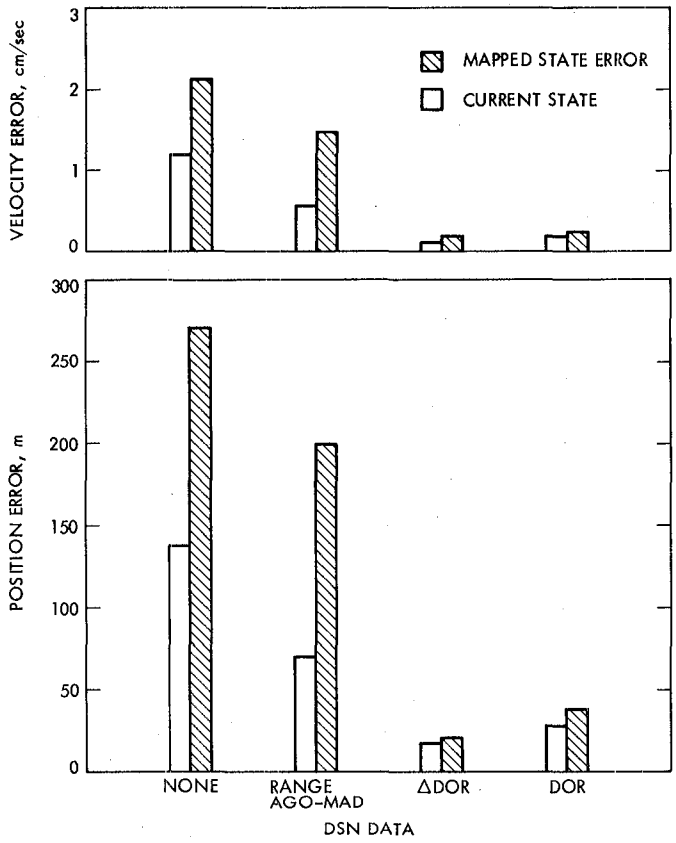

Fig. 6. TDRS-East mapped state errors

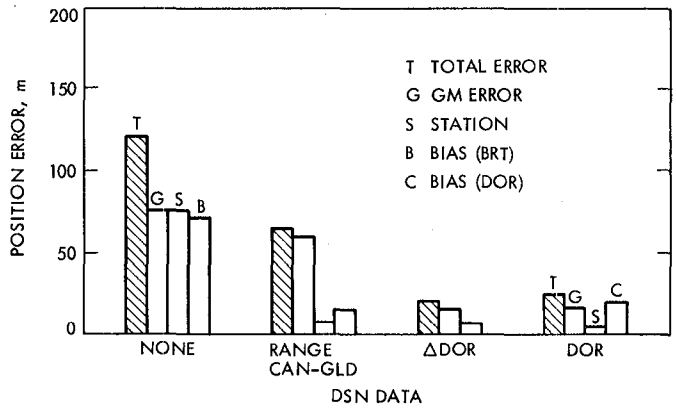

Fig. 7. TDRS-West OD performance

Temperature Stabilized Phase Detector

Yeeman Lo
Communications Systems Research Section

This article presents the construction, tests, and performance of a temperature stabilized phase detector. It has a frequency stability of 5 parts in 10^{16} at 100 MHz, with a temperature step of 20°C (15 to 35°C).

I. Introduction

A temperature stabilized phase detector has been developed to be used in the stabilized optical fiber distribution system. For a step change of ambient temperature of 20°C, this phase detector has a frequency stability of 5 parts in 10^{16}, which is two times better than the intermediate goal of 1 part of 10^{15}.

This report describes the temperature stabilized phase detector and its performance.

II. Description

The construction and layout of the phase detector are shown in Fig. 1. In the block diagram (Fig. 2), the temperature stabilized phase detector has been separated into five functional blocks. Starting with the heater winding, it has a low temperature coefficient of resistance (5×10^{-6} ohm/ohm/°C) and its resistivity is 138 μohm-m. The winding has a total resistance of 50 Ω. The wire is insulated with a thin layer of enamel.

A commercial high-level, double-balanced mixer is used as a phase detector. It is chosen for its low DC offset voltage and high sensitivity. It covers a frequency range of 1 to 400 MHz.

The temperature transducer consists of two precision thermistors and two resistors in a bridge circuit. The thermistors have a nominal resistance of 13.28 kΩ at the operating temperature of 45°C. The resistors are chosen to match the resistance of the thermistors at the operating temperature. When the phase detector is not operating at 45°C, a voltage appears at the output of the bridge. This voltage is then amplified and converted to current to drive the heater winding. A schematic of the circuit is shown in Fig. 3.

III. Heater Winding and Thermistor Location

To achieve good loop stability in the temperature control circuit, the thermistors have to be in good thermal contact with the case and the heater winding. Two different heater winding configurations were tried. Tests showed that the best stability is obtained by winding the heater wire as shown in Fig. 1a. Several locations of the thermistors were also tried. The best location was found to be on the under-side of the phase detector.

IV. Test

The voltage out of an ideal phase detector is a function of only the phase difference between the inputs. In a practical phase detector, the output voltage is also, to a smaller degree,

a function of temperature. The temperature stabilizing circuit is designed to minimize the effect of temperature changes on the output voltage. Tests were made to determine the stability of the phase detector versus temperature.

Refer to the block diagram of the test setup shown in Fig. 4. A stable 100-MHz signal is split into two paths. One path goes to the R port of the phase detector while the other signal goes through an amplifier and phase shifter before entering the LO port of the phase detector. The phase shifter is used to set the operating point of the phase detector at the center of the linear range of its voltage versus phase curve, Fig. 5. At this point the output from the I port is zero volts. This corresponds to approximately 90-deg phase difference between the two input signals. These tests were conducted inside an environmental chamber where the ambient temperature was controlled. Coaxial cables with an excellent temperature stability of 10 ppm/°C were used to minimize errors due to the connecting cables. The calculated error due to 0.30 m of this cable is 520 μ-deg/°C at 100 MHz. Thermal insulation was put around the coaxial cable to reduce the phase shift due to temperature changes on the cable. Over the operating temperature range of (15-35°C), the phase shift of the phase detector as a function of temperature is approximately 500 μ-deg/°C, including the coaxial cables. The time constant of the phase detector is 8.7 minutes.

V. Conclusion

The test results show that this temperature stabilized phase detector has a stability limited by the coaxial cables. The phase stability of 500 μ-deg/°C with the time constant of 8.7 minutes and a step change in temperature of 20°C can be converted to a frequency stability of 5 parts in 10^{16} (refer to Fig. 6), which meets the intermediate goal. The long-term goal of 1 part in 10^{17} can be met if the stability of the coaxial cables at the input and output ports of the phase detector are improved. The test results indicate that the temperature stabilized phase detector is suitable for application in a stable reference frequency distribution system.

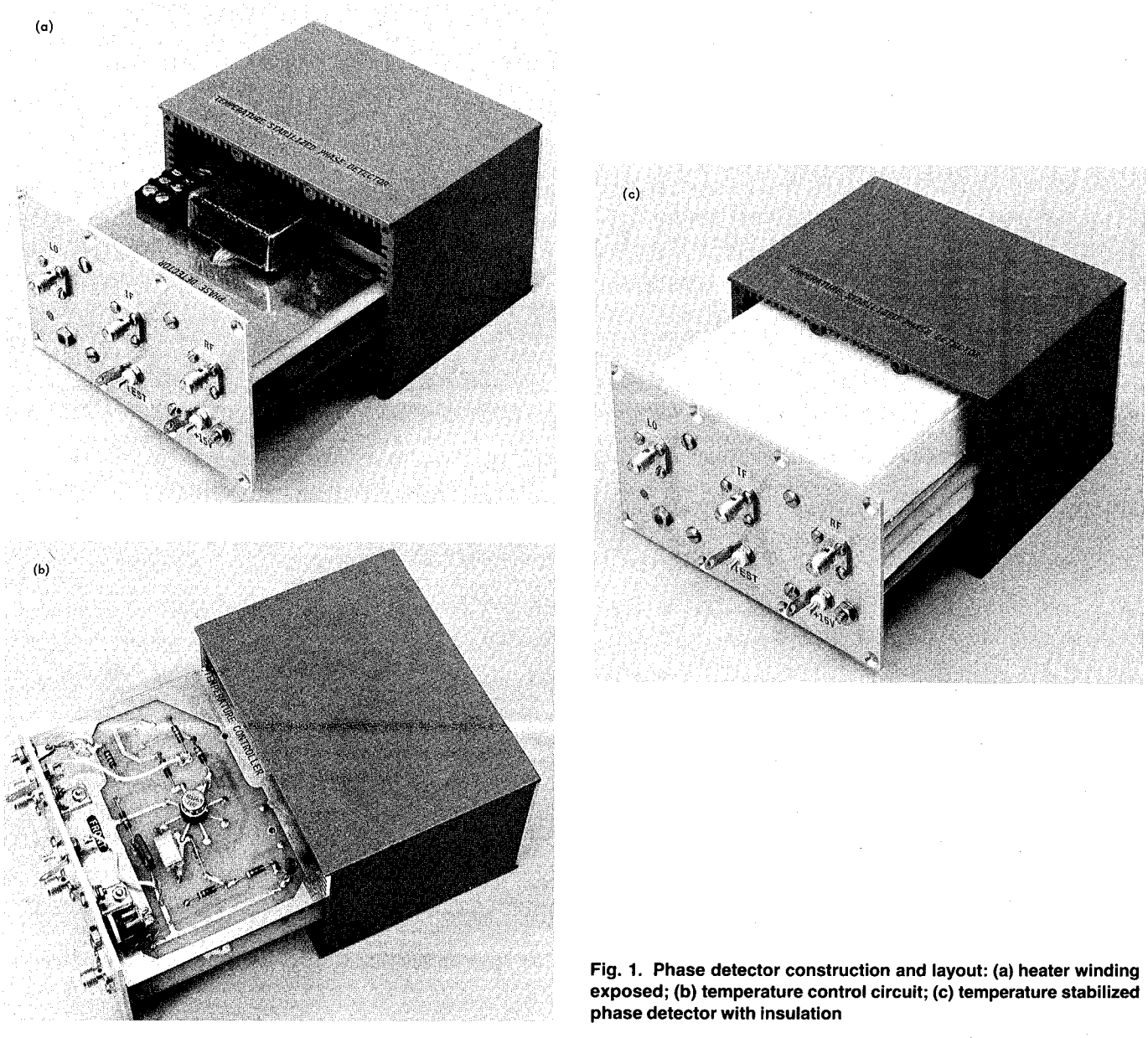

Fig. 1. Phase detector construction and layout: (a) heater winding exposed; (b) temperature control circuit; (c) temperature stabilized phase detector with insulation

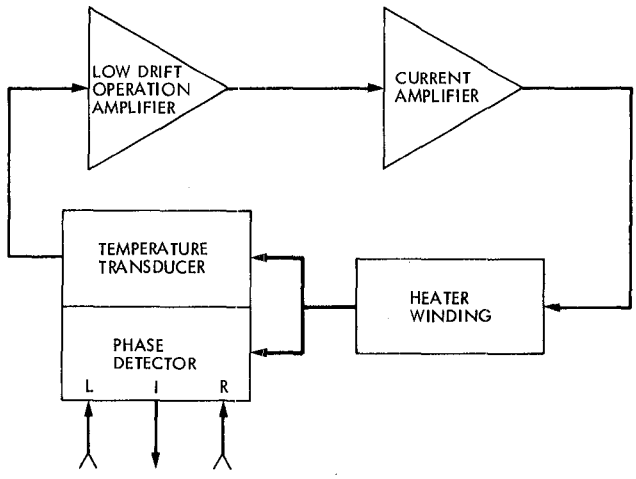

Fig. 2. General block diagram of the temperature stabilized phase detector

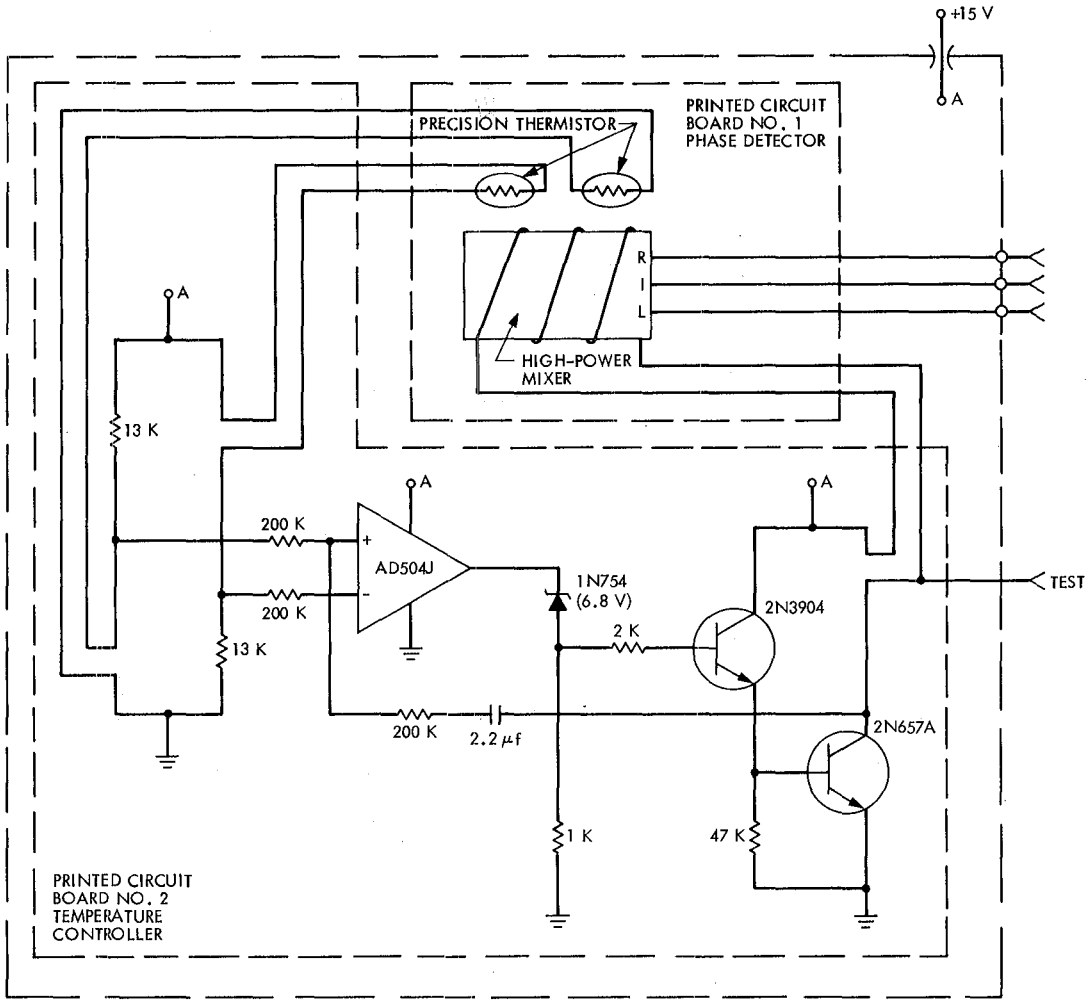

Fig. 3. Schematic of the temperature stabilized phase detector

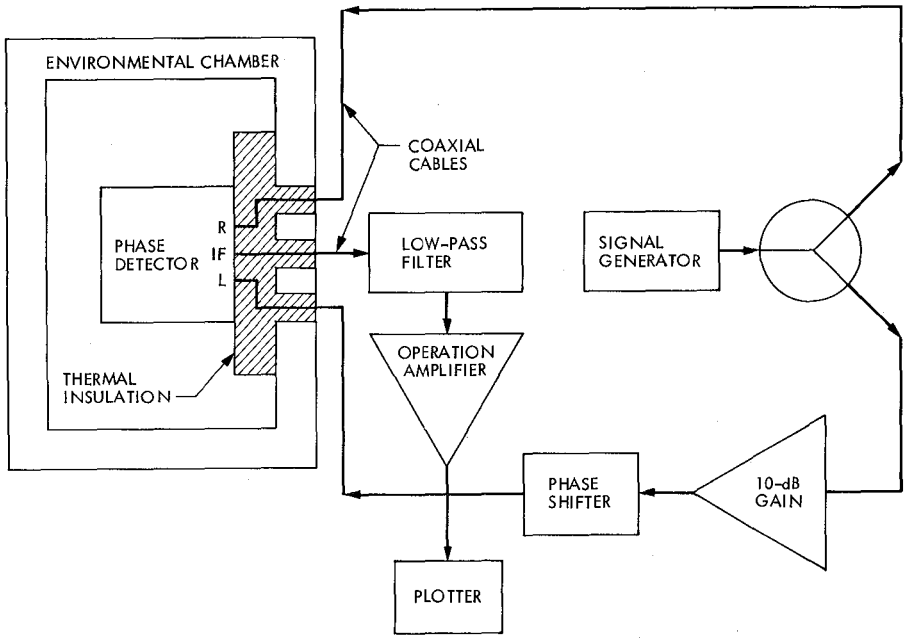

Fig. 4. Block diagram of the test setup

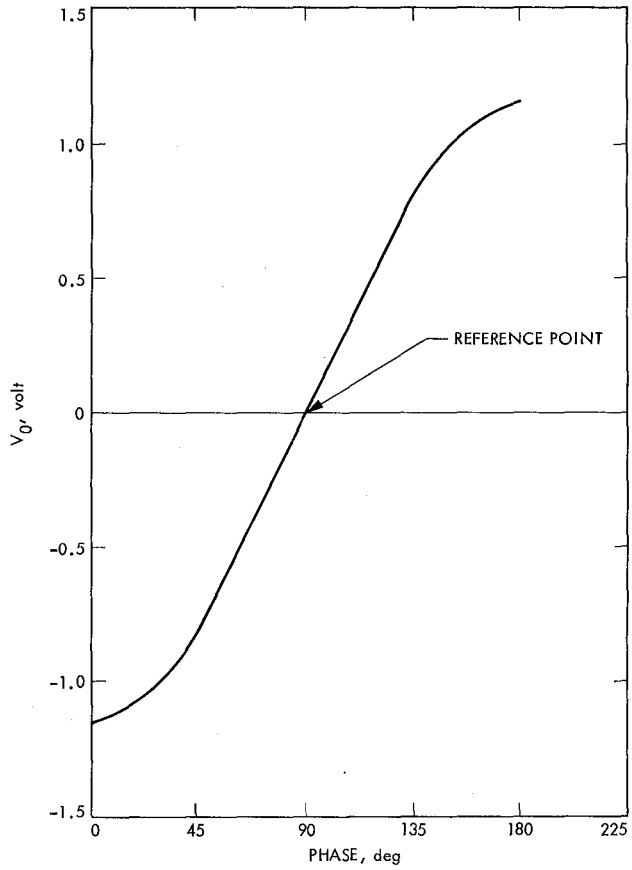

Fig. 5. Voltage vs phase curve of the phase detector

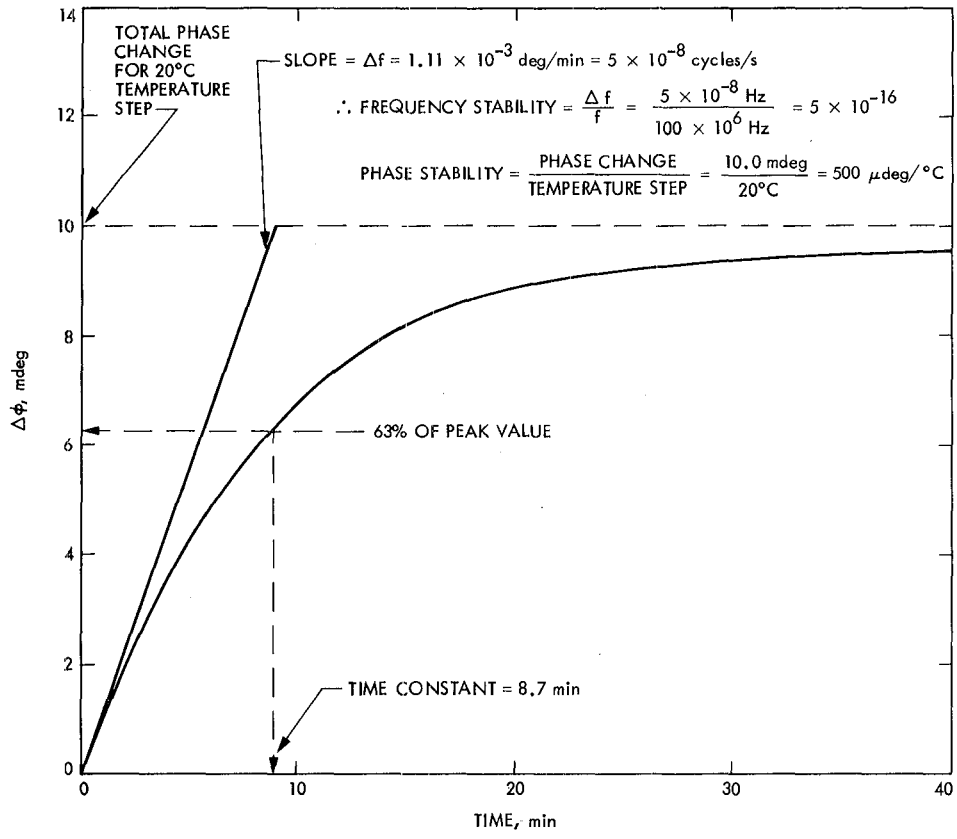

Fig. 6. Phase change vs time for a 20°C step change in temperature

Analysis of Tracking Performance of the MTDD Costas Loop for UQPSK Signal

Y. H. Park
Telecommunications Systems Section

Even though the Costas loop for the Multimegabit Telemetry Demodulator/Detector (MTDD) System was originally designed for support of BPSK signalling, its inherent tracking capability for an unbalanced quadriphase shift-keyed (UQPSK) signal is well known. This paper summarizes analytic results to predict rms phase jitter of the MTDD Costas loop for a UQPSK signal. The Costas loop has a hard-limited in-phase channel.

I. Introduction

This paper summarizes the analytic results to predict the tracking performance of the breadboard Costas loop (Refs. 1, 2) for the Multimegabit Telemetry Demodulator/Detector (MTDD) System using an unbalanced quadriphase-shift-keyed (UQPSK) signal. The particular Costas loop is a biphase polarity-type with passive arm filters. The loop contains a hard-limiter in front of the third multiplier, which is a chopper-type device. The merits of the polarity-type Costas loop have been well explained in Refs. 3 and 4.

Reference 4 has an excellent analysis on the polarity-type Costas loop tracking performance. However, the numerical results shown in the paper are not directly applicable to the prediction of the MTDD Costas loop at or in the vicinity of the design point SNR level. Basically, this paper extends the analysis of Ref. 4 to low input SNR cases.

The rms phase jitter predictions made in this paper have also been verified experimentally (Ref. 2).

II. Analysis

Since most of the analysis has been well documented in Ref. 4, only the minimum necessary equations will be summarized in this section for the sake of self-containment.

A. Loop Equation

The loop under consideration is shown in Fig. 1. Let the input signal be an unbalanced quadriphase-shift-keyed (UQPSK) signal.

$$s(t) = \sqrt{2P_2}\, m_2(t) \sin \Phi(t) + \sqrt{2P_1}\, m_1(t) \cos \Phi(t) \tag{1}$$

where

$$\Phi(t) \triangleq \omega_0 t + \theta(t)$$

ω_0 = angular carrier frequency

$\theta(t)$ = received carrier phase

$= \theta_0 + \Omega_0 t$

θ_0 = a random phase

Ω_0 = a doppler frequency offset

$m_2(t), m_1(t)$ = binary data respectively for in-phase (I) and quadrature-phase (Q) channels

P_2, P_1 = average signal power respectively for I and Q channels.

The total received signal with additive noise is:

$$x(t) = s(t) + n_i(t) \tag{2}$$

where $n_i(t)$ is the additive bandpass channel noise which can be expressed in the following form (Ref. 5):

$$n_i(t) = \sqrt{2}\left\{N_c(t)\cos\Phi(t) - N_s(t)\sin\Phi(t)\right\} \tag{3}$$

where $N_c(t)$ and $N_s(t)$ are approximately statistically independent, stationary, white Gaussian processes with single-sided noise spectral density N_0(W/Hz).

Define the quadrature reference signals

$$\begin{aligned} r_s(t) &= \sqrt{2}K_1 \sin\hat{\Phi}(t) \\ r_c(t) &= \sqrt{2}K_1 \cos\hat{\Phi}(t) \end{aligned} \tag{4}$$

where K_1^2 is the rms power of the VCO output signal and $\hat{\Phi}(t)$ is the phase estimate of $\Phi(t)$.

Then, phase detector outputs are:

$$\begin{aligned} \epsilon_s(t) \triangleq K_m\, x(t)\, r_s(t) &= K_1 K_m \left[\sqrt{P_2}\, m_2(t) - N_s(t)\right]\cos\phi(t) \\ &\quad - K_1 K_m \left[\sqrt{P_1}\, m_1(t) + N_c(t)\right]\sin\phi(t) \\ \epsilon_c(t) \triangleq K_m\, x(t)\, r_c(t) &= K_1 K_m \left[\sqrt{P_2}\, m_2(t) - N_s(t)\right]\sin\phi(t) \\ &\quad + K_1 K_m \left[\sqrt{P_1}\, m_1(t) + N_c(t)\right]\cos\phi(t) \end{aligned} \tag{5}$$

where $\phi(t) = \Phi(t) - \hat{\Phi}(t) = \theta_0 - \hat{\theta}_0$ is the loop phase error, and K_m is the multiplier gain of the in-phase and quadrature-phase detectors. Then, the output signals of the in-phase and quadrature-phase arm filters with transfer function $G(s)$ are:

$$z_s(t) \triangleq G(p)\,\epsilon_s(t) = K_1 K_m \left\{ \left[\sqrt{P_2}\,\hat{m}_2(t) - \hat{N}_s(t) \right] \cos\phi(t) - \left[\sqrt{P_1}\,\hat{m}_1(t) + \hat{N}_c(t) \right] \sin\phi(t) \right\}$$

$$z_c(t) \triangleq G(p)\,\epsilon_c(t) = K_1 K_m \left\{ \left[\sqrt{P_2}\,\hat{m}_2(t) - \hat{N}_s(t) \right] \sin\phi(t) + \left[\sqrt{P_1}\,\hat{m}_1(t) + \hat{N}_c(t) \right] \cos\phi(t) \right\} \tag{6}$$

where

$$\hat{m}_i(t) = G(p)\,m_i(t) \qquad i = 1, 2$$

$$\hat{N}_\alpha(t) = G(p)\,N_\alpha(t) \qquad \alpha = s, c$$

$G(p)$ = the Heaviside notation of the transfer function

In the derivation of Eq. (6), it is assumed that $\phi(t)$ is small, and unaffected by filtering. The output $z_0(t)$ of the chopper multiplier is given by product of $z_c(t)$ and the hard-limited $z_s(t)$:

$$z_0(t) = z_c(t)\,\mathrm{sgn}\,[z_s(t)] = K_1 K_m \left\{ \sqrt{P_2}\,\hat{m}_2(t)\,\tilde{m}(t) \sin\phi(t) + \sqrt{P_1}\,\hat{m}_1(t)\,\tilde{m}(t) \cos\phi(t) - \hat{N}_s(t)\,\tilde{m}(t) \sin\phi(t) + \hat{N}_c(t)\,\tilde{m}(t) \cos\phi(t) \right\} \tag{7}$$

where

$$\tilde{m}(t) \triangleq \mathrm{sgn}\,[z_s(t)]\,,$$

$$\mathrm{sgn}(x) = x/|x|\,.$$

The instantaneous frequency of the VCO output is related to $z_0(t)$ by

$$\frac{d\hat{\Phi}(t)}{dt} = K_v\,[F(p)\,z_0(t)] + \omega_0 \tag{8}$$

where K_v is the VCO gain in radians/volts. Then, the stochastic integro-differential equation of loop operation becomes

$$2\frac{d\phi(t)}{dt} = 2\Omega_0 - K\,F(p) \left\{ 2\sqrt{P_2}\,\hat{m}_2(t)\,\tilde{m}(t) \sin\phi(t) + 2\sqrt{P_1}\,\hat{m}_1(t)\,\tilde{m}(t) \cos\phi(t) + 2\,\tilde{m}(t)\,\hat{N}[t, \phi(t)] \right\} \tag{9}$$

where $K \triangleq K_1 K_m K_v$, and

$$\hat{N}[t, \phi(t)] \triangleq \hat{N}_c(t) \cos \phi(t) - \hat{N}_s(t) \sin \phi(t) \tag{10}$$

As shown in Ref. 4, in the linear region of the loop the equation of loop operation can be approximately obtained:

$$2 \frac{d\phi}{dt} = 2\Omega_0 - K F(p) \left\{ \sqrt{P_2}\, \tilde{\alpha} f_1(2\phi) + \hat{N}_e(t, 2\phi) \right\} \tag{11}$$

where

$$\hat{N}_e(t, 2\phi) \triangleq 2 \tilde{m}(t) \hat{N}(t, \phi) + n_\Delta(t, 2\phi) \tag{12}$$

n_Δ = self noise

$$= 2\sqrt{P_1}\left[\hat{m}_1(t)\, \tilde{m}(t) - \langle \overline{\hat{m}_1(t)\, \tilde{m}(t)} \rangle\right] \tag{13}$$

$\langle\ \rangle$ denotes the time average.

The overbar denotes the ensemble average

$f_1(x)$ = a nonlinearity which is periodic in x with period 2π and has unit slope at the origin

$\tilde{\alpha}$ = the signal suppression factor

$$= \frac{d}{d\phi}\left[\langle \overline{\hat{m}_2(t)\, \tilde{m}(t)} \rangle \sin \phi(t) + \langle \overline{\hat{m}_1(t)\, \tilde{m}(t)} \rangle \cos \phi(t)\right]_{\phi=0}$$

B. Signal Suppression Factor

Reference 4 first derived the signal suppression factor $\tilde{\alpha}$ for NRZ in-phase channel data and any quadrature channel binary data assuming single-pole (RC) Butterworth arm filters. The total suppression factor $\tilde{\alpha}$ can be expressed conveniently as the sum of α_2 and α_1 where α_2 is actually the suppression factor in the absence of the Q-channel and α_1 is a negative quantity which is a signal suppression due to the interference of the Q-channel. Thus,

$$\tilde{\alpha} = \alpha_2 + \alpha_1 \tag{14}$$

where

$$\alpha_2 = \frac{1}{2} \int_0^1 \left\{1 - 2 \exp[-2(B_i/R_2)x]\right\} \cdot \operatorname{erf}\left\{\sqrt{\frac{\rho_2}{2}} \left\{1 - 2 \exp[-2(B_i/R_2)x]\right\}\right\} dx + \frac{1}{2} \operatorname{erf} \sqrt{\frac{\rho_2}{2}} \tag{15}$$

$$\alpha_1 = -\gamma_p \sqrt{\frac{2\rho_2}{\pi}}\, D_{m_1} \frac{1}{2} \int_0^1 \exp\left\{-\frac{\rho_2}{2} \left\{1 - 2 \exp[-2(B_i/R_2)x]\right\}^2\right\} dx - \gamma_p \sqrt{\frac{2\rho_2}{\pi}}\, D_{m_1} \frac{1}{2} \exp\left(-\frac{\rho_2}{2}\right) \tag{16}$$

$$\gamma_p \triangleq \frac{P_1}{P_2} = Q\text{-to-}I \text{ channel power ratio} \tag{17}$$

$$\rho_2 = \frac{2P_2}{N_0 B_i} \tag{18}$$

$$B_i = \frac{\omega_c}{2} = \text{two-sided arm filter input bandwidth} \tag{19}$$

ω_c = the 3-dB cutoff frequency of the arm filter with a transfer function

$$G(\omega) = \frac{1}{1 + j\,\frac{\omega}{\omega_c}} \tag{20}$$

R_2, R_1 = respectively I and Q channel data rates

D_{m_1} is the mean-squared power for the quadrature-channel data. For *NRZ* Q channel data,

$$D_{m_1} = 1 - \frac{1}{2B_i/R_1}\,[1 - \exp(-2B_i/R_1)] \tag{21}$$

For a Manchester coded modulation in Q channel,

$$D_{m_1} = 1 - \frac{1}{2B_i/R_1}\,[3 - 4\exp(-B_i/R_1) + \exp(-2B_i/R_1)] \tag{22}$$

Using Eqs. (14) through (22), we can calculate the signal suppression factor by numerical integration.

C. Equivalent Noise Spectral Density for Small Input SNR

The equivalent noise spectral density is defined by:

$$N_e \triangleq 2\int R_{\hat{N}_e}(\tau)\,d\tau \tag{23}$$

where

$$R_{\hat{N}_e}(\tau) \triangleq \langle \overline{\hat{N}(t, 2\phi)\,\hat{N}(t+\tau, 2\phi)} \rangle \tag{24}$$

with straightforward derivation, Ref. 4 showed that

$$R_{\hat{N}_e}(\tau) = 8\int_{-\infty}^{\infty} \left[R_{\hat{N}}(\tau) + P_1 R_{\hat{m}_1}(\tau)\right] R_y(\tau)\,d\tau \tag{25}$$

where

$$y(t) \stackrel{\Delta}{=} \operatorname{sgn}\left\{\sqrt{P_2}\,\hat{m}_2(t) - \hat{N}_s(t)\right\} \tag{26}$$

$$R_{\hat{N}}(\tau) = \frac{N_0 B_i}{2}\, e^{-2B_i|\tau|} \tag{27}$$

$R_{\hat{m}_1}(\tau)$ is given below

For a *NRZ* modulation (Ref. 3),

$$R_{m_1}(\tau) = \begin{cases} 1 - \dfrac{|\tau|}{T_1} + \dfrac{e^{-2B_i/R_1}\cosh 2B_i\tau - e^{-2B_i|\tau|}}{2B_i/R_1}\,; 0 \leqslant |\tau|\, T_1 \\ \dfrac{e^{-2B_i|\tau|}\,[\cosh 2B_i/R_1 - 1]}{2B_i/R_1}\,; T_1 \leqslant |\tau| \leqslant \infty \end{cases} \tag{28}$$

For a Manchester coded modulation (Ref. 4),

$$R_{\hat{m}_1}(\tau) = \begin{cases} 1 - 3\dfrac{|\tau|}{T_1} + \dfrac{[4\,e^{-B_i/R_1} - e^{-2B_i/R_1}]\cosh 2B_i\tau - 3\,e^{-2B_i|\tau|}}{2B_i/R_1}\,; 0 \leqslant |\tau| \leqslant \dfrac{T_1}{2} \\ -\left(1 - \dfrac{|\tau|}{T_1}\right) + \dfrac{e^{-2B_i|\tau|}\,[4\cosh B_i/R_1 - 3] - e^{-2B_i/R_1}\cosh 2B_i\tau}{2B_i/R_1}\,; \dfrac{T_1}{2} \leqslant |\tau| \leqslant T_1 \\ \dfrac{e^{-2B_i|\tau|}\,[4\cosh B_i/R_1 - \cosh 2B_i/R_1 - 3]}{2B_i/R_1}\,; T_1 \leqslant |\tau| \leqslant \infty \end{cases} \tag{29}$$

where $T_1 = 1/R_1, T_2 = 1/R_2$

Reference 3 presents approximate expressions for $R_y(\tau)$ corresponding to small ρ_2 and large ρ_2 cases.

Since we are concerned here with the low ρ_2 case, then we have:

$$R_y(\tau) = \frac{2}{\pi}\left[\sin^{-1}\rho_{\hat{N}}(\tau) - \rho_2\,\frac{R_{\hat{m}_2}(0)\,\rho_{\hat{N}}(\tau)}{\sqrt{1-\rho^2_{\hat{N}}(\tau)}} + \rho_2\frac{R_{\hat{m}_2}(\tau)}{\sqrt{1-\rho^2_{\hat{N}}(\tau)}}\right] \tag{30}$$

where

$$\rho_{\hat{N}}(\tau) = e^{-2B_i \tau}$$

$$R_{\hat{m}_2}(\tau) = \begin{cases} 1 - \dfrac{|\tau|}{T_2} + \dfrac{e^{-2B_i/R_2}\cosh 2B_i\tau - e^{-2B_i|\tau|}}{2B_i/R_2}; 0 \leqslant |\tau| \leqslant T_2 \\ \dfrac{e^{-2B_i|\tau|}\left[\cosh 2B_i/R_2 - 1\right]}{2B_i/R_2} \quad ; T_2 \leqslant |\tau| < \infty \end{cases} \tag{31}$$

$$R_{\hat{m}_2}(0) = 1 - \frac{1 - e^{-2B_i/R_2}}{2B_i/R_2} \tag{32}$$

Now we have all the equations needed to compute the equivalent noise spectral density. Since an analytic integration of the integral in Eq. (25) is cumbersome, a numerical integration may be attempted. However, $R_y(\tau)$ in Eq. (30) contains terms which go to infinity when $\tau = 0$. Thus, a change of forms of equation is required.

First let's approximate the integration region $0 \leqslant |\tau| \leqslant 2T_2$. Also let's consider β defined by:

$$\beta = \frac{N_e}{4N_0} \tag{33}$$

Then,

$$\beta = \frac{2}{N_0}\int_{-2T_2}^{2T_2}\left[R_{\hat{N}}(\tau) + P_1 R_{\hat{m}_1}(\tau)\right] R_y(\tau)\, d\tau \tag{34}$$

As in the calculation of the signal suppression factor, the total equivalent noise factor β may be expressed as the sum of two factors β_1 and β_2:

$$\beta = \beta_2 + \beta_1$$

where

$$\beta_2 = \frac{2}{N_0}\int_{-2T_2}^{2T_2} R_{\hat{N}}(\tau) R_y(\tau)\, d\tau \tag{35}$$

$$\beta_1 = \frac{2P_1}{N_0}\int_{-2T_2}^{2T_2} R_{\hat{m}_1}(\tau) R_y(\tau)\, d\tau \tag{36}$$

It is observed that β_2 is the noise factor in the absence of Q channel and β_1 is the increase of noise due to the presence of Q channel data.

By change of variable $2T_2 x = \tau$, we have

$$\beta_2 = 4 \frac{B_i}{R_2} \int_0^1 \exp(-4B_i/R_2) R_y \left(\frac{2x}{R_2}\right) dx \tag{37}$$

$$\beta_1 = 4 \rho_1 \frac{B_i}{R_2} \int_0^1 R_{\hat{m}_1} \left(\frac{2x}{R_2}\right) R_y \left(\frac{2x}{R_2}\right) dx \tag{38}$$

where

$$\rho_1 = \frac{2P_1}{N_0 B_i} \tag{39}$$

$$R_{\hat{m}_1} \left(\frac{2x}{R_2}\right) = 1 - 2x \frac{R_1}{R_2} + \frac{\exp(-2B_i/R_1) \cosh \left(4 \frac{B_i}{R_2} x\right) - g(x)}{2 \frac{B_i}{R_1}} \tag{40}$$

$$g(x) = \exp \left(-4 \frac{B_i}{R_2} x\right) \tag{41}$$

For $0 \leqslant x < 0.5$,

$$R_y \left(\frac{2x}{R_2}\right) = \frac{2}{\pi} \left[\sin^{-1} g(x) + \rho_2 \left(\frac{\sqrt{1 - g(x)}}{\sqrt{1 + g(x)}} + \frac{\exp(-2B_i/R_2) \sqrt{1 - g^2(x)}}{4B_i/R_2 \qquad g(x)} \right) \right.$$

$$\left. - \rho_2 \cdot 2x \cdot \frac{1}{\sqrt{1 + g(x)} \sqrt{h(x)}} \right] \tag{42}$$

$$h(x) = 1 - g(x) = ax \left(1 - \frac{ax}{2} + \frac{(ax)^2}{3!} - \frac{(ax)^3}{4!} + \frac{(ax)^4}{5!} \ldots\right) \tag{43}$$

$$a = 4B_i/R_2 \tag{44}$$

Equation (42) is obtained from (30) and (31) after straightforward derivation. Taylor series expansion of $g(x)$ is used to prevent an overflow in a numerical integration at the vicinity of $x = 0$. For $0.5 < x \leqslant 1$, a straightforword substitution in Eq. (30), (31) and (32) gives

$$R_y \left(\frac{2x}{R_2}\right), 0.5 < x \leqslant 1.0 .$$

D. RMS Phase Jitter

In a linear region of the loop, the rms phase jitter of ϕ is given (Ref. 4) by

$$\sigma_\phi^2 = \frac{1}{\rho S_L} \tag{45}$$

$$\rho = \frac{P}{N_0 B_L} \tag{46}$$

where

$P = P_1 + P_2$

B_L = single-sided loop bandwidth

N_0 = single-sided noise spectral density

S_L = squaring loss

$$= \frac{1}{(1+\gamma_p)} \frac{\tilde{\alpha}^2}{\beta} \tag{47}$$

$\gamma_p = P_1/P_2$

We already have obtained all necessary equations to calculate the squaring loss S_L. Thus the only thing left is to express the loop bandwidth B_L as a function of input SNR.

The loop filter of the Costas loop under consideration is of the imperfect second-order loop type with the following transfer function:

$$F(s) = \frac{1+\tau_2 s}{1+\tau_1 s} \tag{48}$$

The bandwidth of the loop is shown in Ref. 6 to be

$$B_L = \frac{\omega_n}{2}\left(\zeta + \frac{1}{4\zeta}\right) \tag{49}$$

where

$\omega_n = \sqrt{\frac{K}{\tau_1}}$ = natural angular frequency

$\zeta = \frac{1+K\tau_2}{2\omega_n \tau_1}$ = loop damping factor

K = total loop gain

Suppose K_0 is the loop gain at the design point, i.e., at $PT_2/N_0 = -4$ dB (Ref. 1). Then, the loop gain at a arbitrary SNR is given by:

$$K = K_0 \cdot \frac{\tilde{\alpha}}{\tilde{\alpha}_0} \cdot \frac{g\sqrt{P}}{(g_0\sqrt{P})} \tag{50}$$

where $\tilde{\alpha}_0$, $\tilde{\alpha}$ are the signal suppression factors respectively at the design point and a desired SNR, g_0, g are the AGC or MGC IF gain control factor at the design point or a desired SNR.

Using (49) and (50), we can obtain the loop bandwidth at any SNR level. Thus we are now ready to calculate the rms phase jitter at any SNR level.

III. Numerical Results and Discussions

Figures 2-9 show the plots of squaring loss for various conditions. Figure 10 shows the rms phase jitter for the MTDD breadboard Costas loop with various conditions (see also Ref. 7). The rms phase jitter is a function of PT_2/N_0, γ_p and R_2/R_1. Obviously, the phase jitter will decrease as PT_2/N_0 increases, γ_p decreases or R_2/R_1 increases.

Generally, for low input SNR or PT_2/N_0 in the range from -4 to +2 dB, the squaring loss is an increasing function of PT_2/N_0. At higher PT_2/N_0 the trend reverses (Ref. 4). However, as mentioned above, the rms phase jitter is a monotonically decreasing function of PT_2/N_0.

References

1. Stevens, G., and Woo, K. T., "Design of a Costas Loop to Operate with the Block III Receiver and Its Prediced Performance," in *The DSN Progress Report Vol. 42-51, March and April 1979*, Jet Propulsion Laboratory, Pasadena, Calif.
2. Park, Y. H., "Experimental Results on Tracking Performance of the MTDD Breadboard Costas Loop with UQPSK Signal," published in *TDA Progress Report* (this issue).
3. Simon, M. K., "Tracking Performance of Costas Loops with Hard-limited In-phase Channel," *IEEE Trans. Comm.*, Vol. COM-26, No. 4, April 1978.
4. Simon, M. K., and Alem, W. K., "Tracking Performance of UQPSK Demodulators, Part III – Biphase Polarity-type Costas Loop with Passive Arm Filters," Axiomatix Report No. R7803-1, Axiomatix, Calif., March 1978.
5. Lindsey, W. C., and Simon, M. K., *Telecommunication Systems Engineering*, Prentice-Hall, Englewood Cliffs, N.J., 1973.
6. Blanchard, A., *Phase-Locked Loops*, Wiley-Interscience, John Wiley & Sons, N.Y., 1976.

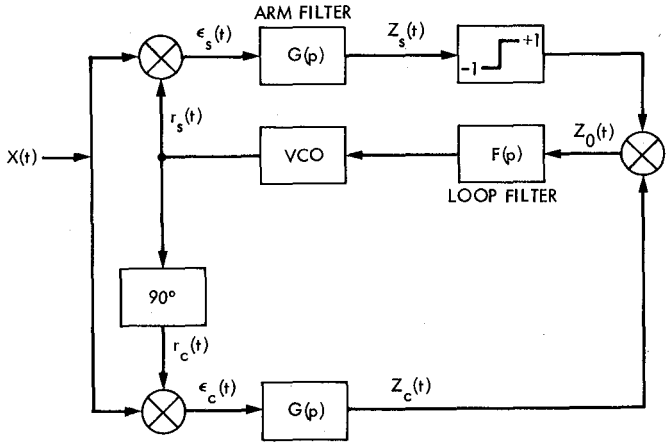

Fig. 1. Costas loop block diagram

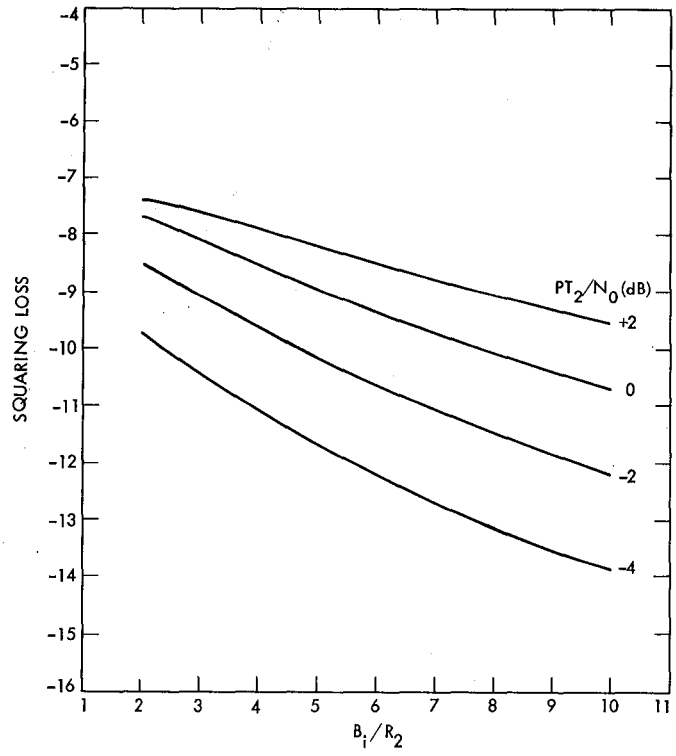

Fig. 2. Squaring loss (R_2/R_1 = 1.0; γ_p = 0.25)

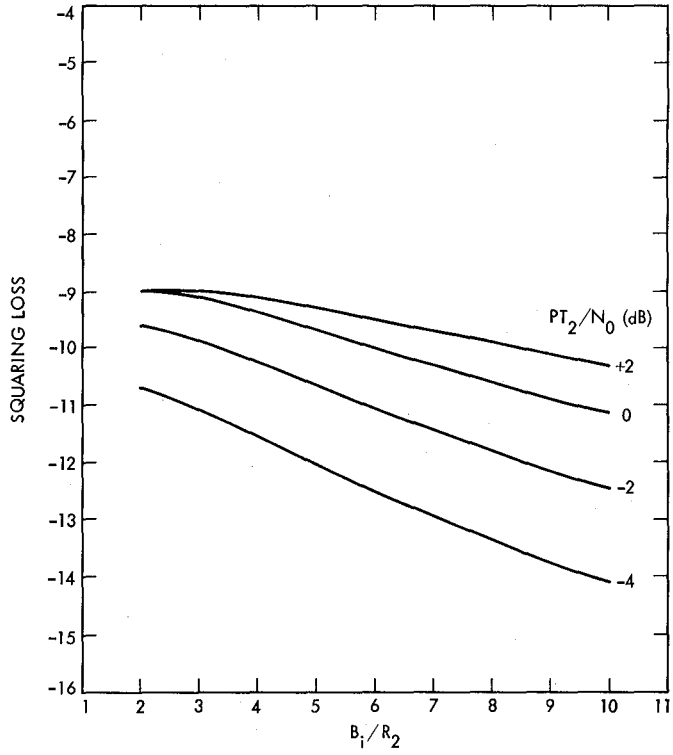

Fig. 3. Squaring loss (R_2/R_1 = 5.0; γ_p = 0.25)

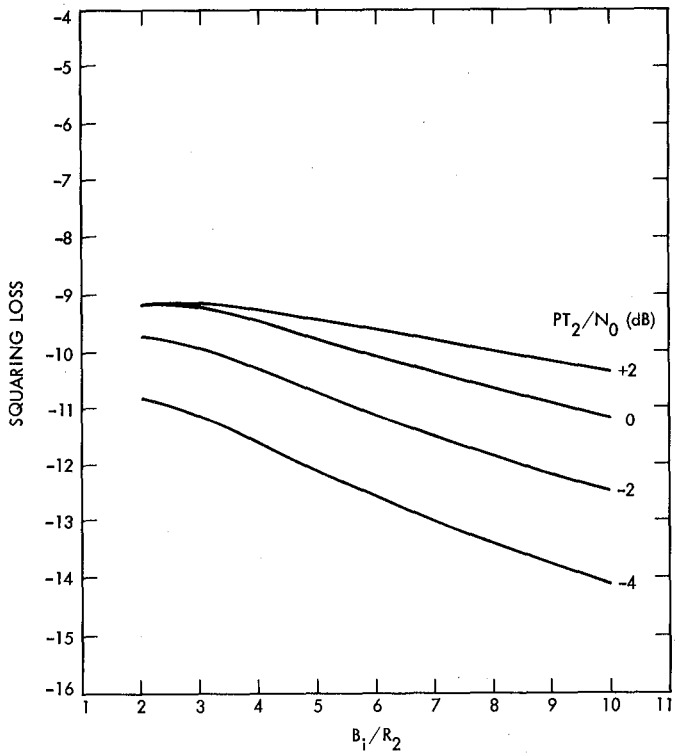

Fig. 4. Squaring loss (R_2/R_1 = 10; γ_p = 0.25)

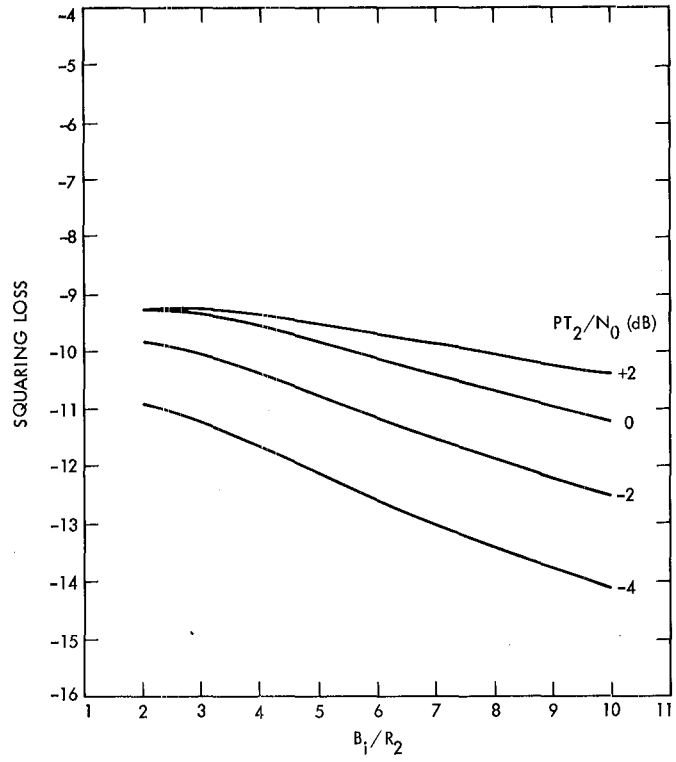

Fig. 5. Squaring loss ($R_2/R_1 = 20$; $\gamma_P = 0.25$)

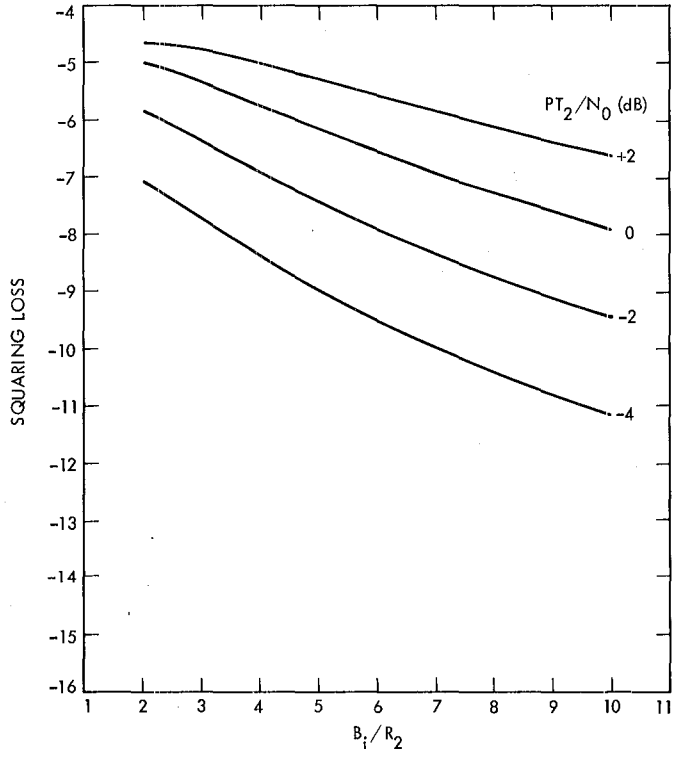

Fig. 6. Squaring loss ($R_2/R_1 = 1.0$; $\gamma_P = 0.1$)

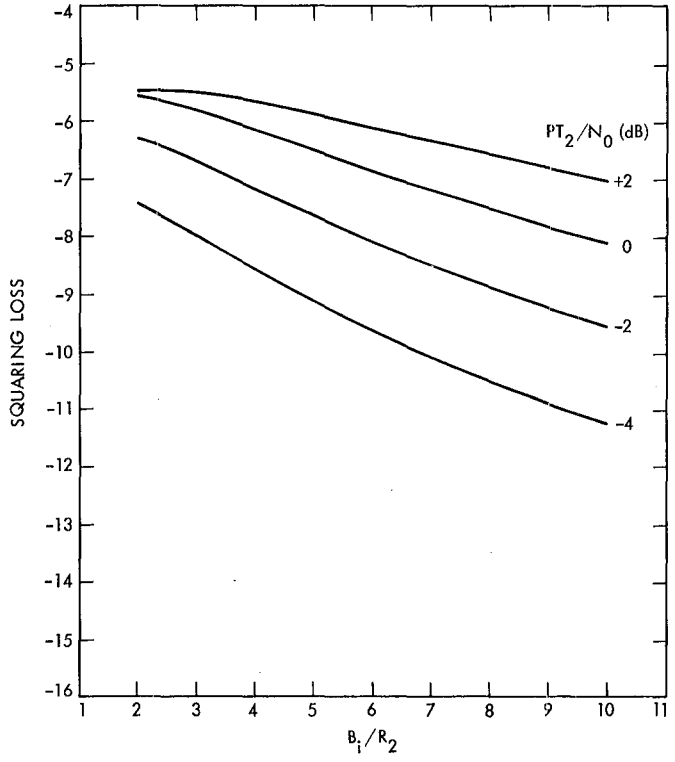

Fig. 7. Squaring loss ($R_2/R_1 = 5$; $\gamma_P = 0.1$)

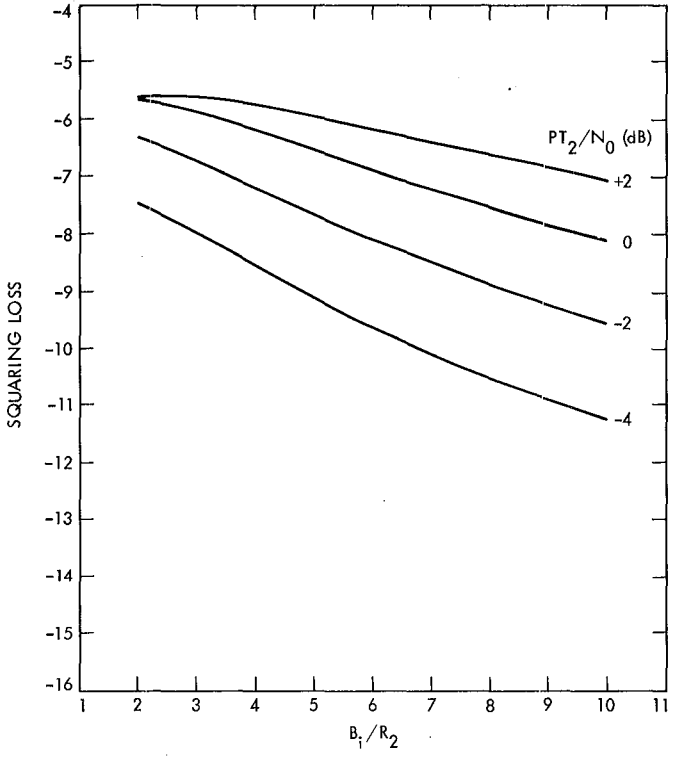

Fig. 8. Squaring loss ($R_2/R_1 = 10$; $\gamma_P = 0.1$)

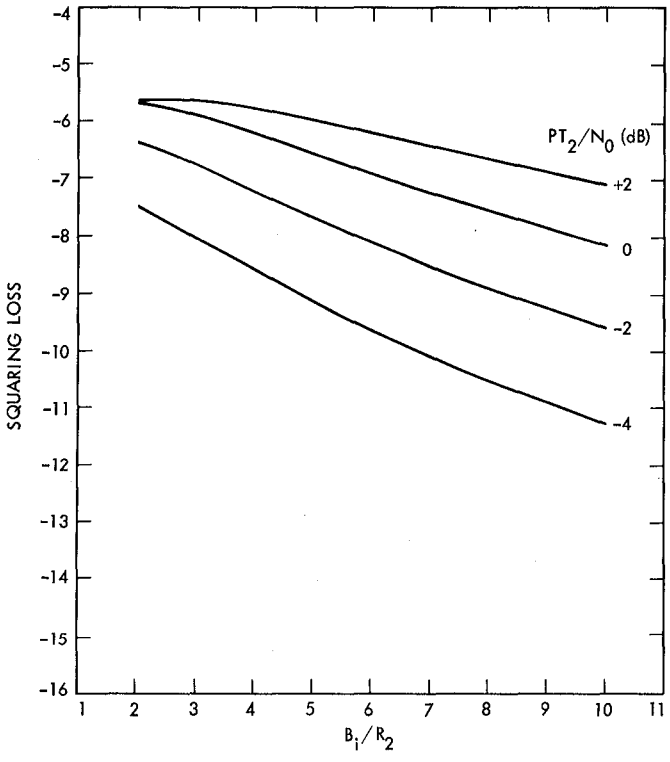

Fig. 9. Squaring loss ($R_2/R_1 = 20$; $\gamma_P = 0.1$)

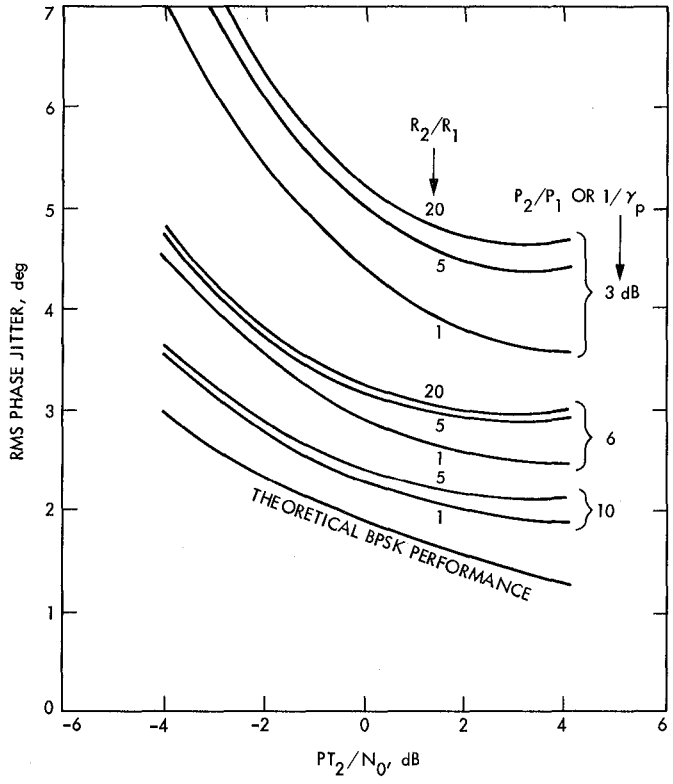

Fig. 10. Theoretical rms phase jitter calculated with low input SNR approximation for MTDD breadboard Costas loop using UQPSK signals

Experimental Results on Tracking Performance of the MTDD Costas Loop With UQPSK Signal

Y. H. Park
Telecommunications Systems Section

The carrier tracking performance of the breadboard Costas Loop of the Multimegabit Telemetry Demodulator Detector System was tested with unbalanced quadriphase shift keying (UQPSK) signals. An S-band UQPSK modulator has been built for the tests. The experimental results are very close to the theoretical rms phase error calculations.

The test and analysis show that the rms phase error for UQPSK signals is less than 5 deg at the design point if the I-to-Q channel power ratio is larger than 6 dB.

I. Introduction

To accommodate a megabit rate of telemetry data from future deep space missions, e.g., Venus Orbiting Image Radar (VOIR), a Costas Loop is being developed for the DSN as a part of the Multimegabit Telemetry Demodulator and Detector (MTDD) System (Refs. 1 and 2). So far, considerable attentions have been made to verify the carrier tracking performance of the MTDD Costas Loop with a suppressed carrier binary phase shift keying (BPSK) signal (Refs. 3 and 4). However, tracking performance of the loop has not been verified using an unbalanced quadriphase shift keying (UQPSK) until the present work.

Even though the MTDD Costas Loop was designed primarily for BPSK signalling (Refs. 1 through 5), the UQPSK signalling was considered to accommodate both a ranging signal on the quadrature channel and high-rate telemetry data on the in-phase chanel (Ref. 2). Another option is the transmission of a separate telemetry data signal on the quadrature channel The VOIR, a possible first user of the MTDD system, does not have any ranging requirement, nor is there any definite plan to use UQPSK signalling. However, the intrinsic tracking capability of the Costas Loop for UQPSK should be verified before its implementation in DSN stations.

The breadboard Costas Loop (Refs. 1, 3, and 4) was used in conjunction with the Block III receiver in the Telecommunication Development Laboratory (TDL). An S-band UQPSK modulator has been built and used in the tests.

II. Test Configurations

Figure 1 shows the configuration used to test the tracking performance of the Costas Loop with a UQPSK signal. This test setup is exactly the same as that used for the BPSK tracking performance test (Ref. 3) except that the input signal is here supplied by the UQPSK modulator. The TDL telemetry simulator provided the high-rate, in-phase channel data stream (PN signal), and the HP8006 word generator was used to supply Q-channel data.

The rms phase jitter measurements were obtained in exactly the same manner as those described in Ref. 3. The Doppler

extractor receives the exciter output signal (reference signal) and the VCO output signal and provides basically the phase error signal.

The analog phase error signal is converted to a digital form through the control of an Altair 8800 microcomputer. The digitized phase error is processed by a Modcomp II minicomputer, and a printer interfaced with the Modcomp II provides the rms phase jitter measurements.

Figure 2 shows a more detailed Costas Loop interface with the TDL Block III receiver.

Figure 3 is the block diagram of the S-band UQPSK modulator. The reference S-band signal is fed to a 90-deg hybrid through an isolator, which in turn generates I and Q channel carriers. On the other hand, the interface unit provides balanced data (logic '1' and '0' have the same magnitude of voltage level) from either transistor-transistor logic or a balanced-type data generator. The attenuators in I and Q channels can select the I and Q channel power ratio. The selected levels of the I and Q channel data are mixed with the respective carriers. Those two modulated carriers are summed to produce a UQPSK signal. Of course, a balanced QPSK signal can also be generated with the modulator. However, it is not used for a balanced QPSK signalling since the present Costas Loop cannot track a balanced QPSK signal. The modulator was aligned using a network analyzer. All four possible vectors observed in the network analyzer were calibrated within 1.5 deg in-phase and 0.1 dB in amplitude from an ideal modulator condition. The measured carrier suppression was larger than 35 dB.

III. Tracking Performance of UQPSK Signal

The tests performed are intended to verify the tracking performance of the breadboard Costas Loop for various conditions.

The rms phase jitter is expected to be a function of total signal power-to-noise density, the I-to-Q channel data rate ratio, and the I-to-Q channel power ratio (Refs. 6 and 7). Since the breadboard Costas Loop was designed to have appropriate arm filters and loop filters for 100-, 250-, 500-kbps and 1-Mbps data rates, the rms phase jitters for the above I channel data rates are supposed to be the same if other parameters are the same.

Tests were performed for 1-Mbps and 100-kbps I channel data rates. Figures 4 and 5 summarize the test results for respective I channel data rates. Rms phase jitters were measured for various PT/N_0 (total power within the I channel data rate bandwidth-to-noise density ratio), parameter R (the I channel-to-Q channel data rate ratio), and parameter P_I/P_Q (the I-to-Q channel power ratio), where $P = P_I + P_Q$ and $T = I$ channel symbol width. The ranges of parameters are:

(1) $PT/N_0 = -4, -2, 0, 2, +4$ (dB)

(2) $R = 20, 5, 1$

(3) $P_I/P_Q = 6, 10$ (dB)

Throughout the tests, a PN signal was used for I channel data and a squarewave was used for Q channel. It is expected to have similar results if a PN signal is used for Q channel instead of a squarewave.

The tests results agree very well with the theoretical calculations shown in Figure 6. Also shown in Figure 6 is the theoretical phase jitter performance of the loop with BPSK signal. The phase jitter performance for the UQPSK signal does not degrade too much from that for the BPSK signal. For the 6-dB P_I/P_Q ratio, the degradation is less than 2 deg.

IV. Theoretical Predictions

The basic derivations for rms phase jitter of the Costas Loop with the UQPSK signal are documented in Refs. 6 and 7. However, for the sake of self-containment, the method of calculation is summarized here.

Basically, the rms phase jitter is given by (Ref. 7):

$$\sigma_\phi^2 = \frac{1}{\frac{PT}{N_0}\frac{1}{B_L T} S_L} \tag{1}$$

where

σ_ϕ = rms phase jitter

P = total carrier power

T = I channel data bit width

N_0 = Noise spectral density

B_L = single-sided loop bandwidth

S_L = squaring loss

The calculation of squaring loss is given in Ref. 7. The loop bandwidth is given by:

$$B_L = \frac{\omega_n}{2}\left(\zeta + \frac{1}{4\zeta}\right) \tag{2}$$

where B_L = single-sided loop bandwidth for an imperfect second-order loop with a transfer function of

$$F(s) = \frac{1 + \tau_2 s}{1 + \tau_1 s}$$

$$\omega_n = \sqrt{\frac{K}{\tau_1}} = \text{natural angular frequency}$$

$$\zeta = \frac{1 + K\tau_2}{2\omega_n \tau_2} = \text{loop damping factor}$$

$$K = \text{total loop gain}$$

If K_0 is the loop gain at the design point, the loop gain at an arbitrary SNR is given by:

$$K = K_0 \cdot \frac{\alpha}{\alpha_0} \cdot \frac{g\sqrt{P}}{(g\sqrt{P})_0} \tag{3}$$

where

α_0 is the signal suppression factor at design point

α is the signal suppression factor at a desired SNR

$(g\sqrt{P})_0$ is the total IF gain control voltage at design point

$(g\sqrt{P})$ is the total IF gain control voltage at a desired SNR

Using Eqs. (1), (2), and (3), rms phase jitters for various PT/N_0, R, and P_I/P_Q were calculated and plotted in Figure 6. The squaring loss was calculated from a low input SNR approximation shown in Ref. 7.

V. Conclusions

An S-band UQPSK modulator was built. Using the modulator, the carrier tracking performance of the MTDD breadboard Costas Loop was tested in the TDL for UQPSK signal. The experimental results were compared with the theoretical predictions.

Experimental and analytical results agree with each other very closely. Finally, it can be concluded that the presence of Q channel data – either a telemetry or a ranging signal – does not degrade the tracking performance to much compared to the BPSK case.

Acknowledgment

The author wishes to thank P. Stanton, J. Sumida, and J. Packard for their contributions to building the S-band UQPSK modulator.

References

1. Stevens, G., and Woo, K. T., "Design of a Costas Loop to Operate With the Block III Receiver and Its Predicted Performance," *The Deep Space Network Progress Report 42-51*. Jet Propulsion Laboratory, Pasadena, California, March-April 1979.

2. Lesh, J., "Tracking Loop and Modulation Format Considerations for High Rate Telemetry," *The Deep Space Network Progress Report 42-44*, Jet Propulsion Laboratory, Pasadena, California, January-February 1978.

3. Reasoner, R., et al., "Costas Loop Demodulation of Suppressed Carrier BPSK Signals in the DSN Environment – Experimental Results Obtained at TDL," *The Deep Space Network Progress Report 42-51*, Jet Propulsion Laboratory, Pasadena, California, March-April 1979.

4. Park, Y. H., "Data Pattern Sensitivity in Tracking Performance of an AC Coupled Costas Loop with Hard-Limited In-Phase Channel," *Proc., ITC.*, San Diego, California, 1979.

5. Simon, M. K., "Tracking Performance of Costas Loops with Hard-Limited In-Phase Channel," *IEEE Trans. on Communications*, Vol. COM-26, No. 4, April 1978.

6. Simon, M. K., Alem, W. K., *Tracking Performance of UQPSK Demodulator, Part III – Biphase Polarity-type Costas Loop with Passive Arm Filters*, Axiomatix Report R7803-1, Axiomatix, Los Angeles, California, March 1978.

7. Park, Y. H., "Analysis of Tracking Performance of the MTDD Costas Loop for UQPSK Signal," *The Deep Space Network Progress Report 42-64*. Jet Propulsion Laboratory, Pasadena, California, May-June 1981 (this volume).

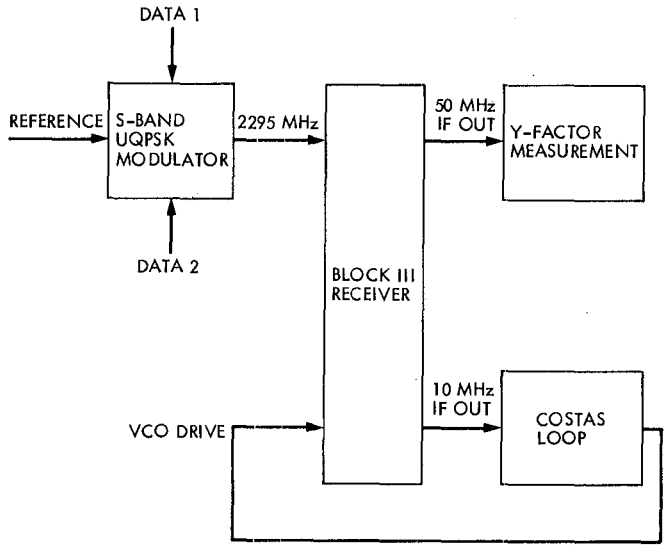

Fig. 1. Test setup in TDL

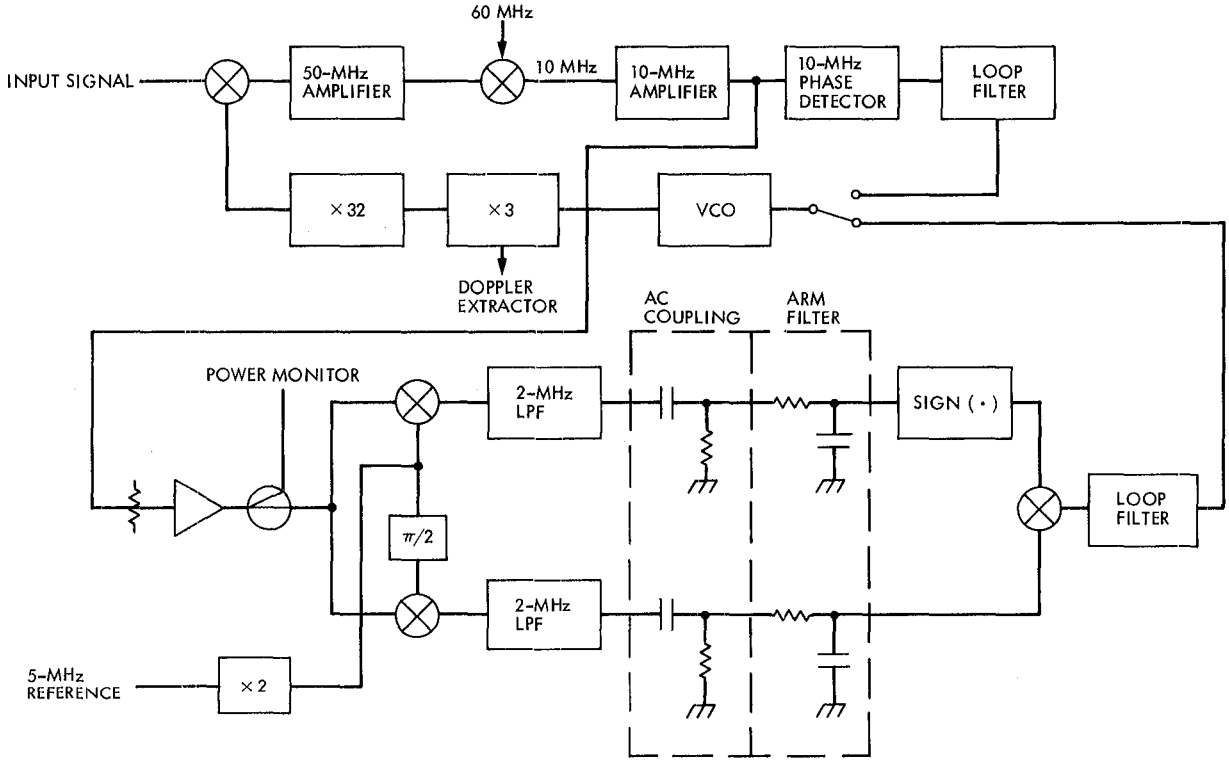

Fig. 2. Configuration of Costas Loop interface with TDL Block III receiver

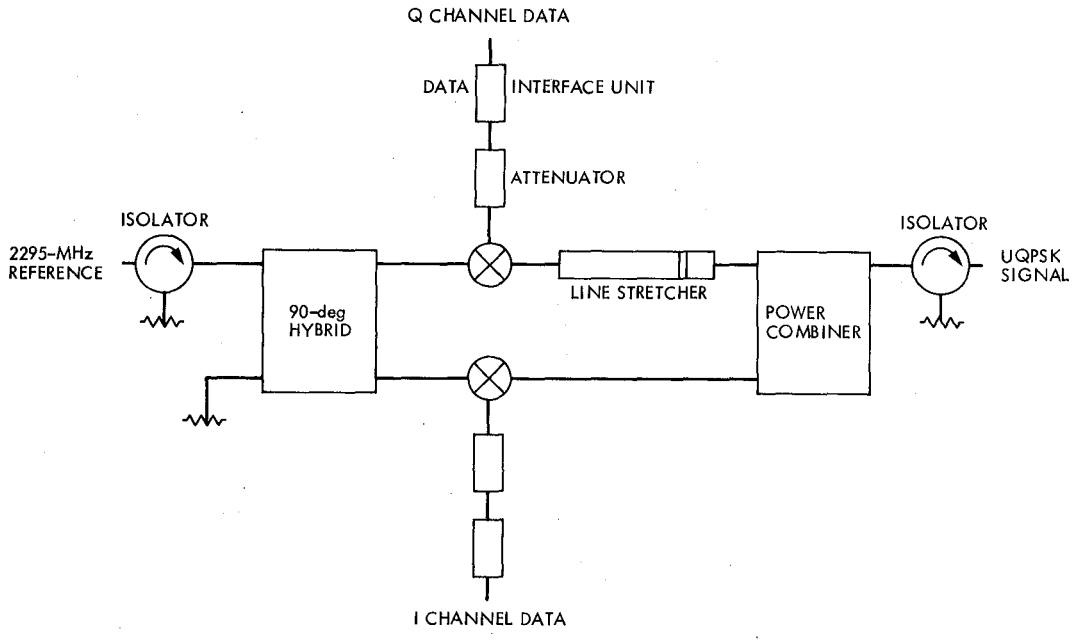

Fig. 3. UQPSK modulator diagram

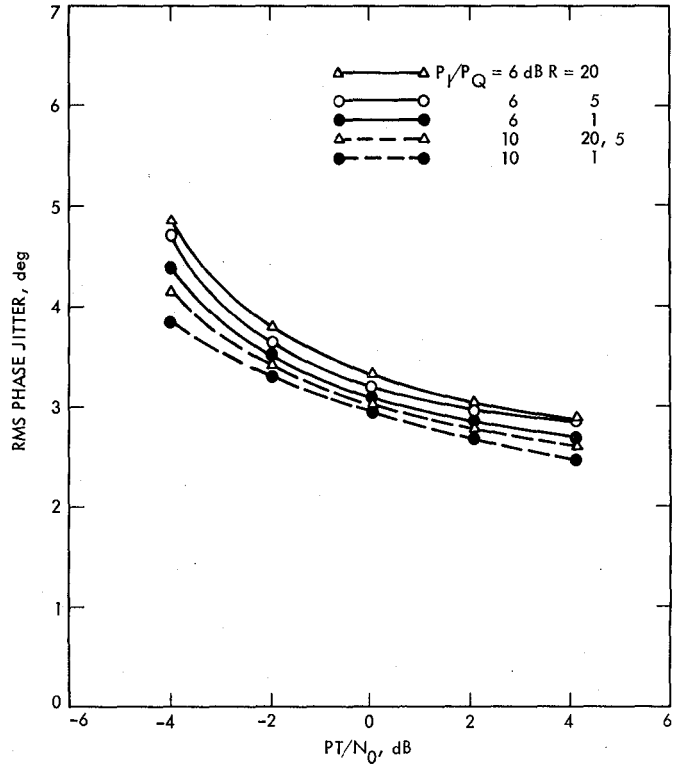

Fig. 4. Measured rms phase jitter for I channel data rate of 1 Mbps

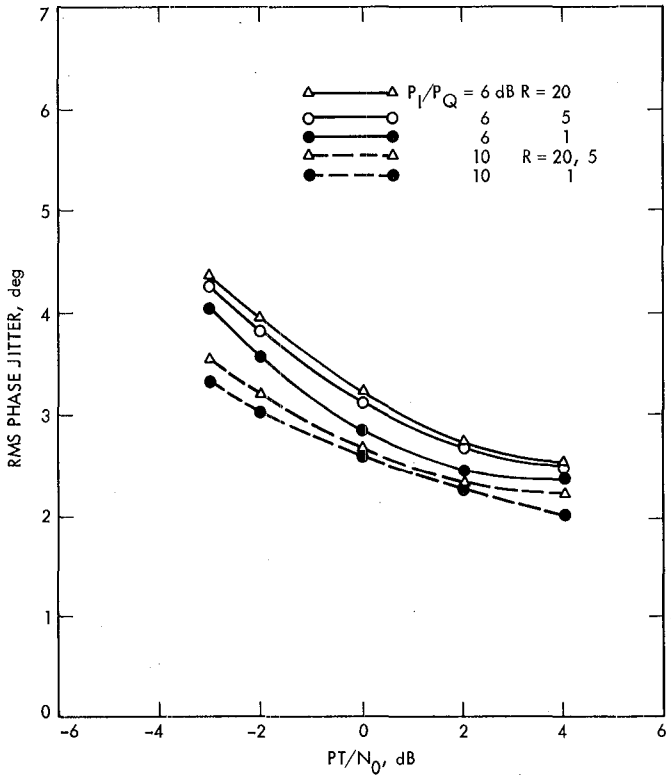

Fig. 5. Measured rms phase jitter for I channel data rate of 100 kbps

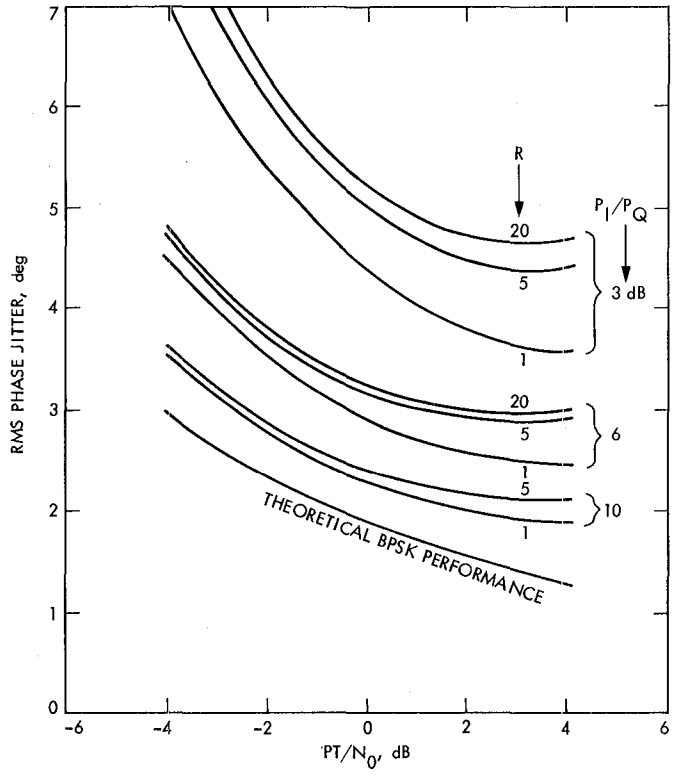

Fig. 6. Theoretical rms phase jitter calculated with low input SNR approximation for MTDD breadboard Costas Loop using UQPSK signals

Boresighting Techniques for the Antenna Control Assembly (ACA)

K. P. Abichandani
DSN Engineering Section

J. E. Ohlson
Stanford Telecommunications Inc.

Comparison of four scanning schemes including CONSCAN indicates that CONSCAN with signal cleanup and protection processes has the greatest merit in terms of accuracy, dependability and automatic unattended operation. Specific problem areas, error sources, and corrective measures are discussed.

I. Introduction

CONSCAN has been used in the DSN since early work showed its usefulness (Refs. 1 and 2). There have been many problems attributed to CONSCAN. Some of these are due to the present operational CONSCAN scheme being a very austere program, some are due to unrealistic expectations from any automatic scheme, and some are due to operator misunderstandings or errors. Several other automatic boresighting schemes exist, and interest is high in replacing CONSCAN with one or more of these new schemes such as STEPSCAN or TRISCAN. Further requirements of unattended operation and of K-band commitments make this a timely investigation.

II. Goals

The purpose of the study was to provide a recommendation for automatic acquisition and boresighting, by 64- and 34-meter antennas, of spacecraft and extragalactic radio sources within specified error limits. The gain loss limits considered for pointing were 0.05 dB and 0.1 dB from peak signal for 64-meter and 34-meter antennas respectively. The study was also required to assess the problems with respect to CONSCAN, such as the effects of signal level variation, signal dropouts, and automatic gain control (AGC) changes. Tradeoffs were to be made to evaluate comparative merits of different acquisition schemes such as raster, spiral or stepped scan.

III. Types of Problems

There are several types of problems which can affect the performance of an automatic boresighting system. Prime among these is the sensitivity of the boresighting system to anomalous or unexpected variations in the signal level. Common problems of this type include temporary loss of signal, signal level change due to spacecraft transmit mode change, and periodic cycling of spacecraft. Other significant problems are the sensitivity of performance to shape of the

antenna beam, the computation requirements for the algorithms employed, and the effect of angle encoder quantization errors. All of these were considered in this study.

Certain types of problems were not to be considered in this study since they were not expected to affect tradeoffs between the candidate boresighting schemes. The problems not considered included consideration of refraction models, gravity droop, temperature effects and the manner of generating and updating a correction matrix for improving pointing predictions. Fully electronic boresighting schemes were not to be considered, nor were schemes such as monopulse which would require antenna feed modification.

IV. Comparison of Candidate Boresighting Schemes

Table 1 presents a comparison of the candidate boresighting schemes on the basis of several different points. The four schemes compared are described briefly in the Appendix. The points of comparison are grouped by importance with respect to accuracy and dependability during unattended operation. Each of the criteria for comparison will now be described.

(1) *Overall accuracy.* This criterion includes consideration of accuracy under ideal conditions and also when signal anomalies occur. Under ideal conditions, all four of the schemes are nearly equivalent. CONSCAN is slightly better in this case because the other three schemes require settling time during the scan.

(2) *Insensitivity to signal anomalies.* It is highly desirable that an unattended boresighting system be insensitive to changes of signal level or dropouts such as mentioned in Section III. It is assumed that all four schemes will be implemented with algorithms to test the data for these problems. CONSCAN is much better suited for these tests since the signal power will nominally be constant throughout the CONSCAN cycle. The other three schemes spend much of the time in a transient mode and do not readily permit detection of signal level changes.

(3) *Efficiency.* CONSCAN is using all of the data all of the time. The other schemes have the requirement for settling times during the scans. Hence, CONSCAN more efficiently uses the available data and has a somewhat better accuracy under ideal conditions.

(4) *Insensitivity to beam shape.* All four of the schemes have a degree of sensitivity to the asymmetry of the antenna beam shape. TRISCAN has the most sensitivity since it samples the beam in only three places; STEPSCAN is next, and CONSCAN has the least sensitivity since it averages around the entire scan. SINGLE-AXIS SCAN is in between because it averages, but only in one dimension.

(5) *Computation for scan.* CONSCAN has the largest computation requirement for the scan control because of the large number of distinct pointing commands which must be generated. SINGLE-AXIS SCAN is less complex because of only one axis motion. STEPSCAN and TRISCAN are simplest because of few points to command during a scan.

(6) *Computation for correction.* CONSCAN has the largest computation requirement for the correction calculation due to the crosscorrelation calculations needed for the two coordinates. SINGLE-AXIS SCAN has less correlation requirement and STEPSCAN and TRISCAN are the simplest.

In several respects all four schemes have comparable quality, specifically:

(1) Each scheme can be run for a while to update pointing and then have the scan turned off and "coast" for a substantial period. The advantage of this feature is that there would be no possibility of the antenna accidentally moving off the source due to some totally unexpected anomaly.

(2) Each scheme can be run with an error correction matrix to utilize empirically determined corrections for improvement of pointing predictions.

(3) Each scheme is about equally sensitive to the quantization error in the digital shaft angle encoders. In all cases the scanning is superimposed upon the nominal predicted position of the radio source or spacecraft which is moving with respect to the Earth. Hence, all schemes are vulnerable to this type of pointing error. It has been claimed that TRISCAN is "exact" because it can use an integral number of encoder steps, while CONSCAN cannot (Ref. 3). This is not true because even with TRISCAN the antenna is constantly drifting through encoder quantization steps. In all cases, however, a significant averaging effect occurs due to the slow response time for the antenna. This then results in an antenna position versus time which is quite smooth and relatively unaffected by encoder quantization. A common question about CONSCAN is what effect there is due to the circular scan being an irregular polygon due to discretization in both time and angle. The argument above indicates that the response time of the antenna system causes an averaging effect which results in a very circular scan even though the commands are irregularly spaced around the scan.

V. Signal Cleanup and Protection During Track

No matter what scheme is to be employed, it is mandatory that a substantial effort be applied to provide cleanup of the raw input data (automatic gain control or radiometer output). This is not done effectively with the current CONSCAN system, and it is probably the main reason that CONSCAN has received some bad publicity in the past. At the end of a study, several suggestions were made for the formal implementation of CONSCAN in the DSN. Very few of these suggestions were implemented due to a lack of memory in the APS computer. As a result, CONSCAN was able to do some bizarre things on occasion, which would not have happened had the recommended data quality tests and limit tests been implemented.

VI. Proposed Signal Cleanup and Protection During Track

The signal inputs are, (1) Automatic Gain Control (AGC) voltage for spacecraft tracking and (2) square law detector output for radio sources. The anomalies that are likely to occur that will affect the received signal power level may be listed as follows:

(1) Change in spacecraft transmitter or antenna mode.

(2) Signal dropout due to momentary receiver lockout, operator error, or some unexpected transient (glitch) in the receiving system.

(3) Spacecraft antenna pointing direction change with spacecraft limit cycling, thermal variation in radio source, or some other change on board the spacecraft causing variation in the downlink signal strength.

(4) In the case of spin-stabilized spacecraft, modulation in the signal level due to the spin rate.

The procedure for testing for the above anomalies may be according to an algorithm encompassing the following steps.

(1) Expected signal level should be provided to the antenna control assembly (ACA) so that a signal level test can be performed to verify that boresight is close to the spacecraft.

(2) For radio sources, the system temperature and expected radio source temperature should be provided so a check can again be run. This will entail a precise setup for the radiometer gain to ensure accurate comparisons. A table of temperatures for common radio stars could easily be put into system memory.

(3) The signal level at the beginning and end of scan should be tested for near equality.

(4) If slow cycling is a problem, a multiple scan least squares curve fit should be implemented to subtract off the ramping from the signal level.

(5) Once ramping is removed, the sine and cosine correlations can be performed to find the sine wave component. This can then be subtracted to give residuals whose rms value can then be calculated and tested against an anomaly limit.

(6) In lock test: Receiver signal level (binary) monitoring during CONSCAN operation will effectuate correction whenever in-lock status is indicated.

Calculation for correction is carried out by correlating sine and cosine components (Ref. 1). The corrections thus obtained should be tested against previously specified limits. The limits may be broadly categorized as "First Limit," and "Second Limit." If the calculated correction exceeds the first limit, but is less than or equal to the second limit, the correction will be effected at the first limit value. If the succeeding calculated correction *also* exceeds the first limit, no correction will be made and a warning must go to the responsible operator. Of course if any calculated correction exceeds the second limit, no correction will be made, and the responsible operator will be warned.

The corrected pointing of the antenna must be continuously compared to the predicted pointing. The difference will be due to the accumulation of residuals. This total offset must be compared to two other (previously specified, a priori) limits. The error is permitted to exceed the first limit; the operator must be kept informed. CONSCAN operation is not affected thus far. However, as soon as the second limit is reached, manual intervention by the operator becomes imperative; the operator will receive an urgent warning that CONSCAN is trying to correct an out-of-limit condition. To avoid false alarms during acquisition or encounter, this limit may be made larger or overridden altogether with the approval of a next higher ranked operator.

VII. Needed CONSCAN Improvements

In response to criticism due to problems encountered in the current operation of CONSCAN, improvements in automatic gain control (AGC) calculations, acquisition mode, and tracking mode must be effected to enhance accuracy and dependability.

(1) For spacecraft tracking, the AGC voltage automatically is scaled so the open loop gain remains fixed for CONSCAN. Hence, the response time stays fixed, independent of signal level.

(2) For radio source tracking, there is no AGC. Therefore, the receiver noise temperature and radio source temperature must be used as inputs to allow the CONSCAN algorithm to calculate the gain needed within the algorithm to provide a desired response time.

(3) In acquisition/tracking modes a continuous CONSCAN mode of operation is recommended. An optional mode of periodic update (by CONSCAN), say for 5 minutes every 30 to 60 minutes, should be available when (continuous) CONSCAN is not being executed. Provision should be made such that an operator can be flagged by the program when the signal level is dropping so that he may initiate a predetermined period of CONSCAN update.

The AGC and radiometer data testing for anomalies, and algorithm for implementing corrections to the pointing offset, should follow the procedure outlined in Section VI.

VIII. Conclusions

The primary conclusion of the study is that CONSCAN is the best overall scheme to implement for the Antenna Control Assembly. Under unattended automatic operation, CONSCAN has the major advantage of being able to readily detect anomalous conditions and then to reject bad data. It is necessary that the new CONSCAN implementation includes many features not presently employed. These features concern various signal cleanup and limit tests to preclude wild behavior under unusual circumstances. Substantial work on details of these features is underway and will be reported subsequently.

References

1. Ohlson, J. E., and Reid, M. S., "Conical-Scan Tracking With the 64-m-diameter Antenna at Goldstone," Technical Report 32-1605, Jet Propulsion Laboratory, Pasadena, Calif., October 1, 1976.

2. Gosline, R. M., "CONSCAN Implementation at DSS 13," Technical Report 32-1526, pp. 87-90, Jet Propulsion Laboratory, Pasadena, Calif., April 15, 1973.

3. Bunce, R. C., "TRISCAN: A Method of Precision Antenna Positioning," *TDA Progress Report 42-59, July and August 1980*, Jet Propulsion Laboratory, Pasadena, Calif., Oct. 15, 1980.

Table 1. Comparison of candidate boresight schemes[a]

	CONSCAN	STEPSCAN	TRISCAN	SINGLE-AXIS SCAN
High importance				
a. Overall accurracy	5	4	4	4
b. Insensitivity to signal anomalies	5	4	4	2
Moderate importance				
c. Efficiency	5	4	4	4
d. Insensitivity to beam shape	5	4	4	4
Low importance				
e. Computation for scan	Much	Little	Little	Medium
f. Computation for correction	Much	Little	Little	Medium

[a]Scale of 0 to 5, with 5 best.

Appendix A

Candidate Boresighting Schemes

I. STEPSCAN

STEPSCAN is an automatic boresighting scheme which measures signal power at a small angle off boresight along one axis (two points) or along two orthogonal axes (four points). Comparison of the signal powers measured then provides a measurement of the boresight error in one or both axes.

II. TRISCAN

TRISCAN is very similar to STEPSCAN except that only three points are used and measurements of errors in both axes are provided.

III. CONSCAN

CONSCAN obtains angle error measurements by continuously scanning the antenna beam at a constant angle offset (squint) from the boresight axis, resulting in a circular scan pattern. Angle error information is obtained by correlating the received signal power level with two quadrature sinusoids which are synchronous with the scanning in order to provide elevation and azimuth corrections.

IV. SINGLE-AXIS SCAN

SINGLE-AXIS SCAN is a boresighting scheme wherein the antenna scans once along one axis at constant rate through the anticipated boresight position. By fitting the measured signal power to a nominal beam shape, the peak gain angle can be determined for that axis. Repeating this procedure for the other axis then permits a boresight to be obtained.

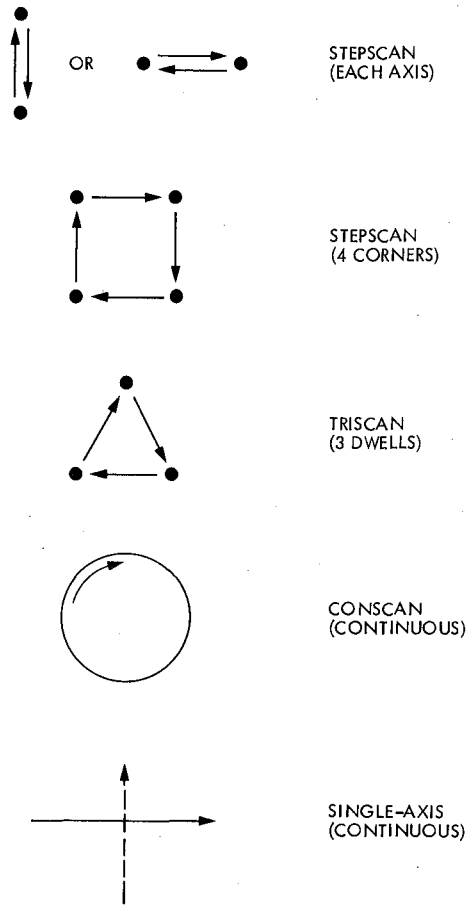

Fig. A-1. Candidate boresighting schemes

DSS 14 64-Meter Antenna – Computed RF Pathlength Changes Under Gravity Loadings

M. S. Katow
DSN Engineering Section

Using a computer model of the reflector structure and its supporting assembly of the 64-m antenna rotating about the elevation axis, the radio frequency (RF) pathlengths changes resulting from gravity loadings were computed. A check on the computed values was made by comparing the computed foci offsets with actual field readings of the Z or axial focussing required for elevation angle changes.

I. Introduction

The Cassegrainian geometry of the radio frequency (RF) reflectives surfaces of the 64-m antenna is set or rigged to the design values at 45 degrees elevation angle. A change in the elevation angle then results in a gravity loading increment. This gravity loading deflects the parabolic reflector and the subreflector position and results in a change of the RF path distance from the target or RF source to the RF feed's phase center on the antenna.

Only the pathlength changes resulting from gravity loading are considered in this article. The very long baseline interferometry (VLBI) target locating system may be affected by the RF path changes under all environmental loading conditions on the antenna. Reporting on wind loading effects on path changes will follow.

The distortion analyses were made using the NASTRAN structural computing program. The analytical model consisted of a half-symmetrical model using all of the stressed bars and plates of the reflector structure attached to its elevation wheel truss structure. All bars of the quadripod truss supporting the subreflector were also in the model.

II. Analysis Description

The RF optics system is illustrated in Fig. 1, where the equivalent zero gravity loading condition is at the rigging angle. At this elevation angle, the surface panels of the main reflector are set to the design paraboloid and the hyperboloid is aligned on the paraboloid's axis. When the elevation angle is changed from the rigging angle, the gravity loading resulting from the rotation of the gravity vector with respect to the symmetric axes of the antenna distorts the reflector structure. Its RF performance is then defined by best fitting a paraboloid to the displaced surface panel's supporting joints. The computed best fit paraboloid (Ref. 1) data are shown in Table 1 as changes from the rigging angle. Figure 2 illustrates the data along with the central ray starting from the virtual focus of the hyperboloid system and reflected from the vertex of the best fit paraboloid.

The manufactured and gravity distortions of the surface panels as well as the small gravity distortions of the hyperboloid's surface were considered to have negligible effect on RF path changes. The deflection of the hyperboloid's axis results in offsets at the primary focus from the RF feed and at the virtual secondary focus from the focus of the best fit paraboloid. These offsets will result in path length changes.

Figure 3 illustrates the central RF ray from the RF feed through the hyperboloid system and reflected from the vertex of the best fit paraboloid. The hyperboloid was simulated on the structural model by its vertex node 2093 and a node 2094 on axis. From the displacement output of these two nodes the positions of the hyperboloid's axis were calculated and noted in Table 2. The phase centers offsets were calculated and noted on Table 3 and illustrated in Fig. 3.

The RF pathlength changes were calculated by tracing the length changes of the central ray for two cases. For the first case (a), the hyperboloid was not controlled, which resulted in off Z focus operation of the paraboloid. In the second case (b), the hyperboloid was always moved in Z direction to the focussed position where the gain was maximized. For case (a), the pathlength changes are summarized in Table 4 and plotted in Fig. 4. For case (b), the pathlength changes are summarized in Table 5 and plotted in Fig. 4.

III. Field Check

A field check of the important computed numbers was available from the console indication of the hyperboloid's Z axis position as the Cassegrain system was maintained in focus through the elevation angle range. In Ref. 2, a record of the indicated control room position of the hyperboloid was kept for the focussed case with the antenna receiving at X- and K-band. The readout in the control room indicates only the Z extension or contraction of the jackscrews. Thus, corrections for the deflections of the jackscrews bolted on the apex of the quadripod were made. The hyperboloid's system corrections were also made. Table 6 illustrates the field data corrected to output the Z foci offsets and plotted in Fig. 5. Also plotted are the computed Z offsets.

IV. Conclusions

(1) Although the "no Z focus curve" of Fig. 4 shows much smaller pathlength changes, there will be gain losses due to foci offsets at X-band operation which may result in signal deterioration or loss. Also, the computed central ray pathlength changes may not accurately reflect the pathlength changes of the actual completely integrated RF wave front when the paraboloid is operated off focus. Table 7 shows the gain losses at X-band (8.45 GHz) for the computed foci offsets.

(2) The 64-m antennas are presently equipped with an electronic cam device which adjusts the hyperboloid's Z position with respect to the elevation angle. The curve is close to that given in Ref. 3 to maintain focus. The Y or lateral focussing is not available at present. However, when the pointing computer is upgraded, this function can be easily added.

(3) The match of the two curves on Fig. 5 should indicate the accuracy of the computed central pathlength changes.

(4) The pathlength changes are applicable only for the 64-m antenna at DSS 14. The overseas reflector structures are not alike until the "braces" described in Ref. 3 are attached.

(5) At the present time, there is available a second recording of the field focussed position (Ref. 5), which is different by about 0.25 cm at the extreme elevation angles from that of Ref. 2. These differences are not explainable at present, and may affect conclusion (3) above.

References

1. Katow, M. S., and Schmele, L. W., "Antenna Structures: Evaluation Techniques of Reflector Distortions," in *Supporting Research and Advanced Development, Space Programs Summary 37-40*, Vol. IV, pp. 176-184, Jet Propulsion Laboratory, Pasadena, Calif., Aug. 31, 1965.

2. Freiley, A. J., "Radio Frequency Performance of DSS 14 64-m Antenna at 3.56 and 1.96-cm Wavelength," Technical Report 32-1526, Vol. XIX, p. 110, Jet Propulsion Laboratory, Pasadena, Calif., Feb. 15, 1974.

3. Lobb, V. B., and Katow, M. S., "64-Meter-Diameter Antenna with New Braces: Installation Description and Computed Performance for Gravity Loads," Technical Report 32-1526, Vol. XVII, pp. 93-99, Jet Propulsion Laboratory, Pasadena, Calif., Oct. 15, 1973.

4. Katow, M. S., and Bartos, K. P., "Tricone Multiple Cassegrain Feed System for the 210-ft Antenna," in *Space Programs Summary 37-56*, Vol. II, pp. 121-124, Jet Propulsion Laboratory, Pasadena, Calif., Mar. 31, 1969.

5. Freiley, A. J., "Radio Frequency Performance of DSS 14 64-m Antenna at X-Band Using a Dual Hybrid Mode Feed," *DSN Progress Report 42-53, July and August 1979*, pp. 132-140, Jet Propulsion Laboratory, Pasadena, Calif.

Table 1. Best fit paraboloid data – gravity loading

Elevation angle, deg	Best-fit paraboloid data						
	Vertex		Focal length, m	Axis rotation, rad	Focus displacement		Best-fit rms mm
	Y-cm (d′)	Z-cm (d)	(e)	(f)	Y-cm (g)	Z-cm (h)	
10	5.089	0.191	27.09639	0.001132	2.023	−1.099	0.47
25	3.656	0.103	27.10246	0.000810	1.460	−0.580	0.26
35	2.059	0.048	27.10609	0.000455	0.827	−0.270	0.13
45	0	0	27.10927	0	0	0	0
55	−2.455	−0.041	27.11189	−0.000541	−0.987	0.221	0.12
65	−5.233	−0.074	27.11387	−0.001153	−2.106	0.384	0.24
80	−9.817	−0.104	27.11552	−0.002160	−4.214	0.514	0.39

$g = c - (f \times e)$
$h = d' + (e \times \cos f) - 27.10927$

Table 2. Hyperboloid axis displacements – gravity loading

Elevation angle, deg	RF feed phase center		Hyperbolid				Rotations	
			Vertex		Node 2094	Secondary focus change	Axis	Path
	Y-cm (m)	Z-cm (n)	Y-cm (i)	Z-cm (j)	Y-cm (ii)	Z-cm (v)	rad (p)	rad (o)
10	−0.667	0.221	−1.461	0.513	−1.420	0.081	0.000370	−0.000697
25	−0.472	0.183	−1.039	0.272	−1.008	0.043	0.000281	−0.000499
35	−0.263	0.057	−0.583	0.127	−0.564	0.020	0.000164	−0.000280
45	0	0	0	0	0	0	0	0
55	0.311	0.049	0.690	−0.105	0.667	−0.018	−0.000203	0.000333
65	0.659	0.089	1.466	−0.185	1.418	−0.031	−0.000436	0.000709
90	1.230	0.130	2.741	−0.252	2.648	−0.043	−0.000837	0.001328

$p = (ii - i) \times 111.35$
$o = (i - m)/(1137.993 + j - n)$

Table 3. Hyperboloid phase centers offsets – gravity loading

Elevation angle, deg	Ray incidence angle, rad	Y offsets				Z offsets	
		cm	cm	cm	cm	cm	cm
	(q)	(r)	(s)	(t)	(u)	(w)	(x)
10	0.001067	1.215	0.086	0.249	−1.126	0.592	−1.693
25	0.000780	0.888	0.066	0.182	−0.791	0.315	−0.895
35	0.000444	0.505	0.038	0.104	−0.441	0.147	−0.417
45	0	0	0	0	0	0	0
55	−0.000536	−0.610	−0.047	−0.125	0.518	−0.123	0.344
65	−0.001145	−1.303	−0.102	−0.268	1.096	−0.216	0.600
80	−0.002165	−2.463	−2.463	−0.506	2.039	−0.295	0.809

r = q × (a + j (Table 2) + n (Table 2))
s = p × (b + v (Table 2))
t = q × (b + v (Table 2))
u = i (Table 2) – (s + t)
w = j (Table 2) + v (Table 2)
x = h (Table 1) – w

Table 4. RF pathlength changes with no Z focussing

Elevation angle, deg	Hyperboloid vertex Z displacement	Primary RF feed Z displacement	Best-fit vertex offset	Pathlength change
	cm	cm	cm	cm
	(j)	(n)	(d)	(aa)
10	0.513	0.221	0.191	0.42
25	0.272	0.120	0.103	0.22
35	0.127	0.057	0.048	0.10
45	0	0	0	0
55	−0.105	−0.049	−0.041	−0.08
65	−0.185	−0.089	−0.074	−0.13
80	−0.252	−0.130	−0.104	−0.17

aa = (2 *j) – n – 2d

Table 5. RF pathlength changes with Z axial focussing

Elevation angle, deg	Displacement at focus Z	Primary RF feed displacement	Best-fit vertex offset	Pathlength change
	cm	cm	cm	cm
	(h)	(n)	(d)	(aa)
10	−1.099	0.221	0.191	−2.80
25	−0.580	0.120	0.103	−1.49
35	−0.270	0.057	0.048	−0.69
45	0	0	0	0
55	0.221	−0.049	−0.041	0.57
65	0.384	−0.089	−0.074	1.01
80	0.514	−0.130	−0.104	1.37

Table 6. Field data to foci offset data

Elevation angle, deg	Indicated control room position cm *	Adjust to 0 at 45° cm (A)	Jackscrews Z displacement				Sum A + B + C cm (D)	Hyperboloid virtual focus correction cm (E)	Z foci offset D + E cm
			Node 2182 cm	Node 2185 cm	Weighted average cm (B)	Bending displacement cm (C)			
10	−2.57	−2.11	0.041	0.493	0.460	0.081	−1.567	−0.079	−1.65
25	−1.52	−1.06	0.206	0.267	0.241	0.043	−0.782	−0.041	−0.82
35	−0.97	−0.51	0.091	0.127	0.112	0.020	−0.376	−0.020	−0.40
45	−0.46	0	0	0	0	0	0	0	0
55	−0.08	0.38	−0.066	−0.109	−0.091	−0.018	0.272	0.015	0.29
65	0.23	0.69	−0.102	−0.196	−0.158	−0.031	0.498	0.028	0.53
80	0.51	0.97	−0.102	−0.285	−0.211	−0.043	0.711	0.038	0.75

*May 1973 data (Ref. 2) for mechanism description (Ref. 4)

Table 7. Foci offsets gain loss – X band (8.45 GHz)

Elevation angle, deg	Foci offset		Gain loss	
	Y-cm (bb)	Z-cm (cc)	Y-dB, db	Z-dB, db
10	3.147	−1.694	0.13	0.79
25	2.250	−0.894	0.07	0.22
35	1.265	−0.416	0.02	0.05
45	0	0	0	0
55	−1.303	0.343	0.02	0.03
65	−3.205	0.599	0.13	0.09
80	−6.253	0.810	0.51	0.18

bb = g + u
cc = h + j + v

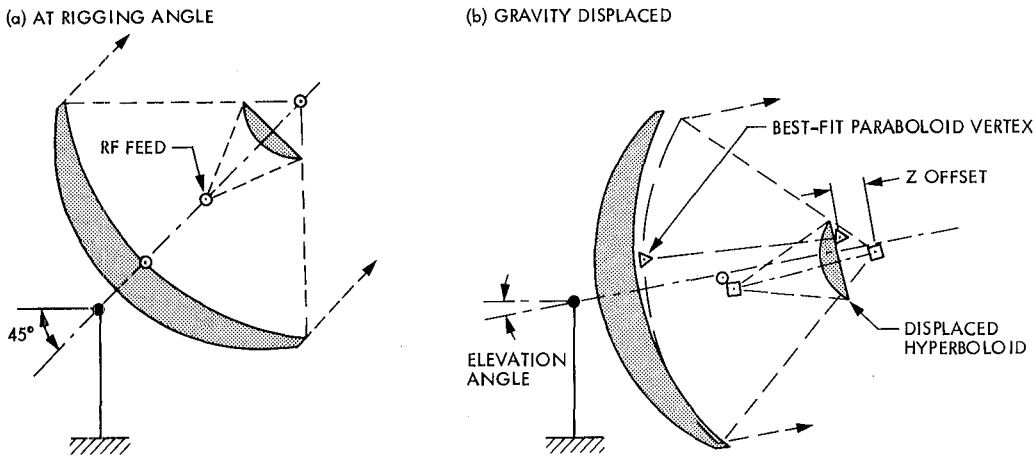

Fig. 1. 64-m antenna – RF optics

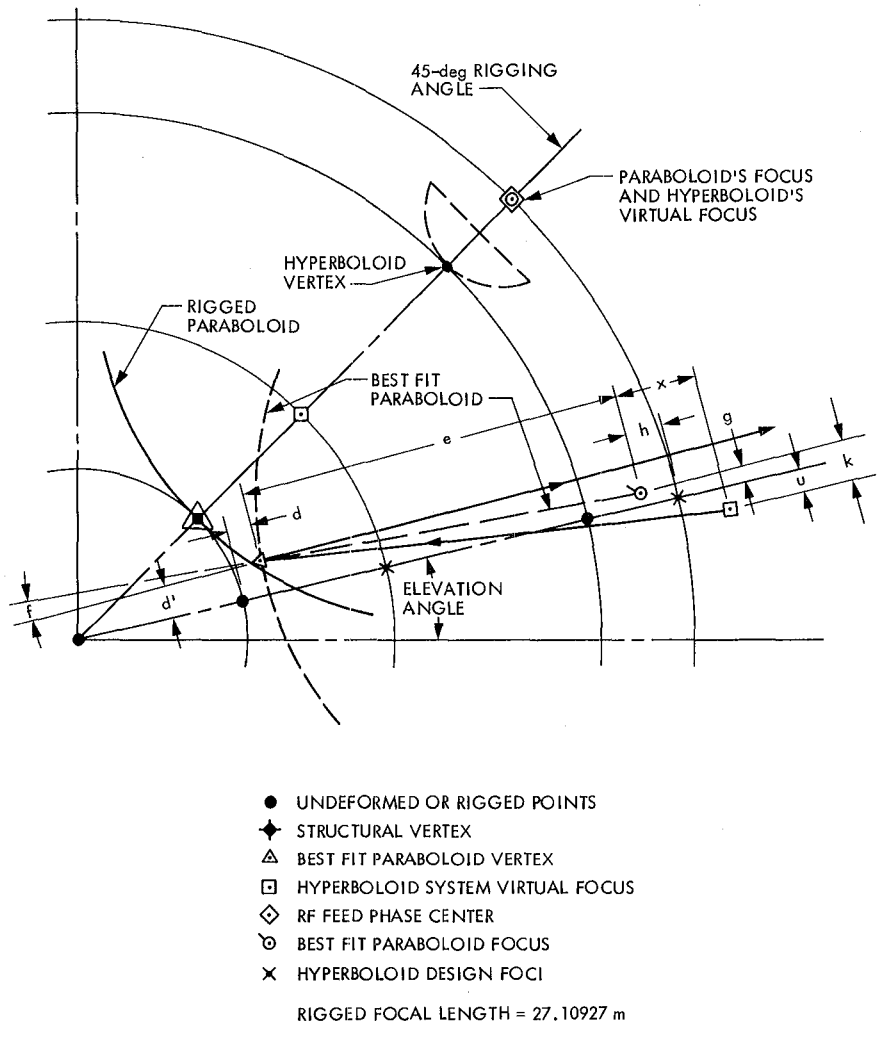

Fig. 2. Best fit paraboloid displacements – gravity loading

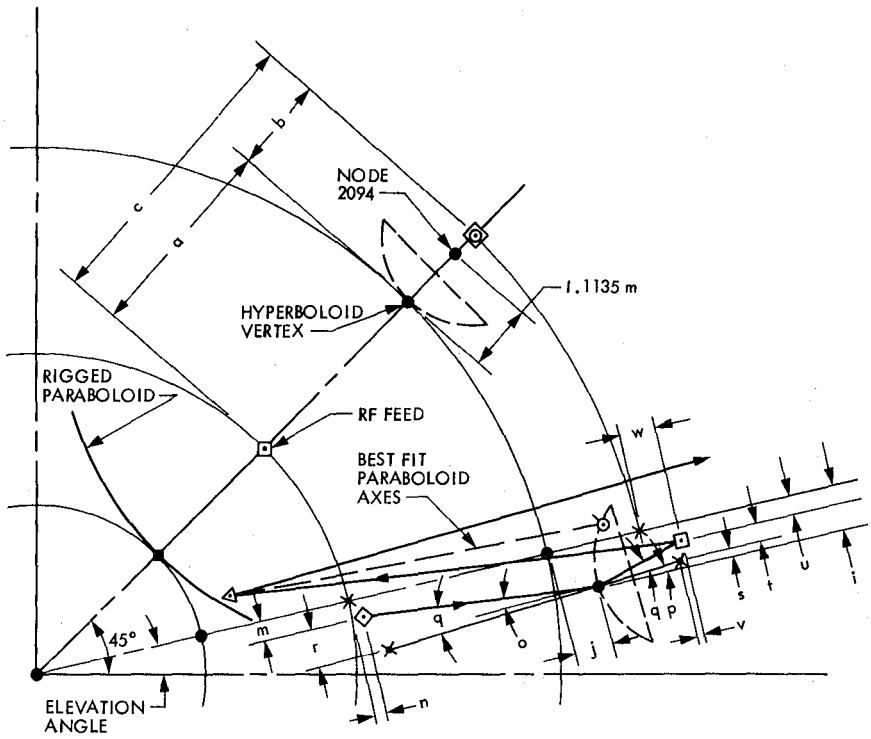

- UNDEFORMED OR RIGGED POINTS
- STRUCTURAL VERTEX
- BEST FIT PARABOLOID VERTEX
- HYPERBOLOID SYSTEM VIRTUAL FOCUS
- RF FEED PHASE CENTER
- BEST FIT PARABOLOID FOCUS
- HYPERBOLOID DESIGN FOCI

HYPERBOLOID DATA

a = 11.37993 m

b = 2.33607 m

c = 13.7160 m

Fig. 3. Hyperboloid system displacements – gravity loading

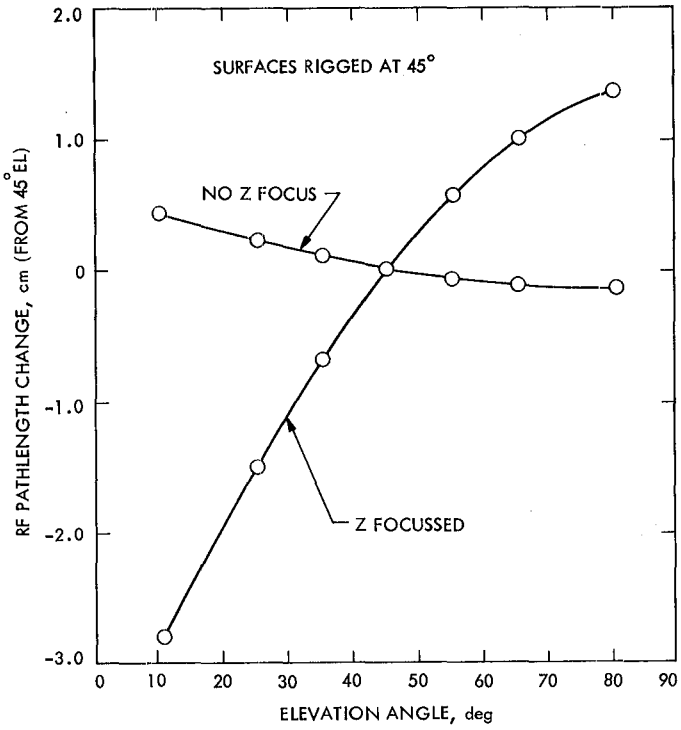

Fig. 4. RF pathlength changes vs elevation angle

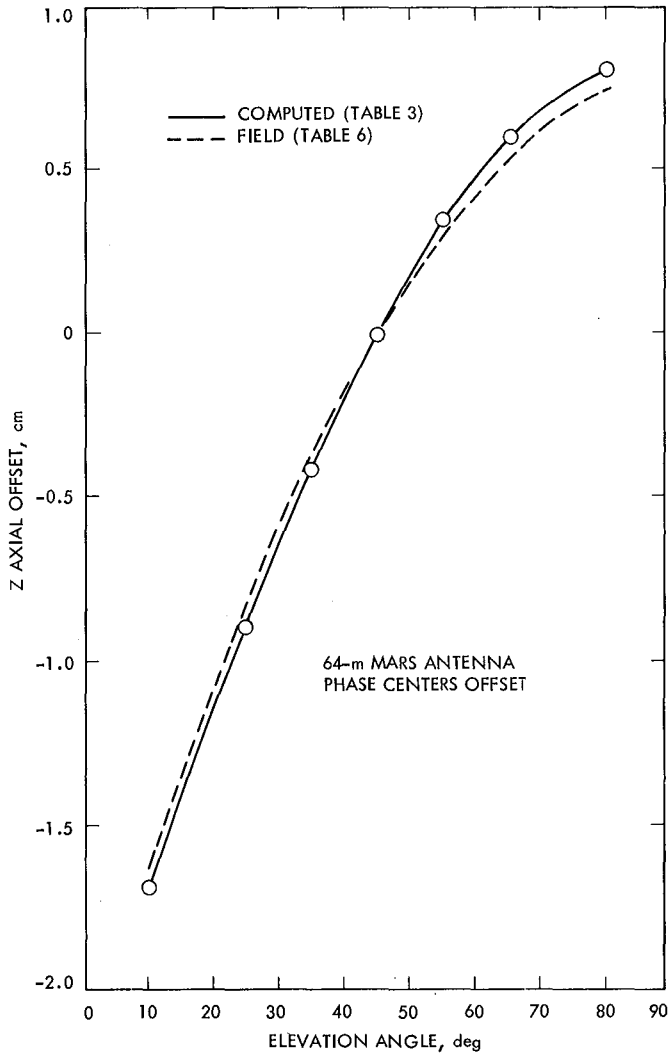

Fig. 5. 64-m phase centers offset – computed vs field

20.7- and 31.4-GHz Atmospheric Noise Temperature Measurements

S. D. Slobin, M. M. Franco, and C. T. Stelzried
Radio Frequency and Microwave Subsystems Section

The 20.7/31.4-GHz Water Vapor Radiometer (WVR) located on the JPL Mesa in Pasadena was used for atmospheric noise temperature measurements. Tipping curve data and on/off sun data taken on March 24, 1981 are compared. The analysis technique is described in detail. During the time of the data collection (7:00 a.m. to 12:20 p.m.), the sky was clear and the ground temperature and humidity varied from 14°C to 24°C and 65% to 51% respectively. The tipping curve data is felt to be the most accurate. The averaged results of this data for 13 measurements during this time period are:

	1 atmosphere	
Frequency, GHz	*Noise temperature contribution*	*Attenuation, dB*
20.7	*16.3 ± 1.7*	*0.26 ± 0.03*
31.4	*11.6 ± 1.2*	*0.18 ± 0.02*

The indicated errors are 1σ statistical and do not represent overall measurement accuracy. Although this data is consistent with data taken previously at the Goldstone DSS 13 station, it is not necessarily representative of long-term atmospheric noise temperature average.

I. Introduction

The 20.7/31.4-GHz Water Vapor Radiometer (WVR) located on the JPL Mesa in Pasadena was used for atmospheric noise temperature measurements. The data taken on March 24, 1981 is reported. The sky was clear, the ground relative humidity varied from 65% (7:00 a.m.) to 51% (12:20 p.m.) and the ground temperature varied from 14°C to 24°C over the same time period.

Periodically, the antenna was moved in zenith angle between zenith and 60° (30° elevation) for a direct atmospheric noise temperature measurement (tipping curve method). For each calibration, both radiometers were switched between the antenna, hot load and base (ambient load). In addition, the antenna was peaked on the sun and a difference measurement made between on-sun and off- (in azimuth) sun (on/off sun method).

II. Tipping Curve Method

Assuming a flat earth (Fig. 1) with a horizontally stratified nonchanging atmosphere, and a narrow-beam antenna radiometer system, the atmospheric loss factor L is given by

$$L = L_0^{\sec z} \tag{1}$$

or

$$L\,(\mathrm{dB}) = L_0\,(\mathrm{dB}) \sec z$$

where

z = zenith angle

L, L_0 = atmospheric loss at zenith angle z and vertical respectively, ratio $(L, L_0 \geqslant 1)$

The atmospheric loss factor is squared (doubled in dB) for the case of $z = 60°$ with reference to zenith. The noise temperature contribution of the atmosphere is given by

$$T'' = T_p \left(1 - \frac{1}{L}\right) \tag{2}$$

where

T_p = equivalent physical temperature of the atmosphere[1] (≅280 K), K

The increase in system noise temperature at z with reference to zenith is given by

$$\Delta T'' = T_p \left(1 - \frac{1}{L}\right) - T_p \left(1 - \frac{1}{L_0}\right) + \frac{T_c}{L} - \frac{T_c}{L_0}$$

$$= (T_p - T_c) \left(\frac{1}{L_0} - \frac{1}{L_0^{\sec z}}\right) \tag{3}$$

where

T_c = cosmic background noise temperature (≅2.7 K), K

The increase in system noise temperature at $z = 60°$ (looking through two atmospheres) with reference to zenith is given by

$$\Delta T_0'' = (T_p - T_c)\left(\frac{1}{L_0} - \frac{1}{L_0^2}\right)$$

$$= \frac{T_0''}{L_0} - T_c \left(1 - \frac{1}{L_0}\right)$$

$$\cong T_0'' \tag{4}$$

which indicates that for low loss ($L_0 \cong 1$) the increase in noise temperature is approximately equal to the noise temperature contribution at zenith (T_0''), for this type of tipping curve. Tables 1 and 2 [and 3 and 4][2] indicate the results of this type of measurement tabulated under $\Delta T_0''$. Using Eq. (4) gives

$$L_0 = \frac{1}{2x}\left(1 - \sqrt{1 - 4x}\right) \cong 1 + x + 2x^2 + 5x^3 + \ldots \tag{5}$$

where

$$x = \frac{\Delta T_0''}{(T_p - T_c)}$$

and

$$T_0'' = L_0\,\Delta T_0'' + T_c\,(L_0 - 1) \tag{6}$$

The measured values of $\Delta T_0''$ from Tables 1 and 2 [and 3 and 4] are used with Eqs. (5) and (6) to compute averaged L_0 and T_0'':

20.7 GHz

$L_0 \cong (0.26 \pm 0.03)$ dB [(0.26 ± 0.02) dB]

$T_0'' \cong (16.3 \pm 1.7)$ K [(16.1 ± 1.5) K]

31.4 GHz

$L_0 \cong (0.18 \pm 0.02)$ dB [(0.18 ± 0.02) dB]

$T_0'' \cong (11.6 \pm 1.2)$ K [(11.5 ± 1.1) K]

[1] Reference 1 indicates a technique for estimating T_p.

[2] The data were analyzed in two ways for comparison: (1) individual calibrations of the radiometer gain factor (kelvins/volt) and (2) a daily average radiometer gain factor (2nd method shown in brackets).

III. On/Off Sun Method

Again assuming a flat earth (Fig. 1) with a horizontally stratified nonchanging atmosphere

$$\Delta T'_{sun} = \Delta T_{sun} L_0^{-\sec z} \tag{7}$$

where

$\Delta T'_{sun}$, ΔT_{sun} = antenna temperature of the sun with and without atmospheric loss, K

$\Delta T'_{sun}$ is measured using the radiometer with an on/off sun technique. The antenna temperature of the sun is always less than the equivalent black body disk temperature of the sun for wide-beamwidth antennas.

Equation (7) becomes:

$$\log \Delta T'_{sun} = \log \Delta T_{sun} - \sec z \log L_0 \tag{8}$$

This is the equation of a straight line $y = A + Bx$, where

$$y = \log \Delta T'_{sun}$$

$$A = \log \Delta T_{sun}$$

$$B = -\log L_0$$

$$x = \sec z$$

so that with a log $\Delta T'_{sun}$ vs sec z plot, the y intercept A gives log ΔT_{sun} and the slope gives log L_0 (Ref. 2). Figures 2 and 3 [and Figs. 4 and 5] show this type of plot for the data from Tables 1 and 2 [and Tables 3 and 4]. The solid lines are obtained from a computer least squares fit (Ref. 3, using Eq. (4)), which also computes goodness of fit ($\sigma \Delta T_{sun}$ and σL_0, dB). The results are

20.7 GHz

ΔT_{sun} = (35.1 ± 0.7) K [(35.9 ± 0.5) K]

L_0 = (0.15 ± 0.05) dB [(0.19 ± 0.03) dB]

31.4 GHz

ΔT_{sun} = (29.7 ± 0.8) K [(29.9 ± 0.7) K]

L_0 = (0.086 ± 0.06) dB [(0.083 ± 0.05) dB]

For comparison, L_0 can be translated to an equivalent atmospheric noise temperature contribution using Eq. (2). The results are

20.7 GHz

$T''_0 \cong$ (9.5 ± 3) K [(12.0 ± 2) K]

31.4 GHz

$T''_0 \cong$ (5.5 ± 3) K [(5.3 ± 3) K]

IV. Conclusion

The errors indicated are all 1σ statistical and do *not* contain the bias errors to indicate overall accuracy. The differences in results between the two methods are slightly greater than the sum of the statistical errors in some cases. This is an indication of the bias error magnitude. It is felt that the tipping curves give the most accurate result. The primary advantage of the tipping curve is the relative ease and fast results. The on/off sun method requires more operator skill in peaking the antenna beam on the sun with subsequent error possibility. Further, the temperature and humidity are changing during the day so that the atmospheric uniformity assumed in the derivation is not strictly true both spatially and temporally.

Further refinement might include more days of data, different weather conditions, correction for antenna size, etc. Although the data presented is consistent with data taken previously on the Mesa and at the Goldstone DSS 13 station, it is not necessarily representative of long-term data average. The WVR output at DSS 13 has been connected to the data collection system (MASDAS), which simultaneously collects data from the X-band atmospheric noise temperature monitoring system.

References

1. Slobin, S. D., and Stelzried, C. T., "Calculation of Atmospheric Loss From Microwave Radiometer Noise Temperature Measurements," *Tracking and Data Acquisition Progress Report 42-62*, Jet Propulsion Laboratory, Pasadena, Calif., April 15, 1981.

2. Coates, R. J., "Measurements of Solar Radiation and Atmospheric Attenuation at 4.3-Millimeters Wavelength," *Proceedings of the IRE*, Volume 46, No. 1, pp. 122-126, January 1958.

3. Stelzried, C. T., and Rusch, W. V. T., "Improved Determination of Atmospheric Opacity from Radio Astronomy Measurements," *J. Geophys. Res.*, Vol. 72, No. 9, p. 2445, May 1, 1967.

Table 1. 20.7-GHz WVR data results (data taken on the JPL Mesa, Pasadena, on 3/24/81)

Local time	EL	z	$\Delta T''_0$	$\Delta T'_{sun}$	log $\Delta T'_{sun}$	sec z	Relative humidity, %
7:00 am	18.5	71.5	15.3	30.5	1.484	3.152	65
7:20	20.8	69.2	16.4	32.5	1.511	2.816	64
7:45	24.0	66.0	16.4	32.8	1.515	2.459	63
8:00	27.0	63.0	15.8	32.9	1.517	2.203	63
8:30	33.0	57.0	16.7	33.9	1.531	1.836	63
8:41	34.9	55.1	16.9	33.2	1.521	1.748	63
9:30	44.0	46.0	12.2	32.8	1.516	1.440	60
9:45	46.0	44.0	14.7	32.7	1.515	1.390	59
10:30	51.6	38.4	13.3	32.3	1.510	1.276	56
10:45	53.0	37.0	13.3	33.8	1.528	1.252	56
11:30	54.0	36.0	15.2	33.2	1.521	1.236	54
11:50	57.2	32.8	16.1	34.4	1.536	1.190	50
12:20 pm	56.9	33.1	15.1	34.6	1.539	1.194	51

Table 2. 31.4-GHz WVR data results (data taken on the JPL Mesa, Pasadena, on 3/24/81)

Local time	EL	z	$\Delta T''_0$	$\Delta T'_{sun}$	log $\Delta T'_{sun}$	sec z	Relative humidity, %
7:00 am	18.5	71.5	11.2	28.1	1.449	3.152	65
7:20	20.8	69.2	11.7	28.4	1.454	2.816	64
7:45	24.0	66.0	11.6	28.2	1.450	2.459	63
8:00	27.0	63.0	11.9	27.4	1.438	2.203	63
8:30	33.0	57.0	12.6	30.5	1.484	1.836	63
8:41	34.9	55.1	12.5	27.7	1.443	1.748	63
9:30	44.0	46.0	10.4	27.7	1.443	1.440	60
9:45	46.0	44.0	9.9	28.3	1.452	1.390	59
10:30	51.6	38.4	9.6	29.4	1.468	1.276	56
10:45	53.0	37.0	9.1	30.0	1.478	1.252	56
11:30	54.0	36.0	10.7	28.1	1.448	1.236	54
11:50	67.2	32.8	11.9	29.5	1.469	1.190	50
12:20 pm	56.9	33.1	10.3	29.7	1.472	1.194	51

Table 3. 20.7-GHz WVR data results using an average gain K/V = 42.9 (data taken on the JPL Mesa, Pasadena, on 3/24/81)

Local time	$\Delta T''_0$	$\Delta T'_{sun}$	log $\Delta T'_{sun}$	sec z
7:00 am	15.0	30.9	1.490	3.152
7:20	16.3	32.6	1.513	2.816
7:45	16.3	32.6	1.513	2.459
8:00	15.4	32.6	1.513	2.203
8:30	16.3	33.5	1.525	1.836
8:41	16.3	32.6	1.513	1.748
9:30	12.4	34.3	1.536	1.440
9:45	15.0	33.9	1.530	1.390
10:30	13.3	33.0	1.519	1.276
10:45	13.3	34.7	1.541	1.252
11:30	15.0	33.5	1.525	1.236
11:50	15.9	34.3	1.536	1.190
12:20 pm	15.0	34.7	1.541	1.194

Table 4. 31.4-GHz WVR data results using an average gain K/V = 53.1 (data taken on the JPL Mesa, Pasadena, on 3/24/81)

Local time	$\Delta T''_0$	$\Delta T'_{sun}$	log $\Delta T'_{sun}$	sec z
7:00 am	11.2	28.1	1.449	3.152
7:20	11.7	28.7	1.457	2.816
7:45	11.7	28.7	1.457	2.459
8:00	11.7	27.6	1.441	2.203
8:30	12.1	30.3	1.481	1.836
8:41	12.2	27.6	1.441	1.748
9:30	10.6	28.7	1.457	1.440
9:45	10.1	29.2	1.465	1.390
10:30	9.6	29.7	1.473	1.276
10:45	9.0	30.3	1.481	1.252
11:30	10.6	28.1	1.449	1.236
11:50	11.7	29.2	1.465	1.190
12:20 pm	10.1	29.2	1.465	1.194

Table 5. Summary of 20.7/31.4-GHz radiometric calibrations for 3/24/81

Frequency, GHz	Method			
	Tipping curve		On/off sun	
	T_0'' (kelvins)	L_0 (dB)	T_0'' (kelvins)	L_0 (dB)
20.7	16.3 ± 1.7 [16.1 ± 1.5]	0.26 ± 0.03 [0.26 ± 0.02]	9.5 ± 3 [12.0 ± 2]	0.15 ± 0.05 [0.19 ± 0.03]
31.4	11.6 ± 1.2 [11.5 ± 1.1]	0.18 ± 0.02 [0.18 ± 0.02]	5.5 ± 3 [5.3 ± 3]	0.086 ± 0.06 [0.083 ± 0.05]

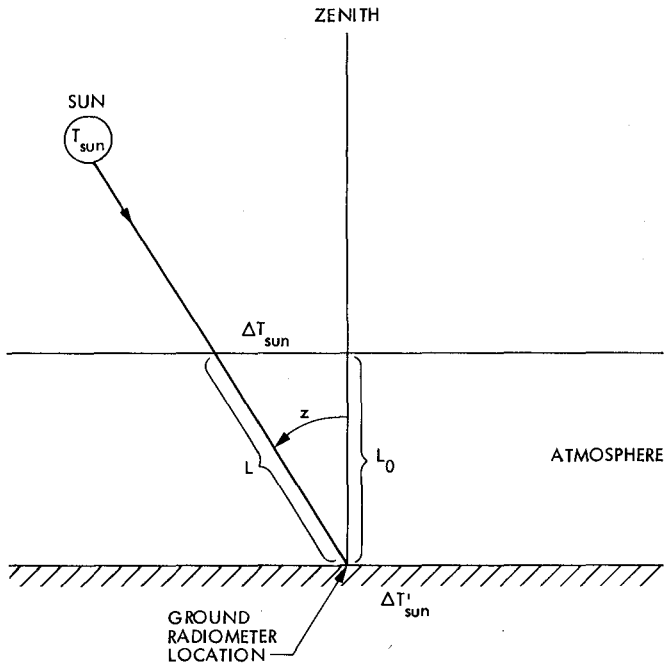

Fig. 1. Representation of radiometer configuration used in atmospheric loss calibrations

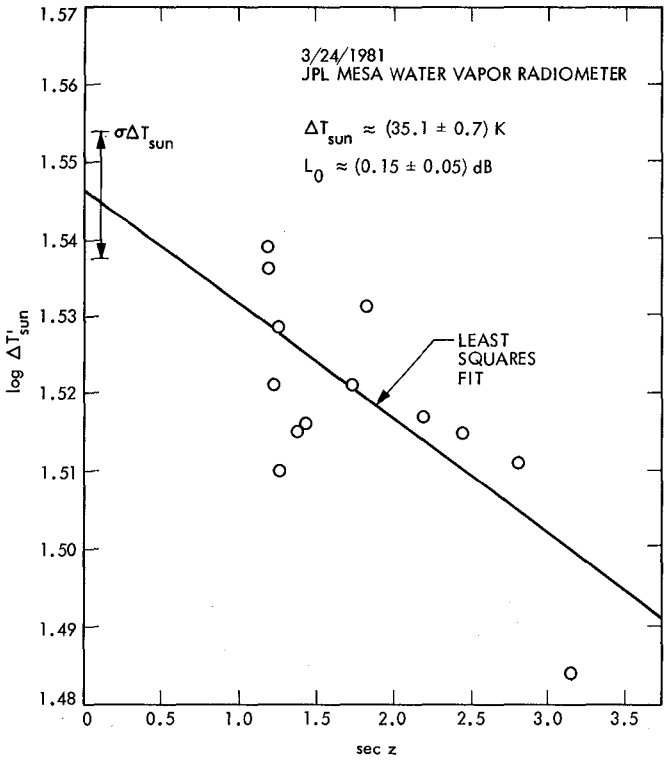

Fig. 2. Plot of log $\Delta T'_{sun}$ vs sec z @ 20.7 GHz using individual radiometer gain calibrations

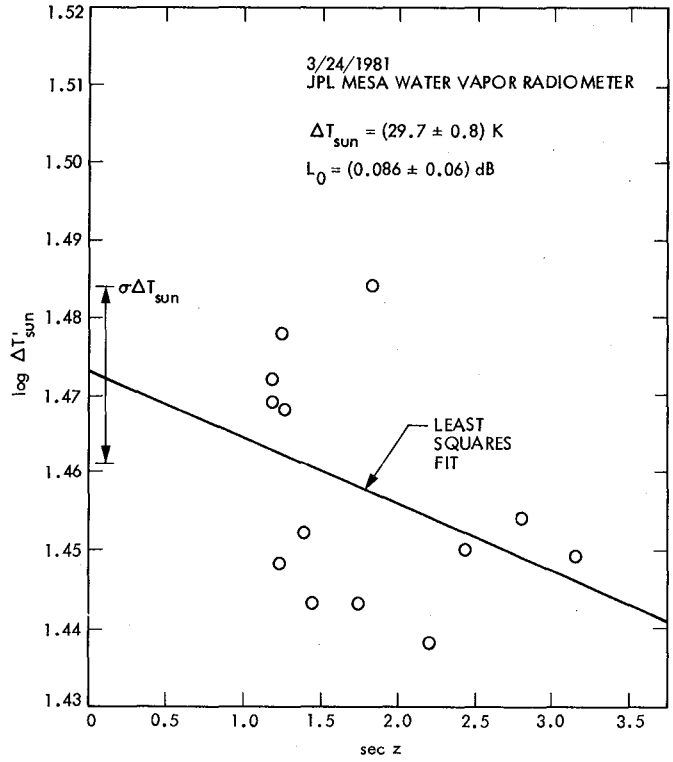

Fig. 3. Plot of log $\Delta T'_{sun}$ vs sec z @ 31.4 GHz using individual radiometer gain calibrations

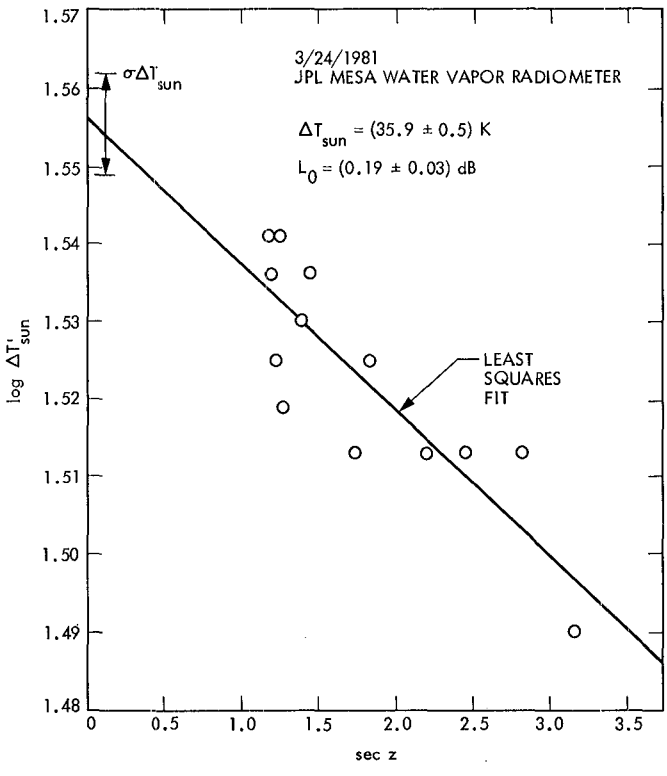

Fig. 4. Plot of log $\Delta T'_{sun}$ vs sec z @ 20.7 GHz using averaged radiometer gain calibrations

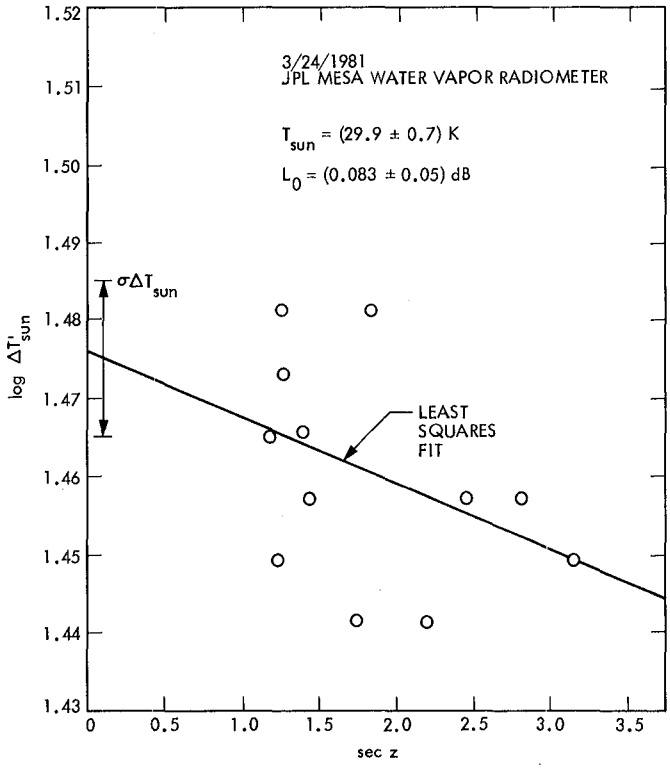

Fig. 5. Plot of log $\Delta T'_{sun}$ vs sec z @ 31.4 GHz using averaged radiometer gain calibrations

20.7- and 31.4-GHz Solar Disk Temperature Measurements

M. M. Franco, S. D. Slobin, and C. T. Stelzried
Radio Frequency and Microwave Subsystems Section

The 20.7/31.4 GHz Water Vapor Radiometer (WVR-R06) located at the JPL Mesa in Pasadena was used for atmospheric noise temperature measurements on March 24, 1981. The equivalent sun disk temperature measurements computed from the results of the previously reported sun antenna temperature measurements (Ref. 1) are:

Frequency, GHz	T_{sun}, K *(This report)*	T_{sun}, K *(Ref. 6)*
20.7	*10,530 ±210 (1σ)*	*11,430*
31.4	*9,170 ±250 (1 σ)*	*9,960*

Comparison of the results of this report with Ref. 6 at the same frequency indicates satisfactory radiometer performance. The results of the horn antenna HPBW (half power beamwidth) evaluation indicate that the design goal of approximately equal beamwidths at 20.7 and 31.7 GHz was achieved.

I. Introduction

The 20.7/31.4-GHz Water Vapor Radiometer (WVR-R06) located at the JPL Mesa in Pasadena was used for atmospheric noise temperature measurements on March 24, 1981 (Ref. 1). The on/off sun method used as an alternative method of atmospheric loss calibrations yielded estimates of the antenna sun temperature corrected for atmospheric loss. This report converts this data to equivalent solar disk temperatures. Comparison with other measurements can be used as an indication of radiometer performance. Measurements and analysis of the horn beamwidths are presented.

II. Analysis

The equivalent disk temperature of a source of small solid angle compared to that of the antenna is given by (Ref. 2, p. 100)

$$T_S = T_A \, \Omega_A / \Omega_S \qquad (1)$$

where

T_A = antenna temperature contribution due to source, K

Ω_A = antenna beam solid angle, rad^2

Ω_S = source solid angle, rad^2

The source solid angle is given by (sun radius $\cong 0.270°$ from the *Nautical Almanac* for 3/24/81)

$$\Omega_s = \Omega_{sun} \cong \pi r^2$$

$$= \pi(0.270)^2/(57.296)^2$$

$$= 6.9764 \times 10^{-5}, \text{rad}^2 \qquad (2)$$

The beam solid angle of the horn antenna is given by (Ref. 3)

$$\Omega_A = 4\pi/G_M \tag{3}$$

where

G_M = maximum antenna gain, power ratio

III. Results

G_M was computed for the 20.7- and 31.4-GHz WVR horns using P. Potter's computer program (Ref. 4)[1] as indicated on the last page of the computer printouts shown in Figs. 1 and 2. The previously reported (Ref. 1) sun noise temperature measurements made with the 20.7/31.4-GHz Water Vapor Radiometer (WVR-R06) located at the JPL Mesa in Pasadena were used in Eq. (1). The results are tabulated in Table 2. The reported errors are 1σ statistical and do not represent overall measurement accuracy. The equivalent solar disk temperature (solar brightness temperature) results compare favorably (Fig. 5 and Table 2) with Linsky (Ref. 6, Fig. 2, Eq. (3)), using his quadratic regression curve. This agreement indicates satisfactory radiometer performance. The HPBWs (half power beamwidths) of the antennas were evaluated by performing radio metric drift curves using the sun as a source[2] (experimental, Fig. 6) and by fitting a Gaussian curve to the computer-generated patterns (theoretical). The results are tabulated in Table 3. These indicate that the design goal for approximately equal HPBWs at 20.7 and 31.4 GHz was achieved. We have (Ref. 2, assuming $\theta_{HPBW} = \phi_{HPBW}$)

$$\Omega_A = \frac{k_p(\theta_{HPBW})^2}{\epsilon_M} = k(\theta_{HPBW})^2 \tag{4}$$

where k_p and ϵ_M are defined in Ref. 2, pp. 220 and 221.

Using Ω_A tabulated in Table 2 results in the values for k shown in brackets in Table 3. These results for k are consistent with values of 1.33 and 1.51 obtained with uniform and Gaussian illuminations of an antenna aperture (Refs. 2 and 3).

[1] For completeness, the computer program printouts for 20.7 and 31.4 GHz are shown in Figs. 1 and 2. Figures 3 and 4 show amplitude and phase plots of this data. Table 1 tabulates the dimensions of the WVR horns.

[2] This was performed at 20.7 and 31.4 GHz using the WVR-R04 located at the JPL DSS 13 Goldstone station. The measurements were made at meridian crossing so the antenna could be moved ahead of the sun by moving only the azimuth coordinate (since the AZ-EL antenna mount is manually controlled). The results were not corrected for finite source size.

Acknowledgments

R. Clauss suggested converting the previously measured solar antenna temperature results to an equivalent solar disk temperature. D. Bathker, V. Galindo, and B. Seidel provided useful suggestions. T. Otoshi generated Ref. 3, which was especially useful in this report. W. Williams supplied the antenna computer output. E. Woods, Jr. (Petersen Instruments, Inc.), N. Yamane, and G. Resch supplied the horn dimensions.

References

1. Slobin, S. D., Franco, M. M., and Stelzried, C. T., "20.7/31.4 GHz Atmospheric Noise Temperature Measurements," in *The Telecommunications and Data Acquisition Progress Report 42-64* (This issue).

2. Kraus, J. D., *Radio Astronomy,* McGraw-Hill, 1966.

3. Otoshi, T., "Relationship of Beam Solid Angle to Antenna Half Power Beamwidths," in *The Telecommunications and Data Acquisition Progress Report 42-64* (this issue).

4. Potter, P. D., "Efficient Antenna Systems: A New Computer Program for the Design and Analysis of High-Performance Conical Feedhorns," TR 32-1526, Jet Propulsion Laboratory, Pasadena, Calif., Vol. XIII, pp. 92-107, Feb. 15, 1973.

5. Janssen, M., Bednarczyk, S., Gulkis, S., Marlin, H., Smoot, G., "Pattern Measurement of a Low-Sidelobe Horn Antenna," *IEEE Transactions on Antenna and Propagation*, Vol. AP-27 No. 4, pp. 551-555, July 1979.

6. Linsky, J. L., "A Recalibration of the Quiet Sun Millimeter Spectrum Based on the Moon as an Absolute Radiometric Standard," *Solar Physics*, Vol. 28, pp. 419-424, 1973.

Table 1. Horn dimensions for the original 33.0-GHz design (Ref. 5), scaled to 21.0 GHz for use at 20.7 GHz; the original 33-GHz design is used at 31.4 GHz

	Dimensions	
Operating frequency, GHz	20.7	31.4
Design frequency, GHz	21.0	33.0
Length of phasing section, in.	0.000	0.000
Diameter at input, in.	0.588	0.380
Axial length of flare, in.	19.675	12.451
Aperture diameter, in.	7.417	4.720
Groove depth, in.	0.196	0.125
Flare half angle, deg	9.883	9.883

Table 2. Tabulation of 20.7/31.4-GHz WVR computed horn parameters and results of Mesa, Pasadena, sun measurements

Frequency GHz	Computed G_M, dB	Computed Ω_A, rad^2 (Eq. 3)	Measured $^*\Delta T_{sun}$, K (Ref. 1)	T_{sun}, K (This article)	T_{sun}, K (Ref. 6)
20.7	27.785	0.020927	35.1 ±0.7 (1σ)	10,530 ±210 (1σ)	11,430
31.4	27.658	0.021548	29.7 ±0.8 (1σ)	9170 ±250 (1σ)	9,960

*Same as T_A in Eq. (1)

Table 3. Tabulation of WVR horn beamwidth (HPBW) and *k* value (defined Eq. 4)

Frequency, GHz	WVR horn beamwidth (HPBW), deg	
	Experimental	Theoretical
20.7	6.875 ($k \cong 1.453$)	6.881 ($k \cong 1.451$)
31.4	6.775 ($k \cong 1.541$)	7.016 ($k \cong 1.437$)

HYBRID MODE HORN PROGRAM

7.417 INCH, APERTURE, 19.675 INCH LONG, 0.196 INCH GROOVES 9.883 DEG FLARE

ALL DIMENSIONS IN INCHES

CARD OUTPUT FOR FAR-FIELDS

LENGTH OF PHASING SECTION= .00000

DIAMETER OF PHASING SECTION= .58800

AXIAL LENGTH OF FLARE SECTION= 19.67500

APERTURE DIAMETER= 7.41700

GROOVE DEPTH= .19600

THE FAR-FIELD PHASE REFERENCE POINT IS .00000 INSIDE THE HORN APERTURE

FLARE SECTION HALF ANGLE= 9.84534 DEGREES

RADIUS FROM VERTEX TO APERTURE CAP= 21.68849

SPECIFIED FREQUENCY= 20.70000 GHZ.

NUMBER OF POINTS USED IN FLARE SECTION PHASE SHIFT INTEGRATION= 11

MODE PHASES AT BEGINNING OF PHASING SECTION
AND APERTURE LONGITUDINAL FIELD AMPLITUDES

	HE MODES		EH MODES	
MODE	VOLTS	DEG	VOLTS	DEG
1	1.00000	.00000	.00000	.00000

Fig. 1. 20.7-GHz horn computer printout

ANTENNA FEED EFFICIENCY

FREQ=,20.7GHZ, GROOVES=0.3438LAMBDA 0

7.417 INCH, APERTURE, 19.675 INCH LONG, 0.196 INCH GROOVES 9.883 DEG FLARE

THETA	ETA T (OVERALL)	ETA S (SPILL)	ETA I (ILLUM)	ETA X (X-POL)	ETA P (PHASE)	ETA B (BLOCK)	ETA M (M=1)
1.000	.04425	.04423	.99992	1.00069	1.00000	1.00000	1.00000
2.000	.16146	.16161	.99869	1.00038	1.00000	1.00000	1.00000
3.000	.31386	.31579	.99381	1.00009	1.00000	1.00000	1.00000
4.000	.46182	.47021	.98236	.99984	.99995	1.00000	1.00000
5.000	.58109	.60374	.96304	.99974	.99968	1.00000	1.00000
6.000	.66638	.71180	.93720	.99977	.99915	1.00000	1.00000
7.000	.72238	.79749	.90711	.99983	.99875	1.00000	1.00000
8.000	.75290	.86353	.87306	.99986	.99879	1.00000	1.00000
9.000	.75788	.91104	.83312	.99984	.99867	1.00000	1.00000
10.000	.73844	.94214	.78582	.99980	.99762	1.00000	1.00000
11.000	.70152	.96132	.73297	.99979	.99581	1.00000	1.00000
12.000	.65717	.97360	.67951	.99981	.99355	1.00000	1.00000
13.000	.61163	.98225	.62927	.99983	.98971	1.00000	1.00000
14.000	.56496	.98838	.58232	.99983	.98177	1.00000	1.00000
15.000	.51599	.99226	.53692	.99982	.96870	1.00000	1.00000
16.000	.46705	.99447	.49287	.99981	.95306	1.00000	1.00000
17.000	.42160	.99584	.45211	.99982	.93657	1.00000	1.00000
18.000	.37984	.99694	.41615	.99982	.91572	1.00000	1.00000
19.000	.34001	.99782	.38423	.99982	.88701	1.00000	1.00000
20.000	.30266	.99839	.35473	.99982	.85475	1.00000	1.00000
21.000	.26980	.99870	.32711	.99982	.82602	1.00000	1.00000
22.000	.24136	.99891	.30217	.99982	.79976	1.00000	1.00000
23.000	.21633	.99913	.28035	.99982	.77245	1.00000	1.00000
24.000	.19544	.99933	.26093	.99982	.74965	1.00000	1.00000
25.000	.17908	.99945	.24293	.99982	.73772	1.00000	1.00000
26.000	.16577	.99952	.22611	.99982	.73363	1.00000	1.00000
27.000	.15445	.99957	.21091	.99982	.73278	1.00000	1.00000
28.000	.14479	.99964	.19749	.99982	.73354	1.00000	1.00000
29.000	.13546	.99970	.18538	.99982	.73107	1.00000	1.00000
30.000	.12588	.99974	.17406	.99982	.72350	1.00000	1.00000
31.000	.11683	.99976	.16340	.99982	.71526	1.00000	1.00000
32.000	.10860	.99978	.15367	.99982	.70703	1.00000	1.00000
33.000	.10148	.99981	.14496	.99982	.70030	1.00000	1.00000
34.000	.09575	.99983	.13705	.99982	.69888	1.00000	1.00000
35.000	.09053	.99985	.12962	.99982	.69868	1.00000	1.00000
36.000	.08527	.99986	.12254	.99982	.69604	1.00000	1.00000
37.000	.08015	.99987	.11596	.99982	.69140	1.00000	1.00000
38.000	.07535	.99988	.11000	.99982	.68527	1.00000	1.00000
39.000	.07134	.99989	.10456	.99982	.68243	1.00000	1.00000
40.000	.06785	.99991	.09948	.99982	.68219	1.00000	1.00000
41.000	.06429	.99991	.09462	.99982	.67960	1.00000	1.00000
42.000	.06081	.99991	.08999	.99982	.67594	1.00000	1.00000
43.000	.05765	.99992	.08569	.99982	.67292	1.00000	1.00000
44.000	.05495	.99992	.08176	.99982	.67221	1.00000	1.00000
45.000	.05238	.99993	.07813	.99982	.67063	1.00000	1.00000

Fig. 1 (contd)

THETA	ETA T (OVERALL)	ETA S (SPILL)	ETA I (ILLUM)	ETA X (X-POL)	ETA P (PHASE)	ETA B (BLOCK)	ETA M (M=1)
46.000	.04973	.99994	.07470	.99982	.66591	1.00000	1.00000
47.000	.04736	.99994	.07139	.99982	.66350	1.00000	1.00000
48.000	.04526	.99994	.06822	.99982	.66365	1.00000	1.00000
49.000	.04323	.99994	.06524	.99981	.66279	1.00000	1.00000
50.000	.04119	.99995	.06249	.99981	.65935	1.00000	1.00000
51.000	.03939	.99995	.05993	.99981	.65733	1.00000	1.00000
52.000	.03775	.99996	.05752	.99981	.65635	1.00000	1.00000
53.000	.03606	.99996	.05522	.99981	.65316	1.00000	1.00000
54.000	.03451	.99996	.05298	.99981	.65156	1.00000	1.00000
55.000	.03311	.99996	.05083	.99981	.65165	1.00000	1.00000
56.000	.03172	.99996	.04879	.99981	.65028	1.00000	1.00000
57.000	.03039	.99996	.04690	.99981	.64814	1.00000	1.00000
58.000	.02921	.99997	.04512	.99981	.64743	1.00000	1.00000
59.000	.02801	.99997	.04344	.99981	.64492	1.00000	1.00000
60.000	.02688	.99997	.04184	.99981	.64264	1.00000	1.00000
61.000	.02586	.99997	.04030	.99981	.64186	1.00000	1.00000
62.000	.02483	.99997	.03880	.99981	.64006	1.00000	1.00000
63.000	.02387	.99997	.03735	.99981	.63936	1.00000	1.00000
64.000	.02298	.99998	.03595	.99981	.63920	1.00000	1.00000
65.000	.02208	.99998	.03464	.99981	.63766	1.00000	1.00000
66.000	.02126	.99998	.03340	.99981	.63683	1.00000	1.00000
67.000	.02047	.99998	.03223	.99981	.63538	1.00000	1.00000
68.000	.01970	.99998	.03111	.99981	.63332	1.00000	1.00000
69.000	.01899	.99998	.03005	.99981	.63222	1.00000	1.00000
70.000	.01828	.99998	.02902	.99981	.63007	1.00000	1.00000
71.000	.01763	.99998	.02803	.99981	.62893	1.00000	1.00000
72.000	.01699	.99999	.02707	.99981	.62761	1.00000	1.00000
73.000	.01637	.99999	.02614	.99981	.62646	1.00000	1.00000
74.000	.01580	.99999	.02524	.99981	.62603	1.00000	1.00000
75.000	.01523	.99999	.02436	.99981	.62518	1.00000	1.00000
76.000	.01469	.99999	.02351	.99981	.62501	1.00000	1.00000
77.000	.01417	.99999	.02270	.99981	.62427	1.00000	1.00000
78.000	.01367	.99999	.02193	.99981	.62363	1.00000	1.00000
79.000	.01320	.99999	.02119	.99981	.62283	1.00000	1.00000
80.000	.01273	.99999	.02049	.99981	.62170	1.00000	1.00000
81.000	.01229	.99999	.01981	.99981	.62083	1.00000	1.00000
82.000	.01186	.99999	.01916	.99981	.61944	1.00000	1.00000
83.000	.01146	.99999	.01853	.99981	.61847	1.00000	1.00000
84.000	.01106	.99999	.01793	.99981	.61700	1.00000	1.00000
85.000	.01068	.99999	.01734	.99981	.61595	1.00000	1.00000
86.000	.01031	.99999	.01678	.99981	.61454	1.00000	1.00000
87.000	.00996	.99999	.01624	.99981	.61342	1.00000	1.00000
88.000	.00961	.99999	.01571	.99981	.61213	1.00000	1.00000
89.000	.00929	.99999	.01520	.99981	.61099	1.00000	1.00000
90.000	.00897	.99999	.01471	.99981	.60982	1.00000	1.00000
91.000	.00866	1.00000	.01423	.99981	.60870	1.00000	1.00000
92.000	.00836	1.00000	.01376	.99981	.60764	1.00000	1.00000
93.000	.00807	1.00000	.01331	.99981	.60657	1.00000	1.00000
94.000	.00780	1.00000	.01288	.99981	.60561	1.00000	1.00000
95.000	.00753	1.00000	.01245	.99981	.60460	1.00000	1.00000
96.000	.00727	1.00000	.01204	.99981	.60372	1.00000	1.00000
97.000	.00702	1.00000	.01165	.99981	.60277	1.00000	1.00000
98.000	.00678	1.00000	.01126	.99981	.60195	1.00000	1.00000

Fig. 1 (contd)

THETA	ETA T (OVERALL)	ETA S (SPILL)	ETA I (ILLUM)	ETA X (X-POL.)	ETA P (PHASE)	ETA B (BLOCK)	ETA M (M=1)
99.000	.00654	1.00000	.01088	.99981	.60107	1.00000	1.00000
100.000	.00631	1.00000	.01052	.99981	.60031	1.00000	1.00000
101.000	.00609	1.00000	.01017	.99981	.59950	1.00000	1.00000
102.000	.00588	1.00000	.00982	.99981	.59880	1.00000	1.00000
103.000	.00567	1.00000	.00949	.99981	.59806	1.00000	1.00000
104.000	.00547	1.00000	.00916	.99981	.59740	1.00000	1.00000
105.000	.00528	1.00000	.00885	.99981	.59673	1.00000	1.00000
106.000	.00509	1.00000	.00854	.99981	.59612	1.00000	1.00000
107.000	.00491	1.00000	.00825	.99981	.59551	1.00000	1.00000
108.000	.00473	1.00000	.00796	.99981	.59495	1.00000	1.00000
109.000	.00456	1.00000	.00768	.99981	.59440	1.00000	1.00000
110.000	.00440	1.00000	.00740	.99981	.59389	1.00000	1.00000
111.000	.00424	1.00000	.00714	.99981	.59339	1.00000	1.00000
112.000	.00408	1.00000	.00688	.99981	.59292	1.00000	1.00000
113.000	.00393	1.00000	.00663	.99981	.59247	1.00000	1.00000
114.000	.00378	1.00000	.00639	.99981	.59204	1.00000	1.00000
115.000	.00364	1.00000	.00615	.99981	.59164	1.00000	1.00000
116.000	.00350	1.00000	.00592	.99981	.59125	1.00000	1.00000
117.000	.00337	1.00000	.00570	.99981	.59090	1.00000	1.00000
118.000	.00324	1.00000	.00548	.99981	.59054	1.00000	1.00000
119.000	.00311	1.00000	.00527	.99981	.59023	1.00000	1.00000
120.000	.00299	1.00000	.00507	.99981	.58990	1.00000	1.00000
121.000	.00287	1.00000	.00487	.99981	.58962	1.00000	1.00000
122.000	.00276	1.00000	.00468	.99981	.58932	1.00000	1.00000
123.000	.00264	1.00000	.00449	.99981	.58907	1.00000	1.00000
124.000	.00253	1.00000	.00431	.99981	.58879	1.00000	1.00000
125.000	.00243	1.00000	.00413	.99981	.58858	1.00000	1.00000
126.000	.00233	1.00000	.00396	.99981	.58833	1.00000	1.00000
127.000	.00223	1.00000	.00379	.99981	.58812	1.00000	1.00000
128.000	.00213	1.00000	.00363	.99981	.58790	1.00000	1.00000
129.000	.00204	1.00000	.00347	.99981	.58771	1.00000	1.00000
130.000	.00195	1.00000	.00332	.99981	.58752	1.00000	1.00000
131.000	.00186	1.00000	.00317	.99981	.58734	1.00000	1.00000
132.000	.00178	1.00000	.00303	.99981	.58717	1.00000	1.00000
133.000	.00170	1.00000	.00289	.99981	.58699	1.00000	1.00000
134.000	.00162	1.00000	.00275	.99981	.58686	1.00000	1.00000
135.000	.00154	1.00000	.00262	.99981	.58668	1.00000	1.00000
136.000	.00146	1.00000	.00250	.99981	.58657	1.00000	1.00000
137.000	.00139	1.00000	.00237	.99981	.58639	1.00000	1.00000
138.000	.00132	1.00000	.00225	.99981	.58629	1.00000	1.00000
139.000	.00125	1.00000	.00214	.99981	.58614	1.00000	1.00000
140.000	.00119	1.00000	.00203	.99981	.58603	1.00000	1.00000
141.000	.00112	1.00000	.00192	.99981	.58591	1.00000	1.00000
142.000	.00106	1.00000	.00182	.99981	.58579	1.00000	1.00000
143.000	.00100	1.00000	.00171	.99981	.58570	1.00000	1.00000
144.000	.00095	1.00000	.00162	.99981	.58557	1.00000	1.00000
145.000	.00089	1.00000	.00152	.99981	.58549	1.00000	1.00000
146.000	.00084	1.00000	.00143	.99981	.58536	1.00000	1.00000
147.000	.00079	1.00000	.00134	.99981	.58529	1.00000	1.00000
148.000	.00074	1.00000	.00126	.99981	.58518	1.00000	1.00000
149.000	.00069	1.00000	.00118	.99981	.58509	1.00000	1.00000
150.000	.00064	1.00000	.00110	.99981	.58501	1.00000	1.00000
151.000	.00060	1.00000	.00103	.99981	.58489	1.00000	1.00000

Fig. 1 (contd)

THETA	ETA T (OVERALL)	ETA S (SPILL)	ETA I (ILLUM)	ETA X (X-POL.)	ETA P (PHASE)	ETA B (BLOCK)	ETA M (M=1)
152.000	.00056	1.00000	.00095	.99981	.58485	1.00000	1.00000
153.000	.00052	1.00000	.00088	.99981	.58473	1.00000	1.00000
154.000	.00048	1.00000	.00082	.99981	.58467	1.00000	1.00000
155.000	.00044	1.00000	.00075	.99981	.58458	1.00000	1.00000
156.000	.00041	1.00000	.00069	.99981	.58449	1.00000	1.00000
157.000	.00037	1.00000	.00064	.99981	.58444	1.00000	1.00000
158.000	.00034	1.00000	.00058	.99981	.58432	1.00000	1.00000
159.000	.00031	1.00000	.00053	.99981	.58428	1.00000	1.00000
160.000	.00028	1.00000	.00048	.99981	.58420	1.00000	1.00000
161.000	.00025	1.00000	.00043	.99981	.58411	1.00000	1.00000
162.000	.00022	1.00000	.00039	.99981	.58407	1.00000	1.00000
163.000	.00020	1.00000	.00034	.99981	.58396	1.00000	1.00000
164.000	.00018	1.00000	.00030	.99981	.58392	1.00000	1.00000
165.000	.00016	1.00000	.00027	.99981	.58384	1.00000	1.00000
166.000	.00014	1.00000	.00023	.99981	.58370	1.00000	1.00000
167.000	.00012	1.00000	.00020	.99981	.58369	1.00000	1.00000
168.000	.00010	1.00000	.00017	.99981	.58357	1.00000	1.00000
169.000	.00008	1.00000	.00014	.99981	.58345	1.00000	1.00000
170.000	.00007	1.00000	.00012	.99981	.58343	1.00000	1.00000
171.000	.00006	1.00000	.00010	.99981	.58326	1.00000	1.00000
172.000	.00004	1.00000	.00008	.99981	.58314	1.00000	1.00000
173.000	.00003	1.00000	.00006	.99981	.58308	1.00000	1.00000
174.000	.00002	1.00000	.00004	.99981	.58283	1.00000	1.00000
175.000	.00002	1.00000	.00003	.99981	.58271	1.00000	1.00000
176.000	.00001	1.00000	.00002	.99981	.58252	1.00000	1.00000
177.000	.00001	1.00000	.00001	.99981	.58204	1.00000	1.00000
178.000	.00000	1.00000	.00000	.99981	.58182	1.00000	1.00000
179.000	.00000	1.00000	.00000	.99981	.58046	1.00000	1.00000
180.000	.00000	1.00000	.00000	.99981	.00138	1.00000	1.00000

MAXIMUM EFFICIENCY F/D =3.285

8.704	.75895	.89867	.84573	.99984	.99880	1.00000	1.00000

GAIN = 27.785 DB $= 600.482 = G_M$ ←

FEED BLOCKAGE ANGLE = .000 DEGREES

TOTAL RADIATED POWER FOR GIVEN PATTERN = .277858-04 WATTS

TOTAL RADIATED POWER REFERENCE PATTERN = .277858-04 WATTS

ETAR = 1.00000 (GIVEN PAT. POWER / REF. PAT. POWER)

NUMBER OF TERMS USED IN INTERPOLATIONS = 3

EFFICIENCY CALCULATED FOR M = (1, EVEN) CASE ONLY

FREQ=.20.7GHZ, GROOVES=0.3438LAMBDA

7.417 INCH, APERTURE, 19.675 INCH LONG, 0.196 INCH GROOVES 9.883 DEG FLARE

Fig. 1 (contd)

```
                    HYBRID MODE HORN PROGRAM

4.720INCH, APERTURE,12.451NCH LONG,0.125INCH GROOVES,9.883 DEG FLARE

ALL DIMENSIONS IN INCHES
CARD OUTPUT FOR FAR-FIELDS
LENGTH OF PHASING SECTION=     .00000
DIAMETER OF PHASING SECTION=     .38000
AXIAL LENGTH OF FLARE SECTION=  12.45100
APERTURE DIAMETER=    4.72000
GROOVE DEPTH=     .12500
THE FAR-FIELD PHASE REFERENCE POINT IS     .00000 INSIDE THE HORN APERTURE
FLARE SECTION HALF ANGLE=    9.88639 DEGREES
RADIUS FROM VERTEX TO APERTURE CAP=  13.74530
SPECIFIED FREQUENCY=  31.40000 GHZ.
NUMBER OF POINTS USED IN FLARE SECTION PHASE SHIFT INTEGRATION=    11

            MODE PHASES AT BEGINNING OF PHASING SECTION
            AND APERTURE LONGITUDINAL FIELD AMPLITUDES

       HE MODES                          EH MODES
  MODE    VOLTS      DEG                 VOLTS      DEG
    1   1.00000     .00000               .00000     .00000
```

Fig. 2. 31.4-GHz horn computer printout

ANTENNA FEED EFFICIENCY

FREQ=.31.4GHZ, GROOVES=0.3263LAMBDA 0

4.720INCH, APERTURE,12.451NCH LONG,0.125INCH GROOVES,9.883 DEG FLARE

THETA	ETA T (OVERALL)	ETA S (SPILL)	ETA I (ILLUM)	ETA X (X-POL.)	ETA P (PHASE)	ETA B (BLOCK)	ETA M (M=1)
1.000	.04306	.04304	.99993	1.00063	1.00000	1.00000	1.00000
2.000	.15779	.15792	.99881	1.00037	.99999	1.00000	1.00000
3.000	.30855	.31028	.99432	1.00012	.99999	1.00000	1.00000
4.000	.45665	.46436	.98352	.99989	.99999	1.00000	1.00000
5.000	.57675	.59808	.96471	.99976	.99987	1.00000	1.00000
6.000	.66196	.70567	.93875	.99976	.99950	1.00000	1.00000
7.000	.71706	.79042	.90819	.99982	.99909	1.00000	1.00000
8.000	.74784	.85627	.87435	.99986	.99902	1.00000	1.00000
9.000	.75582	.90502	.83609	.99986	.99902	1.00000	1.00000
10.000	.74111	.93812	.79151	.99982	.99825	1.00000	1.00000
11.000	.70780	.95886	.74086	.99980	.99656	1.00000	1.00000
12.000	.66455	.97175	.68782	.99981	.99445	1.00000	1.00000
13.000	.61926	.98052	.63697	.99983	.99168	1.00000	1.00000
14.000	.57431	.98692	.59008	.99984	.98634	1.00000	1.00000
15.000	.52815	.99133	.54587	.99984	.97617	1.00000	1.00000
16.000	.48075	.99399	.50294	.99983	.96182	1.00000	1.00000
17.000	.43513	.99552	.46195	.99983	.94635	1.00000	1.00000
18.000	.39352	.99658	.42482	.99983	.92967	1.00000	1.00000
19.000	.35492	.99747	.39224	.99983	.90730	1.00000	1.00000
20.000	.31799	.99817	.36302	.99983	.87771	1.00000	1.00000
21.000	.28392	.99861	.33577	.99983	.84691	1.00000	1.00000
22.000	.25429	.99884	.31032	.99983	.82053	1.00000	1.00000
23.000	.22850	.99902	.28746	.99983	.79583	1.00000	1.00000
24.000	.20582	.99922	.26743	.99983	.77036	1.00000	1.00000
25.000	.18706	.99939	.24950	.99983	.75034	1.00000	1.00000
26.000	.17235	.99950	.23282	.99983	.74077	1.00000	1.00000
27.000	.16018	.99955	.21718	.99983	.73799	1.00000	1.00000
28.000	.14966	.99960	.20298	.99983	.73774	1.00000	1.00000
29.000	.14054	.99966	.19041	.99983	.73847	1.00000	1.00000
30.000	.13168	.99972	.17909	.99983	.73560	1.00000	1.00000
31.000	.12254	.99976	.16853	.99983	.72740	1.00000	1.00000
32.000	.11392	.99978	.15853	.99983	.71887	1.00000	1.00000
33.000	.10617	.99979	.14927	.99983	.71150	1.00000	1.00000
34.000	.09938	.99981	.14095	.99983	.70533	1.00000	1.00000
35.000	.09386	.99984	.13344	.99983	.70366	1.00000	1.00000
36.000	.08894	.99986	.12645	.99983	.70354	1.00000	1.00000
37.000	.08389	.99987	.11980	.99983	.70051	1.00000	1.00000
38.000	.07897	.99988	.11349	.99983	.69607	1.00000	1.00000
39.000	.07437	.99988	.10768	.99983	.69086	1.00000	1.00000
40.000	.07037	.99990	.10242	.99983	.68733	1.00000	1.00000
41.000	.06702	.99991	.09757	.99983	.68708	1.00000	1.00000
42.000	.06367	.99992	.09299	.99983	.68484	1.00000	1.00000
43.000	.06028	.99992	.08860	.99983	.68052	1.00000	1.00000
44.000	.05718	.99993	.08440	.99983	.67762	1.00000	1.00000
45.000	.05446	.99993	.08051	.99983	.67659	1.00000	1.00000

Fig. 2 (contd)

THETA	ETA T (OVERALL)	ETA S (SPILL)	ETA I (ILLUM)	ETA X (X-POL)	ETA P (PHASE)	ETA B (BLOCK)	ETA M (M=1)
46.000	.05203	.99993	.07694	.99983	.67635	1.00000	1.00000
47.000	.04952	.99994	.07363	.99983	.67264	1.00000	1.00000
48.000	.04709	.99995	.07051	.99983	.66803	1.00000	1.00000
49.000	.04503	.99995	.06751	.99983	.66714	1.00000	1.00000
50.000	.04308	.99995	.06460	.99983	.66692	1.00000	1.00000
51.000	.04113	.99995	.06185	.99983	.66511	1.00000	1.00000
52.000	.03926	.99996	.05928	.99983	.66244	1.00000	1.00000
53.000	.03764	.99996	.05690	.99983	.66165	1.00000	1.00000
54.000	.03607	.99996	.05467	.99983	.65997	1.00000	1.00000
55.000	.03448	.99997	.05255	.99983	.65616	1.00000	1.00000
56.000	.03308	.99997	.05052	.99983	.65493	1.00000	1.00000
57.000	.03176	.99997	.04854	.99983	.65437	1.00000	1.00000
58.000	.03043	.99997	.04663	.99983	.65273	1.00000	1.00000
59.000	.02920	.99997	.04482	.99983	.65167	1.00000	1.00000
60.000	.02808	.99997	.04312	.99982	.65141	1.00000	1.00000
61.000	.02695	.99997	.04153	.99982	.64917	1.00000	1.00000
62.000	.02589	.99998	.04003	.99982	.64697	1.00000	1.00000
63.000	.02493	.99998	.03860	.99982	.64609	1.00000	1.00000
64.000	.02394	.99998	.03722	.99982	.64340	1.00000	1.00000
65.000	.02304	.99998	.03590	.99982	.64204	1.00000	1.00000
66.000	.02219	.99998	.03461	.99982	.64132	1.00000	1.00000
67.000	.02134	.99998	.03336	.99982	.63990	1.00000	1.00000
68.000	.02056	.99998	.03215	.99982	.63963	1.00000	1.00000
69.000	.01981	.99998	.03100	.99982	.63921	1.00000	1.00000
70.000	.01907	.99999	.02990	.99982	.63778	1.00000	1.00000
71.000	.01839	.99999	.02887	.99982	.63718	1.00000	1.00000
72.000	.01772	.99999	.02788	.99982	.63563	1.00000	1.00000
73.000	.01708	.99999	.02694	.99982	.63395	1.00000	1.00000
74.000	.01648	.99999	.02604	.99982	.63292	1.00000	1.00000
75.000	.01588	.99999	.02518	.99982	.63071	1.00000	1.00000
76.000	.01533	.99999	.02435	.99982	.62971	1.00000	1.00000
77.000	.01478	.99999	.02354	.99982	.62796	1.00000	1.00000
78.000	.01426	.99999	.02277	.99982	.62662	1.00000	1.00000
79.000	.01377	1.00000	.02201	.99982	.62563	1.00000	1.00000
80.000	.01328	1.00000	.02128	.99982	.62420	1.00000	1.00000
81.000	.01283	1.00000	.02057	.99982	.62364	1.00000	1.00000
82.000	.01238	1.00000	.01988	.99982	.62254	1.00000	1.00000
83.000	.01195	1.00000	.01922	.99982	.62202	1.00000	1.00000
84.000	.01154	1.00000	.01857	.99982	.62139	1.00000	1.00000
85.000	.01114	1.00000	.01795	.99982	.62077	1.00000	1.00000
86.000	.01076	1.00000	.01734	.99982	.62044	1.00000	1.00000
87.000	.01039	1.00000	.01676	.99982	.61973	1.00000	1.00000
88.000	.01003	1.00000	.01620	.99982	.61942	1.00000	1.00000
89.000	.00969	1.00000	.01566	.99982	.61873	1.00000	1.00000
90.000	.00935	1.00000	.01513	.99982	.61826	1.00000	1.00000
91.000	.00903	1.00000	.01463	.99982	.61766	1.00000	1.00000
92.000	.00872	1.00000	.01414	.99982	.61701	1.00000	1.00000
93.000	.00842	1.00000	.01367	.99982	.61649	1.00000	1.00000
94.000	.00813	1.00000	.01321	.99982	.61572	1.00000	1.00000
95.000	.00786	1.00000	.01277	.99982	.61523	1.00000	1.00000
96.000	.00758	1.00000	.01234	.99982	.61443	1.00000	1.00000
97.000	.00732	1.00000	.01193	.99982	.61392	1.00000	1.00000
98.000	.00707	1.00000	.01153	.99982	.61316	1.00000	1.00000

Fig. 2 (contd)

THETA	ETA T (OVERALL)	ETA S (SPILL)	ETA I (ILLUM)	ETA X (X-POL)	ETA P (PHASE)	ETA B (BLOCK)	ETA M (M=1)
99.000	.00682	1.00000	.01114	.99982	.61261	1.00000	1.00000
100.000	.00659	1.00000	.01076	.99982	.61194	1.00000	1.00000
101.000	.00636	1.00000	.01040	.99982	.61135	1.00000	1.00000
102.000	.00613	1.00000	.01004	.99982	.61077	1.00000	1.00000
103.000	.00592	1.00000	.00970	.99982	.61015	1.00000	1.00000
104.000	.00571	1.00000	.00937	.99982	.60965	1.00000	1.00000
105.000	.00551	1.00000	.00904	.99982	.60903	1.00000	1.00000
106.000	.00531	1.00000	.00873	.99982	.60859	1.00000	1.00000
107.000	.00512	1.00000	.00842	.99982	.60801	1.00000	1.00000
108.000	.00494	1.00000	.00813	.99982	.60761	1.00000	1.00000
109.000	.00476	1.00000	.00784	.99982	.60708	1.00000	1.00000
110.000	.00459	1.00000	.00756	.99982	.60670	1.00000	1.00000
111.000	.00442	1.00000	.00729	.99982	.60623	1.00000	1.00000
112.000	.00426	1.00000	.00703	.99982	.60587	1.00000	1.00000
113.000	.00410	1.00000	.00677	.99982	.60545	1.00000	1.00000
114.000	.00394	1.00000	.00652	.99982	.60512	1.00000	1.00000
115.000	.00380	1.00000	.00628	.99982	.60476	1.00000	1.00000
116.000	.00365	1.00000	.00604	.99982	.60445	1.00000	1.00000
117.000	.00351	1.00000	.00582	.99982	.60413	1.00000	1.00000
118.000	.00338	1.00000	.00559	.99982	.60383	1.00000	1.00000
119.000	.00325	1.00000	.00538	.99982	.60355	1.00000	1.00000
120.000	.00312	1.00000	.00517	.99982	.60329	1.00000	1.00000
121.000	.00299	1.00000	.00497	.99982	.60304	1.00000	1.00000
122.000	.00287	1.00000	.00477	.99982	.60280	1.00000	1.00000
123.000	.00276	1.00000	.00458	.99982	.60257	1.00000	1.00000
124.000	.00264	1.00000	.00439	.99982	.60235	1.00000	1.00000
125.000	.00253	1.00000	.00421	.99982	.60214	1.00000	1.00000
126.000	.00243	1.00000	.00404	.99982	.60194	1.00000	1.00000
127.000	.00233	1.00000	.00386	.99982	.60176	1.00000	1.00000
128.000	.00223	1.00000	.00370	.99982	.60158	1.00000	1.00000
129.000	.00213	1.00000	.00354	.99982	.60141	1.00000	1.00000
130.000	.00203	1.00000	.00338	.99982	.60125	1.00000	1.00000
131.000	.00194	1.00000	.00323	.99982	.60109	1.00000	1.00000
132.000	.00185	1.00000	.00309	.99982	.60094	1.00000	1.00000
133.000	.00177	1.00000	.00294	.99982	.60080	1.00000	1.00000
134.000	.00169	1.00000	.00281	.99982	.60066	1.00000	1.00000
135.000	.00160	1.00000	.00267	.99982	.60053	1.00000	1.00000
136.000	.00153	1.00000	.00254	.99982	.60041	1.00000	1.00000
137.000	.00145	1.00000	.00242	.99982	.60028	1.00000	1.00000
138.000	.00138	1.00000	.00230	.99982	.60017	1.00000	1.00000
139.000	.00131	1.00000	.00218	.99982	.60006	1.00000	1.00000
140.000	.00124	1.00000	.00207	.99982	.59995	1.00000	1.00000
141.000	.00117	1.00000	.00196	.99982	.59985	1.00000	1.00000
142.000	.00111	1.00000	.00185	.99982	.59974	1.00000	1.00000
143.000	.00105	1.00000	.00175	.99982	.59965	1.00000	1.00000
144.000	.00099	1.00000	.00165	.99982	.59955	1.00000	1.00000
145.000	.00093	1.00000	.00155	.99982	.59947	1.00000	1.00000
146.000	.00087	1.00000	.00146	.99982	.59936	1.00000	1.00000
147.000	.00082	1.00000	.00137	.99982	.59930	1.00000	1.00000
148.000	.00077	1.00000	.00128	.99982	.59920	1.00000	1.00000
149.000	.00072	1.00000	.00120	.99982	.59913	1.00000	1.00000
150.000	.00067	1.00000	.00112	.99982	.59904	1.00000	1.00000
151.000	.00063	1.00000	.00104	.99982	.59897	1.00000	1.00000

Fig. 2 (contd)

THETA	ETA T (OVERALL)	ETA S (SPILL)	ETA I (ILLUM)	ETA X (X-POL)	ETA P (PHASE)	ETA B (BLOCK)	ETA M (M=1)
152.000	.00058	1.00000	.00097	.99982	.59890	1.00000	1.00000
153.000	.00054	1.00000	.00090	.99982	.59882	1.00000	1.00000
154.000	.00050	1.00000	.00083	.99982	.59877	1.00000	1.00000
155.000	.00046	1.00000	.00077	.99982	.59867	1.00000	1.00000
156.000	.00042	1.00000	.00071	.99982	.59863	1.00000	1.00000
157.000	.00039	1.00000	.00065	.99982	.59853	1.00000	1.00000
158.000	.00035	1.00000	.00059	.99982	.59848	1.00000	1.00000
159.000	.00032	1.00000	.00054	.99982	.59841	1.00000	1.00000
160.000	.00029	1.00000	.00049	.99982	.59834	1.00000	1.00000
161.000	.00026	1.00000	.00044	.99982	.59830	1.00000	1.00000
162.000	.00023	1.00000	.00039	.99982	.59821	1.00000	1.00000
163.000	.00021	1.00000	.00035	.99982	.59816	1.00000	1.00000
164.000	.00018	1.00000	.00031	.99982	.59808	1.00000	1.00000
165.000	.00016	1.00000	.00027	.99982	.59803	1.00000	1.00000
166.000	.00014	1.00000	.00024	.99982	.59796	1.00000	1.00000
167.000	.00012	1.00000	.00020	.99982	.59784	1.00000	1.00000
168.000	.00010	1.00000	.00017	.99982	.59782	1.00000	1.00000
169.000	.00009	1.00000	.00015	.99982	.59769	1.00000	1.00000
170.000	.00007	1.00000	.00012	.99982	.59758	1.00000	1.00000
171.000	.00006	1.00000	.00010	.99982	.59756	1.00000	1.00000
172.000	.00005	1.00000	.00008	.99982	.59739	1.00000	1.00000
173.000	.00003	1.00000	.00006	.99982	.59727	1.00000	1.00000
174.000	.00003	1.00000	.00004	.99982	.59718	1.00000	1.00000
175.000	.00002	1.00000	.00003	.99982	.59702	1.00000	1.00000
176.000	.00001	1.00000	.00002	.99982	.59680	1.00000	1.00000
177.000	.00001	1.00000	.00001	.99982	.59647	1.00000	1.00000
178.000	.00000	1.00000	.00000	.99982	.59620	1.00000	1.00000
179.000	.00000	1.00000	.00000	.99982	.59478	1.00000	1.00000
180.000	.00000	1.00000	.00000	.99982	.00187	1.00000	1.00000

MAXIMUM EFFICIENCY			F/D =3.230				
8.852	.75607	.89877	.84217	.99986	.99907	1.00000	1.00000

GAIN = 27.658 DB = 583.176 = G_M ←

FEED BLOCKAGE ANGLE = .000 DEGREES
TOTAL RADIATED POWER FOR GIVEN PATTERN = .286053-04 WATTS
TOTAL RADIATED POWER REFERENCE PATTERN = .286053-04 WATTS
ETAR = 1.00000 (GIVEN PAT. POWER / REF. PAT. POWER)
NUMBER OF TERMS USED IN INTERPOLATIONS = 3

EFFICIENCY CALCULATED FOR M = (1, EVEN) CASE ONLY

FREQ=.31.4GHZ, GROOVES=0.3263LAMBDA 0

4.720INCH, APERTURE,12.451NCH LONG,0.125INCH GROOVES,9.883 DEG FLARE

Fig. 2 (contd)

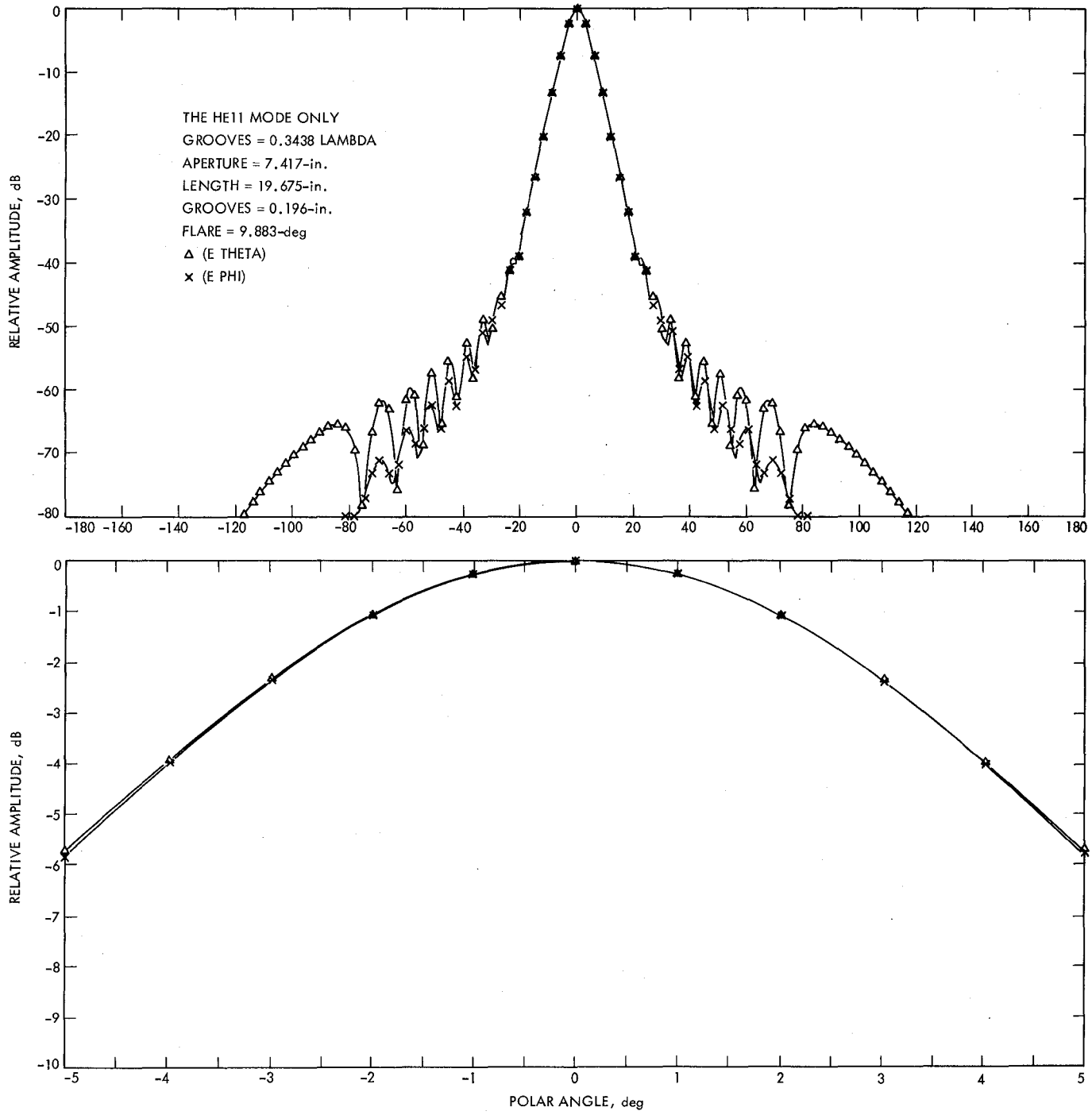

Fig. 3. 20.7-GHz horn computer plot

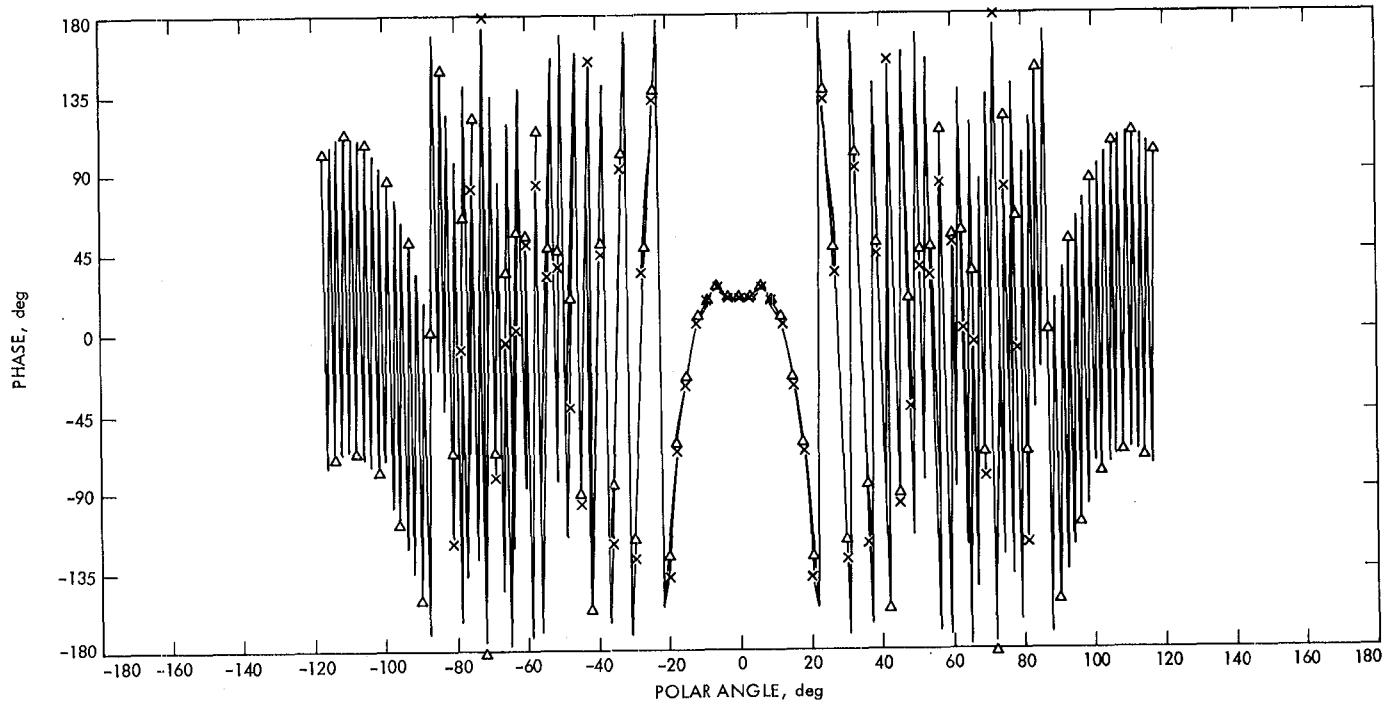
PHASE, deg
180
135
90
45
0
-45
-90
-135
-180
-180 -160 -140 -120 -100 -80 -60 -40 -20 0 20 40 60 80 100 120 140 160 180
POLAR ANGLE, deg

Fig. 3 (contd)

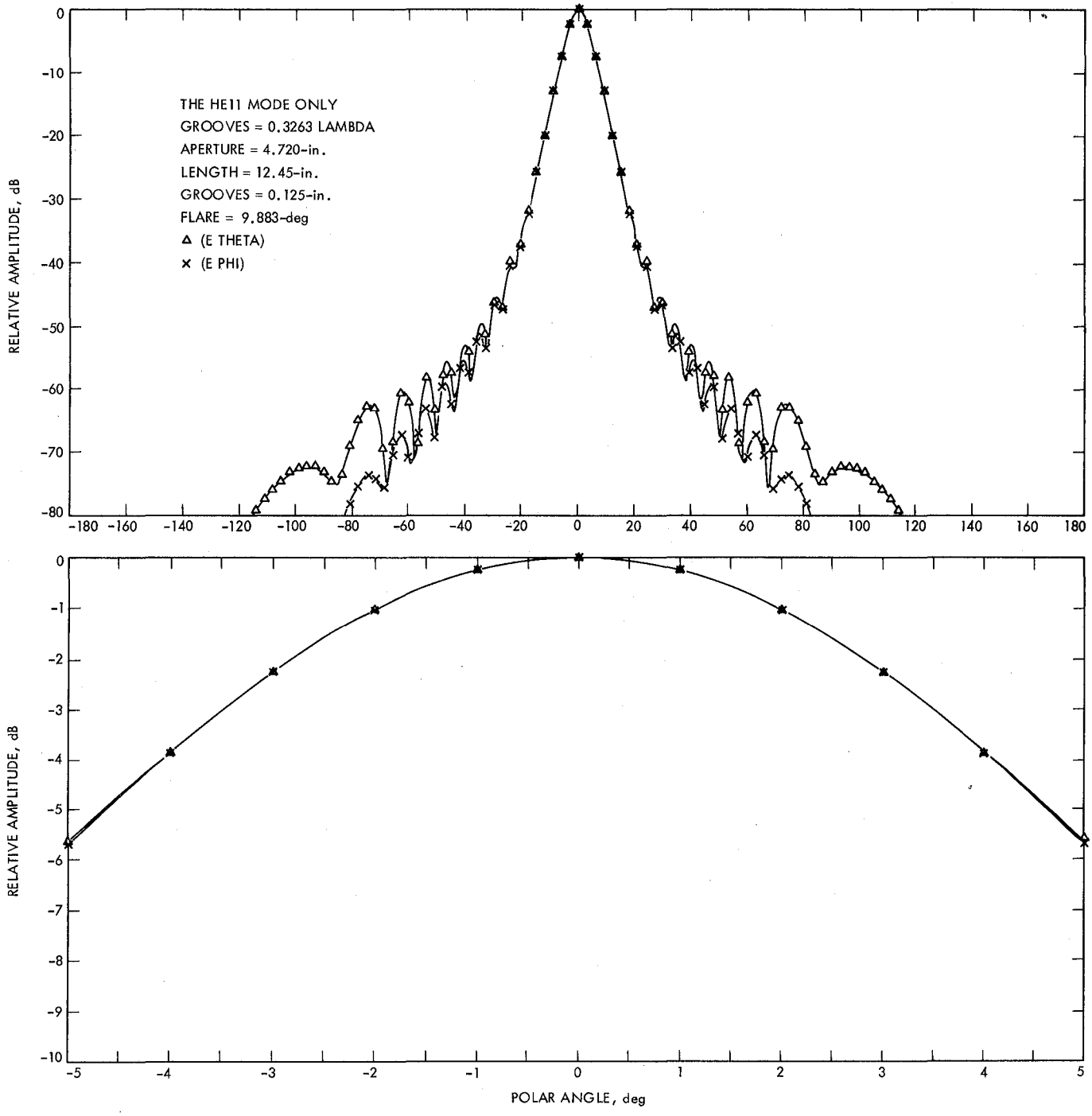

Fig. 4. 31.4-GHz horn computer plot

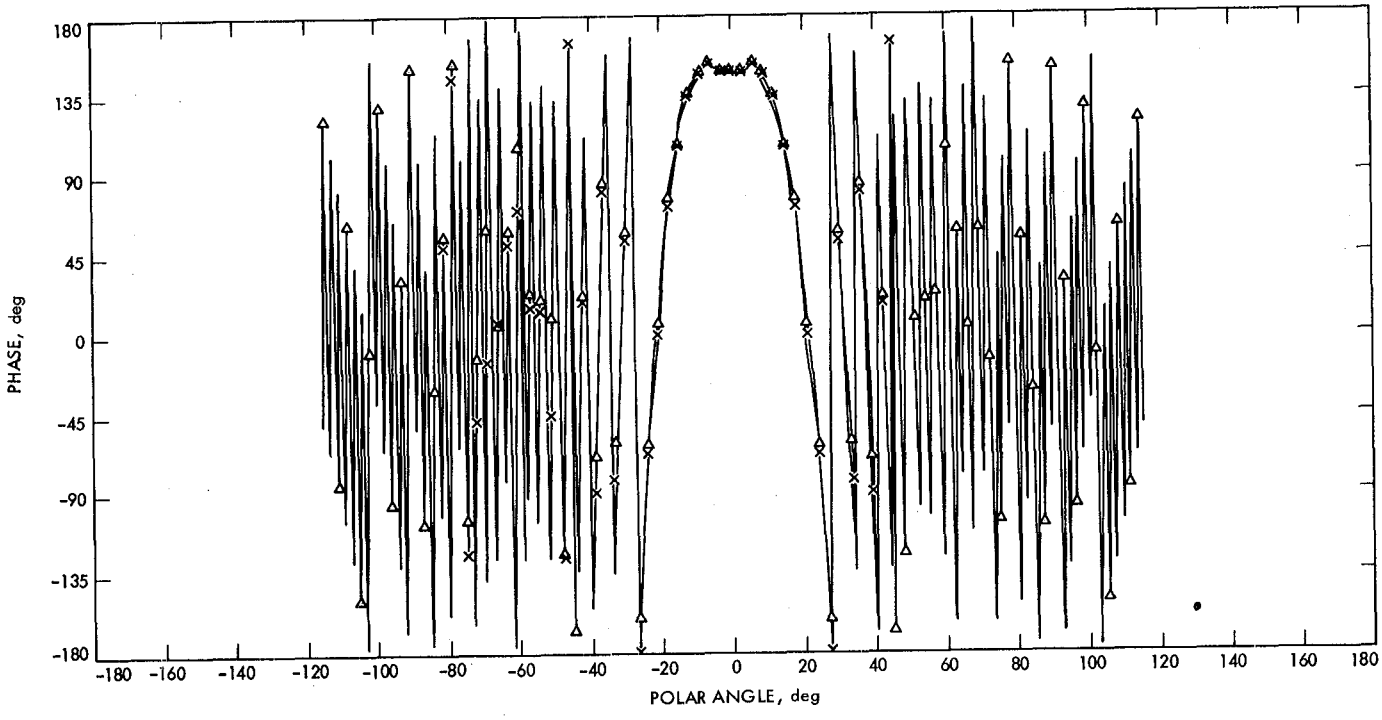
PHASE, deg
180
135
90
45
0
-45
-90
-135
-180
-180 -160 -140 -120 -100 -80 -60 -40 -20 0 20 40 60 80 100 120 140 160 180
POLAR ANGLE, deg

Fig. 4 (contd)

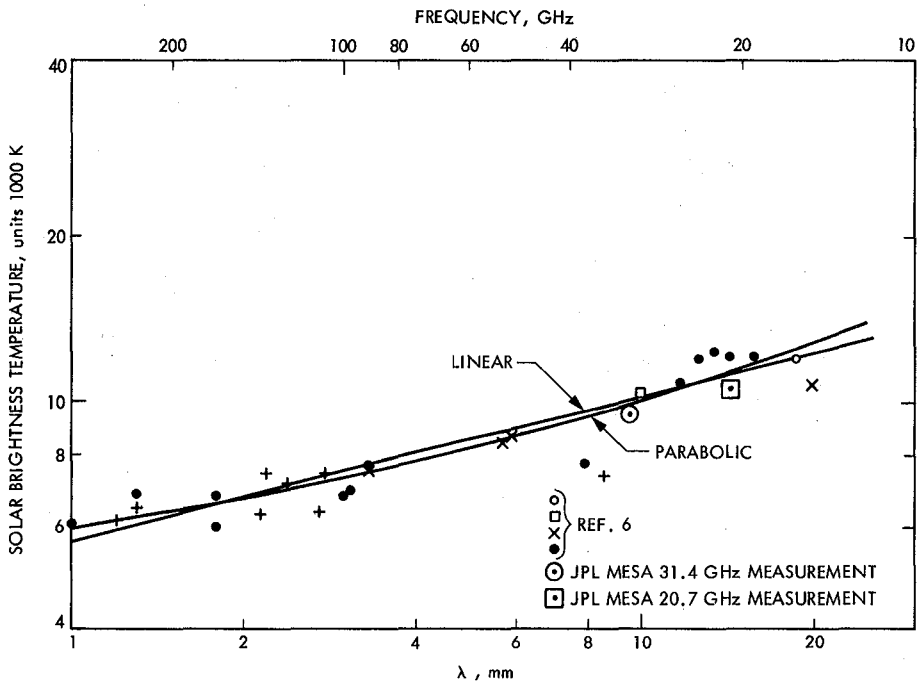

Fig. 5. Comparison of JPL Mesa WVR-R06 solar noise temperature measurements with those taken at other frequencies (Ref. 6, Fig. 2)

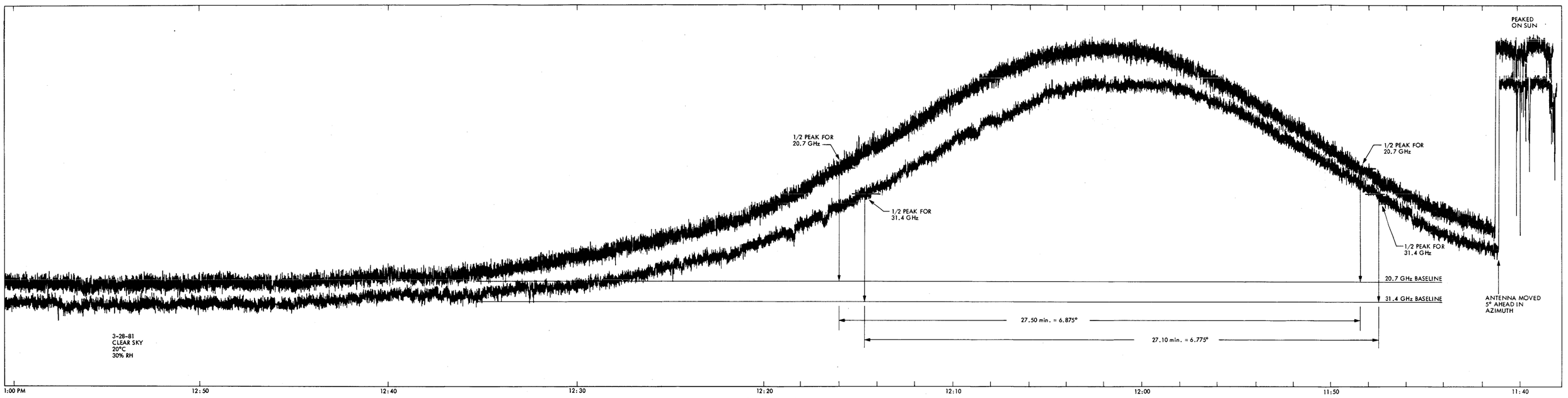

Fig. 6. Experimental drift curves of the 20.7/31.4 GHz radiometers (WVR-R04) taken at DSS13 at meridian crossing using the sun as a source

This Page Intentionally Left Blank

X-Band Atmospheric Noise Temperature Statistics at Goldstone, DSS 13, 1979 and 1980, and Clear Air Noise Temperature Models for Goldstone

S. D. Slobin, C. T. Stelzried, E. M. Andres, and M. M. Franco
Radio Frequency and Microwave Subsystems Section

X-band noise temperature data have been taken at Goldstone DSS 13 continuously since August 1975. This article updates the statistics of noise temperature increase above quiescent baseline for the years 1979 and 1980. The X-band data base now consists of five complete years of measurements. This article also gives clear air models for Goldstone, showing the seasonal noise temperature effects of changing surface water vapor densities for a particular atmospheric model.

I. X-Band Atmospheric Noise Temperature Statistics at Goldstone, DSS 13, 1979 and 1980

A. Introduction

Previous DSN Progress Reports (Refs. 1-3) have presented descriptions of the Goldstone DSS 13 X-band radiometer used for the microwave weather project. Statistics of zenith noise temperature increase above quiescent baseline for the years 1975-1978 have also been presented. 1977 was a very dry year and 1978 was a very wet year. Cumulative distributions of noise-temperature increase for these two years tend to bracket the data for all the years. Comparisons with the existing CCIR (International Radio Consultative Committee) arid region global rain model (Ref. 4) and the cloud-based theoretical model of the DSN Flight Project Interface Design Handbook show the actual Goldstone measurements to lie between the two. This indicates that the existing models should be used and interpreted with caution for mission planning purposes.

The noise temperature increases described are due to the atmosphere alone and do not include the effects of ground and waveguide contribution. Included in the noise temperature data, however, are small *decreases* in cosmic background contribution due to increases in the atmospheric attenuation. This effect is quite small compared to actual atmospheric changes.

B. Noise Temperature Statistics

The cumulative distributions of noise temperature increase above quiescent baseline are shown in Fig. 1 for the years 1975 through 1980. As an example, for the year 1980, 90 percent of the time the zenith atmospheric noise temperature increase above the quiescent (undisturbed) baseline is 1 kelvin or less; 98 percent of the time the increase is 3 kelvins or less. Because of radiometer bias errors during the year, the 1980 curve is the result of adjusting the noise temperature values 0.5 kelvins higher; i.e., the initial data reduction yielded 0.5 kelvins at the 90 percent level; the adjusted value is 1.0 kelvins at the same percentage level. Table 1 shows cumulative distribu-

tions by year-quarter for 1979. Table 2 shows 1980 data biased such that only 10 percent of the values for each year-quarter lie below 0 kelvins increase. A negative increase is statistically valid because it includes the effects of radiometer jitter above and below a nominal value.

The change in zenith atmospheric attenuation associated with any noise temperature change may be calculated from the following expression:

$$\Delta A(dB)_z = 10 \log_{10} \left[\frac{T_p}{T_p - \Delta T \, 10^{A_0/10}} \right]$$

where

T_p = effective physical temperature of the atmosphere, $\cong 280$ K

ΔT = noise temperature increase above baseline, kelvins

A_0 = baseline atmospheric attenuation at zenith, ≈ 0.036 dB at X-band at DSS 14

The atmospheric attenuation change at an elevation angle other than zenith may be approximated by:

$$\Delta A(dB)_\theta = \frac{\Delta A(dB)_z}{\sin \theta}$$

where

$\Delta A(dB)_z$ = attenuation change at zenith

θ = nonzenith elevation angle

The noise temperature change at the nonzenith elevation angle may be calculated from:

$$\Delta T_\theta = T_P \left[1 - \frac{1}{10^{\Delta A_\theta/10}} \right] \cdot 10^{-A_0/10}$$

where all quantities are defined above.

II. Clear Air Noise Temperature Models for Goldstone

A. Effects of Various Surface Water Vapor Densities

The equation of radiative transfer has been integrated (for a particular atmospheric model) to determine microwave noise temperature as a function of surface water vapor density and elevation angle for various commonly used microwave frequencies. Since water vapor is the most commonly changing component of the troposphere, its temporal variation will introduce uncertainties in what is normally referred to as the "clear sky" baseline. These variations in noise temperature may be rather large, particularly at frequencies near the "water vapor line" (22.235 GHz). Tables 3 and 4 present noise temperature and attenuation values for two antenna locations, sea level (as a reference) and a ground level of 1.032 km, the altitude of DSS 14 at Goldstone. For comparison, the altitudes of the other 64-meter antennas are 0.670 km (DSS 43, Canberra) and 0.796 km (DSS 63, Madrid).

The primary effect of changing altitude in these models is to alter the amount of oxygen through which the antenna looks. The water vapor contributions will remain substantially the same, subject only to the line-width pressure broadening effect of the total atmospheric pressure.

The particular atmospheric model used in these calculations is:

(1) Water vapor density profile: $\rho = \rho_0 \, e^{-h/2.0}$

where

ρ_0 = surface water vapor density

h = height above surface, km

(2) Temperature profile: 20°C at surface, -6.3 K/km lapse rate, 220 K minimum temperature

(3) Sea level pressure 1013.6 mb, pressure profile

$$P = P_0 \, e^{-0.116 \, h},$$

h in km, pressure scale height = 8.62 km

The water vapor and oxygen absorption coefficients are calculated from expressions in Bean and Dutton (Ref. 5) modified slightly to yield agreement with values calculated by the J. W. Waters radiative transfer program (Ref. 6).

B. Seasonal Clear Air X- and K_A-Band Noise Temperature Models for Goldstone DSS 13

Using figures for yearly water vapor distribution in Bean and Dutton (Ref. 5), clear air (oxygen and water vapor) models for noise temperature may be developed for Goldstone DSS 13. The results for DSS 14 will be very similar since both stations are at nearly equal heights above sea level (DSS 13 = 1.094 km, DSS 14 = 1.032 km). Surface absolute humidity

(AH) amounts at Goldstone for "dry" and "wet" months are given in Table 5.

Assuming a normal (Gaussian) distribution of absolute humidity (not strictly true, however), 98% of the time (99% - 1%) the absolute humidity will lie within 2.33 standard deviations (2.33 σ) of its mean value. Thus, for February, 1σ = ((9-2)/4.66) = 1.5 g/m^3. For August, 1σ = ((14-5)/4.66) = 1.9 g/m^3

Table 6 gives the water vapor seasonal *surface* models for the Goldstone area.

Based on previously calculated DSS 13 (very similar to DSS 14) models of oxygen and water vapor effects (using the model described above), the effects of these atmospheric components are given in Table 7.

Using Tables 6 and 7, the seasonal water vapor and oxygen noise temperature effects (mean $\pm 1\sigma$) can be calculated (Table 8). The mean is just the average of all year-quarters (two quarters each being the mean of the wet and dry quarters). The yearly standard deviation (σ) of the sum of four normal seasonal distributions of different means and standard deviations is found from

$$\sigma^2 = \frac{1}{4}\sum_{i=1}^{4} (\sigma_i^2 + \mu_i^2) - \mu^2$$

where

σ_i = standard deviation of each seasonal distribution

μ_i = mean of each seasonal distribution

μ = yearly mean

The numbers in parentheses in Table 8 are the $\pm 1\sigma$ spread. For a normal distribution (which the four seasons are postulated to have, but not the year), approximately 68% of the time the values will lie between $\pm 1\sigma$.

References

1. Reid, M. S., et al., "An X-Band Radiometer for the Microwave Weather Project," in *The Deep Space Network Progress Report 42-29*, Jet Propulsion Laboratory, Pasadena, Calif., Feb. 15, 1975, pp. 54-59.

2. Slobin, S. D., et al., "X-Band Atmospheric Noise Temperature Statistics at Goldstone DSS 13, 1975-1976," in *The Deep Space Network Progress Report 42-38*, Jet Propulsion Laboratory, Pasadena, Calif., Apr. 15, 1977, pp. 70-76.

3. Slobin, S. D., et al., "X-Band Atmospheric Noise Temperature Data and Statistics at Goldstone, DSS 13, 1977-1978," in *The Deep Space Network Progress Report 42-52*, Jet Propulsion Laboratory, Pasadena, Calif., Aug. 15, 1979, pp. 108-116.

4. CCIR Study Group, WARC-79, Document P/105-E, "Rain Attenuation Prediction," Geneva, Switzerland, 6 June 1978.

5. Bean, B. R., and Dutton, E. J., *Radio Meteorology*, Dover Publications, New York, 1968.

6. Smith, E. K., and Waters, J. W., "A Comparison of CCIR Values of Slant Path Attenuation and Sky Noise Temperature With Those From the JPL Radiative Transfer Program," presented at URSI National Radio Science Meeting, Boulder, Colorado, January 12-16, 1981.

Table 1. Cumulative distributions of zenith atmospheric noise temperature increases above quiescent baseline at Goldstone, 1979

TZX[a]	1st year-quarter	2nd year-quarter	3rd year-quarter	4th year-quarter	Year total
0	0.081	0.203	0.234	0.281	0.182
1	0.880	0.983	0.983	0.890	0.936
2	0.916	0.995	0.991	0.938	0.960
3	0.930	0.998	0.993	0.964	0.970
4	0.941	0.999	0.994	0.986	0.977
5	0.948	0.999	0.995	0.995	0.980
6	0.955	0.999	0.995	0.996	0.983
7	0.960	0.999	0.995	0.997	0.985
8	0.964	0.999	0.995	0.997	0.986
9	0.968	0.999	0.996	0.997	0.988
10	0.971	0.999	0.996	0.997	0.989

[a]TZX = X-band zenith atmospheric noise temperature increase above quiescent baseline, K; e.g., 1st year-quarter, TZX = 3, 93.0% of data below 3-K increase.

Table 2. Cumulative distributions of zenith atmospheric noise temperature increases above quiescent baseline at Goldstone, 1980 (with biases, see text)

TZX[a]	1st year-quarter	2nd year-quarter	3rd year-quarter	4th year-quarter	Year total
0	0.100	0.100	0.100	0.100	0.320
1	0.650	0.850	0.700	0.928	0.885
2	0.905	0.977	0.989	0.997	0.975
3	0.920	0.981	0.998	0.999	0.980
4	0.930	0.982	0.999	0.999	0.982
5	0.940	0.983	1.000	1.000	0.984
6	0.947	0.984	1.000	1.000	0.986
7	0.953	0.984	1.000	1.000	0.987
8	0.956	0.985	1.000	1.000	0.988
9	0.961	0.985	1.000	1.000	0.989
10	0.966	0.986	1.000	1.000	0.990

[a]TZX = X-band zenith atmospheric noise temperature increase above quiescent baseline, K; e.g., 2nd year-quarter, TZX = 3, 98.1% of data below 3-K increase.

Table 3. Clear air noise temperature and attenuation, 90° elevation angle (W = surface water vapor density)

Location and altitude	Atmosphere components	90° elevation							
		2.3 GHz		8.5 GHz		21.0 GHz		32.0 GHz	
	0_2 + W g/m^3 WV	T, K	A, dB	T, K	A, dB	T, K	A, dB	T, K	A, dB
Sea level	0_2 + 0.0 g/m^3	2.12	0.035	2.29	0.038	3.23	0.053	6.38	0.106
H = 0.000 km	0_2 + 3.0 g/m^3	2.13	0.035	2.48	0.041	10.30	0.163	9.54	0.154
	0_2 + 7.5 g/m^3	2.15	0.035	2.78	0.045	20.50	0.327	14.29	0.228
	0_2 + 10.0 g/m^3	2.16	0.036	2.94	0.048	25.98	0.417	16.94	0.270
	0_2 + 15.0 g/m^3	2.18	0.036	3.28	0.053	36.52	0.597	22.24	0.355
DSS 14	0_2 + 0.0 g/m^3	1.68	0.028	1.80	0.030	2.54	0.042	5.03	0.083
H = 1.032 km	0_2 + 3.0 g/m^3	1.69	0.028	1.98	0.032	9.95	0.157	7.87	0.127
	0_2 + 7.5 g/m^3	1.70	0.028	2.24	0.036	20.65	0.328	12.14	0.193
	0_2 + 10.0 g/m^3	1.71	0.028	2.39	0.038	26.37	0.423	14.52	0.230
	0_2 + 15.0 g/m^3	1.73	0.029	2.69	0.043	37.40	0.611	19.30	0.306

Table 4. Clear air noise temperature and attenuation, 30° elevation angle (W = surface water vapor density)

Location and altitude	Atmosphere components	30° elevation							
		2.3 GHz		8.5 GHz		21.0 GHz		32.0 GHz	
	0_2 + W g/m^3 WV	T, K	A, dB	T, K	A, dB	T, K	A, dB	T, K	A, dB
Sea level	0_2 + 0.0 g/m^3	4.21	0.070	4.56	0.075	6.41	0.106	12.61	0.212
H = 0.000 km	0_2 + 3.0 g/m^3	4.24	0.070	4.94	0.081	20.22	0.326	18.76	0.309
	0_2 + 7.5 g/m^3	4.28	0.071	5.53	0.090	39.56	0.654	27.87	0.457
	0_2 + 10.0 g/m^3	4.30	0.071	5.86	0.095	49.64	0.835	32.89	0.540
	0_2 + 15.0 g/m^3	4.35	0.072	6.52	0.105	68.48	1.194	42.80	0.710
DSS 14	0_2 + 0.0 g/m^3	3.34	0.055	3.60	0.059	5.06	0.084	9.98	0.167
H = 1.032 km	0_2 + 3.0 g/m^3	3.36	0.056	3.94	0.065	19.57	0.314	15.52	0.253
	0_2 + 7.5 g/m^3	3.40	0.056	4.46	0.072	39.83	0.656	23.77	0.385
	0_2 + 10.0 g/m^3	3.42	0.056	4.75	0.077	50.37	0.846	28.32	0.460
	0_2 + 15.0 g/m^3	3.46	0.057	5.35	0.086	70.01	1.221	37.34	0.611

Table 5. Surface absolute humidity values for Goldstone area

Month	AH exceeded 99% of time	Mean	AH exceeded 1% of time
Feb. (dry)	2 g/m^3	5 g/m^3	9 g/m^3
Aug. (wet)	5 g/m^3	10 g/m^3	14 g/m^3

Table 6. Surface water vapor density for Goldstone area

Month	Surface water vapor density, g/m^3
February (dry)	AH = 5.0 ±1.5 (1σ)
August (wet)	AH = 10.0 ±1.9 (1σ)

Table 7. Noise temperature effects for oxygen and water vapor (DSS 13)

Component	X-band (8.5 GHz)		K_A-band (32 GHz)	
	90° elevation	30° elevation	90° elevation	30° elevation
Oxygen	1.78 K	3.54 K	4.96 K	9.84 K
Water vapor 1 g/m^3	0.058 K	0.12 K	0.94 K	1.82 K

Table 8. Seasonal clear-air noise temperature models for DSS 13, mean ±1 std deviation

Elevation angle	Atmospheric noise temperature, K at X-band (8.5 GHz)			Atmospheric noise temperature, K at K_A-band (32 GHz)		
	Feb	Aug	Year	Feb	Aug	Year
90°	2.07 ±0.09 (1.98 - 2.16)	2.36 ±0.11 (2.25 - 2.47)	2.22 ±0.10 (2.12 - 2.32)	9.68 ±1.41 (8.27 - 11.09)	1439 ±1.79 (12.60 - 16.18)	12.04 ±2.30 (9.74 - 14.34)
30°	4.12 ±0.17 (3.95 - 4.29)	4.69 ±0.22 (4.47 - 4.91)	4.41 ±0.24 (4.17 - 4.65)	18.94 ±2.73 (16.21 - 21.67)	28.04 ±3.46 (24.58 - 31.50)	23.49 ±4.47 (19.02 - 27.96)

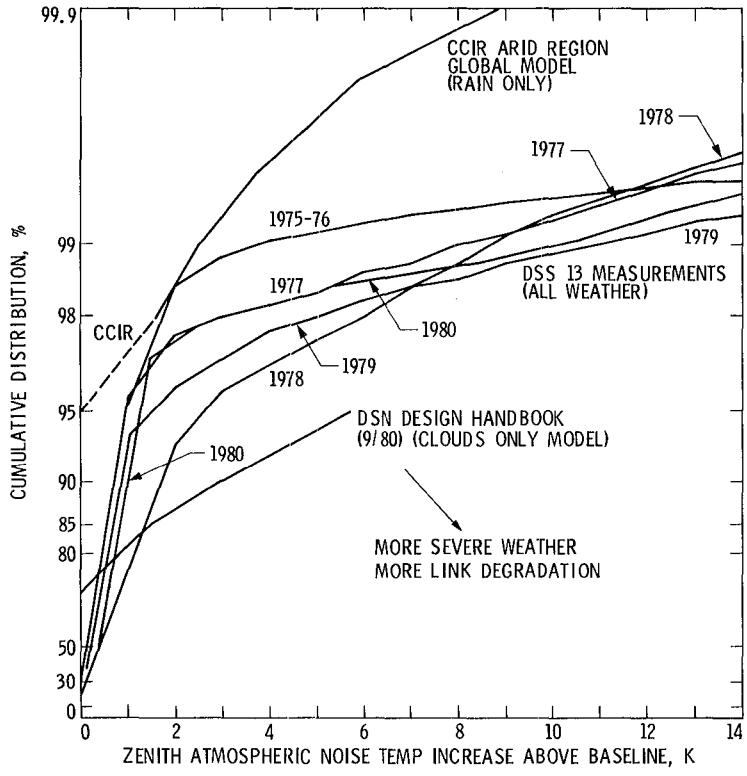

Fig. 1. Cumulative distributions of X-band zenith atmospheric noise temperature increase above quiescent baseline at Goldstone DSS 13

Antenna Beam Solid Angle Relationships

T. Y. Otoshi
Radio Frequency and Microwave Subsystems Section

Antenna beam solid angle is a critical system parameter whose value needs to be known accurately for some types of radio science experiments and radiometer system evaluations. Methods for determining antenna beam solid angle are not well known because this subject has not been discussed extensively in technical literature. This article fulfills the need for a summary of useful formulas and methods for determining antenna beam solid angle.

I. Introduction

A method used by Franco et al. (Ref. 1) for verifying the performance of a 20.7/31.4-GHz Water Vapor Radiometer (WVR) system was to experimentally record the system noise temperature during the time that the sun drifted through the peak of the main beam of the WVR horn. Comparison of the measured to the known noise temperature of the sun provided a means for determining the accuracy of the WVR system. The main drawback to this particular method is that it is necessary to know the precise values of the antenna beam solid angle of the WVR horn for the frequencies at which the drift curve data were obtained. It was originally believed that knowledge of the antenna half-power beamwidths was sufficient information for computing antenna beam solid angle. This assumption turned out to be incorrect for the general case and this discovery made it necessary to determine antenna beam solid angle by another method discussed in this article.

The purpose of this article is to present some of the useful formulas and methods for determining antenna beam solid angle. To this author's knowledge, these formulas cannot be readily found in well-known textbooks or publications and, therefore, this article should be useful to experimenters performing similar types of radiometer system evaluations in the future.

II. General Case Antenna Relationships

In order to show the relationships of beam solid angle to such antenna parameters as half-power beamwidths and antenna gain, it is helpful to begin with some basic definitions given by Kraus in Ref. 2. Antenna beam solid angle Ω_A is the angle through which all the power from a transmitting antenna would stream if the power (per unit solid angle) were constant and equal to the maximum value. A pictorial description of this definition may be helpful and is depicted in Fig. 1. Expressed mathematically

$$\Omega_A = \int_0^{2\pi} \int_0^{\pi} P_n(\theta,\phi) \sin\theta d\theta d\phi \qquad (1)$$

where (θ, ϕ) are spherical coordinate angles and $P_n(\theta, \phi)$ is the antenna power pattern normalized to the maximum value and

expressed mathematically as

$$P_n(\theta,\phi) = \frac{P(\theta,\phi)}{P_{max}} \tag{2}$$

The main beam or main lobe solid angle Ω_M is expressed as

$$\Omega_M = \iint_{\substack{main \\ beam}} P_n(\theta,\phi) \sin\theta \, d\theta \, d\phi \tag{3}$$

Beam efficiency is determined from

$$\epsilon_M = \frac{\Omega_M}{\Omega_A} = \left[\frac{\iint_{\substack{main \\ beam}} P(\theta,\phi) \sin\theta \, d\theta \, d\phi}{\iint_{\substack{all \\ space}} P(\theta,\phi) \sin\theta \, d\theta \, d\phi} \right] \tag{4}$$

It follows that

$$\Omega_A = \frac{\Omega_M}{\epsilon_M} \tag{5}$$

It is often convenient to relate main beam solid angle to the antenna half-power beamwidth, i.e., the full beamwidth between the 3-dB points. In Ref. 2, the relationship is given by Kraus as

$$\Omega_M = k_p \theta_{HP} \phi_{HP} \tag{6}$$

where

k_p = factor between about 1.0 for uniform aperture distribution and 1.13 for a Gaussian power pattern

θ_{HP} = full beamwidth between half-power points on the θ-plane power pattern, rad

ϕ_{HP} = full beamwidth between half-power points on the ϕ-plane power pattern, rad

Substitution of Eq. (6) into Eq. (5) results in

$$\Omega_A = \frac{k_P}{\epsilon_M} \theta_{HP} \phi_{HP} \tag{7}$$

which is a relationship not found in Kraus (Ref. 2) or Ko (Ref. 3). For an example application of the above formula, consider a large antenna with uniform aperture illumination. Substitutions of $k_P = 1.0$ and $\epsilon_M = 0.75$ values given by Kraus (Ref. 2) into Eq. (7) give the special case result of

$$\Omega_A = \frac{4}{3} \theta_{HP} \phi_{HP}$$

The above formula given by Eq. (7) is useful when the values of k_P and ϵ_M for the horn or antenna are known or have been previously determined. In the general case, however, these values are not known and not easy to determine except for very special cases. A more direct approach to finding Ω_A is desirable.

A second method for finding Ω_A is to obtain theoretical or experimental far-field patterns of the antenna at the desired frequencies of operation. Then one could use the fundamental definition of antenna beam solid angle given by Eq. (1) and perform a numerical integration of the normalized pattern. The pattern integrations can be carried out through the use of numerical methods similar to those used in JPL antenna computer programs (Ref. 4). The disadvantage of this method might be that antenna pattern data, except in the case of small horns, might be difficult to obtain experimentally.

A third method for determining Ω_A is to use knowledge of maximum directive gain of the antenna. The directive gain is given as

$$D(\theta,\phi) = \frac{P_n(\theta,\phi)}{\frac{1}{4\pi}\int_0^{2\pi}\int_0^{\pi} P_n(\theta,\phi)\sin\theta \, d\theta \, d\phi} = \frac{4\pi}{\Omega_A} P_n(\theta,\phi) \tag{8}$$

where

$$P_n(\theta,\phi) = \frac{P(\theta,\phi)}{P_{max}} = \text{normalized power pattern}$$

Then at $\theta = \theta_0, \phi = \phi_0$ corresponding to $P(\theta,\phi) = P_{max}$

$$P_n(\theta_0,\phi_0) = \frac{P(\theta_0,\phi_0)}{P_{max}} = 1$$

and the *maximum* directive gain is

$$D(\theta_0,\phi_0) = D_M = \frac{4\pi}{\Omega_A}$$

so that

$$\Omega_A = \frac{4\pi}{D_M} \tag{9}$$

Note that $D(\theta, \phi)$ is based entirely on *antenna pattern data* and that loss information is not required. The directive antenna gain differs from the actual antenna gain in that the latter includes losses in the antenna structure and feed. Fortunately in the case of most WVR horns, the mismatch and waveguide losses are small and little accuracy would be lost if the actual antenna gain value were substituted for directive gain in Eq. (9). Antenna gain is a value that is generally known and, if not known, experimental techniques for determining maximum antenna gain are well documented.

It is of interest at this point to derive a more general expression for k_p, which is a constant used by Kraus and Ko for classifying antennas with various types of aperture illuminations. From previous equations given above

$$k_p = \frac{\Omega_M}{\theta_{HP}\,\phi_{HP}}$$

$$\Omega_M = \Omega_A\,\epsilon_M = \frac{4\pi\,\epsilon_M}{D_M}$$

so that

$$k_p = \frac{4\pi\,\epsilon_M}{D_M\,\theta_{HP}\,\phi_{HP}} \tag{10}$$

III. Check Case

In order to verify the relationships given in this article, calculations were performed for a circular aperture antenna with uniform aperture illumination. As given in Silver (Ref. 5), the normalized far-field pattern is of the form

$$P_n(\theta) = \frac{P_E(\theta)}{P_{max}} = \frac{P_H(\theta)}{P_{max}} = |\,\Lambda_1(u)|^2 \tag{11}$$

where $P_E(\theta)$ and $P_H(\theta)$ are E- and H-plane power patterns, and

$$\Lambda_1(u) = \frac{2J_1(u)}{u} \qquad \text{for } 0 \leqslant \theta \leqslant \frac{\pi}{2}$$

$$= 0 \qquad \text{for } \frac{\pi}{2} < \theta \leqslant \pi \tag{12}$$

$J_1(u)$ = Bessel function of the first kind, first order

$$u = \frac{\pi d}{\lambda}\sin\theta$$

and d is the antenna aperture diameter and λ_0 is the operating free space wavelength. To perform a check case, a value of $d/\lambda_0 = 8.5732$ was selected because it results in a half-power beamwidth value identical to that for one of the WVR horns used in a radiometer performance evaluation (Ref. 1). Theoretical pattern data were calculated from the above equation and then used as input data for a JPL Efficiency Program of the type described in Ref. 4. The resulting values from the computer program were

$$\epsilon_M = 0.84028$$

$$\theta_{HP} = 0.1201 \text{ rad } (6.881 \text{ deg})$$

$$\phi_{HP} = 0.1201 \text{ rad } (6.881 \text{ deg})$$

$$10\log_{10} D_M = 28.61 \text{ dB}$$

which agree with values of gain and half-power beamwidths directly calculated from exact formulas given in Silver (Ref. 5) for this special case. Substitution of these computed values into the above Eq. (10) resulted in a value of $k_p = 1.008$, which is in exact agreement with the value published by Ko (Ref. 3) for the uniform illumination case.

Agreement with Ko's value of $k_p = 1.13$ was also obtained for the case of calculated far-field patterns for a Gaussian aperture illumination.

IV. Conclusions

General case relationships for determining antenna beam solid angle have been derived and presented. If the maximum antenna gain of the antenna is known, then the expression given by Eq. (9) is the easiest one to use for computing antenna beam solid angle. The relationships given in this article should prove useful to experimenters desiring to use a drift curve method to evaluate radiometric system performance.

References

1. Franco, M., Slobin, S., and Stelzried, C., "20.7/31.4 GHz Solar Disk Temperature Measurements," in *The Tracking and Data Acquisition Progress Report 42-64* (this issue).

2. Kraus, J. D., *Radio Astronomy*, McGraw-Hill, 1966, Chapter 6

3. Ko, H. C., "Radio-Telescope Antenna Parameters," *IEEE Trans. Military Electronics*, July/Oct. 1964, p. 227, Eq. 11.

4. Ludwig, A. C., "Computer Programs for Antenna Feed System Design and Analysis, Volume 1: Programs and Sample Cases," *Technical Report 32-979*, Jet Propulsion Laboratory, Pasadena, Calif., April 15, 1967 (see Antenna Feed Efficiency Program, p. 9).

5. Silver, S., *Microwave Antenna Theory and Design*, Radiation Laboratory Series, Vol. 12, 1949, Chpt. 6, pg. 194.

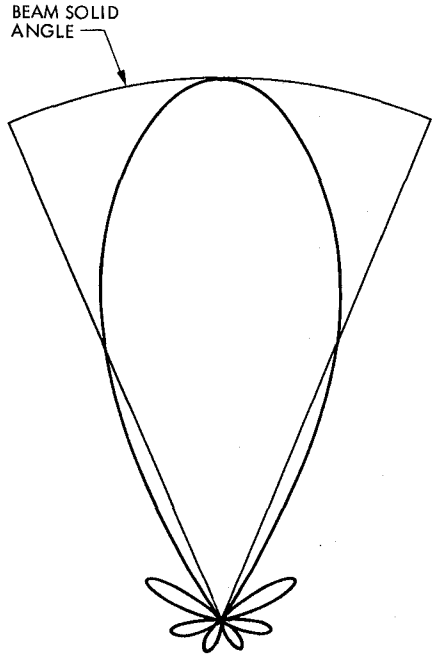

Fig. 1. Relation of antenna beam solid angle to antenna pattern

On Counters Used for Node Synchronization

C. A. Greenhall
Communications Systems Research Section

A node synchronization algorithm for a quick-look convolutional decoder was given in a previous article, which left two assertions unproved. The present article proves these assertions and gives an estimate for the distribution of the time to false alarm.

I. Introduction

A suboptimal quick-look decoding algorithm for the Deep Space Network (DSN) (7, 1/2) convolutional code is discussed in Refs. 1 to 3. Figure 1 shows the encoding and decoding schemes (without error correction, which does not concern us here). To detect node synchronization, one can use an up-down counter driven by the syndrome bits p_n as follows: If $p_n = 0$, then the counter is decremented by 1; if $p_n = 1$, then the counter is incremented by a fixed positive integer $k-1$. The counter is not allowed to become negative, however, and a false-sync condition is declared if the counter reaches a certain threshold T.

The probability of false alarm, P_{FA}, is the probability of reaching T during the total time of use, given that sync is true. We want P_{FA} to be small. References 2 and 3 give estimates for E_{FA}, the expected time to false alarm, and execute a counter design based in part on the requirement $E_{FA} >> n_b$, the total number of bits seen by the decoder (specifically, $E_{FA} > 100\ n_b$). This is dangerous because the ratio E_{FA}/n_b by itself gives no information about P_{FA}.

We have three aims here. First, the behavior of the node sync counter, called Counter 1, is estimated in Ref. 2 by comparing it to a certain random walk with independent steps, called Counter 2. Reference 2 asserts that Counter 1 is never above Counter 2. At the time, we carelessly regarded this assertion as obvious; in fact, it requires a substantial proof, which we give below. Second, we prove that the first-passage times of Counter 2 have finite expectation; Ref. 2 gives estimates for these expectations without proving their existence. Third, we give a crude (but still useful) estimate for P_{FA}.

II. Proof That Counter 1 ≤ Counter 2

First, we review the generation of the syndrome (p_n). According to Fig. 1, the syndrome is obtained by combining the outputs of two shift registers fed by the corrupted channel symbols s^*_{1n}, s^*_{2n}. The shift register taps are given by the polynomials

$$C_1(x) = 1 + x^2 + x^3 + x^5 + x^6$$

$$C_2(x) = 1 + x + x^2 + x^3 + x^6$$

Let e_{1n}, e_{2n} be the binary channel symbol *errors*, with associated formal power series

$$E_1(x) = \sum e_{1n} x^n, E_2(x) = \sum e_{2n} x^n.$$

Then, if

$$P(x) = \sum p_n x^n,$$

we have

$$P(x) = C_2(x)E_1(x) + C_1(x)E_2(x) \pmod 2 \qquad (1)$$

Next, we define the counters. Let ϵ_t ($t = 1/2, 1, 3/2, 2, \cdots$) be the multiplexed symbol error stream, that is, $\epsilon_{n-1/2} = e_{1n}$, $\epsilon_n = e_{2n}$. Counters 1 and 2 both start at zero. Let $K_1(n)$ = counter 1 state at bit time n, $K_2(t)$ = counter 2 state at time $t = 1/2, 1, 3/2, 2, \cdots$. For our purpose we can ignore the absorbing barrier at T. Let k be a fixed integer $\geqslant 2$. By definition,

$$K_1(0) = K_2(0) = 0$$

$$K_1(n) - K_1(n-1) = k - 1 \quad \text{if } p_n = 1$$

$$= -1 \quad \text{if } p_n = 0, K_1(n-1) > 0$$

$$= 0 \quad \text{if } p_n = 0, K_1(n-1) = 0$$

$$K_2(t) - K_2\left(t - \frac{1}{2}\right) = 5k - \frac{1}{2} \quad \text{if } \epsilon_t = 1$$

$$= -\frac{1}{2} \quad \text{if } \epsilon_t = 0, K_2\left(t - \frac{1}{2}\right) > 0$$

$$= 0 \quad \text{if } \epsilon_t = 0, K_2\left(t - \frac{1}{2}\right) = 0$$

Theorem: Assume that $e_{1n} = e_{2n} = 0$ for $n \leqslant 0$. For any symbol error sequence (e_{1n}, e_{2n}: $n \geqslant 1$), we have

$$K_1(n) \leqslant K_2(n) \quad (n = 1, 2, \cdots)$$

If there were no reflecting barrier, the theorem would be obvious, for let K_i' be Counter i without the barrier. For example, $K_1'(n) - K_1'(n-1) = kp_n - 1$ for all n. Then, as Ref. 2 points out,

$$K_1'(n) = k\sum_{j=1}^{n} p_j - n \leqslant 5k \sum_{t \leqslant n} \epsilon_t - n = K_2'(n)$$

since each $\epsilon_t = 1$ propagates a pattern of 5 parity errors into the future, and these patterns are added modulo 2.

To prove the theorem with the barrier, we introduce another sequence $q_1, q_2, \cdots$ and a third counter K_3. The formal power series

$$Q(x) = \sum q_n x^n$$

is defined by

$$Q(x) = C_2(x)E_1(x) + C_1(x)E_2(x)$$

which is just Eq. (1), except that now the arithmetic is *not* performed modulo 2. Thus, $p_n = q_n \bmod 2 \leqslant q_n$. The counter K_3 is driven from the q_n just as K_1 is driven from the p_n. By definition, $K_3(0) = 0$ and

$$K_3(n) - K_3(n-1) = kq_n - 1 \quad \text{if } q_n > 0$$

$$= -1 \quad \text{if } q_n = 0, K_3(n-1) > 0$$

$$= 0 \quad \text{if } q_n = 0, K_3(n-1) = 0$$

Our purpose is to prove that

$$K_1(n) \leqslant K_3(n), K_3(n) \leqslant K_2(n) \text{ for all } n \qquad (2)$$

Since $p_n \leqslant q_n$, we have $K_1(n) - K_1(n-1) \leqslant K_3(n) - K_3(n-1)$. This proves the first half of Eq. (2).

To prove the second half, we introduce the notion of *burst event*. We shall say that a burst event starts at the integer m if $e_{1m} = 1$ or $e_{2m} = 1$, and the previous 6 bit times are free of symbol errors. It ends (at integer time $r > m$) as soon as 6 consecutive error-free bit times have occurred (at times $r - 5, \cdots, r$). (The event goes on forever if a run of 6 good bit times never occurs after m.)

Let a burst event start at m. Let K_3' be K_3 without the reflecting barrier. We shall prove that

$$K_3(n) - K_3(m-1) = K_3'(n) - K_3'(m-1) \qquad (3)$$

for all n in the burst event. This means that the barrier does not influence the motion of K_3 during the burst event. If Eq. (3) holds for $k = 2$, then it holds for all $k > 2$ because the counter increments are greater. So assume $k = 2$.

The proof goes by induction on n. Equation (3) holds for $n = m - 1$. Let n be in the burst event and assume that Eq. (3)

holds through time $n-1$. There is an integer i between $n-6$ and n such that $e_{1i}=1$ or $e_{2i}=1$. By assumption,

$$K_3(i-1)-K_3(m-1)=K_3'(i-1)-K_3'(m-1) \qquad (4)$$

If $e_{1i}=1$, then $C_2=1111001$ propagates into the q_n stream. If there are no other symbol errors from time i onward, then $K_3(j)-K_3(i-1)$ takes values 1, 2, 3, 4, 3, 2, 3 for $j=i,\cdots,i+6$. Similarly, $e_{2i}=1$ by itself propagates $C_1=1011011$ and causes $K_3(j)-K_3(i-1)$ to take values 1, 0, 1, 2, 1, 2, 3. Although the counter dips to zero in this case (if $K_3(i-1)=0$), the next increment, being positive, moves the counter away from the barrier. Since any other symbol errors between i and $i+6$ cause the counter to take values above those just displayed, we have shown that

$$K_3(j)-K_3(i-1)=K_3'(j)-K_3'(i-1)$$

for $i\leqslant j\leqslant i+6$, in particular, for $j=n$. With Eq. (4), this completes the induction and proves Eq. (3) over the whole burst event.

Consider now the behavior of K_2 during a burst event starting at m. Each symbol error (at time n or $n-1/2$) contributes $5k$ to K_2' immediately (combined with a constant drift of -1 per bit), whereas the $5k$-contribution to K_3' is spread over the times $n, n+1,\cdots,n+6$. Therefore

$$K_3'(n)-K_3'(m-1)\leqslant K_2'(n)-K_2'(m-1)$$

(In fact, the two sides are equal at the end of the burst event.) In view of Eq. (3) and the relation

$$K_2'(t)-K_2'(s)\leqslant K_2(t)-K_2(s)$$

valid whenever $s\leqslant t$, we have

$$K_3(n)-K_3(m-1)\leqslant K_2(n)-K_2(m-1) \qquad (5)$$

for all n in the burst event.

We are almost done. Before the first burst event (if it exists), $K_3(n)=K_2(n)=0$. During the first event, $K_3(n)\leqslant K_2(n)$ by Eq. (5). If the first event ends, then K_3 and K_2 both start to decrease at the same rate until they hit zero or the second burst event starts (if it exists). Just before the start of the second event, $K_3\leqslant K_2$. By Eq. (5), $K_3\leqslant K_2$ during the second event, and so on. This proves the second half of Eq. (2), and completes the proof of the theorem.

III. Proof That the Mean Absorption Times of Counter 2 Are Finite

Since Counter 2 takes half-integral values with time steps of length 1/2, a simple change of variables (as in Ref. 2) brings the notation into line with the discussions of integer-valued random walks in Feller (Ref. 4). When we do this, we have a random walk, with independent steps, starting at height 1. Each step is equal to $d=10k-1$ with probability p, and -1 with probability $q=1-p$. The walk is not allowed to go below 1 (reflecting barrier at 0) and stops if it reaches or exceeds an absorbing barrier at $a=2T+1$.

Reference 2 uses the difference-equation method of Ref. 4 to get bounds on the expected absorption time (without first proving that the expectation exists). Here, we use the same method to estimate the generating function of the absorption-time distribution. For $1\leqslant j\leqslant a-1$ and $n\geqslant 1$, let $u_{j,n}$ be the probability that the walk is absorbed at time n, given that it starts at height j. The first step is to $j+d$ or $j-1$ and so

$$u_{j,n+1}=pu_{j+d,n}+qu_{j-1,n} \qquad (6)$$

for $2\leqslant j\leqslant a-d-1$, $n\geqslant 1$. If we account for the absorbing and reflecting barriers by imposing the boundary conditions

$$\begin{aligned} u_{0,n}&=u_{1,n}, u_{j,n}=0 \quad (a\leqslant j\leqslant a+d-1, n\geqslant 1)\\ u_{j,0}&=0 \qquad\qquad (0\leqslant j\leqslant a-1) \qquad (7)\\ u_{j,0}&=1 \qquad\qquad (a\leqslant j\leqslant a+d-1)\end{aligned}$$

then Eq. (6) holds for $1\leqslant j\leqslant a-1$, $n\geqslant 0$. Introduce the generating functions

$$U_j(s)=\sum_{n=0}^{\infty}u_{j,n}s^n \quad (0\leqslant j\leqslant a+d-1)$$

which converge at least for $|s|\leqslant 1$. Equations (6) and (7) are equivalent to the equations

$$U_j(s)=psU_{j+d}(s)+qsU_{j-1}(s) \quad (1\leqslant j\leqslant a-1) \qquad (8)$$

$$U_0(s)=U_1(s)$$

$$U_j(s)=1 \qquad\qquad (a\leqslant j\leqslant a+d-1)$$

Fix an s, $0 < s < 1$. The characteristic equation of Eq. (8),

$$pz^d + qz^{-1} = \frac{1}{s} \tag{9}$$

has exactly two real, positive roots, $\lambda_1(s), \lambda_2(s)$, which satisfy $0 < \lambda_1(s) < 1 < \lambda_2(s)$. The sequence

$$E_j(s) = \frac{(\lambda_2 - 1)\lambda_1{}^j + (1 - \lambda_1)\lambda_2{}^j}{\lambda_1{}^a(\lambda_2 - 1) + \lambda_2{}^a(1 - \lambda_1)}$$

satisfies an equation analogous to Eq. (8), plus the boundary conditions

$$E_0(s) = E_1(s), E_a(s) = 1$$

Because $E_j(s)$ is also convex in j, we have

$$E_j(s) \geq 1 \quad (a \leq j \leq a + d - 1)$$

Let $\Delta_j(s) = E_j(s) - U_j(s)$ for $0 \leq j \leq a + d - 1$. Then

$$p\Delta_{j+d}(s) + q\Delta_{j-1}(s) = \frac{1}{s}\Delta_j(s) \quad (1 \leq j \leq a - 1) \tag{10}$$

$$\Delta_0(s) = \Delta_1(s) \tag{11}$$

$$\Delta_j(s) \geq 0 \qquad (a \leq j \leq a + d - 1) \tag{12}$$

We assert that $\Delta_j(s) \geq 0$ for $0 \leq j \leq a + d - 1$. To prove this let

$$m = \Delta_r(s) = \min\{\Delta_j(s): 0 \leq j \leq a + d - 1\}$$

We want to show $m \geq 0$. If $a \leq r \leq a + d - 1$, we are done, by Eq. (12). Otherwise, we can assume $r \geq 1$ because of Eq. (11), and we have, from Eq. (10),

$$p\left(\Delta_{r+d} - \frac{m}{s}\right) + q\left(\Delta_{r-1} - \frac{m}{s}\right) = 0$$

Since $\Delta_{r+d} \geq m$, $\Delta_{r-1} \geq m$, we have

$$pm\left(1 - \frac{1}{s}\right) + qm\left(1 - \frac{1}{s}\right) \geq 0$$

and so $m \geq 0$.

We have thus derived the bound

$$U_1(s) \leq E_0(s) \tag{13}$$

By a similar argument,

$$U_1(s) \geq F_0(s) \tag{14}$$

where $F_0(s)$ is like $E_0(s)$ except that a is replaced by $a + d - 1$.

From now on, assume that $q > pd$. An inspection of Eq. (9) shows that

$$\frac{1 - \lambda_1(s)}{1 - s} \to \frac{1}{q - pd}, \lambda_2(s) \to \lambda > 1$$

as $s \to 1-$. From this we see that $(1 - E_0(s))/(1 - s)$ and $(1 - F_0(s))/(1 - s)$ both tend to finite limits as $s \to 1-$. Hence, $(1 - U_1(s))/(1 - s)$ tends to a finite limit D_1. This shows, first, that the absorption time is finite with probability 1, and second, that its expectation is D_1. In fact, the above limits give the same upper and lower bounds on D_1 as Ref. 2 gives, namely

$$\frac{1}{q - pd}\left(\frac{\lambda^a - 1}{\lambda - 1} - a\right) \leq D_1 \leq \frac{1}{q - pd}\left(\frac{\lambda^b - 1}{\lambda - 1} - b\right) \tag{15}$$

where $b = a + d - 1$, and λ is the unique real number satisfying $\lambda > 1, p\lambda^d + q\lambda^{-1} = 1$. Therefore, as in Ref. 2, we have

$$E_{FA} \geq \frac{1}{2(q - pd)}\left(\frac{\lambda^a - 1}{\lambda - 1} - a\right)$$

because Counter 2 operates twice each bit time.

IV. A Tail Estimate for the Absorption Time

Let τ be the absorption time for the random walk discussed in the last section, where the walk starts at height 1. Equation (15) gives bounds for $E(\tau) = D_1$, and we now desire a bound for the left-hand tail probabilities $P\{\tau < n\}$.

We say that our random walk X_n is reflected at time $n \geq 1$ if $X_{n-1} = 1$, $X_n = 1$. In other words, the walk returns to 1 and then tries to get to 0. There is a certain probability α that the random walk is absorbed at a without ever undergoing a reflection. If, however, the walk is reflected, it "starts from scratch;" again it has probability α of being absorbed before reflection. Thus, if N is the number of reflections before final absorption, we have

$$P\{N = 0\} = \alpha, P\{N = 1\} = (1 - \alpha)\alpha, \cdots$$

$$P\{N = n\} = (1 - \alpha)^n \alpha, \cdots$$

We invoke the absurdly simple inequality

$$\tau \geqslant N$$

and its consequence

$$P\{\tau < n\} \leqslant P\{N < n\} = 1 - (1-\alpha)^n \tag{16}$$

For our situation this estimate is not bad; because $p \ll 1$ and the average drift rate $pd - q$ is negative, most of the intervals between reflections have length 1. To use Eq. (16) we need to compute α. This is the familiar gambler's ruin problem with barriers at 0 and a. Again using the difference equation technique, Ref. 4, Chap. XIV, Eq. (8.12) gives

$$\frac{\lambda - 1}{\lambda^{a+d-1} - 1} \leqslant \alpha \leqslant \frac{\lambda - 1}{\lambda^a - 1} \tag{17}$$

Letting $\alpha^* = (\lambda - 1)/(\lambda^a - 1)$, we have

$$P\{\tau < n\} \leqslant 1 - (1-\alpha^*)^n$$

$$\approx 1 - e^{-n\alpha^*}$$

for $n\alpha^{*2} \ll 1$. Since Counter 2 operates twice each bit time, the false-alarm probability P_{FA} for Counter 1 satisfies

$$P_{FA} \leqslant 1 - \exp(-2n_b\,\alpha^*)$$

$$\approx 2n_b\,\alpha^* \text{ for } 2n_b\alpha^* \ll 1 \tag{18}$$

Finally, observe that

$$E(\tau) \geqslant E(N) = \frac{1}{\alpha} - 1 \geqslant \frac{\lambda^a - \lambda}{\lambda - 1} \tag{19}$$

The quality of Eq. (16) can be judged by comparing Eq. (19) with Eq. (15). Essentially, we are giving up a factor $q - pd$ in the mean.

V. Numerical Example

Let us substitute numbers from the design given in Ref. 2. The parameters are $p = 6.13 \times 10^{-3}$, $k = 8$, $T = 511$. Then we have $d = 79$, $a = 1023$, $q - pd = 0.5096$, $\lambda = 1.016408599$, $\alpha^* = (\lambda - 1)/(\lambda^a - 1) = 1/(1.037 \times 10^9)$.

For the false-alarm probability during n_b bits, and the expected false-alarm time, we have

$$P_{FA} \lesssim \frac{2n_b}{10^9} \text{ for } 2n_b \ll 10^9 \tag{20}$$

$$E_{FA} \gtrsim \frac{\alpha^*}{2(0.5096)} \approx 10^9 \text{ bits} \tag{21}$$

In particular, if $n_b = 10^9/100 = 10^7$ bits, then $P_{FA} \lesssim 0.02$.

VI. Conclusions

We have seen that it is not difficult to get practical estimates for the behavior of Counter 2, a random walk with independent steps. It appears that the false-alarm time for Counter 2 is approximately exponentially distributed; estimates for the distribution and its mean have been given. Although these estimates could be refined, we think that the real loss comes from the estimate "Counter 1 $\leqslant$ Counter 2;" a brief simulation showed that the excursions of Counter 2 were much greater than those of Counter 1. The real P_{FA} of Counter 1 is probably much less than the 0.02 upper bound based on Counter 2 theory.

Acknowledgment

I thank Gary Lorden for helping me with the estimation of absorption time probabilities.

References

1. Greenhall, C. A., and Miller, R. L., "Quick-Look Decoding Schemes for DSN convolutional Codes," *DSN Progress Report 42-51*, 162-166, Jet Propulsion Laboratory, Pasadena, Calif., 1979.

2. Greenhall, C. A., and Miller, R. L., "Design of a Quick-Look Decoder for the DSN (7, 1/2) Convolutional Code," *DSN Progress Report 42-53*, 93-101, Jet Propulsion Laboratory, Pasadena, Calif., 1979.

3. Greenhall, C. A., Miller, R. L., and Butman, S. A., "A Quick-Look Decoder With Isolated Error Correction and Node Synchronization," *IEEE Transactions on Communications*, July 1981 (to appear).

4. Feller, W., *An Introduction to Probability Theory and Its Applications*, Vol. 1, 3rd Edition, Wiley and Sons, New York, N. Y., 1968.

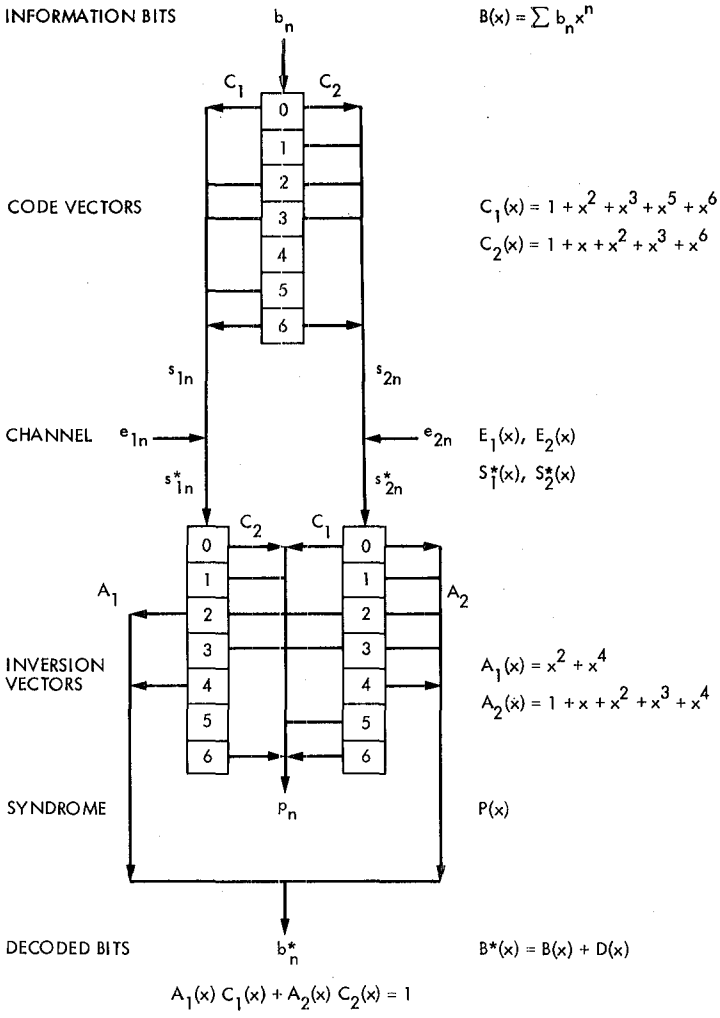

Fig. 1. Quick-look decoder for the DSN (7, 1/2) code

The Deep-Space Optical Channel: I. Noise Mechanisms

J. Katz
Communications Systems Research Section

The noise due to various sources in the deep space optical channel with a space-based receiver is analyzed. It is found that the worst case conditions occur during the encounter phase with planets.

I. Introduction

The DSN is currently considering optical frequencies for deep space communications. The basic parameters of optical communication systems are reviewed in Ref. 1. It is clear that a comprehensive understanding of the various noise mechanisms existing in the channel must supplement any system design.

It is the purpose of this article to discuss the effects of the noise in the optical link. In the following it is assumed that the receiving station of the link is located in space. This seems almost a necessity if one wants to utilize the potential advantages of optical communication. When the receiving telescope is located on earth, additional disturbing effects must be taken into account. Those are not considered here, and can be found elsewhere (Ref. 2).

II. Noise in the Optical Link

In this part we analyze the noise mechanisms that exist in the deep space optical link. First we consider the noise that exists in the channel, i.e., background photons in the propagating medium. Then the various noise components in the receiver are reviewed.

Assuming that the receiving telescope is located in space, the three main sources of noise in the optical region (from UV to IR) of the spectrum are:

(1) Zodiacal light (ZL).

(2) Integrated star light (ISL) from our galaxy (the "Milky Way").

(3) Noise from planets in flyby encounters.

The first two sources are spacially continuous. The third source, and noise from other similar sources (i.e., bright stars), is discrete. Less important noise sources are from diffuse galactic and extragalactic contributions. At certain wavelengths the background radiation can be very much higher due to the existence of specific atomic transitions. However, the number of such strong lines is very small and all of them lie in the UV region.

If the receiver is located on the earth, then, in addition to atmospheric attenuation, there will be noise due to airglow, scattered sunlight, moonlight, and other scattering phenomena in the atmosphere. These effects will not be discussed here.

A. Zodiacal Light (Refs. 3, 4, 5, 8, and 9)

Zodiacal light is sunlight reflected by interplanetary dust. It has both spectral and spatial features. In its spectral dependence, we distinguish between two regions. For wavelengths shorter than about 3 μm, the spectrum is similar to that of the sun, i.e., a black body at approximately 5700 K. For wavelengths longer than 3 μm, the spectrum is mainly due to self-thermal radiation of the dust (i.e., similar to a 500 K black body). The spatial features of the zodiacal light are due to its distribution in the solar system (a disk in the ecliptic plane, about 4 AU in diameter and about 0.5 AU in height) and due to the angular dependence of the light scattering mechanism.

Table 2 of Ref. 3 contains information about the amount of zodiacal light for different directions of observation. The data in that table is for $\lambda = 5500$ Å, and the results should be divided by a factor of two when applied to our case (i.e., $\lambda \sim 0.8$ to 0.9 m). Figure 1 presents the results for the most common case, which is operation in or about the ecliptic plane. As an example, for $\epsilon = 90$ deg, which is a typical case (the meaning of ϵ is explained in the insert of Fig. 1), we obtain $n_\lambda \sim 7 \times 10^8$ ph $\cdot$ s^{-1} $\cdot$ cm^{-2} $\cdot$ m^{-1} $\cdot$ sr^{-1}. For a possible system design (which assumes the Large Space Telescope (LST), as the receiving antenna, a 2-μrad detector field of view and a 10 Å optical filter in front of the detector), this translates to about 10^{-2} noise photons per second.

B. Integrated Starlight (Refs. 3, 6, 7, 8, and 9)

Integrated starlight comes from direct starlight and from starlight scattered by interstellar dust. As zodiacal light, integrated starlight also has spectral and spatial features. For wavelengths shorter than 0.4 μm, the spectrum contains some yet unexplained details, with an apparent minimum wavelength in the 0.2 to 0.3 μm region ($n_\lambda \sim 10^8$ ph $\cdot$ s^{-1} $\cdot$ cm^{-2} $\cdot$ μm^{-1} $\cdot$ sr^{-1}). For wavelengths longer than 0.4 μm, the spectrum is similar to that of a star that is somewhat hotter than the sun. The amount of noise is maximum in the galactic plane, and is about one order of magnitude lower at high galactic latitudes. A typical maximum value near the galactic plane is about $n_\lambda \sim 10^9$ ph $\cdot$ s^{-1} $\cdot$ cm^{-2} $\cdot$ μm^{-1} $\cdot$ sr^{-1} at 0.9 μm. This is about the same as that for zodiacal light.

C. Noise from Planets in Flyby Situations

When a spacecraft carrying an optical transmitter is in the encounter phase with a planet, the main source of received background noise is sunlight reflected from the planet. The irradiance E_λ at the receiving aperture plane is given by (Ref. 10):

$$E_\lambda = \frac{P_\lambda H_\lambda}{R_{p_\odot}^2 \left(\frac{R}{R_p}\right)^2} \quad , \quad \frac{\text{ph}}{\text{sec} \cdot \text{cm}^2 \cdot \mu\text{m}} \tag{1}$$

where

$H_\lambda = 4.5 \cdot 10^{17} \dfrac{\text{ph}}{\text{sec} \cdot \text{cm}^2 \cdot \mu\text{m}}$ at 0.9 μm (sun irradiance at 1 AU)

P_λ = geometric albedo of the planet (related to the reflection coefficient)

$R_{P_\odot}$ = sun-planet distance, AU

R = Earth-planet distance, km

R_p = Planet radius, km

Relevant data for such calculations appear in Table 1. (We assume $R = R_{p_\odot}$.) The last column of Table 1 presents the results for the amount of noise photons per second that are received in the system described earlier in this section. The detailed dependence of the amount of noise photons collected on the receiving telescope field of view is shown in Fig. 2, which also includes, for comparison, the noise due to the following sources:

(1) Noise from the sky; we have this noise when the receiver is located on earth (daytime and nighttime conditions).

(2) Noise from the zodiacal light and from the integrated starlight (considered in the previous sections).

(3) Noise from a weak star ($m_v = 6$) in the field of view.

We can conclude this section by saying that when the receiver is located in space, the dominant noise mechanism is the background noise of the planets during flyby encounters. However, this noise is still much lower than that for daytime reception with earth-based telescopes.

III. Noise in the Optical Receiver

In this section we will calculate the total amount of noise in the receiver. Again, we will assume that the optical receiver is composed of the large space telescope (Ref. 11) followed by a quantum detector. The telescope aperture is 2.4 m and the detector field of view is assumed to be 2 μrad.

A block diagram depicting the major noise components in the receiver is shown in Fig. 3. We will follow this figure in calculating the magnitude of the noise components.

a. N_b is the background radiation. Taking a Jupiter flyby as an example, we have (see Table 1) about $2 \cdot 10^5$ ph/s at the detector faceplate if we put a 10 Å filter in front of it. (The results scale linearly with the filter bandwidth.) The background radiation is about three orders of magnitude lower in a Uranus flyby.

b. N_s is the stray light from the sun. Due to departures from the ideal in any practical telescope, some amount of light that is not admitted in the designed field of view nevertheless reaches the detector. From the specifications of the Large Space Telescope (Ref. 12), this noise is about 10^3 ph $\cdot$ s^{-1} $\cdot$ cm^{-2} $\cdot$ μm^{-1} $\cdot$ sr^{-1} at 0.9 μm, which gives a negligible contribution to the total noise.

c. N_{th} is the thermal noise from the telescope body, roughly given by

$$N_{th} \cong A \cdot 2\pi \cdot \Delta\lambda \cdot 9.1 \cdot 10^{22}\, e^{-\frac{1.54 \cdot 10^4}{T}}, \quad \frac{\text{ph}}{\text{s}} \qquad (2)$$

at $\lambda = 0.9$ μm, where A is the area of the detector in cm^2, $\Delta\lambda$ is the optical bandwidth in Å, and T is the telescope temperature in K. We assume that the detector sees the telescope body through an angle of 2π sr. For T= 300 K, $\Delta\lambda$ = 10 Å, and A = 1 cm^2, we get about 50 ph/s, which is negligible. We note that because of the exponential dependence of N_{th} on the temperature, relatively small changes in T can cause huge changes in N_{th}. For example, if T is increased to 400 K, N_{th} increases to $3 \cdot 10^7$ ph/s, which is no longer negligible.

d. N_1 is the total noise at the output plane of the receiving telescope. The worst case conditions are during flyby encounters, in which case $N_1 \cong N_b$. In other situations, N_{th} can become the dominant component (but this case can be avoided by cooling the detector and restricting the angle at which it sees the telescope body (Fig. 4)).

e. N_γ is the Cherenkov noise due to cosmic-ray activity at the vicinity of the detector (Ref. 13). The basic mechanism is: A high-energy particle enters the photomultiplier faceplate, and photons are emitted and detected by the photocathode. As a rough order of magnitude, the cosmic ray flux above the earth's atmosphere is 1 particle/s-cm^2, and each particle emits about 100 photons. For photomultipliers with 5-cm^2 faceplates this amounts to about 500 ph/s created at the faceplate. Due to geometric considerations and other design procedures, the number actually detected by the photocathode can be reduced by about an order of magnitude. Furthermore, the resulting noise event due to one particle is expected to be a single strong pulse, followed by a few smaller pulses. One could conceivably detect the presence of such an event and partially, if not almost totally, remove its effects.

f. N_d is the noise due to photodetector dark current. Every dark-emitted electron is equivalent to $1/n_p$ noise photons, where n_p is the photodetector quantum efficiency. (In the near infrared, photomultiplier tube (PMT) quantum efficiencies are about 4% at 0.9 μm, 18% at 0.85 μm, and more than 20% at 0.8 μm. Operation around 0.85 μm is probably the most practical due to the availability of laser sources.) The main cause of the dark current at room temperature is thermionic emission, which for typical near-infrared photomultipliers is about 10^4 to 10^5 dark counts per second. This number can be reduced by 3 orders of magnitude by cooling the PMT to about -20°C. An estimate for the photocathode dark current per unit area can be obtained from the Richardson's equation (Ref. 14):

$$I_d = 120\, T^2\, e^{-\frac{E_w}{kT}}, \quad \frac{A}{\text{cm}^2} \qquad (3)$$

where E_w is the photocathode work function (1.38 eV for GaAs). Due to the exponential dependence on the temperature, thermionic emission is negligible once the PMT has been sufficiently cooled.

Other causes of dark current are ohmic leakage, secondary electrons released by ionic bombardment of the photocathode, cold emission from the electrodes, and light feedback to the photocathode. These contributions can be neglected in most practical cases.

g. N_o is the total number of noise photons at the output of the detector obtained by summing the contributions of each noise source. It is important to note that by using a photodetector with high internal gain, one can design the system so that white thermal noise (of the form 4KTB) is not an important noise factor.

IV. Conclusions

In the preceding sections we have surveyed the various noise mechanisms that exist in the link. From the system's operation point of view there are two very different situations. The first occurs during flyby, where the number of noise photons is of the order of 10^5 ph/s (Jupiter and Saturn flyby). The second is not during encounters, where the limiting factor is noise due to other mechanisms, for example, Cherenkov radiation. An intermediate situation is flyby near the outer planets (Uranus and beyond).

References

1. Katz, J., and Lesh, J., *Optical Communication for Deep Space Missions Using Integrated Semiconductor Injection Laser*, JPL Publication. Jet Propulsion Laboratory, Pasadena, Calif., (in preparation).
2. See, for example, Hodara, H., "Laser Wave Propagation Through the Atmosphere," *Proc. IEEE*, Vol. 54, pp. 368-375, 1966.
3. Daniels, G. M., A Night Sky Model for Satellite Search Systems, *Opt. Eng.*, Vol. 16, pp. 66-71, 1977.
4. Roser, S., and Stande, H. J., "The Zodiacal Light from 1500 Å to Micron," *Astron. Astrophys.*, Vol. 67, pp. 381-394, 1978.
5. Leinert, C., "Zodiacal Light – A Measure of the Interplanetary Dust," *Space Sci. Rev.*, Vol. 18, pp. 281-339, 1975.
6. Roach, F. E., and Megill, L. R., "Integrated Starlight over the Sky," *Astrophys. J.*, Vol. 133, pp. 228-242, 1961.
7. Mattila, K., *Synthetic Spectrum of the Integrated Starlight*, Observatory and Astrophysics Laboratory, Tähtitornin mäki, SF-00130, Helsinki, Finland (unpublished).
8. *RCA Electro-Optics Handbook*, chapter 6. Radio Corporation of America, Solid-State Division/Electro-Optics and Devices, Lancaster, Pa., 1974.
9. Harwit, M., *Infrared Astronomical Background Radiation, Infrared Astronomy*, G. Setti and G. G. Facio, editors; pp. 173-180. P. Reidel, Holland, 1978.
10. *The Planets Uranus, Neptune, and Pluto*, NASA SP-8103. National Aeronautics and Space Administration, Washington, D.C., 1971.
11. *The Space Telescope*, NASA SP-392. National Aeronautics and Space Administration, Washington, D.C.
12. *The Space Telescope, Level II*, Interface Requirement Document #STR-02A, July 20, 1978.
13. Young, A. T., "Cosmic Ray Induced Dark Current in Photomultipliers," *Rev. Sci. Inst.*, Vol. 37, pp. 1472-1481, Nov. 1966.
14. See, for example, Angelo, E. J., Jr., *Electronic Circuits*, pp. 60-61, McGraw Hill, New York, 1958.

Table 1. Data for calculating flyby noise from the outer planets

Planet	Approximate distance from the sun $R_{p\odot}$, AU	Radius R, km	Linear FOV from earth, μrad	Geometric albedo at 0.9 μm P_λ	Approximate photon flux E_λ at 0.9 μm, $\frac{\text{ph}}{\text{s-cm}^2\text{-}\mu\text{m}}$	Approximate number of noise photons/s (LST receiver, 10-Å optical filter, 2-μrad detector field of view)
Jupiter	5	71,000	200	0.33	$5 \cdot 10^7$	$2 \cdot 10^5$
Saturn	10	60,000	90	0.33	$4 \cdot 10^{6a}$	$9 \cdot 10^4$
Uranus	20	26,000	17	0.05 ±0.05	$4 \cdot 10^3$	$4 \cdot 10^2$
Neptune	30	25,000	11	0.05 ±0.05	$8 \cdot 10^2$	$9 \cdot 10^1$
Pluto	40	3,000	1	0.15 ±0.1	$1 \cdot 10^1$	$5 \cdot 10^1$

[a]This is an average value; the exact contribution due to the rings must be calculated separately for each case.

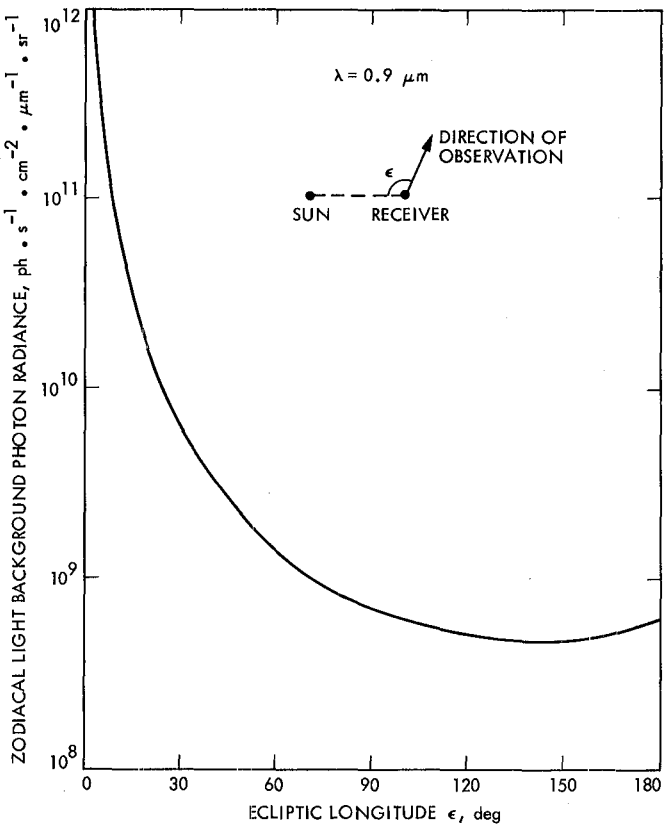

Fig. 1. Zodiacal light photon radiance in the ecliptic plane

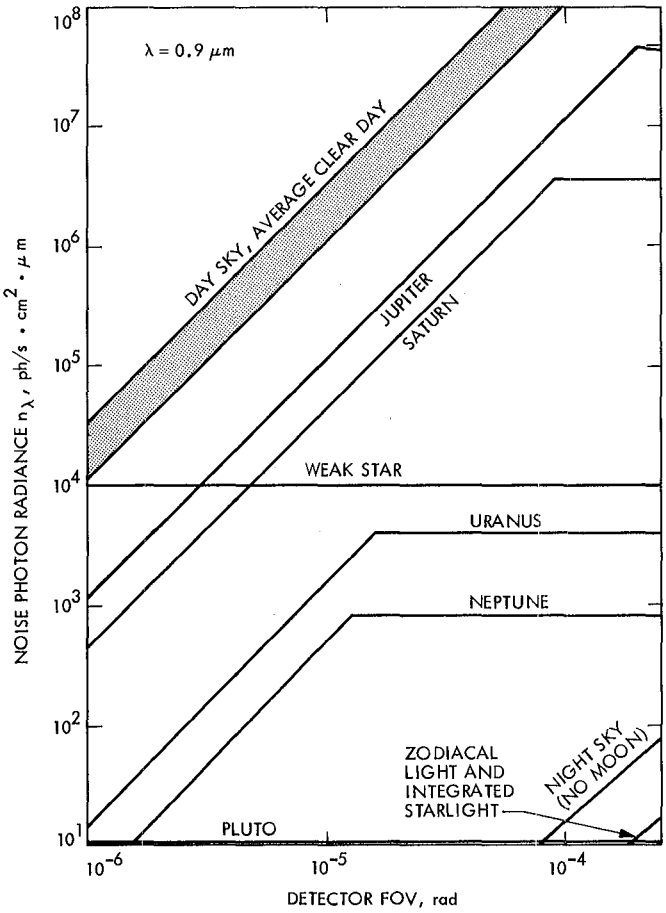

Fig. 2. Background noise radiance vs optical detector field of view

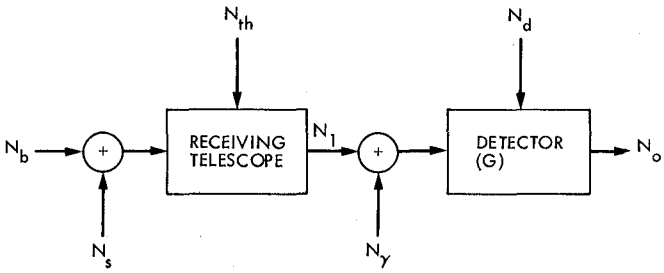

N_b BACKGROUND RADIATION

N_s STRAY LIGHT FROM THE SUN

N_{th} THERMAL RADIATION OF THE TELESCOPE BODY

N_1 TOTAL NOISE OF THE OUTPUT PLANE OF THE RECEIVING TELESCOPE

N_γ CLERNKOV NOISE DUE TO COSMIC RAYS

N_d PHOTODETECTOR DARK CURRENT (DUE TO THERMIONIC EMISSION AND OTHER EFFECTS)

N_o TOTAL NOISE AT THE RECEIVER OUTPUT

NOTE: SINCE A PHOTODETECTOR WITH HIGH GAIN IS USED, THERMAL NOISE IS NEGLIGIBLE

ALL PARAMETERS IN PHOTONS PER SECOND

Fig. 3. Block diagram of noise mechanisms in the optical link

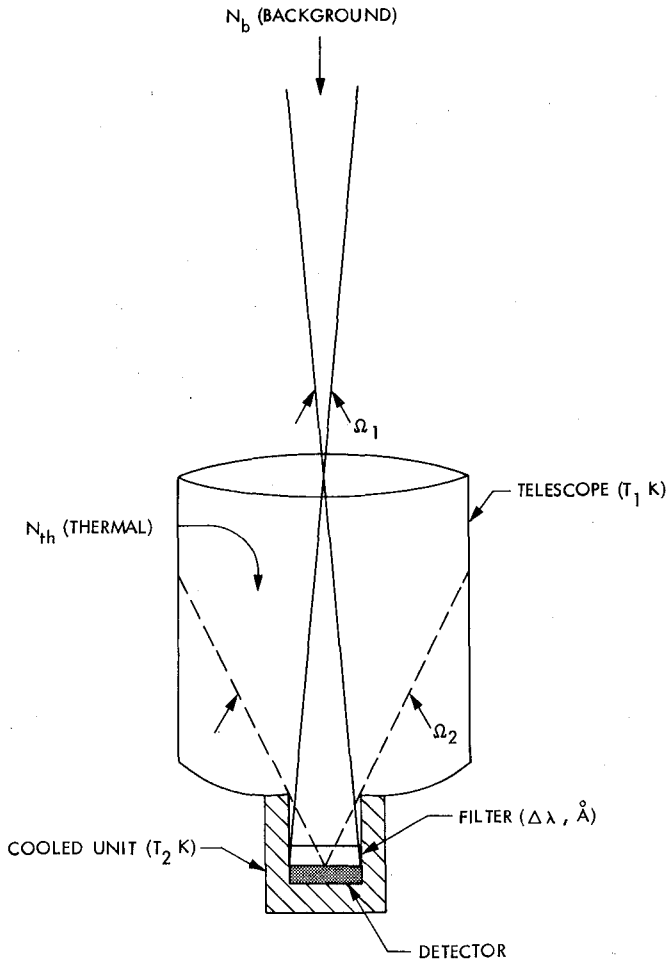

Fig 4. Schematic configuration for noise calculations. The detector "sees" the background noise coming from the angle Ω_1, and the noise due to the telescope thermal radiation coming from the angle Ω_2. With a proper design, one can obtain $\Omega_2 << 2$sr.

Burst Statistics of Viterbi Decoding

L. J. Deutsch and R. L. Miller
Communications Systems Research Section

A mathematical model of Viterbi decoder burst error performance is presented. This model allows for computer generation of Viterbi-like error sequences quickly and inexpensively for applications where large amounts of data are required. The model was corroborated through comparisons with actual software decoder simulations.

I. Introduction

It is well known that the bit errors produced by Viterbi decoding are not at all independent. Instead, they tend to group together in error clumps known as "bursts." This happens because error events in a Viterbi decoder are caused by excursions from the correct path in the code trellis structure (Ref. 1). Hence the implementation of convolutional encoding with Viterbi decoding transforms a Gaussian channel (such as the deep space channel) into a fading channel (see Fig. 1).

The DSN has adopted convolutional coding as a standard for deep space missions. The standard code is a (7, 1/2) convolutional code, which is currently decoded by Viterbi decoders.

Until now, the preferred method for studying the Viterbi channel has been with actual Viterbi decoding hardware or software. Running Viterbi decoder hardware for the purposes of such studies can be much more expensive than computer simulation. On the other hand, the software approach is usually so slow as to be prohibitively expensive. In this article, a method is presented for producing Viterbi-like error sequences both quickly and inexpensively using Monte-Carlo techniques.

Software Viterbi decoder simulations (of the type described in Ref. 2) have shown that burst lengths, as well as the times between consecutive bursts (known as "waiting times"), are very nearly geometrically distributed. The parameters needed to define these distributions are the average burst length, $\bar{B}$, the average waiting time, $\bar{W}$, and the average density of errors in a burst, θ. Given these parameters, Viterbi decoder burst lengths, B, were observed to be distributed according to

$$pr(B = m) = p\,(1 - p)^{m-1} \qquad (m > 0) \qquad (1)$$

where

$$p = 1/\bar{B}.$$

Errors within bursts occur randomly with probability θ. Waiting times, W, were observed to be distributed according to

$$pr\,(W = n) = q\,(1 - q)^{n-K+1} \qquad (n \geq K - 1) \qquad (2)$$

where K is the constraint length of the code and

$$q = 1/(\bar{W} - K + 2)$$

This description of Viterbi decoder burst statistics is called the "geometric model."

II. Summary of Results

A Monte Carlo software routine was written to generate Viterbi error sequences directly from Eqs. (1) and (2). The advantage of doing this is that Viterbi decoder simulation software requires several orders of magnitude more calculations per decoded bit than such random number generation techniques. On the computer used for this study (an XDS Sigma-5), the software Viterbi decoder required about 2^{K-7} hours per million bits for a code of constraint length K, while the geometric model required an average of five minutes per billion bits.

In order to validate the geometric model of Viterbi burst error statistics, the Viterbi channel of Fig. 1 was embedded in a Reed-Solomon coding scheme as shown in Fig. 2. The Reed-Solomon code used is a (255, 223) code capable of correcting up to 16 8-bit symbol errors per codeword. This concatenated coding scheme is a proposed NASA standard for deep space missions (Ref. 3). Normally, the Reed-Solomon symbols would be interleaved to a depth of four or five so as to minimize the effects of Viterbi burst errors. In this article the symbols were not interleaved, in order to maximize the effects of the bursts. The resulting Reed-Solomon word and bit error probabilities were calculated by tabulating the errors generated using both a Viterbi software decoder and a Monte-Carlo routine that generated random bursts and waiting times according to the geometric model.

The results of these comparison runs are shown for various convolutional codes in Figs. 3 to 8. (Some of the curves exhibited in these figures run off the edge of the page since the next data point was too low to be plotted on the same scale.) At high signal-to-noise ratios (SNRs), fewer error events were observed, and hence the uncertainty in the results is higher at these points. Error bars indicating a 90% confidence interval are included in Fig. 5. It can be seen that the geometric model and the actual data agree to within the uncertainty of the experiments.

III. The Definitions of "Burst" and "Waiting Time"

Denote the constraint length of the convolutional code under consideration by K. Consider a sequence of bits output by the Viterbi decoder of the form

$$\underbrace{ccc\ldots c}_{K-1}\ \underbrace{e\,xxx\ldots x\,e}_{B}\ \underbrace{ccc\ldots c}_{K-1}$$

where the letter c represents a correctly decoded bit, an e represents a bit error, and an x may be either correct or in error. Suppose also that there is no string of $K-1$ consecutive c's in the sequence $xxx\ldots x$. Then the string $exxx\ldots xe$ is called a "burst" of length B. The motivation behind this definition of a burst is that a string of $K-1$ consecutive correct bits will return the Viterbi decoder to the correct decoding path. A string of c's between two bursts will be referred to as a "waiting time."

IV. Derivation of the Geometric Model of Burst Statistics

A random variable X is said to be geometrically distributed with parameter $p \in [0, 1]$ if

$$pr\,(X = s) = p\,(1-p)^s \qquad (s = 0, 1, 2, \ldots).$$

For the purposes of this section, a random variable Y satisfies a "modified geometric distribution" of parameter $p \in [0, 1]$ if there exists a positive integer d such that

$$pr\,(Y = s) = p\,(1-p)^{s-d} \qquad (s = d, d+1, d+2, \ldots).$$

In this case, Y will be called d-geometrically distributed.

It is shown in Ref. 4 by a random coding argument that burst lengths for an "average convolutional code" have a distribution that may be upper-bounded by a 1-geometric distribution. In this report, it will be shown that for convolutional codes of constraint lengths seven through ten, burst lengths are, in fact, very nearly 1-geometrically distributed. Moreover, the waiting times are $(K-1)$-geometrically distributed.

The tests that were used to exhibit these facts were essentially the same for burst lengths and waiting times. For this reason, only the test for burst lengths will be described below.

Suppose that a software Viterbi decoder simulation is performed and N bursts are observed. Let B_i be the length of the i^{th} burst ($i = 1,2,3, \ldots, N$). Let B be the random variable representing burst length (so B_i is the i^{th} sample of the random variable B). It must be shown that

$$pr(B_i = s) = p(1-p)^{s-1} \qquad (s = 1,2,3, \ldots)$$

for some $p \in [0,1]$. The fact that these probabilities must sum to one forces $p = 1/\overline{B}$.

For each $m = 1,2,3, \ldots$ let N_m be the number of bursts of length greater than or equal to m. If the burst lengths were indeed 1-geometrically distributed with parameter $1/\overline{B}$, then the expected value of N_m/N_n would be

$$E(N_m/N_n) = \left(\sum_{s=m}^{\infty} p(1-p)^{s-1}\right) \Big/ \left(\sum_{s=n}^{\infty} p(1-p)^{s-1}\right)$$

$$= (1-p)^{m-n} = \left(1 - \frac{1}{\overline{B}}\right)^{m-n}.$$

In other words, for N sufficiently large,

$$1 - 1/\overline{B} \approx (N_m/N_n)^{1/(m-n)}$$

Since N is only moderately large in the software simulations that were performed for this study (on the order of 200 to 500), the performance of this test can be improved by grouping bursts of several consecutive lengths into bins. Enough bursts were placed into each bin so that $1 - 1/\overline{B}$ could be approximated to within 0.05 with 90% accuracy for each bin. These approximations remained reasonably constant between bins, indicating a successful test.

As remarked in Section II, waiting times were found, by a similar test, to be $(K - 1)$-geometrically distributed with parameter $q = 1/(\overline{W} - K + 2)$, where $\overline{W}$ is the average waiting time and K is the constraint length of the code.

The geometric model of Viterbi burst error statistics states that these bursts occur randomly according to these two modified geometric distributions. Errors within a burst occur essentially randomly (except for the fact that each burst starts and ends with an error) with probability θ. To generate error sequences similar to those produced by a Viterbi decoder, only the quantities $\overline{B}$, $\overline{W}$, and θ must be known. These are tabulated for several codes and channel SNRs in Tables 1 to 4.

References

1. McEliece, R. J. *The Theory of Information and Coding*, Addison-Wesley, London, 1977.
2. Butman, S. A., Deutsch, L. J., and Miller, R. M., "Performance of Concatenated Codes for Deep Space Missions," *TDA Progress Report 42-63, March and April 1981,* Jet Propulsion Laboratory, Pasadena, Calif., June 15, 1981.
3. Hooke, A. J., "Multimission Packet Telemetry Guidelines and Standards for Deep Space Missions," Document No. 663-9, Jet Propulsion Laboratory, Pasadena, Calif., November 1979 (an internal document).
4. Viterbi A. J., and Omura, J. K., *Principles of Digital Communication and Coding*, McGraw-Hill Book Company, New York, 1979.

Table 1. Viterbi decoder burst statistics, 3233013 (7, 1/2) convolutional code

E_b/N_0, dB	$\overline{B}$	$\overline{W}$	θ
0.5	25.84	131.2	0.564
0.75	23.46	158.5	0.566
1.0	21.07	220.5	0.571
1.1	19.78	275.8	0.574
1.2	19.27	293.2	0.574
1.3	18.02	371.2	0.573
1.4	17.46	430.6	0.573
1.5	17.01	474.1	0.578
1.6	15.76	600.8	0.578
1.7	15.21	702.2	0.579
1.8	14.32	847.0	0.586
1.9	13.50	931.7	0.584
2.0	12.89	1122	0.590
2.5	10.17	3258	0.599
3.0	8.67	9596	0.584
3.5	6.70	3.7E4	0.630
4.0	4.40	2.0E5	0.591

Table 2. Viterbi decoder burst statistics, 7376147 (7, 1/3) convolutional code

E_b/N_0, dB	$\overline{B}$	$\overline{W}$	θ
0.5	16.80	228.3	0.596
0.6	15.79	258.6	0.598
0.7	15.31	290.1	0.601
0.8	14.70	308.2	0.602
0.9	13.94	355.5	0.605
1.0	13.24	440.1	0.612
1.1	13.13	473.5	0.611
1.2	12.13	567.1	0.613
1.3	12.01	663.4	0.615
1.4	11.40	787.2	0.620
1.5	11.30	980.8	0.624
1.6	10.79	1146	0.622
2.0	9.46	2556	0.636
2.5	7.53	8613	0.653
3.0	6.35	2.9E4	0.685
3.5	7.25	1.2E5	0.672

Table 3. Viterbi decoder burst statistics, 3103320323 (10, 1/2) convolutional code

E_b/N_0, dB	$\overline{B}$	$\overline{W}$	θ
0.5	37.98	162.4	0.511
0.6	35.99	184.8	0.512
0.7	32.72	221.7	0.517
0.8	30.11	248.5	0.515
0.9	28.07	292.9	0.518
1.0	26.98	353.0	0.523
1.2	25.16	526.7	0.530
1.3	22.86	601.0	0.530
1.4	21.15	857.6	0.537
1.5	21.13	983.6	0.531
1.6	20.86	1217	0.545
1.7	18.80	1566	0.541
2.0	16.95	4048	0.551
2.5	14.14	2.5E4	0.585
3.0	11.25	2.5E5	0.622

Table 4. Viterbi decoder burst statistics, 7461776427 (10, 1/3) convolutional code

E_b/N_0, dB	$\overline{B}$	$\overline{W}$	θ
0.5	25.29	398.1	0.533
0.6	24.84	455.3	0.532
0.7	22.06	549.4	0.539
0.8	21.37	642.4	0.541
0.9	20.76	813.0	0.540
1.0	19.34	990.1	0.540
1.2	17.68	1606	0.546
1.3	16.33	2094	0.555
1.5	14.08	3245	0.566
2.0	11.21	1.6E5	0.566
2.5	8.20	6.8E5	0.646

Fig. 1. The Viterbi channel

Fig. 2. The concatenated channel

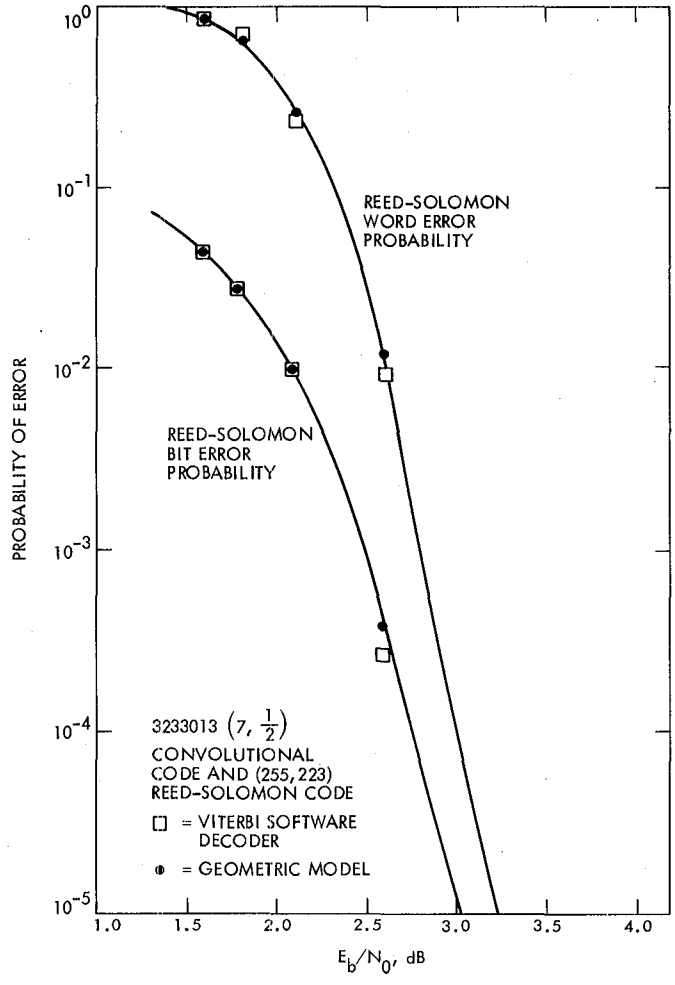

Fig. 3. Non-interleaved performance statistics for concatenated coding scheme assuming no system losses, (7, 1/2) convolutional code

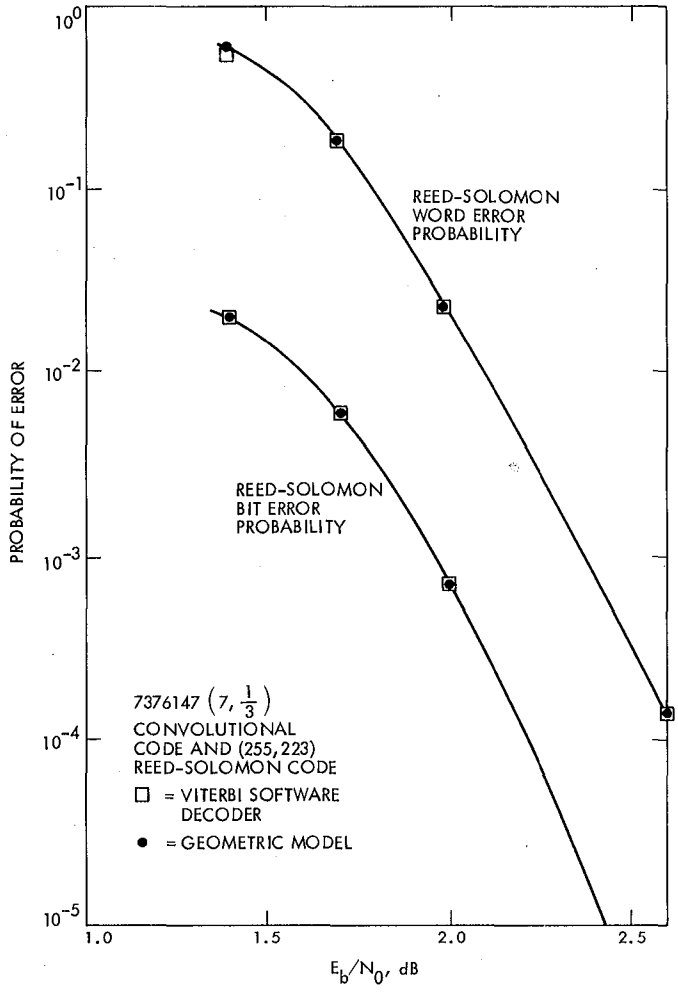

Fig. 4. Non-interleaved performance statistics for concatenated coding scheme assuming no system losses, (7, 1/3) convolutional code

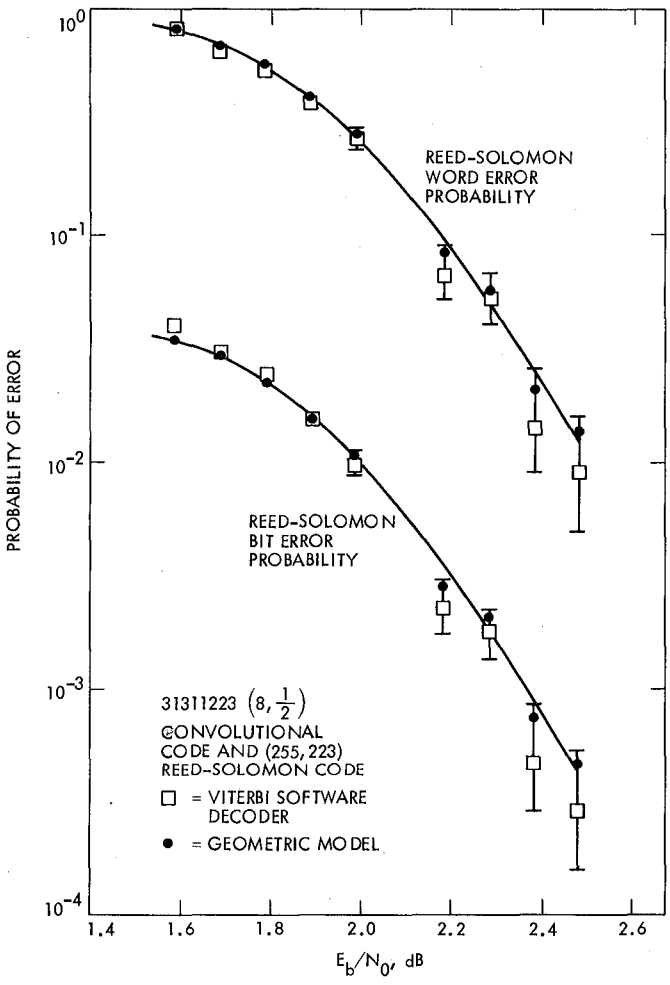

Fig. 5. Non-interleaved performance statistics for concatenated coding scheme assuming no system losses, (8, 1/2) convolutional code

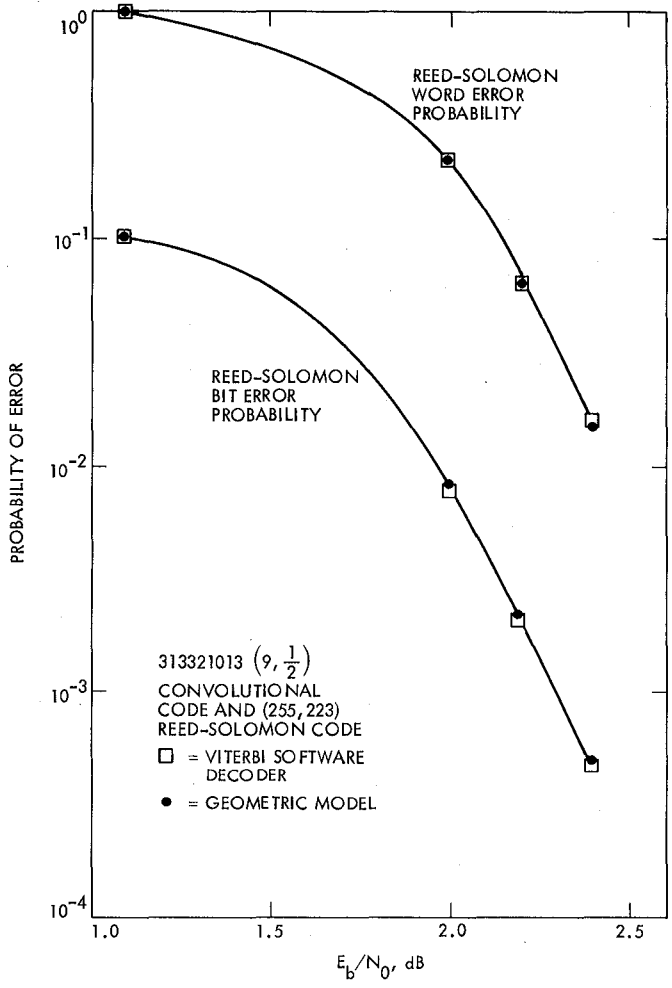

Fig. 6. Non-interleaved performance statistics for concatenated coding scheme assuming no system losses, (9, 1/2) convolutional code

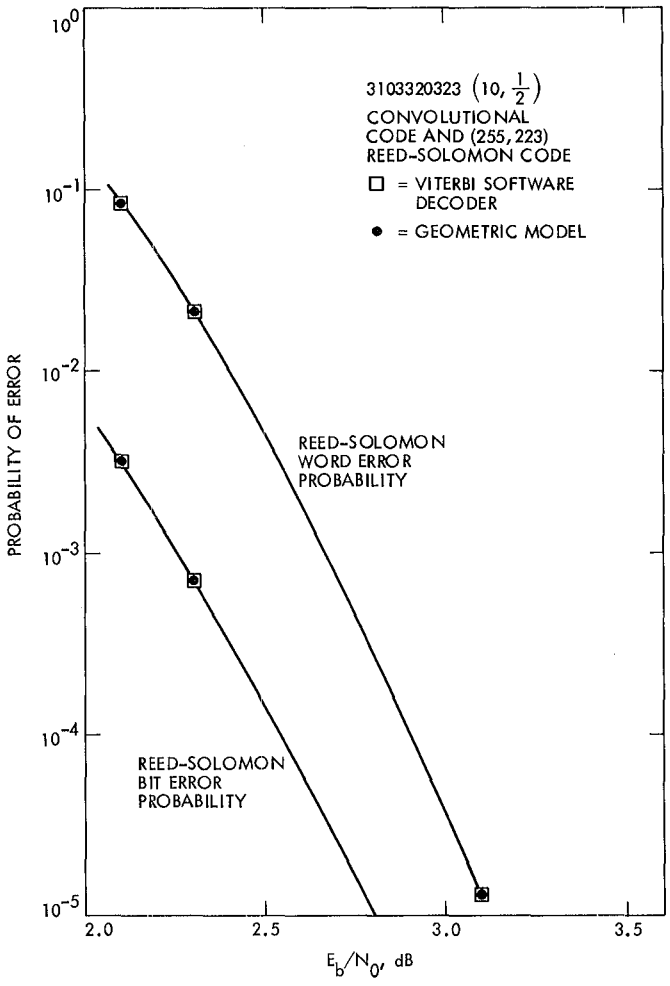

Fig. 7. Non-interleaved performance statistics for concatenated coding scheme assuming no system losses, (10, 1/2) convolutional code

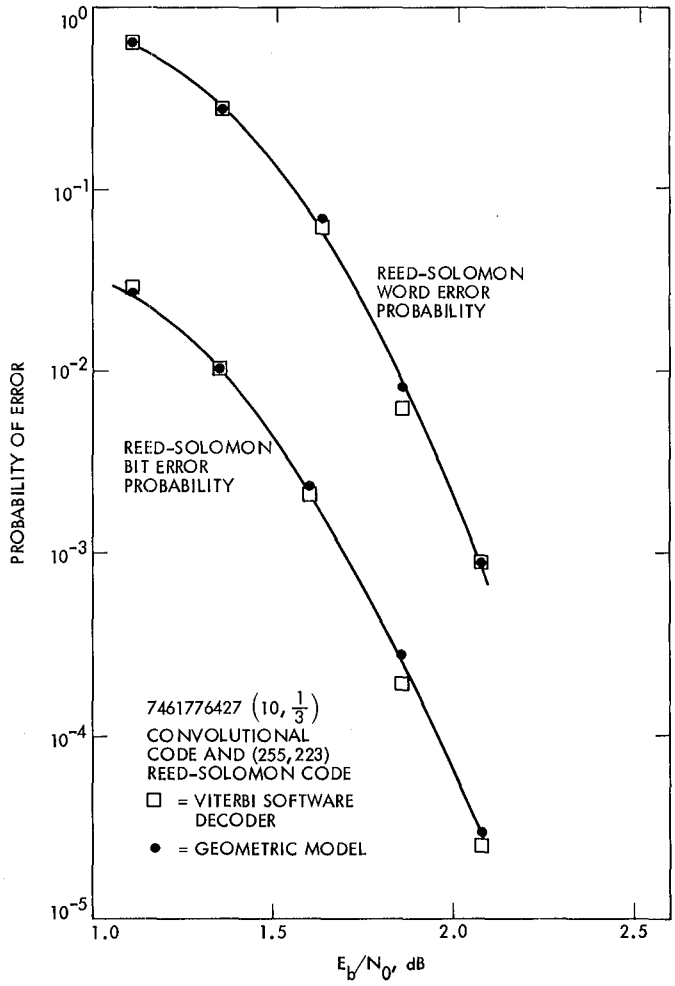

Fig. 8. Non-interleaved performance statistics for concatenated coding scheme assuming no system losses, (10, 1/3) convolutional code

An Efficient Technique for the Performance Evaluation of Antenna Arrays with Noisy Carrier Reference

T. Y. Yan and L. Clare
Communications Systems Research Section

An efficient computational technique is developed to evaluate the performance of coherent receivers with noisy carrier reference and multiple antennas. The received signal is assumed to be uncoded residual carrier BPSK (binary phase shift keying), with a PLL used for extracting the carrier. Explicit relationships between the error probabilities and the various system parameters are given. Specific results are given for the performance gain of combined carrier referencing over baseband only combining when the channel alignment process is ideal. A simple asymptotic expression for the performance gain is determined when the number of antennas used is increased without bound. An example using a Block III DSN PLL illustrates the performance of each arraying structure. The technique used in this paper is applicable to the performance evaluation for other receivers having similar decision statistics.

I. Introduction

This paper presents a technique for computing the probability of an uncoded bit detection error for a coherent receiver with a noisy carrier reference. The received signal is assumed to be a BPSK (binary phase shift keying) waveform, with a residual carrier that is extracted by means of a phase locked loop (PLL). The generality of the technique allows the application to multiple antenna receivers. In this paper, we compare two basic designs for antenna arraying: combined carrier referencing and baseband only combining.

The structures of these two basic designs are illustrated in Figs. 1 and 2. Due to the different path lengths between the antennas and the transmitting source, the received RF signals will be delayed relative to each other. We assume that no attempt to compensate for these delays is made prior to the point of input illustrated in Figs. 1 and 2.

In baseband only combining (Fig. 1), each IF channel has its own PLL. Each PLL derives a reference which is used to demodulate that channel to baseband. The alignment of the baseband signals is then performed, after which they are coherently added together. Bit detection is then accomplished using the combined signal.

In combined carrier referencing (Fig. 2), the alignment is performed immediately at IF (intermediate frequency) thus allowing coherent summation and a resultant SNR gain at IF. A single PLL is now used to derive the carrier reference. The loop SNR is correspondingly higher than in the baseband case, hence the derived reference will have a smaller phase error. This reference is used to mix down to baseband, whereupon the detection is performed as in the baseband case.

This paper compares the performance of each of these structures under the assumption that the alignment processes

are perfect. We will see that combined carrier referencing yields superior performance. The problem, of course, is that it is more difficult to align at IF than at baseband. Thus combined carrier referencing will be more costly and will depend more critically on alignment errors.

The development of the technique presented in this paper was motivated by the anticipated need for antenna arraying at Voyager Uranus encounter. For this mission $B_L T_b$ will be much smaller than unity, where B_L is the PLL loop bandwidth and T_b is the bit interval. The technique given provides an efficient means for evaluating the performance of a multiple antenna coherent receiver of uncoded BPSK data whenever $B_L T_B \ll 1$.

Lindsey (Ref. 1) showed that when $B_L T_b \ll 1$ the performance evaluation of a (single antenna) coherent receiver reduces to calculating an integral of the form

$$\int_0^{\pi} \frac{\exp[\rho \cos\phi]}{\pi I_0(\rho)} Q(\alpha \cos\phi)\, d\phi \tag{1}$$

where I_0 is the zeroth order modified Bessel function and

$$Q(x) = \int_x^{\infty} \frac{e^{-t^2/2}}{\sqrt{2\pi}}\, dt \tag{2}$$

The integral (1) may be computed by numerical integration. Alternatively, the integration may be carried out analytically, yielding an infinite series of Bessel functions. Neither of these methods are as efficient as the one described in this paper.

Layland (Ref. 2) essentially showed that for baseband only combining (1) becomes a volume integral of dimensionality equal to the number of antennas. Results are given in Ref. 2 for the two antenna baseband array.

In the case of $B_L T_b \gg 1$ the performance is easily computed; expressions for the multiple antenna case are given in this paper. Exact performance evaluation for intermediate values of $B_L T_b$ is difficult, and has been approached using a Gaussian approximation for the phase error as well as the approximation $\cos\phi \cong 1 - \phi^2/2$ for the detector characteristic (Refs. 3-5). Layland used these ideas for some of his two antenna baseband array results. We will not be concerned with these intermediate ranges in this paper. However, it should be noted that the performance for intermediate values of $B_L T_b$ can be bounded by the results obtained using the $B_L T_b \ll 1$ and $B_L T_b \gg 1$ techniques; this is verified using convexity arguments (Ref. 3).

Recent work on evaluating the performance of antenna arrays has been done by Divsalar, Hansen and Yuen (Ref. 12), and Deutsch, Miller and Butman (Ref. 13). Both of these papers are concerned with coded BPSK signals, and use numerical multidimensional integration to obtain specific results. Additionally, simulation results are reported in Ref. 13. Here we evaluate the performance for the uncoded BPSK signal. An upper bound on the bit error probability for the coded case can be obtained by applying the union bound to the uncoded results (Ref. 14).

This paper is organized into six sections. The mathematical model will be developed in section II. The derivation and general form for the basic computational technique is presented in section III. In section IV we determine the relative asymptotic performance between the two arraying structures as the number of antennas increases without bound. Section V gives numerical results using receiver specifications from the Deep Space Network (DSN). Finally, the last section presents a summary and describes possible extensions of the technique.

II. Mathematical Model

Suppose that the incoming IF signals illustrated in Figs. 1 and 2 are given by

$$y_m(t) = \sqrt{2P_m} \cos[\omega_I (t - t_m) + \theta_0 + \theta D(t - t_m)] + n_m(t), m = 1, \cdots, M \tag{3}$$

where

M = number of antennas

ω_I = radian IF

θ_0 = unknown constant phase

θ = modulation index

$D(t)$ = NRZ (nonreturn to zero) data stream, consisting of equiprobable + or −1 symbols during each interval $[(k-1)T_b, kT_b)$, k integer

T_b = bit interval

P_m = signal power in the m^{th} channel

t_m = delay in m^{th} channel due to path differences

$n_m(t)$ = white Gaussian thermal noise in m^{th} channel, assumed to be independent of $D(t)$ and of $n_l(t)$ for $l \neq m$

$N_m/2$ = two-sided power spectral density of $n_m(t)$

In our analysis we assume the alignment process is perfect in either case; thus we may take $t_m = 0$ for all m.

A. Baseband Only Combining

Each PLL forms a carrier reference

$$r_m(t) = \sqrt{2} \sin [\omega_I t + \theta_0 + \phi_m(t)] \quad m = 1, \cdots, M \tag{4}$$

where $\phi_m(t)$ is the phase reference error. From Ref. 6, the stochastic process $\phi_m(t)$ has a stationary probability density given by

$$p(\phi_m) = \lim_{t \to \infty} P(\phi_m(t)) = \frac{\exp [\rho_m \cos \phi_m]}{2\pi I_0 (\rho_m)}, \; -\pi \leqslant \phi_m < \pi \tag{5}$$

where I_0 is the zeroth order modified Bessel function, and where ρ_m is the loop equivalent SNR:

$$\rho_m = \frac{P_{cm}}{N_m B_m (P_{cm}/N_m)} \tag{6}$$

where

P_{cm} = m^{th} channel residual carrier power

$= P_m \cos^2 \theta$

and

$B_m(\cdot)$ = m^{th} PLL loop bandwidth, which is a function of P_{cm}/N_m

Mixing $r_m(t)$ and $y_m(t)$ yields the baseband signals

$$U_m(t) = \sqrt{P_m} \sin \theta \, D(t) \cos [\phi_m(t)] + q_m(t) \quad m = 1, \cdots, M \tag{7}$$

where $q_m(t)$ may be taken to still be white noise with density $N_m/2$. We approximate the situation by assuming $q_m(t)$ and $\phi_m(t)$ are independent processes. The bias term

$$\sqrt{P_m} \cos \theta \sin [\phi_m(t)]$$

has been subtracted out of (7). In practice, this term is spectrally isolated by multiplying $D(t)$ by a squarewave subcarrier.

At this point the signals are aligned. We then form the weighted sum

$$\sum_{m=1}^{M} W_m U_m(t)$$

(Note that the values of the optimal weights are not obvious due to the noisy phase term.)

The detector then finds (assuming perfect bit synchronization)

$$Y_B = \int_0^{T_b} \sum_{m=1}^{M} W_m \left\{ \sqrt{P_m} \sin \theta \, D(t) \cos [\phi_m(t)] + q_m(t) \right\} dt$$

$$= D(0) \sum_{m=1}^{M} W_m \sqrt{P_m} \sin \theta \int_0^{T_b} \cos [\phi_m(t)] \, dt + \nu \tag{8}$$

where ν is a zero mean Gaussian random variable with variance

$$\sigma_B^2 = \sum_{m=1}^{M} W_m^2 \frac{N_m T_b}{2} \tag{9}$$

The Bayes estimate of $D(0)$ is

$$\hat{D}(0) = \begin{cases} +1 \text{ if } Y_B > 0 \\ -1 \text{ if } Y_B < 0 \end{cases} \tag{10}$$

Assuming $D(0) = +1$ was sent, a bit detection error is made with probability

$$PE_B = Pr \{ Y_B < 0 \mid D(0) = +1 \} \tag{11}$$

B. Combined Carrier Referencing

In this case the signals are aligned immediately at IF. Then the weighted sum is formed

$$z(t) = \sum_{m=1}^{M} W'_m y_m(t) \tag{12}$$

The optimum weights are given by

$$W'_m = c \frac{\sqrt{P_m}}{N_m} \tag{13}$$

for any constant $c \neq 0$.

The total signal power is

$$\left(\sum_{m=1}^{M} W'_m \sqrt{P_m} \right)^2 \tag{14}$$

and the residual carrier power is

$$P_c = \left(\sum W'_m \sqrt{P_m} \cos \theta \right)^2 \tag{15}$$

Since the noise adds noncoherently, the resultant two-sided noise power spectral density is

$$\frac{N}{2} = \sum_{m=1}^{M} W'^2_m \frac{N_m}{2} \tag{16}$$

The case of combined carrier referencing is equivalent to a single antenna with the above power levels. The reference phase error ϕ has a density of the form given by (5) where the loop SNR is

$$\rho_c = \frac{P_c}{NB_L (P_c/N)} \tag{17}$$

where $B_L(\cdot)$ is the (single) PLL loop bandwidth. If optimal weighting is used then

$$\rho_c = \sum_{m=1}^{M} \frac{P_m \cos^2 \theta}{N_m B_L (P_c/N)} \tag{18}$$

The detector output is then

$$Y_c = D(0) \int_0^{T_b} \cos [\phi(t)]\, dt \left(\sum_{m=1}^{M} W'_m \sqrt{P_m} \sin \theta \right) + \nu' \tag{19}$$

where ν' is a zero mean Gaussian random variable with variance

$$\sigma_c^2 = \sum_{m=1}^{M} W'^2_m \frac{N_m T_b}{2} \tag{20}$$

Using a decision rule similar to (10), we obtain a bit detection error with probability

$$PE_c = Pr \{Y_c < 0 \mid D(0) = +1\} \tag{21}$$

III. Performance Evaluation

The decision statistics given by (8) and (19) depend on the evaluation of the integral

$$\frac{1}{T_b} \int_0^{T_b} \cos [\phi(t)]\, dt \tag{22}$$

In general, we require the joint density function for every finite set of points to characterize the stochastic process $\phi(t)$. However, if we assume $B_L T_b << 1$, the integrand will essentially be constant over the entire bit duration. Since the decision process is independent from one interval to the other, we can write

$$\frac{1}{T_b} \int_0^{T_b} \cos [\phi(t)]\, dt \approx \cos \phi \tag{23}$$

where ϕ is a random variable with density function given by (5). Hence for baseband only combining, from (8)

$$Y_B = D(0) \sum_{m=1}^{M} \alpha_m \cos \phi_m + \nu \tag{24}$$

where ϕ_m is the phase reference error from the m^{th} PLL, and

$$\alpha_m = W_m T_b \sqrt{P_m} \sin \theta \quad , \quad m = 1, \ldots, M.$$

Also, for combined carrier referencing, from (19)

$$Y_c = D(0)\, \alpha' \cos \phi' + \nu' \tag{25}$$

where ϕ' is the phase reference error from the single PLL and

$$\alpha' = T_b \sum_{m=1}^{M} W'_m \sqrt{P_m} \sin\theta$$

As was pointed out in section II, determination of the performance of a carrier array is mathematically equivalent to that of a single antenna with the appropriate parameter settings. Therefore, we will concentrate on evaluating the baseband array performance, and identify the carrier array result as a special case.

For baseband only combining, if we condition on $D(0) = +1$, the decision statistic Y_B involves a random variable of the form

$$X = \sum_{m=1}^{M} \alpha_m \cos\phi_m$$

where the α_m's are constants and the ϕ_m's are independent random variables with density functions $p(\phi_m)$ given by (5).

We extend the density function $p(\phi_m)$ to $\hat{p}(\phi_m)$ such that

$$\hat{p}(\phi_m) = \sum_{n=-\infty}^{\infty} p(\phi_m + 2n\pi)$$

Hence

$$\hat{p}(\phi_m) = \hat{p}(\phi_m + 2\pi)$$

and

$$\hat{p}(\phi_m) = \sum_{n=-\infty}^{\infty} C_{n,m} e^{jn\phi_m}$$

where

$$C_{n,m} = \frac{1}{2\pi} \int_{-\pi}^{\pi} p(\phi_m)\, e^{-jn\phi_m}\, d\phi_m$$

From (5)

$$C_{n,m} = \frac{1}{2\pi} \frac{I_n(\rho_m)}{I_0(\rho_m)} \tag{26}$$

where $I_n(\rho)$ is the n^{th} order modified Bessel function.

The characteristic function of the random variable X can be found to be

$$\Phi_X(u) = E[e^{-juX}] = \prod_{m=1}^{M} \sum_{n=-\infty}^{\infty} 2\pi j^n C_{n,m} J_n(-u\alpha_m) \tag{27}$$

where $J_n(\cdot)$ is the n^{th} order Bessel function.

Substituting (26) into (27) and using the identities (Ref. 7, p. 30)

$$I_n(\rho) = j^n J_n(-j\rho)$$

and

$$J_0(x+y) = \sum_{n=-\infty}^{\infty} J_{-n}(x) J_n(y) \quad ,$$

we obtain

$$\Phi_X(u) = \prod_{m=1}^{M} \frac{I_0(\rho_m - ju\alpha_m)}{I_0(\rho_m)} \tag{28}$$

From (24) (or (25)), the decision statistic is of the form

$$Y = X + n \tag{29}$$

where X and n are independent and where n is a Gaussian random variable with zero mean and variance σ_n^2.

The characteristic function of the random variable Y will be given by

$$\Phi_Y(u) = \Phi_X(u)\, e^{-\frac{1}{2}\sigma_n^2 u^2}$$

$$= e^{-\frac{1}{2}\sigma_n^2 u^2} \prod_{m=1}^{M} \frac{I_0(\rho_m - ju\alpha_m)}{I_0(\rho_m)} \tag{30}$$

From (11) (or (21)), the probability of making an error based on the statistic Y in (29) can be written as

$$PE = \int_{-\infty}^{0} \left[\frac{1}{2\pi} \int_{-\infty}^{\infty} \Phi_Y(u)\, e^{juy}\, du \right] dy \tag{31}$$

Assuming we can interchange the order of integration, and recognizing (Ref. 8, p. 42)

$$\int_{-\infty}^{0} e^{juy}\, dy = \pi\delta(u) + \frac{1}{ju}$$

we can write

$$PE = \frac{1}{2} + \frac{1}{2\pi j} \int_{-\infty}^{\infty} \frac{1}{u} e^{-\frac{1}{2}\sigma_n^2 u^2} \Phi_X(u)\, du$$

From the Taylor Series Expansion of $\Phi_X(u)$, after some mathematical manipulation, we obtain (Ref. 9, p. 302)

$$PE = \frac{1}{2} + \sum_{k=1}^{\infty} \frac{(-1)^k E[X^{2k-1}]}{(2k-1)!} \int_0^{\infty} u^{2(k-1)} e^{-\frac{1}{2}\sigma_n^2 u^2}\, du$$

$$= \frac{1}{2} - \frac{1}{\sqrt{\pi}} \sum_{n=0}^{\infty} \frac{(-1)^n}{n!\,(2n+1)} E\left[\left(\frac{X}{\sqrt{2}\sigma_n}\right)^{2n+1}\right] \quad (32)$$

The probability of error for baseband only combining is determined using (32) with the appropriate moments. From (24) and (9) these can be written as

$$E\left[\left(\frac{X}{\sigma_n}\right)^{2n+1}\right] = E\left[\left(\sum_{m=1}^{M} \beta_m \cos\phi_m\right)^{2n+1}\right] \quad (33)$$

where

$$\beta_m = W_m \sqrt{\frac{2E_m}{\sum_{k=1}^{M} W_k^2 N_k}} \sin\theta, \quad m = 1, \ldots, M \quad (34)$$

and

$$E_m = P_m T_b$$

is the energy per bit at the m^{th} antenna input. The moments (33) can be evaluated by the iterative procedure shown in the Appendix. The technique given there is similar to the one used by (Ref. 10, 11).

The probability of error for combined carrier referencing is also computed using (32). In this case (25) and (20) imply

$$E\left[\left(\frac{X}{\sigma_n}\right)^{2n+1}\right] = E\left[(\beta' \cos\phi')^{2n+1}\right] \quad (35)$$

where

$$\beta' = \frac{\sum_{k=1}^{M} W_k' \sqrt{2E_k}}{\sqrt{\sum_{l=1}^{M} W_l'^2 N_l}} \sin\theta \quad (36)$$

It is interesting to note that if X in (32) is almost surely constant then

$$E\left[\left(\frac{X}{\sqrt{2}\sigma_n}\right)^{2n+1}\right] = \left(\frac{X}{\sqrt{2}\sigma_n}\right)^{2n+1}$$

and

$$PE = \frac{1}{2} - \frac{1}{\sqrt{\pi}} \sum_{n=0}^{\infty} \frac{(-1)^n}{n!\,(2n+1)} \left(\frac{X}{\sqrt{2}\sigma_n}\right)^{2n+1} = Q\left(\frac{X}{\sigma_n}\right) \quad (37)$$

where $Q(x)$ is given by (2). Equation (37) is the well known result for the error probability of using BPSK across a white Gaussian noise channel with no phase reference error.

In the next section, we will show that for a large number of antennas, essentially the Strong Law of Large Numbers guarantees that the k^{th} moment converges to the first moment to the k^{th} power. This has been observed in computations using the algorithm of the appendix.

IV. Asymptotic Performance

In this section we determine the performance of baseband only combining as the number of antennas approaches infinity, and compare it to that of combined carrier referencing. The antennas are assumed to be identical and are weighted equally. For baseband only combining all the β_m's of (34) are equal and given by

$$\beta_m = \frac{1}{M}\sqrt{\frac{2ME_b}{N_0}} \sin\theta \quad (38)$$

where $E_b = E_m$ and $N_o = N_m$ for $m = 1, 2, \cdots, M$. Using (8) and (11), by first conditioning on the vector of phase errors, we obtain

$$PE_B = E[Q(B)] \quad (39)$$

where $Q(\cdot)$ is given by (2), and B is the random variable

$$B = \sqrt{\frac{2ME_b}{N_0}} \sin\theta \frac{1}{M} \sum_{m=1}^{M} \frac{1}{T_b} \int_0^{T_b} \cos\phi_m(t)\, dt \quad (40)$$

The variance of B is

$$\text{Var}[B] = \frac{2E_b}{N_0} \sin^2\theta \text{ Var } [Z_1] \quad (41)$$

where

$$Z_1 = \frac{1}{T_b} \int_0^{T_b} \cos\phi_1(t)\, dt \quad (42)$$

Since $|Z_1| \leq 1$, Var $[Z_1] \leq 1$. If we fix the total system energy per bit

$$E_s = ME_b$$

then

$$\text{Var } [B] \leq \frac{1}{M} \frac{2E_s}{N_0} \sin^2\theta$$

tends to zero as M increases, and we may approximate B by its mean. Taking the expectation inside the integral (42) and using the density function (5) we obtain

$$E[Z_1] = \frac{I_1(\rho_B)}{I_0(\rho_B)} \quad (43)$$

where ρ_B is the common loop SNR for each PLL. Thus for $E_b/N_0 << 1$ (typically true for $M >> 1$ and fixed E_s/N_0)

$$PE_B \approx Q\left[\sqrt{\frac{2ME_b}{N_0}} \sin\theta \frac{I_1(\rho_B)}{I_0(\rho_B)}\right], \frac{E_b}{N_0} << 1 \quad (44)$$

To compare this with the performance of combined carrier referencing, PE_c can be evaluated by (32) and (35), and is available in graphical form (Ref. 6). Alternatively, it may be possible to approximate PE_c as well. Assuming a similar PLL is used, $M >> 1$ implies $\rho_c >> \rho_B$ so that the phase error will be essentially zero. Then from (35) and (37)

$$PE_c \approx Q\left[\sqrt{\frac{2ME_b}{N_0}} \sin\theta\right], \rho_c >> 1 \quad (45)$$

From (44) and (45) we can define the asymptotic power loss L_∞ due to baseband only combining relative to combined carrier referencing as

$$L_\infty(\rho_B) = \left[\frac{I_1(\rho_B)}{I_0(\rho_B)}\right]^2, \frac{E_b}{N_0} << 1, \rho_c >> 1 \quad (46)$$

The conditions required by (46) will typically be satisfied when $M >> 1$.

The results given thus far in this section are independent of any assumption on $B_L T_B$. If $B_L T_B >> 1$ (slow rate model) then (42) can be treated as a time average, and (44) will be true for any M and E_b/N_0. PE_c may be obtained using (44) and replacing ρ_B by ρ_C. Thus we may define the relative power loss for this case as

$$L(\rho_B, \rho_C) = \frac{\left[\frac{I_1(\rho_B)}{I_0(\rho_B)}\right]^2}{\left[\frac{I_1(\rho_c)}{I_0(\rho_c)}\right]^2} \quad (47)$$

V. Numerical Example

In both (33) and (35), the density functions of ϕ' and ϕ_m, $m = 1, \ldots, M$, depend on the corresponding loop SNRs. The loop SNR depends on the loop bandwidth B_L, which in turn is a nonlinear function of the input signal and noise levels. The specific PLL design we use for our numerical example is based on Deep Space Network Block III receiver data. The nominal loop bandwidth is $2B_{LO} = 12$ Hz. Hence for any given T_b, θ, and set of E_m/N_m and $W_m, m = 1, 2, \ldots, M$, the corresponding loop SNR can be determined from either (6) or (17).

We consider an example where all antennas are identical and have unity weights (the theory does not require this assumption). In this case, all E_m/N_m, $m = 1, 2, \ldots, M$ become identical and are given by E_b/N_0, where E_b/N_0 is the energy per bit to noise ratio at each antenna input. Figure 3 shows the error probability based on the bit interval being 50 μs and the modulation index being 80°. Since $B_L T_b$ is much

smaller than unity, (32) will yield exact performance results under the assumption the channel alignment process is ideal.

Figure 4 shows the comparative performance difference between the two arraying structures for the same example. Since combined carrier referencing always gives superior performance over baseband only combining, Fig. 4 shows the additional amount of signal energy required at each antenna input of the baseband array in order to obtain the same error probabilities as the carrier array. Note that when E_b/N_0 is small, there is not enough signal power for the PLL to extract the phase reference in the baseband array. A large number of antennas is then necessary to match the performance of combined carrier referencing. However, when E_b/N_0 increases, the performance of baseband only combining matches that of combined carrier referencing with a small number of antennas.

VI. Summary and Future Extension

In this paper, we have examined the performance of two antenna arraying techniques which may be used in the Deep Space Network. The computational technique developed can be applied to any combination of antennas. These antennas need not be identical. A simple expression is given to determine the asymptotic comparative performance between the two arraying structures.

Specifically, we have shown that with a Block III DSN PLL and three identical antennas, combined carrier referencing will provide a 0.2 to 0.3 dB improvement over baseband only combining for the range of interest. Explicit error probability versus E_b/N_o is given for either configuration. As shown in Fig. 4, the ultimate gain to be achieved by using combined carrier referencing over baseband only combining is quickly approached with a small number of antennas.

Throughout this paper it has been assumed that a BPSK signal is used. It would seem likely that the same technique can be used to determine the error probability for DPSK (differential phase shift keying). Also, in attempting to study the case of MPSK (M-ary phase shift keying) signals, one encounters the following generalization of (31):

$$PE(k) = \int_{-\infty}^{\infty}\int_{-\infty}^{\infty} \Phi_Y(u,v) \left[\int_{-\infty}^{\infty}\int_{-\infty}^{\infty} I_k(x,y)\, e^{j(ux+vy)}\, dxdy\right] du\, dv$$

where $PE(k)$ is the error probability conditioned on the k^{th} message being sent, Φ_Y is the characteristic function for the two-dimensional statistic $\underline{Y}$, and I_k is the indicator function for the k^{th} decision region. Evaluation of the inner double integral via generalized functions may provide an easily evaluatable expression for $PE(k)$.

References

1. Lindsey, W. C., "Optimal Design of One-Way and Two-Way Coherent Communication Links," *IEEE Trans. Comm. Technology*, Vol. COM-14, No. 4, pp. 418-431, Aug. 1966.

2. Layland, J. W., "Noisy Reference Effects on Multiple-Antenna Reception," Deep Space Network Progress Report 42-25, pp. 60-64, Jet Propulsion Laboratory, Pasadena, Calif., Feb. 15, 1975.

3. Tauseworthe, R. C., "Efficiency of Noisy Reference Detection," in *Supporting Research and Advanced Development*, Space Programs Summary 37-54, Vol. III, pp. 195-201, Jet Propulsion Laboratory, Pasadena, Calif., Dec. 31, 1968.

4. Blake, J. F., and Lindsey, W. C., "Effects of Phase-Locked Loop Dynamics on Phase-Coherent Communications," in *Supporting Research and Advanced Development*, Space Programs Summary 37-54, Vol. III, pp. 192-195, Jet Propulsion Laboratory, Pasadena, Calif., Dec. 31, 1968.

5. Layland, J. W., "A Note on Noisy Reference Detection," in *The Deep Space Network Progress Report*, Technical Report 32-1526, Vol. XVII, pp. 83-88, Jet Propulsion Laboratory, Pasadena, Calif., Oct. 15, 1973.

6. Viterbi, A. J., *Principles of Coherent Communications*, pp. 86-96, McGraw-Hill Book Co., Inc., New York, 1966.

7. Watson, G. N., *Theory of Bessel Functions*, Cambridge University Press, London, 1966.

8. Lighthill, M. J., *Fourier Analysis and Generalised Functions*, Cambridge University Press, London, 1958.

9. Abramowitz, M., and Stegum, I. A., *Handbook of Mathematical Functions*, Dover Publications, Inc. New York, 1972.

10. Prabhu, V. K., "Some considerations of error bounds in digital systems," *Bell System Technical Journal*, vol. 50, pp. 3127-3151, Dec. 1971.

11. Benedetto, S., De Vincentiis, G., and Luvison, A., "Error Probability in the Presence of Intersymbol Interference and Additive Noise for Multilevel Digital Signals," *IEEE Trans. on Comm.* Vol. 21, pp. 181-190, March 1973.

12. Divsalar, D., Hansen, D., and Yuen, J., "The Effect of Noisy Carrier Reference on Telemetry with Baseband Arraying," in *The Telecommunications and Data Acquisition Progress Report 42-63*, Jet Propulsion Laboratory, Pasadena, Calif., June 15, 1981.

13. Deutsch, L. J., Miller, R. L., Butman, S. A., "New Results on Antenna Arraying", in *The Telecommunications and Data Acquisition Progress Report 42-62*, Jet Propulsion Laboratory, Pasadena, Calif., April 15, 1981.

14. Viterbi, A. J., and Omura, J. K., *Principles of Digital Communication and Coding*, McGraw-Hill Book Co., Inc., New York, 1979.

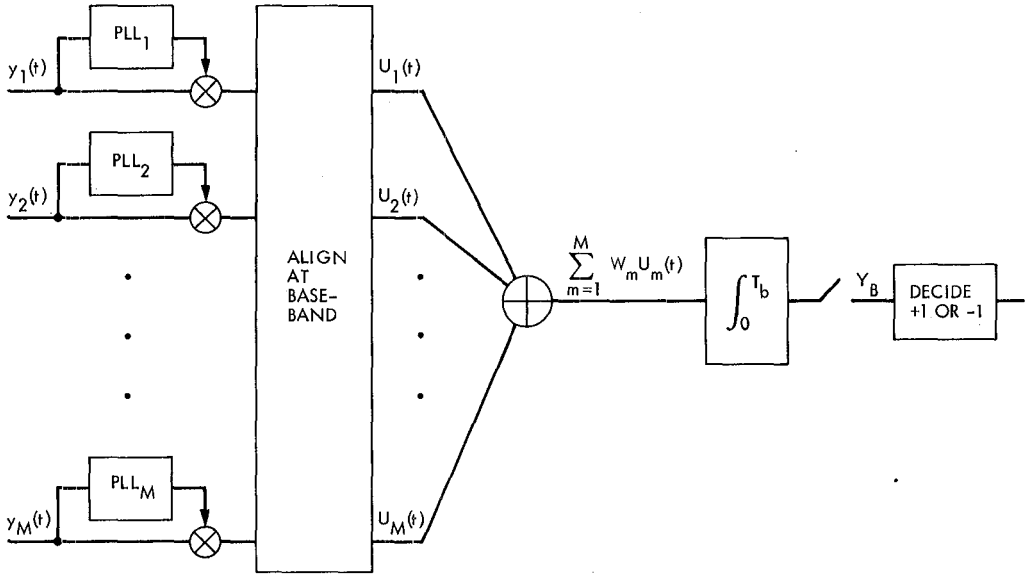

Fig. 1. Baseband only combining model

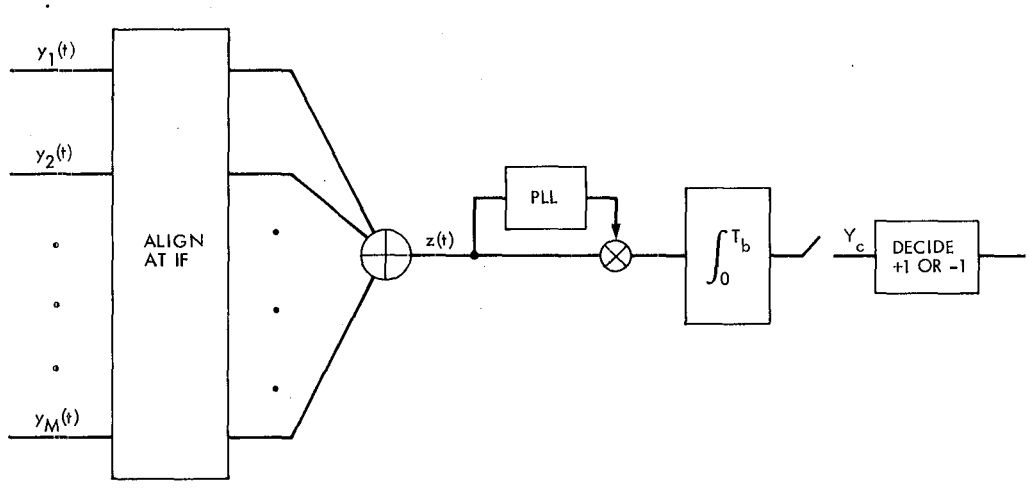

Fig. 2. Combined carrier referencing model

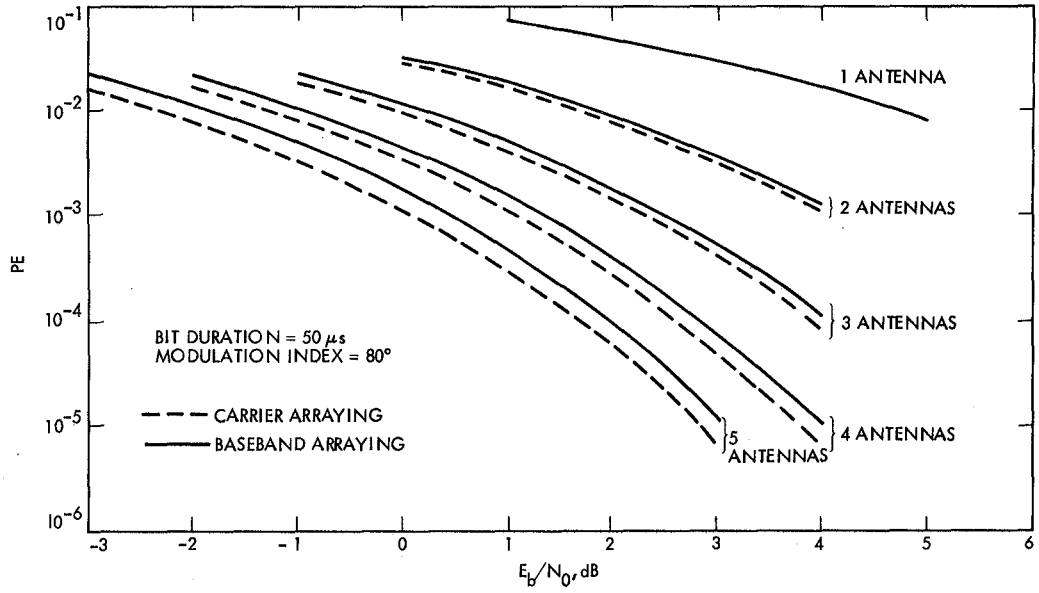

Fig. 3. Error probability versus E_b/N_0 for antenna arrays

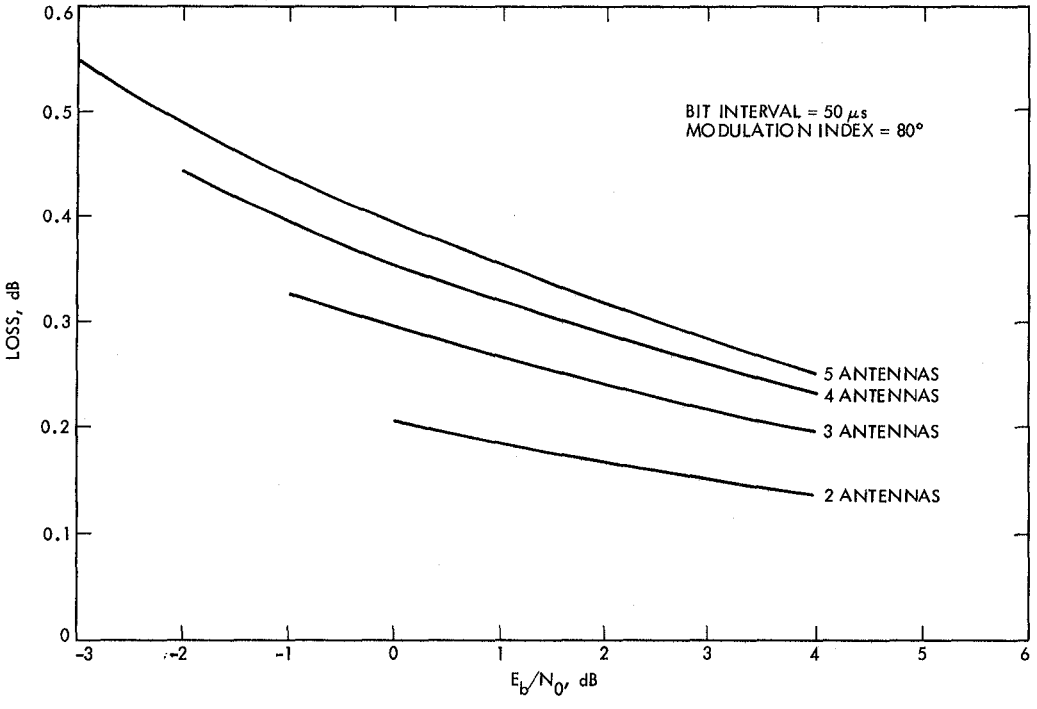

Fig. 4. Comparative performance loss between combined carrier referencing and baseband only combining

Appendix A

Evaluation of Moments

This appendix describes the computation of moments for the random variable.

$$X = \sum_{m=1}^{M} \beta_m \cos \phi_m$$

where β_m's are scalar constants and ϕ_m's are independent random variables with the Tikhonov density functions given by (5).

Define

$$Y_0 = 0$$

and

$$Y_n = Y_{n-1} + \beta_n \cos \phi_n \quad n = 1, \ldots, M \tag{A-1}$$

Then

$$X = Y_M$$

and

$$EX^k = EY_M^k$$

From (A-1)

$$EY_n^k = \sum_{j=0}^{k} \binom{k}{j} \beta_n^{k-j} E(Y_{n-1}^j) E \cos^{(k-j)} \phi_n \tag{A-2}$$

$$n = 1, \ldots, M \quad k = 0, 1, 2, \cdots$$

Hence all the moments of the random variable X can be evaluated recursively by (A-2) given $E(\cos^l \phi_n)$, $l = 1, \ldots, K$, $n = 1, \ldots, M$, where K is the largest moment required. From Ref. 9, p. 376,

$$\frac{d^k I_n(u)}{du^k} = \frac{1}{2^k} \left\{ I_{n-k}(u) + \binom{k}{1} I_{n-k+2}(u) + \binom{k}{2} I_{n-k+4}(u) + \cdots + I_{n+k}(u) \right\}$$

$$k = 0, 1, 2, \cdots \tag{A-3}$$

Then

$$E[\cos^l \phi_n] = \left(\frac{1}{2}\right)^l \sum_{m=0}^{l} \binom{l}{m} \frac{I_{2m-l}(\rho_n)}{I_0(\rho_n)} \tag{A-4}$$

for $l = 1, \cdots, K$ and $n = 1, \cdots, M$

Therefore

$$EY_n^k = \sum_{j=0}^{k} \binom{k}{j} \left(\frac{\beta_n}{2}\right)^{k-j} F_{k-j}(\rho_n) [E Y_{n-1}^j] \tag{A-5}$$

where

$$F_m(\rho) = \sum_{j=0}^{m} \binom{m}{j} \frac{I_{2j-k}(\rho)}{I_0(\rho)}$$

Define

$$E\bar{Y}_n = (EY_n^1, EY_n^2, EY_n^3, \cdots, EY_n^k)' \tag{A-6}$$

Then

$$E\bar{Y}_n = \underline{A}_n E\bar{Y}_{n-1} + \bar{B}_n \quad \text{for } n \geq 1 \tag{A-7}$$

and

$$E\bar{Y}_0 = \bar{0}$$

where

$$\underline{A}_n = \left\{a_{i,j}^{(n)}\right\}, \bar{B}_n = \left\{b_i^{(n)}\right\}$$

and

$$a_{i,j}^{(n)} = \begin{cases} 0 & \text{for } j > i \\ 1 & \text{for } j = i \\ \binom{i}{j}\left(\frac{\beta_n}{2}\right)^{(i-j)} F_{(i-j)}(\rho_n) & \text{for } i > j \end{cases}$$

$$b_i^{(n)} = \left(\frac{\beta_n}{2}\right)^i F_i(\rho_n)$$

Using (A-7)

$$E\overline{X} = E\overline{Y}_M$$

where

$$E\overline{X} = \left(EX, EX^2, EX^3, \cdots, EX^K\right)' .$$

Analysis of Capacitive Heat Exchangers Part I

D. Schonfeld
DSN Engineering Section

Governing equations are developed for a simple capacitive heat exchanger. This type of heat exchanger consists of hot spherical particles falling through an ascending cold gas stream. The assumptions made in deriving the continuity, momentum and energy equations are clearly stated. The analysis yields a system of first-order, ordinary, nonlinear equations which form a complex boundary-value problem. Part II of this report will present the method of solution together with a comparison between the performance of capacitive heat exchangers and conventional counter flow ones.

I. Introduction

Recently published works (Refs. 1, 2 and 3) propose a new concept in heat exchangers. The main idea is to have particles of a "hot" fluid fall through an ascending "cold" fluid. The heat exchange between the hot and cold streams takes place inside a duct which physically contains the two flows. In most analyses, the "cold" fluid is a gas stream. The origin of the hot particles depends on the applications. For example, when the particles are solid, they can originate in a packed bed; when they are fluid droplets, they can represent the cooling of a melt. Because the hot material consists of discrete particles of a different phase than that of the cooling steam, these heat exchangers have been labeled as capacitive.

Three potential advantages are claimed for capacitive heat exchangers. First, the two streams are in direct contact with each other. This eliminates the resistance to heat transfer which occurs when the fluids are separated by a tube wall. Second, the contact area between the two streams is greatly magnified because the heat exchange takes place on the entire surface of each of the particles. Finally, friction between the two fluids is less than when a solid interface is present. This promises reduced pumping power in capacitive heat exchangers.

Numerous heat exchangers exist throughout the Deep Space Network facilities. They range from those heat exchangers serving the hydrostatic oil bearings of the antennas to a cooling tower for the heating, ventilation and air conditioning system. The large number of heat exchangers and their importance in maintaining the performance of the DSN systems require that possible improvements in their efficiency be thoroughly analyzed. As a result, a systematic investigation of capacitive heat exchangers has been performed and the present report gives some of the results of this investigation.

The physical phenomena that occur in capacitive heat exchangers are quite complex. Because of this complexity, the corresponding mathematical models are based on simplifying assumptions. With few exceptions (Ref. 4) the assumptions are not explicitly stated in the literature and the reader is

presented with a set of governing equations whose origin is dubious at best. Thus, one of the aims of this report is to present a detailed and explicit derivation of the basic equations that govern fluid-solid processes. In addition a thermal analysis of a capacitive heat exchanger under a given set of assumptions will also be presented.

In the second part of the report, a numerical solution of the equations will be presented. The numerical model allows a sensitivity analysis to be performed for a certain type of capacitive heat exchanger. Part II of this report will also suggest future lines of research in this field.

The system to be analyzed is shown in Fig. 1. The hot stream is made up of solid particles that fall through an ascending cold gas. The gas forms the continuous phase while the solid particles occupy only discrete volume elements and form the dispersed phase. The two phases (particles and gas) form a heterogeneous mixture with each phase occupying only part of the volume of the mixture.[1] Examples of other possible heterogeneous mixtures are given in Table 1 (Ref. 6).

The particles occupy only a fraction κ out of a unit volume of the mixture. Therefore, the gas occupies the remaining $(1 - \kappa)$ fraction. κ is generally a function of both space and time, $\kappa = \kappa\,(x, y, z, t)$, and is made up of a number of particles per unit volume of the mixture, N_D. If the volume of each particle is denoted by V_D, then

$$\kappa = N_D V_D$$

and N_D is also a function of space and time. The particles are of a material whose density is denoted by ρ_D. Therefore, the particles have a mass per unit volume (of the mixture) given by

$$\lambda_D = \kappa \rho_D = N_D V_D \rho_D$$

λ_D is sometimes called the species (or phase) density of the particles.

The continuous phase occupies $(1 - \kappa)$ out of a unit volume of the mixture and it is made up of a material whose density is denoted by ρ_c. Therefore, the species density for the continuous phase is given by $\lambda_c = (1 - \kappa)\,\rho_c = (1 - N_D V_D)\,\rho_c$. It is important to realize that in the analysis of multiphase flows the species densities are the counterparts of material density in single phase flows.

[1] This is in contrast with homogeneous mixtures (e.g., solutions, alloys, mixtures of gases) in which each component can be considered as occupying the entire volume of the mixture (Ref. 5).

The mathematical model of capacitive heat exchangers can be considerably simplified by assuming that the flow and heat transfer processes are one-dimensional and steady state. The one-dimensional assumption proposes uniformity of the variables in any given y-plane. There is only limited experimental evidence to back these hypotheses.[2] However, the advantage of these two assumptions is that they reduce the governing set of partial differential equations into ordinary ones. Furthermore, as the purpose of this paper is to analyze the simplest model of capacitive heat exchangers, these assumptions seem warranted at this juncture.

Many authors make the additional assumption that the length scale in which the flow parameters change substantially is much larger than the interparticle distance (Refs. 4, 5, 8). This implies a sufficiently large number of particles in a unit volume of the mixture. When N_D is "large enough," the dispersed phase can be treated as a pseudofluid and its governing equations can be written in the usual continuum form. The precise meaning of "large enough" is unclear even though it has important consequences for the physics of capacitive heat exchangers. For example, a very large number of particles tends to reduce radiative heat transfer between the container wall and the particles (Ref. 9). Furthermore, the question of partial pressures in such mixtures is not quite clear (Ref. 4, 5, 10). Examples of systems where it is justified to assume that N_D is "large enough" are fluidized beds and nuclear reactor accident analysis.

In contrast, an alternative approach is to assume that the volume fraction occupied by the particles is small and therefore the interactions between the particles can be neglected. Marble (Ref. 11) points out that even in this case, continuum relations can be written for the solid phase. For such situations, he notes that the velocities, temperatures and densities which appear in the equations are "values averaged over a gas volume containing several particles." This approach has been shown to give adequate results for the dynamics of dusty gases (Refs. 11, 12, 13). Such continuum conservation equations are especially useful when one discusses complex phenomena such as shock waves, for example (Refs. 11, 14). A similar approach, although more simplified, will be used in the next section.

II. Conservation Equations

The phenomena considered in this report are caused by the interactions between the continuous and dispersed phases.

[2] Counter flow experiments reported by El'Kin and Timofeyev (Ref. 7) indicate that at low particle loading ratios ($\eta \leqslant 7$) the distribution of solids over the cross-sectional area is almost uniform except in the entrance region. However, for higher loading ratios, large nonuniformities in the distribution appear both axially and in cross section.

Therefore, a mathematical analysis of the problem must include equations regarding the conservation of mass, momentum and energy of each of the phases. For both continuous and dispersed phases the equations are written in terms of a unit volume of the mixture. The volume fraction occupied by the particles is assumed to be small and therefore the partial pressure of the particles can be neglected. All particles are assumed to be spheres of identical radius r_D; this radius is assumed to be a known quantity. Closure relations for the problem are given by boundary conditions on the temperatures and velocities.

A. Continuity

1. Dispersed phase. No sources or sinks of mass are assumed to exist within the conduit. Therefore, the mass flow rate is given by:

$$\dot{m} = \rho_D \, v_D \, \kappa \, A$$

where A is the cross-sectional area of the conduit. With A a constant and with the one-dimensional and steady-state assumptions, the continuity equation is:

$$\frac{d\dot{m}}{dy} = \frac{d}{dy}(\rho_D \, v_D \, \kappa) = \frac{d}{dy}(\rho_D \, v_D \, N_D \, V_D) = 0$$

If there is no mass transfer, V_D is constant and the equation reduces to:

$$\frac{d\dot{m}}{dy} = \frac{d}{dy}(\rho_D \, v_D \, N_D) = 0 \tag{1}$$

When the material of the particles is such that its density is only a weak function of the temperature, then the continuity equation can be further simplified to:

$$\frac{d}{dy}(v_D \, N_D) = 0 \tag{2}$$

In these equations, v_D and N_D are quantities averaged over a unit volume of the mixture at a given location y. Therefore, Eqs. (1) and (2) can be written respectively as:

$$(\rho_D \, v_D \, N_D)_y = (\rho_D \, v_D \, N_D)_{y+\Delta y} \tag{3}$$

$$(v_D \, N_D)_y = (v_D \, N_D)_{y+\Delta y} \tag{4}$$

2. Continuous phase. In terms of the species densities of the gas, λ_c, the continuity equation is:

$$\frac{\partial \lambda_c}{\partial t} + \nabla \cdot (\lambda_c \, v_c) = 0 \tag{5}$$

With the steady-state and one dimensional assumptions this becomes:

$$\frac{d}{dy}(\lambda_c \, v_c) = \frac{d}{dy}[(1 - \kappa) \rho_c \, v_c] = 0 \tag{6}$$

Alternative forms are:

$$\frac{d}{dy}[(1 - N_D \, V_D) \rho_c \, v_c] = 0 \tag{7}$$

and

$$[(1 - \kappa) \rho_c v_c]_y = [(1 - \kappa) \rho_c \, v_c]_{y+\Delta y} \tag{8}$$

B. Conservation of Momentum

1. Dispersed phase. In terms of the species density, λ_D, conservation of momentum per unit volume of the mixture is given by[3]

$$\lambda_D \frac{Dv_D}{Dt} = \sum F \tag{9}$$

Equation (9) implies that the acceleration of the particles is balanced by the sum of the forces acting on them. The possibility also exists that after an initial acceleration the particles will reach a steady-state velocity. For this case the momentum equation reduces to:

$$\sum F = 0 \tag{10}$$

Both cases will be considered here.

The left-hand side of Eq. (9) is a product between a mass and an acceleration. When an object accelerates through a fluid it must overcome not only the fluid's resistance, but also the inertia of the fluid accelerated by the object. This is known as the added mass effect (Ref. 16). Since this "extra" mass is due to the fluid, it is based on the fluid's density. Therefore, the added mass can be neglected when $\rho_D \gg \rho_c$. This condition is met in gas-particle flows (Ref. 17) such as that discussed here.

The right-hand side of Eqs. (9) and (10) represents the sum of forces acting on the assembly of particles in a unit volume

[3] A distinction is necessary between "(rate of change of momentum) per unit volume" and "rate of change of (momentum per unit volume)." The former is expressed as $\lambda_D \, (Dv_D/Dt)$ while the latter by (D/Dt) $(\lambda_D v_D)$. For a discussion see Ref. 15.

of the mixture. These forces can be classified as (a) body forces, (b) surface forces and (c) interaction forces. The interaction forces can also be divided into (and lumped with) the body and surface forces. They are kept separated here to indicate their different origin, i.e., that they are due to the continuous phase. The only body forces considered in this report are due to gravitational effects and are given by

$$F_{\text{body}} = \rho_D \kappa g$$

A possible surface force is due to electric charges which reside on the particles (Ref. 18). Since in this report all interactions between particles are neglected, electric forces are neglected:

$$F_{\text{electric}} = 0$$

Three principal phase-interaction forces can occur in fluid-particles flows: the Magnus force, the buoyancy force and the drag force. The Magnus force is due to the rotation acquired by the particles while moving through the fluid.[4] Torobin and Gauvin (Ref. 16) divide this rotation into "screw motion," in which the rotation is perpendicular to the air flow direction, and "top spin," in which the rotation parallels the air flow. The latter is said to be more common and yet to have a negligible effect on the resistance to the motion. Experiments conducted at the Von Karman Institute for Fluid Dynamics (Ref. 20, 21) confirm that the Magnus force can be neglected relative to the other forces. The buoyancy force per particle is given by $\rho_c V_D g$. For an assembly of particles in a unit volume of the mixture, the buoyancy force becomes:

$$F_{\text{buoyancy}} = \rho_c \kappa g$$

The most important interaction force is the drag force. This is a product between a characteristic area of the particle, the kinetic energy of the flow per unit volume and the drag coefficient, C_d. The characteristic area is the surface that the body projects to the flow; for the assembly of particles this is $N_D \pi r_D^2$. The kinetic energy term is given by:

$$\frac{1}{2} \lambda_c v_c^2 = \frac{1}{2} (1 - \kappa) \rho_c v_{net}^2 = \frac{1}{2} (1 - N_D V_D) \rho_c v_{net}^2$$

where v_{net} is the net velocity difference between the two phases. To account for the different directions of the velocities, this can be written as

$$v_{net}^2 = (v_c - v_D) |v_c - v_D|$$

[4]The effect has been mentioned by Newton as early as 1672 and analyzed by Robins in 1805. Magnus worked unsuccessfully on the problem around 1877 (Ref. 19).

In general, the drag coefficient for an assembly of spherical particles is very difficult to determine and quite different from that for single spheres. The results given by Brinkman (Ref. 22) and Tam (Ref. 23) are valid only for low Reynolds numbers ($N_{Re} < 10$). Experiments have shown (Ref. 24) that for $N_{Re} < 300$ and for low values of κ, the drag coefficient is not much different from that of single spheres. For higher Reynolds numbers, the data compiled by Soo (Ref. 25) show a wide variety of results. Figure 2 (Ref. 26) illustrates the variation of the drag coefficient vs the Reynolds number for various values of κ. The large uncertainty in the data has led Rudinger (Ref. 14) to observe that "in numerical evaluations of specific flows, at least the sensitivity of the results to various assumptions for the drag coefficient should be assessed."

In this report the drag coefficient is written as $\overline{C}_d$ to denote that it applies to the sum of the particles in a unit volume of the mixture.

By adding all the terms considered in Eq. (9) and after some algebraic manipulation, the following result is obtained

$$v_D \frac{dv_D}{dy} = \frac{3}{8} \overline{C}_d (1 - N_D V_D) \frac{\rho_c}{\rho_D} \frac{(v_c - v_D) |v_c - v_D|}{r_D} - g \left(1 - \frac{\rho_c}{\rho_D}\right) \tag{11}$$

For the nonaccelerating case (Eq. 10) the sum of the forces yields an expression for the steady-state velocity:

$$(v_c - v_D) |v_c - v_D| = \frac{8 r_D g (\rho_D - \rho_c)}{3 \rho_c \overline{C}_d} \tag{12}$$

Except for the nature of the drag coefficient, Eq. (12) is analogous to the settling velocity of single spheres (Ref. 27).

2. Continuous phase. The momentum balance for the continuous phase can be written as

$$\lambda_c \frac{Dv_c}{Dt} = \sum F$$

In the sum of the forces term, the buoyancy and viscous stresses can be neglected. The latter are considered to be small when compared with the drag produced by the particles. When κ is small, it can be assumed that the partial pressure of the particles can be neglected, and therefore the pressure gradient term, dp/dy, refers to the gas pressure. Thus, the sum of the

forces term includes only gravitational, pressure and drag forces. For this case the momentum balance can be written as:

$$v_c \frac{dv_c}{dy} = g - \frac{1}{\lambda_c}\frac{dp}{dy} - \frac{1}{2}\bar{C}_d (v_c - v_D)|v_c - v_D| N_D \pi r_D^2 \tag{13}$$

C. Conservation of Energy

The general energy equation for a single phase continuum can be written as:

$$\rho \frac{DE}{Dt} = \rho Q - \frac{\partial q_i}{\partial x_i} - p\frac{\partial v_i}{\partial x_i} + \tau_{ij}\frac{\partial v_i}{\partial x_j} \tag{14}$$

The left-hand side of this equation represents the net change of internal energy, E, within a control volume. It includes that part of the internal energy which is added through the system's boundaries by material motion. The terms on the right are, respectively, the contribution of energy sources within the control volume, the net rate of heat addition independent of material motion, the thermodynamic work done by pressure forces against volume changes and finally the irreversible rate of energy dissipation into heat due to viscosity (τ_{ij} is the viscous part of the stress tensor).

In deriving the energy equations for capacitive heat exchangers, it is assumed that no energy sources on sinks exist within the fluid ($\rho Q = 0$). Heat can be added to a system independently of material motion by conduction and/or radiation. The relative importance of radiative heat transfer can be judged from the system's characteristic temperature. At temperatures above 2700°R (1500 K), radiation is the most important mode of heat transfer (Ref. 28); below 1400°R (830 K) radiation effects can be neglected (Ref. 29). For the purpose of this paper, radiative heat transfer can be neglected. Conduction between the gas and the particles is also considered negligible. Therefore, the energy equation is reduced to

$$\rho \frac{DE}{Dt} = -p\frac{\partial v_i}{\partial x_i} + \tau_{ij}\frac{\partial v_i}{\partial x_j} \tag{15}$$

In carrying out practical calculations, temperatures are more useful than internal energy. By invoking the first and second laws of thermodynamics, Eq. (15) can be transformed into a temperature equation. It can be shown (Ref. 30, 31) that two such equations are possible:

$$\rho c_p \frac{DT}{Dt} = \mathcal{D} + \frac{Dp}{Dt} \tag{16}$$

$$\rho c_v \frac{DT}{Dt} = \mathcal{D} - p\frac{\partial v_i}{\partial x_i} \tag{17}$$

In both (16) and (17) the terms ρQ and $\partial q_i/\partial x_i$ have been discarded due to the assumptions previously made. For a Newtonian fluid $\mathcal{D}$ stands for:

$$\mathcal{D} = \left[\mu\left(\frac{\partial v_i}{\partial x_k} + \frac{\partial v_k}{\partial x_i}\right)\right]\frac{\partial v_i}{\partial x_k} \tag{18}$$

where the term in brackets is equivalent to τ_{ij} in Eq. (15). Flow velocities in capacitive heat exchangers are relatively low and therefore, from the small Mach number assumption, $\mathcal{D}$ can be considered negligible.

The question is which of the static pressure terms in (16) and (17) is also small? Order-of-magnitude analysis (Ref. 31) shows that Eq. (16) is the one to use for the small Mach number approximation.

1. Dispersed phase. Equation (7) is valid for a single phase continuum. For a multiphase situation an additional heat transfer term must be included on the right side of the equation. This term represents the interphase heat transfer due to temperature differences. Since no radiation and conduction are considered in this model, the interphase heat transfer is due to convection only. Hence, under the previously stated assumptions the energy equation for the dispersed phase is

$$\rho_D N_D V_D c_{p_D} \frac{DT}{Dt} = \beta (T_c - T_D) \tag{19}$$

where β is a heat transfer parameter having units of (heat)/(time × temperature × length^3). With the addition of the steady-state and one-dimensional assumptions. Eq. (19) becomes

$$\rho_D N_D V_D c_{p_D} v_D \frac{dT}{dt} = \beta (T_c - T_D) \tag{20}$$

For convective heat transfer

$$\beta = 4\pi r_D^2 N_D \tag{21}$$

i.e., the convective heat transfer coefficient times the surface area of one particle times the number of particles in a unit volume of the mixture. After some algebra the heat transfer equation for the dispersed phase is:

$$\rho_D c_{p_D} v_D \frac{dT_D}{dy} = \frac{3h}{r_D}(T_c - T_D) \tag{22}$$

A simpler derivation of Eq. (22) can be made through the familiar heat exchanger equations (Ref. 32):

$$q = U \Delta S (T_{HOT} - T_{COLD}) = - \dot{m}_{HOT} c_{p_{HOT}} \Delta T_{HOT} \tag{23}$$

where U is the overall heat transfer coefficient and S the heat transfer surface. The total mass of the particles within a unit volume of the mixture is

$$m_{HOT} = \rho_D V_D N_D = \rho_D \frac{4}{3} r_D^3 N_D \tag{24}$$

The mass within this unit volume moves in a time scale given by:

$$t = \frac{\Delta y}{v_D} \tag{25}$$

Therefore, the mass flow rate (per unit volume of the mixture) is given by:

$$\dot{m}_{HOT} = \rho_D \frac{4}{3} \pi r_D^3 N_D \frac{v_D}{\Delta y} \tag{26}$$

Since only convection is considered, $U = h$, and $\Delta S = N_D \, 4 \pi r_D^2$. Therefore, Eq. (23) becomes in the limit:

$$\rho_D c_{p_D} v_D \frac{dT_D}{dy} = \frac{3h}{r_D} (T_c - T_D) \tag{27}$$

2. Continuous phase. In terms of the heat exchanger formulas:

$$h \Delta s (T_{HOT} - T_{COLD}) = - \dot{m}_{COLD} c_{p_c} \Delta T_{COLD} \tag{28}$$

After some algebra this becomes

$$\rho_c v_c c_{p_c} \frac{dT_c}{dy} = h \left(\frac{3 N_D \pi r_D^2}{\pi r_D^3 N_D - 1} \right) (T_D - T_c) \tag{29}$$

III. Governing System of Equations

Equations (1), (7), (11), (13), (22) and (29) express the conservation of mass, momentum and energy for the dispersed and continuous phases. These six equations contain 12 unknowns as follows:

$$\rho_c, \rho_D, N_D, v_c, v_D, T_c, T_D, p, c_{p_c}, c_{p_D}, h, \bar{C}_d$$

Obviously, additional relations are needed. If one assumes that the continuous phase is made up a perfect gas, then one such additional equation is given by

$$P = \rho_c R T_c \tag{30}$$

Three other relationships must be determined experimentally:

$$c_{p_c} = f_1 (T_c) \tag{31}$$

$$c_{p_D} = f_2 (T_D) \tag{32}$$

$$\rho_D = f_3 (T_D) \tag{33}$$

Note that if ρ_D can be assumed to be constant, Eq. (33) is not needed and Eq. (2) can be used in place of (1).

Relationships for $\bar{C}_d$ and h are more difficult to develop. It is general practice to express these parameters as experimental functions of the dimensionless Reynolds and Prandtl numbers. In a biphasic flow the Reynolds number can be defined as:

$$N_{Re} = \frac{2 \rho_c |v_c - v_D| r_D}{\mu_c} \tag{34}$$

and the Prandtl number as:

$$N_{Pr} = \frac{c_{p_c} \mu_c}{k_c} \tag{35}$$

The heat transfer coefficient, h can be found from the Nusselt number:

$$N_{Nu} = \frac{2h r_D}{k_c} \tag{36}$$

The standard drag curve has been fitted by a number of authors and Clift et al. (Ref. 33) give an up-to-date list of such correlations. In this paper the following references will be used:

From Ref. 34:

$$N_{Re} \leqslant 10, \quad , \quad \bar{C}_d = C_d = 2 + \frac{24}{N_{Re}} \tag{37}$$

From Ref. 35:

$$10 < N_{Re} \leqslant 2000, \quad \bar{C}_d = \frac{27}{N_{Re}^{0.84}} \tag{38}$$

From Ref. 16:

$$2000 < N_{Re} \leqslant 3000, \quad \overline{C}_d = \frac{145}{N_{Re}^{1.16}} \tag{39}$$

These relations are for spheres entrained by the flow, but it is assumed that they can also be used for the counter-current case discussed here. The sensitivity of the results to variations in $\overline{C}_d$ will also be analyzed in the second part of this report.

A reliable heat transfer correlation for single sphere is given in Whitaker (Ref. 36):

$$N_{Nu} = 2 + (0.4\, N_{Re}^{0.5} + 0.06\, N_{Re}^{0.67})\, N_{Pr}^{0.4} \left(\frac{\mu_\infty}{\mu_s}\right)^{0.25} \tag{40}$$

where

$$N_{Nu} \equiv \frac{Q}{4\pi D^2 (\Delta T)}$$

For air Eq. (40) can be approximated by

$$N_{Nu} = 2 + (0.4\, N_{Re}^{0.5} + 0.06\, N_{Re}^{0.67}) \tag{41}$$

because $N_{Pr} = 1$ for air and the viscosity ratio is also about unit. Other relationships are given by Ranz and Marshall (Ref. 37)

$$N_{Nu} = 2.0 + 0.60\, N_{Pr}^{1/3}\, N_{Re}^{1/2} \tag{42}$$

and Bandrowski and Kaczmarzyk (Ref. 38)

$$N_{Nu} = 0.00114\, \kappa^{-0.5984}\, N_{Re}^{0.8159} \tag{43}$$

Equation (42) is derived from experiments on liquid drops and Eq. (43) from experiments on the pneumatic conveying of small spheres. In Eq. (43) $0.00025 < \kappa < 0.05$ and $180 < N_{Re} < 18{,}000$. The sensitivity of the results to the Nusselt number correlation will also be analyzed in the second part of this report.

One final equation is needed to complete the set:

$$\mu_c = f_4 (T_c) \tag{44}$$

This last equation is needed to evaluate the additional unknown, μ_c, which appears in the Reynolds number. Therefore, the complete set includes 13 equations and 13 unknowns.

IV. Method of Solution

The equations and the unknowns are summarized in Table 2. Boundary and/or initial conditions must be established for these equations before any solution is attempted. In order to do this, the hypothetical performance of a capacitive heat exchanger is illustrated in Fig. 3. If all the parameters were known either at $y = 0$ or at $y = H$, this would be a classic initial value problem. However, because of the countercurrent nature of the heat exchanger, only some of the parameters can be assumed known at $y = 0$, while the others are known only at $y = H$. Therefore, this is a two-point boundary value problem.

Initial value problems are relatively easy to solve by numerical methods. They have been used successfully to analyze particle-gas flows in rocket nozzles (Ref. 39). Unfortunately there are no known algorithms for solving an arbitrary two-point boundary value problem. The so-called shooting methods reduce the solution of a boundary value problem to the iterative solution of an initial value problem (Refs. 40, 41, 42, 43, 44). These methods are based essentially on assuming some of the missing information at the initial point ($y = 0$ for example) and iterating this "trial" solution until the end point ($y = H$ for example). This end point value is obtained by a Runge-Kutta process. The value at the end point is then compared with the actual value, and on the basis of this comparison adjustments are made for a new trial solution. By this process, the true end point value is bracketed by trial solutions until a match is made. In the case of linear equations a particularly efficient method exists.

The governing equations present the added difficulty that some of them have derivatives implicitly defined in terms of other derivatives. It can be shown (Appendix A) that derivative implicitness will remain in the system unless

$$\frac{dN_D}{dy} = \text{constant} \tag{45}$$

Equation (45) implies that N_D is a linear function of y. This assumption, if justified, represents an important simplification in the mathematical solution method. Results published by El'Kin and Timofeyev (Ref. 7) indicate that for loading ratios less than 7, κ (and therefore N_D) is practically constant with y; i.e.,

$$N_D = N_D\,|_{y=0} \left(1 + \epsilon \frac{y}{H}\right) \tag{46}$$

where $\epsilon << 1$. When Eq. (46) is valid, in terms of the notation developed in Appendix A,

$$\frac{dx_3}{dy} = \frac{\epsilon x_3|_{y=0}}{H} \tag{47}$$

and the system of equations becomes:

$$\frac{dx_1}{dy} = MP + N \tag{48}$$

$$\frac{dx_2}{dy} = CP + DH \tag{49}$$

$$\frac{dx_3}{dy} = P \tag{50}$$

$$\frac{dx_4}{dy} = E + FK\,(MP + N) + FLI + G \tag{51}$$

$$\frac{dx_5}{dy} = H \tag{52}$$

$$\frac{dx_6}{dy} = I \tag{53}$$

$$\frac{dx_7}{dy} = J \tag{54}$$

$$\frac{dx_8}{dy} = K(MP + N) + LI \tag{55}$$

where none of the terms on the right-hand side contain derivatives.

Numerical techniques for solving such systems have been developed at JPL (Ref. 45). These techniques are described in Part II of this report in which the solution of the system of equations is given. In Part II the results obtained for capacitive heat exchangers will be compared with those obtained for conventional counterflow heat exchangers.

References

1. Decher, R., "The Falling Bead Dry Cooling Tower," Paper 809476 15th Intersociety Energy Conversion Engineering Conference (IECEC), 1980.
2. Shaw, D., Bruckner, A. P., and Hertzberg, A., "A New Method of Efficient Heat Transfer and Storage at Very High Temperatures," Paper 809029, 15th IECEC, 1980.
3. Cease, M. E., "A Model of Direct Contact Heat Transfer for Latent Heat Energy Storage," Paper 809118, 15th IECEC, 1980.
4. Pai, S. I., "A Critical Review of the Fundamental Equations of a Mixture of a Gas and Small Solid Particles," *Z. Flugwiss.*19 (8/9), pp. 353-360, 1971.
5. Nigmatulim, R. I., "Methods of Mechanics of a Continuous Medium for the Description of Multiphase Mixtures," *Prikladnaia Matematika i Mekhanika*, 34(6): 1097-1112, 1970.
6. Kuentzman, P., "French Contribution to Aerodynamics of Gas-Particles Mixtures," in *Flow of Solid Particles in Gases* by G. Rudinger (A. Auriol ed.) AGARD-AG-222, 1976.
7. El'Kin, G. L., and Timofeyev, Yu. B., "Experimental Study of the Distribution of Solid Particles and of the Local Heat Transfer Between the Gas and Solids in a Two-Phase Flow (with One Particle Size)," *Heat Transfer-Sov. Res.*, 8(5), pp. 122-126, 1976.

8. Kraiko, A. N., and Sternin, L. E., "Theory of Flows of a Two-Velocity Continuous Medium Containing Solid or Liquid Particles," *Prikladnaia Matematika i Mekhanika*, 29(3), pp. 418-429, 1965.

9. Guletskaia, I. F., and Lisin, F. N., "Combined Heat Transfer of a Turbulent Dispersed Flow in a Duct," *Zhurnal Prikladnoi Mekhaniki i Technichesksoi Fiziki*, Jul/Aug, pp. 69-79, 1980.

10. Sha, W. T., and Soo, S. L., "Multidomain Multiphase Fluid Mechanics," *Int. J. Heat Mass Transfer*, 21, pp. 1581-1595, 1978.

11. Marble, R. E., "Dynamics of Dusty Gases," *Annual Review of Fluid Mechanics*, Vol. 2, pp. 337-446, 1970.

12. Saffman, P. G., "On the Stability of Laminar Flow of a Dusty Gas," *J. Fluid Mech.*, 13, pp. 120-128, 1962.

13. Genchev, Z. D., and Karpuzov, D. S., "Effects of the Motion of Dust Particles on Turbulence Transport Equations," *J. Fluid Mech.*, 101 (4), pp. 833-842, 1980.

14. Rudinger, G., "Fundamentals and Applications of Gas-Particle Flow", in *Flow of Solid Particles in Gases* by G. Rudinger (A. Auriol ed.), AGARD-AG-222, 1976.

15. Tritton, D. J., *Physical Fluid Dynamics*, Van Nostrand Reinhold, 1977.

16. Torobin, L. B., and Gauvin, W. H., "Fundamental Aspects of Solids-Gas Flow", *Can. J. Chem. Eng.*, 37, pp. 129-141; 37, pp. 167-176; 38, pp. 224-236 (1959); 38, 142-153; 38, pp. 189-200 (1960).

17. Murray, J. D., "On the Mathematics of Fluidization – Part 1. Fundamental Equations and Wave Propagation," *J. Fluid Mech.*, 21(3), pp. 465-493, 1965.

18. Soo, S. L., "Heat Transfer Processes of Particulate Suspensions," in *Advanced Heat Transfer*, (B. T. Chao ed.), U. of Illinois Press, Urbana, 1969.

19. Barkla, H. M., and Auchterlonie, L. J., "The Magnus or Robins Effect on Rotating Spheres," *J. Fluid Mech.*, 47(3), pp. 437-447, 1971.

20. Ribas, R., "Kinetic Model for a Gas-Particle Flow Through a Horizontal Pipe," VKI Project Report, 1977.

21. Ribas, R., Laurenco, L., and Riethmuller, M. L., "A Kinetic Model for a Gas-Particle Flow," VKI preprint 1980-4, Pneumotransport 5 Conference, 1980.

22. Brinkman, H. C., "A calculation of the viscous force exerted by a flowing fluid on a dense swarm of particles", Appl. Sci. Res., A1, p 27ff, 1947.

23. Tam, C.K.W., "The drag on a cloud of spherical particles in low Reynolds number flow," *J. Fluid Mech.*, 38(3), pp. 537-546, 1969.

24. Johnstone, H. F., Pigford, R. L., and Chapin, J. H., "Heat Transfer to Clouds of Falling Particles," *Am. Inst. Chem. Eng.*, pp. 95-133, 1941.

25. Soo, S. L., *Fluid Dynamics of Multiphase Systems*, Blaisdell, Waltham, Mass., 1967.

26. Schetz, J. A., "Two Phase Flows," Ch. 6 in *Injection and Mixing in Turbulent Flow*, Vol. 68, Progress in Astronautics and Aeronautics, AIAA, 1980.

27. Wallis, G. B., *One-dimensional Two-phase Flow*, McGraw-Hill, N.Y., 1969.

28. Schneider, W., "Radiant Interchange Among Suspended Particles and Its Effect on Thermal Relaxation in Gas-Particle Mixtures," 23rd Proc. Heat Transfer and Fluid Mechanics Institute, pp. 353-370, 1972.

29. Tien, C. L., "Heat Transfer by a Turbulently Flowing Fluid-Solids Mixture in a Pipe," ASME., *J. Heat Transfer*, pp. 183-188, 1961.

30. Chao, B. T., "Selected Topics on Convective Heat Transfer," in *Advanced Heat Transfer,* (B. T. Chao ed.), U. of Illinois Press, Urbana, 1969.

31. Corrsin, S., *Notes on Fluid Mechanics,* Johns Hopkins Univ., Baltimore, 1968.

32. Kays, W. M., and London, A. L., *Compact Heat Exchangers*, 2nd ed. McGraw-Hill Book Co., N. Y., 1964.

33. Clift, R., Grace, J. R., and Weber, M. E.,*Bubbles, Drops and Particles,* Academic Press, N. Y., 1978.

34. Kurten, H., Raasch, J., and Rumpf, H., *Chem. Eng. Tech.,* Vol 38, pp. 941-948, 1966 (also in Ref. 33).

35. Ingebo, R. D., *Drag Coefficients for Droplets and Solid Spheres in Clouds Accelerated in Air Streams*, NACA TN 3762, 1956.

36. Whitaker, S., "Forced Convection Heat Transfer Correlations for Flow in Pipes, Past Flat Plates, Single Cylinders, Single Spheres, and for Flow in Packed Beds and Tube Bundles," A. I. Ch. E. J., vol. 18(2), pp. 361-371, 1972.

37. Ranz, W. E., and Marshall, Jr., W. R., "Evaporation from Drops," *Chemical Engineering Progress*, vol. 48(4), pp. 173-179, 1952.

38. Bandrowski, F., and Kaczmarzyk, G., "Gas-to-Particle Heat Transfer in Vertical Pneumatic Conveying of Granular Materials," *Chem. Eng. Sci.*, Vol. 33, pp. 1303-1310, 1978.

39. Neilson, J. H., and Gilchrist, A., "An analytical and experimental investigation of the velocities of particles entrained by the gas flow in nozzles," *J. Fluid Mech.*, Vol. 33 (1), pp. 131-149, 1968.

40. Osborne, M. R., "On Shooting Methods for Boundary Value Problems," *J. Math. Anal. Applic.*, Vol. 27, pp. 417-433, 1969.

41. Stoer, J., and Bulirsch, R., *Introduction to Numerical Analysis*, Springer-Verlag, N.Y., 1980.

42. Carnahan, B., Luther, H. A., and Wilkes, J. O., *Applied Numerical Methods*, J. Wiley, N.Y., 1969.

43. Roberts, S. M., and Shipman, J. S., *Two-Point Boundary Value Problems: Shooting Methods*, Elsevier, N.Y., 1972.

44. Keller, H. B., *Numerical Methods for Two-Point Boundary Value Problems* Blaisdell, London, 1968.

45. Krogh, F. T., Personal Communication, May 1981.

Definition of Symbols

A cross-sectional area of the conduit

c_p specific heat at constant pressure

c_v specific heat at constant volume

$C_d, \bar{C}_d$ drag coefficient

$\mathscr{D}$ kinetic energy dissipation rate

E internal energy

g gravitational acceleration

H maximum length (height) of the heat exchanger

h convective heat transfer coefficient

k conductive heat transfer coefficient

$\dot{m}$ mass flow rate

N_D number of particles per unit volume of mixture

p pressure

Q energy sources per unit volume

q heat per unit volume

R gas constant

r radius

T temperature

t time

V volume

v velocity

y axial distance for the heat exchanger

β heat transfer parameter

η loading ratio, equal to $\lambda_D v_D / \lambda_c v_c$

κ volume fraction occupied by particles

λ species density, equal to volume fraction times material density

μ coefficient of viscosity

ρ material density

τ_{ij} stress tensor

Suffixes

c pertains to continuous phase (gas)

D pertains to dispersed phase (particles)

Table 1. Examples of heterogeneous mixtures

Liquid fluid phase:
Solid dispersed phase: suspension
Liquid dispersed phase: emulsion
Gaseous dispersed phase: foam
Gaseous fluid phase:
Solid dispersed phase: suspension, smoke, fluidized bed
Liquid dispersed phase: mist, fog, aerosol

Table 2. Summary of equations and unknowns

Equation type	Equation	Unknowns
Continuity (continuous phase)	$\frac{d}{dy}\left[(1-N_D V_D)\rho_c v_c\right] = 0$	N_D, ρ_c, v_c
Continuity (dispersed phase)	$\frac{d}{dy}(\rho_D N_D v_D) = 0$	ρ_D, v_D
Momentum (continuous phase)	$v_c \frac{dv_c}{dy} = -g - \frac{1}{\rho_c(1-N_D V_D)}\frac{dp}{dy} + \frac{1}{2}\overline{C}_d v_{net}^2 N_D \pi r_D^2$	$p, \overline{C}_d$
Momentum (dispersed phase)	$v_D \frac{dv_D}{dy} = \frac{3}{8}\overline{C}_d(1-N_D V_D)\frac{\rho_c}{\rho_D}\frac{v_{net}^2}{r_D} - g\left(1-\frac{\rho_c}{\rho_D}\right)$	–
Energy (continuous phase)	$\rho_c v_c c_{p_c}\frac{dT_c}{dy} = -h\left(\frac{4\pi N_D r_D^2}{1-N_D V_D}\right)(T_D - T_c)$	T_D, T_c, h, c_{P_c}
Energy (dispersed phase)	$\rho_D v_D c_{p_D}\frac{dT_D}{dy} = \frac{3h}{r_D}(T_c - T_D)$	c_{P_D}
State	$p = \rho_c R T_c$	–
Drag coefficient correlation	$\overline{C}_d = f_1(N_{Re})$	μ_c
Nusselt Nr. correlation	$h = f_2(N_{Re})$	–
Viscosity correlation	$\mu = f_3(T_c)$	–
c_{p_c} correlation	$c_{p_c} = f_4(T_c)$	–
c_{p_D} correlation	$c_{p_D} = f_5(T_D)$	–
Density correlation	$\rho_D = f_6(T_D)$	–

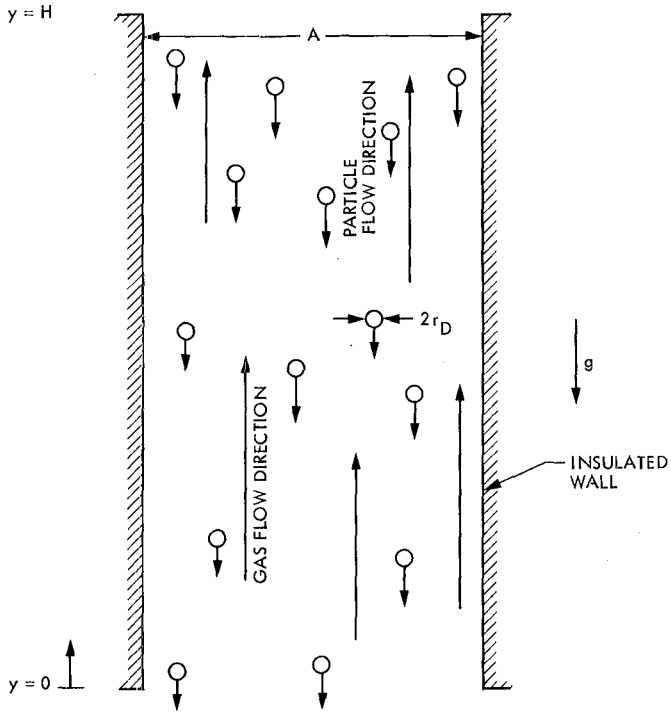

Fig. 1. Capacitive heat exchanger model

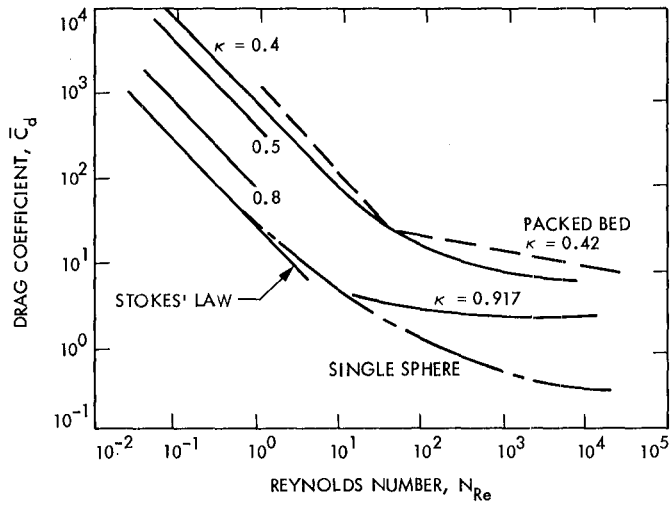

Fig. 2. Drag coefficient of spheres in a cloud

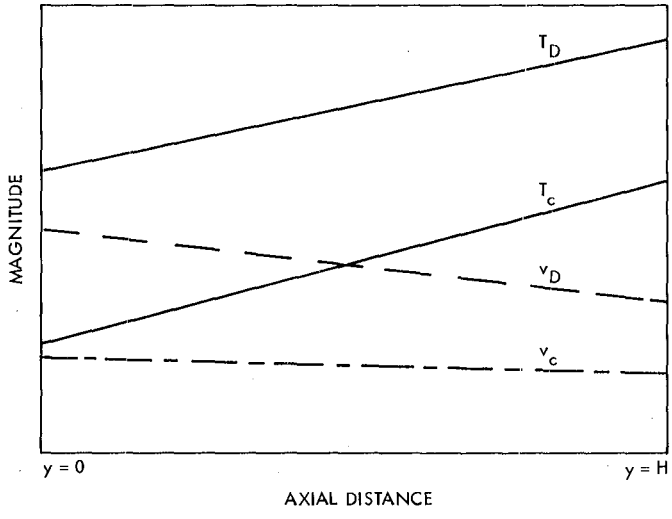

Fig. 3. Hypothetical performance of a capacitive heat exchanger

Appendix A

Elimination of Derivative Implicitness for the System Equations

Consider the following symbol transformation:

$$x_1 = \rho_c \qquad \alpha_1 = V_D = \frac{4}{3}\pi r_D^3$$

$$x_2 = \rho_D$$

$$x_3 = N_D \qquad \alpha_2 = g$$

$$x_4 = v_c$$

$$x_5 = v_D \qquad \alpha_3 = \pi r_D^2$$

$$x_6 = T_c$$

$$x_7 = T_D \qquad \alpha_4 = r_D$$

$$x_8 = p$$

Then, the first seven equations from Table 2 can be written respectively as:

$$\frac{dx_1}{dy} = \frac{\alpha_1 x_1 x_4}{x_4 - \alpha_1 x_3 x_4}\frac{dx_3}{dy} - \frac{x_1 - \alpha_1 x_1 x_3}{x_4 - \alpha_1 x_3 x_4}\frac{dx_4}{dy} \tag{A-1}$$

$$\frac{dx_2}{dy} = \frac{-x_2}{x_3}\frac{dx_3}{dy} - \frac{x_2}{x_5}\frac{dx_5}{dy} \tag{A-2}$$

$$\frac{dx_4}{dy} = \frac{-\alpha_2}{x_4} - \frac{1}{x_1 x_4 (1 - \alpha_1 x_3)}\frac{dx_8}{dy} + \frac{1}{2}\bar{C}_d (x_4 + x_5)^2 \frac{x_3}{x_4}\alpha_3 \tag{A-3}$$

$$\frac{dx_5}{dy} = \frac{3}{8}\bar{C}_d (1 - \alpha_1 x_3)\frac{x_1}{x_2 x_5}\left(\frac{x_4 + x_5}{\alpha_4}\right)^2 - \frac{\alpha_2}{x_5}\left(1 - \frac{x_1}{x_2}\right) \tag{A-4}$$

$$\frac{dx_6}{dy} = \frac{h}{c_{p_c}}\left(\frac{4\alpha_3 x_3}{\alpha_1 x_3 - 1}\right)\frac{(x_7 - x_6)}{x_1 x_4} \tag{A-5}$$

$$\frac{dx_7}{dy} = \frac{3h}{\alpha_4 x_2 x_5 c_{p_D}}(x_6 - x_7) \tag{A-6}$$

$$\frac{dx_8}{dy} = Rx_6\frac{dx_1}{dy} + Rx_1\frac{dx_6}{dy} \tag{A-7}$$

Equation (A-7) was obtained by differentiating (17) with respect to y. Equations (A-1), (A-2), (A-3) and (A-7) define derivatives implicitly in terms of other derivatives. Although the nature of the system is such that this implicitness cannot be eliminated completely, some simplification is possible as follows. Let:

$$A = \frac{\alpha_1 x_1 x_4}{x_4 - \alpha_1 x_3 x_4} \tag{A-8}$$

$$B = \frac{x_1 - \alpha_1 x_1 x_3}{x_4 - \alpha_1 x_3 x_4} \tag{A-9}$$

$$C = \frac{x_2}{x_3} \tag{A-10}$$

$$D = \frac{x_2}{x_5} \tag{A-11}$$

$$E = -\frac{\alpha_2}{x_4} \tag{A-12}$$

$$F = -\frac{1}{x_1 x_4 (1 - \alpha_1 x_3)} \tag{A-13}$$

$$G = \frac{1}{2}\bar{C}_d (x_4 + x_5)^2 \frac{x_3}{x_4}\alpha_3 \tag{A-14}$$

$$H = \frac{3}{8}\bar{C}_d(1-\alpha_1 x_3)\frac{x_1}{x_2 x_5}\left(\frac{x_4+x_5}{\alpha_4}\right)^2 - \frac{\alpha_2}{x_5}\left(1-\frac{x_1}{x_2}\right) \quad \text{(A-15)}$$

$$I = \frac{h}{c_{p_c}}\left(\frac{4\alpha_3 x_3}{\alpha_1 x_3 - 1}\right)\frac{(x_7 - x_6)}{x_1 x_4} \quad \text{(A-16)}$$

$$J = \frac{3h}{\alpha_4 x_2 x_5 c_{p_D}}(x_6 - x_7) \quad \text{(A-17)}$$

$$K = Rx_6 \quad \text{(A-18)}$$

$$L = Rx_1 \quad \text{(A-19)}$$

Then, Eqs. (A-1) through (A-7) can be written as

$$\frac{dx_1}{dy} = A\frac{dx_3}{dy} + B\frac{dx_4}{dy} \quad \text{(A-20)}$$

$$\frac{dx_2}{dy} = C\frac{dx_3}{dy} + D\frac{dx_5}{dy} \quad \text{(A-21)}$$

$$\frac{dx_4}{dy} = E + F\frac{dx_8}{dy} + G \quad \text{(A-22)}$$

$$\frac{dx_5}{dy} = H \quad \text{(A-23)}$$

$$\frac{dx_6}{dy} = I \quad \text{(A-24)}$$

$$\frac{dx_7}{dy} = J \quad \text{(A-25)}$$

$$\frac{dx_8}{dy} = K\frac{dx_1}{dy} + L\frac{dx_6}{dy} \quad \text{(A-26)}$$

From (A-24) and (A-26)

$$\frac{dx_8}{dy} = K\frac{dx_1}{dy} + LI \quad \text{(A-27)}$$

From (A-22) and (A-27)

$$\frac{dx_4}{dy} = E + FK\frac{dx_1}{dy} + FLI + G \quad \text{(A-28)}$$

From (A-20) and (A-28)

$$\frac{dx_1}{dy} = A\frac{dx_3}{dy} + BE + BFK\frac{dx_1}{dy} + BFLI + BG \quad \text{(A-29)}$$

From (A-21) and (A-23)

$$\frac{dx_2}{dy} = C\frac{dx_3}{dy} + DH \quad \text{(A-30)}$$

Equation (A-29) can be written as

$$\frac{dx_1}{dy} = \frac{A}{1-BFK}\frac{dx_3}{dy} + \frac{BE+BFLI+BG}{1-BFK} = M\frac{dx_3}{dy} + N \quad \text{(A-31)}$$

where

$$M = \frac{A}{1-BFK} \text{ and } N = \frac{BE+BFLI+BG}{1-BFK}$$

Then, the two equations

$$\frac{dx_1}{dy} = M\frac{dx_3}{dy} + N \quad \text{(A-31)}$$

$$\frac{dx_2}{dy} = C\frac{dx_3}{dy} + DH \quad \text{(A-30)}$$

Equations (A-30) and (A-31) indicate that derivative implicitness will remain in the system unless further assumptions are made with regard to dx_3/dy.

Coherent Reference Generator Phase Stability

V. N. Korwar
Communications Systems Research Section

The extent of phase noise introduced by the coherent reference generator (CRG) unit in the DSN's Frequency and Timing Subsystem (FTS) has not so far been measured or analyzed. This report calculates approximate phase stability estimates for the CRG. The method used involves estimating the phase noise introduced by CRG components based upon measurements made in the past on similar components in other parts of the FTS and obtaining the CRG phase noise from the component phase noises.

Three estimates of phase stability are calculated – the fractional frequency change for a 5°C step in temperature, the phase noise spectral density and the Allan standard deviation. It is found from these estimates that the CRG phase stability is better than that of the H-maser physics unit + receiver, which has been measured in the past. Thus, the first step in improving FTS phase stability would be to make improvements in the H-maser physics unit + receiver. These results are corroborated by indirect clock stability estimates calculated from Doppler data by R. W. Hellings.

I. Introduction

The DSN's Frequency and Timing Subsystem (FTS) may be divided into three separate subsystems – the primary frequency unit called the physics unit (such as H-maser or Cs standard), the receiver, and the coherent reference generator (CRG). The first two of these together, i.e., the physics unit + receiver, will be referred to as the H-maser system or the Cs system as appropriate. All three subsystems taken together will be referred to as the H or the Cs clock. The receiver that goes with the H-maser system is different from the one that goes with the Cs system. However, the same CRG is used in the DSN, no matter whether the H-maser or the Cs system is used.

So far, measurements of phase noise have been made on the Cs system and on the H-maser system, but none on the CRG (or on the receiver portion alone for either the H-maser or the Cs system). In order to improve the frequency stability of the FTS, it is necessary to identify the prime sources of phase/frequency instability in the FTS. To do this, the first step is to estimate the phase errors of the three subsystems separately, so that improvement can first be made in the poorest of the three subsystems.

This report describes an attempt to estimate the phase instability introduced by the CRG alone and identifies areas needing further work. While the CRG phase noise estimates

given here are very approximate, they do provide a starting point for better estimates.

II. CRG Description

The CRG consists of the circuitry needed to synthesize and distribute signals of frequencies 0.1, 1, 5, 10, 10.1, 45, 50, 55 MHz. The CRG inputs are signals of frequencies 0.1, 5 and 10 MHz, derived from the primary frequency unit + receiver. A block diagram of the CRG is given in Fig. 1 (Fig. 2.1 of Ref. 1).

III. Phase Noise Measures

Three measures of phase noise have been calculated here (wherever possible). They are:

(1) $\Delta f/f$, the fractional frequency variation for a 5°C temperature step. The box in which the CRG is located is assumed to have a response time of $T = 2000$ s. Phase drifts ($\Delta\phi$) with temperature are often measured or specified. From these, $\Delta f/f$ can be calculated as

$$\frac{\Delta f}{f} = \frac{2}{3} \times \frac{\Delta\phi}{T} \times \frac{1}{2\pi f_0} , \qquad (1)$$

where $\Delta\phi$ is in radians, f_0 is the nominal frequency, and $T = 2000$ s.

(2) S_ϕ (10 Hz), the one-sided spectral density of phase noise $S_\phi(f)$ evaluated at $f = 10$ Hz. In all cases considered here, the noise is assumed to be flicker of phase; i.e.,

$$S_\phi(f) = \frac{\text{constant}}{f} , \qquad (2)$$

so that specifying S_ϕ (10 Hz) is sufficient to specify the whole $S_\phi(f)$ curve. This asumption is justified by measurement for multipliers (Ref. 2) and distribution amplifiers (Ref. 3).

(3) $\sigma_y(1\text{ s})$, the Allan standard deviation $\sigma_y(\tau)$ evaluated for $\tau = 1$ s. This is calculated from $S_\phi(f)$, by using the expression given in Ref. 4 and corrected in Ref. 5. After expressing the constant in $S_\phi(f)$ in terms of S_ϕ (10 Hz), this gives

$$\sigma_y(\tau) = \frac{2.42}{f_0 \tau} (S_\phi\ (10\text{ Hz}))^{1/2}\ (1 + 0.13 \ln \tau)^{1/2} \qquad (3)$$

where f_0 is the nominal frequency, and τ is the observation interval for calculating Allan standard deviation.

Since temperature-induced phase drifts are not independent, the overall $\Delta f/f$ introduced in a cascade of identical components is just the sum of the individual $\Delta f/f$ values. If the components are of different types, the $\Delta f/f$'s may actually tend to cancel each other; however, they are assumed to be additive in making the estimates here. The S_ϕ (10 Hz) values are also summed, since they represent noise powers that are uncorrelated. The σ_y (1 s) values are proportional to (S_ϕ (10 Hz))$^{1/2}$, so that the overall σ_y (1 s) is obtained as the root-sum-square (rss) value of the individual σ_y (1 s) values.

IV. Sources of Phase Noise

There are several components in the coherent reference generator (CRG), each potentially a noise source. Unless otherwise stated, "noise" will mean "phase noise" throughout. There are no frequency or phase control loops involving voltage controlled oscillators (VCOs) in the CRG, so that one of the largest of the usual sources of noise is not present in the CRG, as it is in the receiver. However, there are various components, each of which introduces small amounts of noise. In roughly descending order of phase noise introduced, they are: tuned amplifiers and crystal filters, distribution amplifiers, power splitters, mixers and multipliers.

VCOs are noisy because they convert voltage noise, from whatever source present at their inputs, into phase noise. The other components do not have such an I/O property and hence are less noisy.

Tuned amplifiers and crystal filters mainly introduce phase drifts with temperature changes. This is because their transfer functions (both amplitude and phase) are narrowband around a center frequency that changes with temperature as the (L, C) component values defining this center frequency change with temperature. This is especially true with crystal filters.

Distribution amplifiers (DA) usually introduce noise because of the driver amplifiers preceding and/or following the power divider/splitter present in the DA. All driver amplifiers now used in the coherent reference generator (CRG) are Class A amplifiers operating in the linear region of their characteristics, which are much less noisy than Class C amplifiers.

Power splitting is usually accomplished by transformers with the proper turns ratios — these usually introduce negligible phase noise.

V. Direct Method for Estimating Phase Noise

The amounts of phase noise introduced by various components in the CRG are difficult to estimate correctly, because

phase noise measurements on most of these components have not been made, nor is any analysis available. Inquiries with the manufacturers of several of the components (crystals, crystal filters, multipliers) also did not produce any results, except in the case of one multiplier.

The calculations of CRG phase noise described here are obtained by including noise estimates for only those of the components that have some sort of estimate/measurement available, and assuming that all others are zero, so that an estimate of lower bound on the CRG phase noise can be obtained. Even these lower bounds should not be taken as rigid, because the phase noise for many of the components has not been measured for the specific models used in the CRG, but extrapolated from measurements on *similar* components in other subsystems (such as in the maser receiver).

A. The Components

1. Tuned amplifiers and crystal filters. Unfortunately, there are no data available on these components, not even with the manufacturers. These are important sources of phase drift with temperature, but if the temperature is controlled, the phase noise they introduce may be small. However, the coherent reference generator (CRG) is not typically operated in a temperature-controlled environment.

Tuned amplifiers/crystal filters are used only in generating the 10.1-MHz, 45-MHz and 55-MHz outputs, but not the other outputs. Thus the phase noise for these outputs will be higher than the numerical estimates given here, which don't take the tuned amplifiers and crystal filters into account.

2. Distribution amplifiers. Phase noise estimates for the CRG distribution amplifiers (DAs) are calculated from phase drift and S_ϕ (10-Hz) measurements made for DAs used in the H-maser reciever. The DAs in the H-maser receiver consist of an n-way (usually 12-way) power splitter, where each of the n output ports is followed by a driver amplifier (labeled AR2 through AR(n + 1)). The distribution amplifiers in the CRG, on the other hand (see Fig. 2), consist of an input driver amplifier (AR1) followed by the power splitter and driver amplifiers structure used in the receiver DAs.

The input driver amplifier AR1 is different in design from the output driver amplifiers typified by AR2. It is assumed here that the measured distribution amplifier noise in the receiver (Refs. 3, 6) comes entirely from the output driver amplifiers such as AR2; this neglects the power splitter noise, which is reasonable as stated in Section 4. It is then assumed that AR1 has the same noise as AR2. This may not be accurate, since AR1 is an OP AMP (operational amplifier) with many stages of amplification, while AR2 is a hybrid amplifier with one or two stages; so AR1 is probably a little worse than AR2. On the other hand, AR1 has feedback that would reduce the noise to some extent, so that on the whole, AR1 may be assumed to be about as noisy as AR2.

Then the coherent reference generator (CRG) distribution amplifier noise is estimated as the noise introduced by two driver amplifiers like AR2 cascaded together, according to the rules for cascading given in Section III.

3. Frequency multipliers. There are two (frequency) multipliers used in the CRG. The first is a X2 multiplier, which is a harmonic generator, followed by a tuned amplifier. However, as can be seen in Fig. 1, this X2 multiplier is used only as a backup in generating a 10-MHz signal from a 5-MHz input. What is primarily used is an independent 10-MHz input. For this reason the effects of this multiplier and tuned amplifier (on which no data are available) are not important.

The second multiplier used is a X10 multiplier from Zeta Laboratories. This is a chain-type multiplier; i.e., it uses a chain of harmonic generators, filters and mixers to get the desired multiplication. The $\Delta f/f$ for a 5°C step in temperature for this multiplier was estimated from Eq. (1) by using $\Delta\phi$ data supplied by Zeta Laboratories. The S_ϕ (10 Hz) and the σ_y (1 s) for the multiplier were estimated based on measured S_ϕ (10 Hz) data (Refs. 2, 7) for a JPL-built multiplier which had a somewhat similar design (i.e., it was a chain-type multiplier, as opposed to a step-recovery diode or phase-locked loop type). The JPL multiplier was a X14 multiplier, and appropriately scaled-down values were used to estimate the noise on the X10 multiplier used here.

B. Phase Noises for Coherent Reference Generator (CRG) Outputs

Using the phase noise data for individual components described in Section V-A, the phase noises for the various CRG outputs can be estimated as follows:

1. The 0.1, 1, 5, 10 MHz outputs. For these outputs, the only significant contributions to phase noise are from an input driver (D_i) and a distribution amplifier (DA) – there are no mixers or multipliers or filters used in generating these outputs. As an example, consider the 0.1-MHz output. In the block diagram (Fig. 1), the input driver D_i is labeled 9455393-1. The distribution amplifier (DA) is A4A2 or A4A3. Detailed block diagrams of A4A2 and A4A3 show a DA like the one in Fig. 2. Thus the phase noise for this group of CRG outputs is given in Table 1. For uniformity, all data given are referenced to a 100-MHz output; i.e., the phase noise spectral density is what would be present if the outputs were multiplied in frequency, by a perfect multiplier, to 100 MHz.

2. **Other outputs.** All the other CRG outputs have a minimum phase noise given by Table 1, because they all include a DA and an input driver. However, the 10.1-, 45- and 55-MHz outputs will have a larger noise because they all include crystal filters – this is because the 10.1-MHz signal is obtained by mixing the 10- and 0.1-MHz inputs, while the 45- and 55-MHz signals are obtained by mixing 50-MHz and 5-MHz inputs, and the mixed outputs are filtered by a crystal in the 10.1-MHz case and a crystal filter in the 45-MHz and 55-MHz cases. No estimates are available for the extent of noise introduced by the filtering.

The 45-, 50- and 55-MHz signals will have, in addition to the noise in Table 1, a component due to the ×10 multiplier used in generating the 50-MHz signal from a 5-MHz input. The phase estimates for this multiplier are given in Table 2. Thus, we get Table 3 for the 10.1-, 45-, 50-, and 55-MHz CRG outputs.

VI. Indirect Estimates of Coherent Reference Generator (CRG) Noise

A. Very Long Baseline Interferometer (VLBI) Experiments

Some groups performing VLBI experiments have noticed that on days when the Cs clock is used by the DSN, the phase data taken in the VLBI measurements are worse than when the H-maser clock is used. This would indicate that, since the same CRG is used in both cases, (with only the Cs physics unit + receiver being replaced by the H-maser physics unit + receiver), then the CRG stability is at least about as good as the worst of the two – the Cs system and the H-maser system. These results from the VLBI experiments are not very quantitative or very reliable, since the purpose of the experiments was *not* to estimate the noise on the primary standard and, in fact, the experimenters were not always aware of what frequency standard was in use on a particular day. Controlled VLBI experiments, with the same (celestial) source being observed on two successive days, with the Cs clock used on one day and the H-maser clock on the other day, could perhaps be useful. Such experiments would help in getting an indirect estimate of CRG stability.

B. Doppler Tracking Calculations

R. W. Hellings (Ref. 8) made calculations with Doppler tracking data from Voyager (1979) and Viking (1977) that enable estimation of the primary standard phase noise. In 1977, the Cs clock was used, while in 1979, the H-maser clock was used. Hellings was able to infer the phase on the clock by the following method:

In two-way tracking of spacecraft, the ground clock (frequency standard) controls the transmitter frequency ν as well as providing the reference for measuring the Doppler shift $\Delta\nu$ on the return signal. In normal DSN operation, the received signal is tracked in a phase-locked loop, the clock being used to beat the received frequency down to the Doppler tone. If there is a fluctuation $\delta\nu = q(t)$ in the frequency produced by the clock, then since the fluctuation is also present on the return signal a round-trip light time (RTLT) later, the Doppler record has a noise term given by

$$y(t) = -q(t) + q\left\{t - \left(\frac{2r_0}{c}\right)\right\}$$

where r_0 is the distance between the transmitter and the spacecraft.

It can be seen that autocorrelating the Doppler tone (after subtracting the predicted Doppler) will give rise to a negative peak in the autocorrelation function (acf) at $t = 2r_0/c$ having half the magnitude of the peak occurring at $t = 0$.

Other noises like white phase system noise will not produce this second peak, because this noise is present only on the return signal. Other noises like plasma and tropospheric noise have a spectrum that is quite different from the flicker of phase or frequency that is characteristic of clock noise, and hence the autocorrelation function is quite different. Details of spectra are given in Ref. 11. Thus, the clock noise can be identified and measured.

In obtaining both the 1977 and the 1979 data, the DSN 64-m-diameter antennas and S-band transmission frequencies were used. The S-band frequency for the 64-m subnetwork is derived from the 50-MHz CRG output by a multiplication by 48 in a Dana synthesizer. There have been no major changes in the multiplier or the coherent reference generator (CRG) between 1977 and 1979. Thus the difference between the clock noise results of Hellings in 1977 and 1979 shows the difference between the 50-MHz output obtained from the Cs standard + CRG system and the H-maser + CRG system. From the 1977 data, the clock phase noise as measured by its standard deviation was determined to be 10^{-13}; from the 1979 data, the clock phase noise was determined to be below the instrument sensitivity, i.e., $< 3 \times 10^{-14}$. This order-of-magnitude difference is about the same as the ratio of phase stability of the H-maser + receiver to the phase stability of the Cs standard + receiver, as determined by previous measurements. This supports the idea that the CRG phase stability is at least about as good as the stability of the Cs standard + receiver.

VII. Conclusions

The CRG phase noise has been estimated based on data about components similar to the CRG components. The phase noise calculations given here, taken together with the measured data (Refs. 9, 10) for the H-maser + receiver, of

$$\left.\frac{\Delta f}{f}\right|_{5^\circ\text{C step}} = 5 \times 10^{-13}, S_\phi\,(10\text{ Hz}) = -98\text{ dB},$$

$$\sigma_y(1\text{ s}) = 3 \times 10^{-13}$$

show that the coherent reference generator (CRG) phase stability, at least for the 0.1-, 1-, 5-, 10-, 50-MHz outputs, is better than that of the H-maser + receiver system.

The phase noise on the other CRG outputs (10.1, 45, 55 MHz) is expected to be higher, but by an unknown amount, because of crystal filter instabilities that are unknown.

The calculated results for the 50-MHz output corroborate the results that have been obtained indirectly by Hellings from Doppler data.

However, all the estimates here are tentative, because they are based on measurements not made directly on CRG components. The inferences of CRG noise from Hellings' calculations may also be incorrect, because the data were taken in 1977 for the Cs-based clock and in 1979 for the H-maser based clock, and many FTS components may have been changed during the period between the two measurements, although this does not appear to be the case.

VIII. Suggested Areas of Investigation

A. Direct Measurements

No measurements have been made either on the CRG as a whole or on most of its components. The best way to find the CRG stability would be to make direct measurements on it. The equipment needed to make this kind of measurement is not yet available but is soon expected to be.

Alternately, the phase noises of individual CRG components can be measured, as has been done for some of the H-maser receiver components. In particular, the crystals and crystal filters used in the CRG should be measured for phase stability, since no estimates for these are available, and they are expected to be important noise sources in the CRG. The overall CRG stability can be calculated once the individual component stabilities are correctly known.

B. Indirect Measurements

It would be worthwhile to set up a VLBI experiment specifically for the purpose of measuring the relative stability of the Cs and H-based clocks. This would be useful if a direct estimate of CRG noise cannot be made.

This kind of experiment would require using the two standards separately for observing the same celestial source. The two sets of measurements would have to be made within a short period of each other, so as to minimize errors due to different paths to the source. Intermediate phase data, not normally preserved in VLBI experiments, may need to be kept in order to compare clock stabilities.

The direct method of CRG stability estimation would be preferable because there are too many variables, especially atmospheric effects on phase, that cannot be correctly accounted for in VLBI experiments.

Acknowledgments

The author would like to thank Roger Meyer for his many helpful discussions and suggestions throughout; the discussions with Paul Kuhnle, Ronald Hellings and George Madrid are also gratefully acknowledged.

References

1. Coherent Reference Generator Technical Manual, TM 509236, Jet Propulsion Laboratory, Pasadena, Calif., February 1976. (an internal document).
2. Lutes, G., et al. "Hydrogen Maser: Low Phase Noise, L-Band Frequency Multiplier," TR 32-1526, Vol. VII, pp. 81-83, Jet Propulsion Laboratory, Pasadena, Calif., February 1972.
3. Meyer, R., and Sward, A., "Frequency Generation and Control: The Measurement of Phase Jitter," *DSN Space Programs Summary 37-64*, Vol. II, pp. 55-64, Jet Propulsion Laboratory, Pasadena, Calif., August 1970.
4. Barnes, J. A., et al., "Characteristics of Frequency Stability," NBS Technical Note 394, U.S. Department of Commerce, October 1970.
5. Allan, D. W., "Error in Flicker Noise Time Domain Stability Equations," NBS Memo 273.00/PA/PB-6, U.S. Department of Commerce, February 1973.
6. Lutes, G., "Frequency Generation and Control: Distribution Amplifiers for the Hydrogen Maser Frequency Standard," *DSN Space Programs Summary 37-61*, Vol. II, pp. 68-72, Jet Propulsion Laboratory, Pasadena, Calif., January 1970.
7. MacConnell, J., et al., "L-Band Frequency Multipliers: Phase Noise, Stability and Group Delay," *DSN Progress Report 32-1526*, Vol. X, pp. 104-109, Jet Propulsion Laboratory, Pasadena, Calif., August 1972.
8. Hellings, R. W., "Spacecraft-Doppler Gravity Wave Detection," *Physical Review D*, Vol. 23, pp. 832-851, February 1981.
9. Sward, A., "Measurement of the Power Spectral Density of Phase of the Hydrogen Maser," Quarterly Technical Review, Vol. I, No. 4, pp. 30-33, Jet Propulsion Laboratory, Pasadena, Calif., January 1972.
10. Kuhnle, P. F., "Hydrogen Maser Implementation in the Deep Space Network at the Jet Propulsion Laboratory," Proceedings of the 11th Annual Precise Time and Time Interval (PTTI) Applications and Planning Meeting, NASA Conference Publication 2129, pp. 197-210, November 1979.

Table 1. Phase noise estimates for 0.1-, 1-, 5-, 10-MHz outputs of CRG, referenced to a 100-MHz output

	$\Delta f/f$ for 5°C step	S_ϕ(10 Hz)	σ_y(1 s)
1) Input driver (D_i)	3.7×10^{-14}	−111 dB	1×10^{-13}
2) Distribution amplifier (DA)	7.4×10^{-14}	−108 dB	1.4×10^{-13}
Total	1.11×10^{-13}	−106 dB	1.7×10^{-13}

Table 2. ×10 (zeta) multiplier phase noise estimates, referenced to a 100-MHz output

$\Delta f/f$ for 5°C step	S_ϕ(10 Hz)	σ_y(1 s)
1.04×10^{-14}	−133 dB	5.4×10^{-15}

Table 3. Phase noise estimates for 10.1-, 45-, 50-, 55-MHz CRG outputs, referenced to a 100-MHz output

	$\Delta f/f$ for 5°C step	S_ϕ(10 Hz)	σ_y(1 s)	Remarks
50 MHz	1.2×10^{-13}	−106 dB	1.7×10^{-13}	From Tables 1 and 2
10.1 MHz	$>1.1 \times 10^{-13}$	>−106 dB	$>1.7 \times 10^{-13}$	From Table 1 and allowing for filters
45, 55 MHz	$>1.2 \times 10^{-13}$	>−106 dB	$>1.7 \times 10^{-13}$	From Tables 1 and 2 and allowing for filters

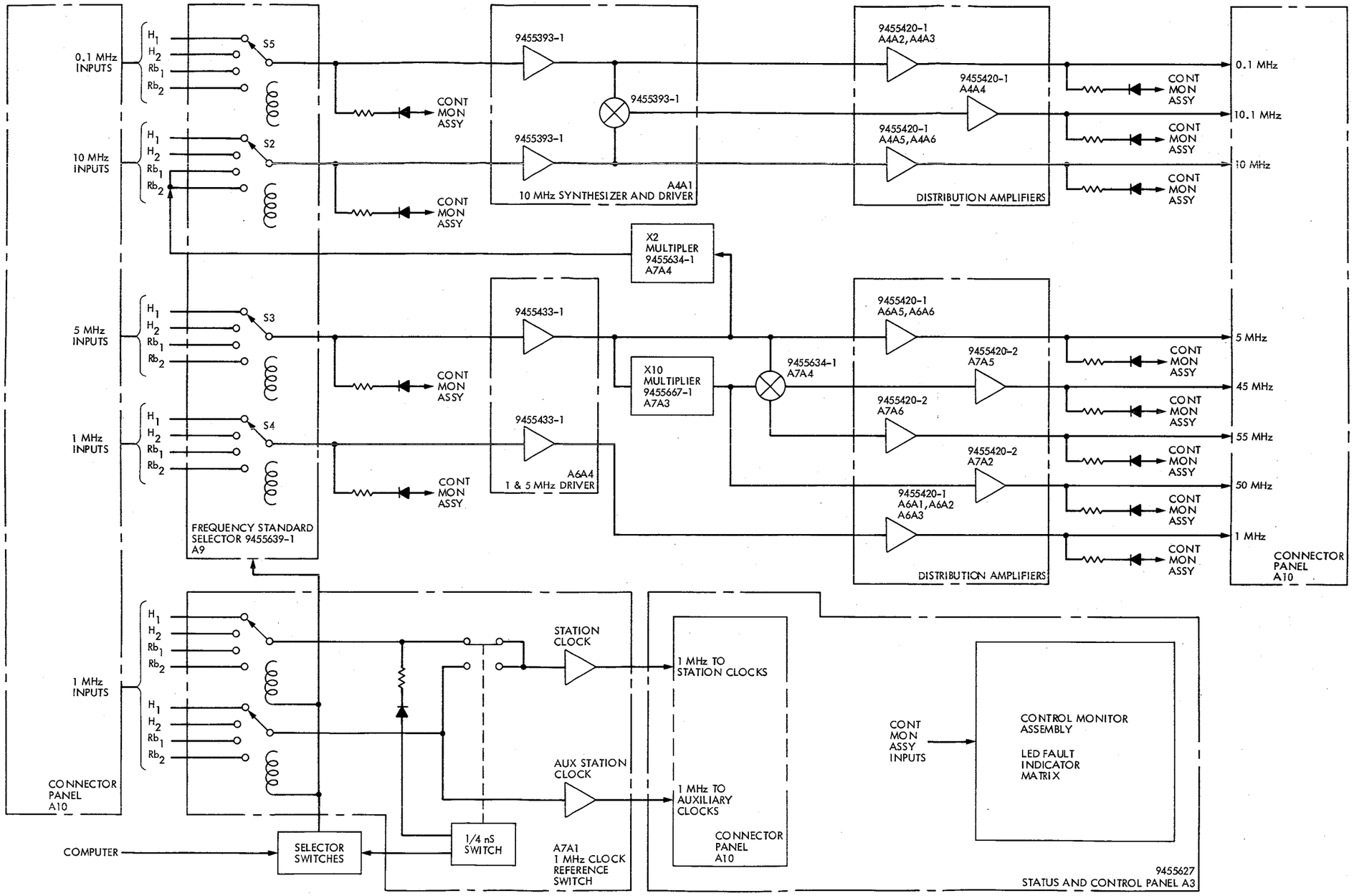

Fig. 1. Coherent reference generator, detailed block diagram

This Page Intentionally Left Blank

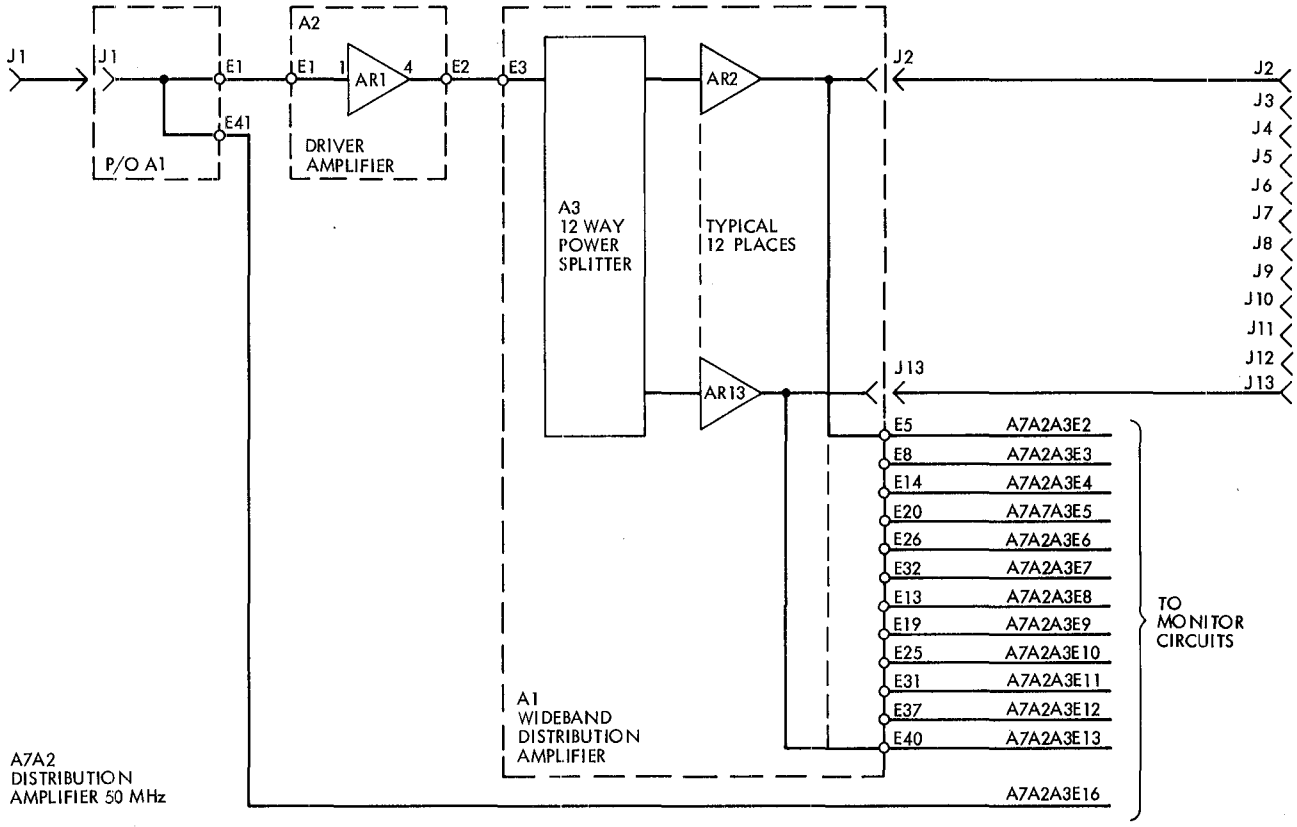

Fig. 2. Typical coherent reference generator distribution amplifier

Current Status of the HAL/S Compiler on the Modcomp Classic 7870 Computer

P. J. Lytle
Data Systems Section

This article presents a brief history of the HAL/S language, including the experience of other users of the language at JPL. The current status of the compiler, as implemented on the Modcomp 7870 Classic computer, and future applications in the DSN are discussed. The primary applications in the DSN will be in the Mark IVA network.

I. Introduction

HAL/S is the NASA standard high-order real-time programming language for avionics applications. Its most significant use to date has been the production of NASA Space Shuttle flight software. Approximately 85% of the Shuttle software is coded in HAL/S: a body of 2 million lines of comments, data declarations and executable lines of code. NASA installations using the HAL/S compiler include Johnson Space Center, AMES, Goddard, Langley, Marshall and Jet Propulsion Laboratory.

II. History of the HAL/S Compiler

HAL/S was designed by Intermetrics, Inc., in 1972. Compilers became available in 1973 and have been in regular use by NASA and NASA contractors since that time. Host compiler systems have been implemented on an IBM 360/370, Data General Eclipse, and the Modcomp IV/Classic computers. Table 1 shows the target-host relationship.

In 1978, JPL contracted with Intermetrics to develop HAL/S compilers for the ITEK ATAC 16M, RCA 1802 and Modcomp II/IV computers hosted on an IBM 360/370, and a Modcomp II/IV compiler hosted on a Modcomp IV. The ATAC and 1802 compilers were planned to be used for the Galileo Project, and the Modcomp compilers for the Deep Space Network and the Automated Optical Navigation Project.

The Galileo Project is developing a major portion of its software for the ATAC 16M on-board flight computer in HAL/S. Development of the Galileo software is being done on an IBM 370 and the code is being downloaded to the flight computers.

The Automated Optical Navigation Project started developing software in HAL/S on a IBM 370 two years before the Modcomp compiler was completed. Their software system consists of approximately 7000 lines of HAL/S code, a few hundred lines of Fortran and no assembly language. They currently are in the process of downloading and interfacing the real-time tasks to a Modcomp IV computer.

III. Current Contractual Status

All contracted HAL/S compilers have been delivered and accepted by JPL. A maintenance service for the Modcomp compiler has been operational since May 1981. HAL/S training courses arc planned for the near future. These courses will be taught by Intermetrics until JPL can provide the courses.

IV. Current Operational Status

The Deep Space Network has an operational HAL/S compiler hosted on a Modcomp Classic 7870 computer under the MAX IV operating system. A Time-Sharing Executive (TSX) transaction processor is used to create a simple multiuser environment. The configuration of this system currently has inputs for up to 10 HAL/S software development programmers.

Since the HAL/S-Modcomp compiler was accepted in April 1981, there have been over 20 discrepancy reports filed on the compiler. Recently, Intermetrics personnel corrected the seven most critical of these as part of the maintenance effort. It is anticipated that most of the discrepancies will be fixed before any major project uses the HAL/S-Modcomp compiler.

V. Future Applications

There are four projected users of HAL/S in the DSN. These projects are the Test Support Assembly (TSA), Antenna Control Assembly (ACA), Link Monitor and Control (LMC), and the Complex Monitor and Control (CMC). The TSA project will consist of up to 75% of HAL/S code, up to 80% for ACA, and up to 90% for both of the LMC and CMC projects. The ACA project will have approximately 25,000 to 40,000 lines of software; 12,000 to 20,000 lines for the TSA project, 10,000 to 35,000 lines for the LMC project, and 16,000 to 35,000 lines for the CMC project.

VI. Summary

HAL/S is useful in applications such as the Mark IVA network project. This language is appropriate for a good portion of the software required, although some assembly language will be needed for I/O handlers and interrupt drivers. In the future, the Data Systems Section intends to provide a software programming environment, including such tools as a screen editor and Development Version Control System (DVCS), to enhance the productivity advantage of coding in a high-level language.

Table 1. HAL/S target-host relationship

Target	Host		
	Eclipse	Modcomp IV	IBM
IBM 360/370			X
IBM AP-101	X		X
Sperry 1819A/1819B			X
Data General Nova			X
Data General Eclipse	X		X
CII Mitra 125			X
Modcomp II		X	X
Modcomp IV		X	X
NASA Std. Spacecraft Computer-1			X
NASA Std. Spacecraft Computer-2			X
ITEK ATAC 16M			X
RCA CDP 1802 COSMAC			X

Relocation of the Network Data Processing Area

R. P. Hurt
Control Center Operations

Rationale for relocation of the Network Data Processing Area is presented along with background information regarding the Network Operations Control Center.

The Network Operations Control Center is the functional entity for centralized operational control of the Network and interfaces with the users. It has two separable functional elements; namely, Network Operations Control and Network Data Processing. The functions of the Network Operations Control are:

(1) Control and coordination of Network support to meet commitments to Network users.

(2) Use of the Network data processing computing capability to generate all standards and limits required for Network operations.

(3) Use of Network data processing computing capability to analyze and validate the performance of all Network systems.

The personnel who carry out the above functions are located in the Space Flight Operations Facility (SFOF), where mission operations functions are carried out by certain flight projects. Network personnel are directed by an Operations Control Chief.

The functions of Network Data Processing are:

(1) Processing of data used by Network Operations Control for control and analysis of the Network.

(2) Generating displays in the Network Operations Control area.

(3) Providing the interface with communications circuits.

(4) Logging of data and production of the intermediate data records.

Prior to relocation, the personnel and equipment that carry out a portion of these functions were located approximately 200 meters from the Space Flight Operations Facility. The equipment is referred to as the Network Data Processing Area (NDPA). The equipment consists of minicomputers for real-time data system monitoring, two XDS Sigma 5s, display devices, magnetic tape recorders, and appropriate interface equipment with the ground communications facility.

Figure 1 is a functional block diagram that depicts data flow from the Deep Space Stations (DSSs) to the Flight Projects. The hashed area is the equipment referred to as the NDPA. As one can readily discern, the functional processes performed by the Network Data Processing Area do not interrupt, delay or alter Project real-time data flow since they are performed in a parallel mode.

As previously stated, the Network Data Processing Area was housed apart from the SFOF, where the bulk of the Network and Mission Control facilities are located. With the consolidation of the Network Operations Control Center (NOCC) and the Mission Control Center Operations coupled with the availability of space in the SFOF (Bldg. 230) an excellent opportunity existed to colocate the NDPA with these major

operations centers. As a result of this colocation some major benefits could be realized:

(1) Lower operations cost.

(2) Improve operations efficiency in the areas of reliability, maintainability, and troubleshooting.

(3) Enhance further NOCC/MCC consolidation.

(4) Provide a more suitable computer operating environment.

(5) Provide a more convenient location for development activities.

(6) Release JPL technical space for other users.

After careful consideration of the above-mentioned factors, a plan was initiated to relocate the NDPA to the SFOF. A move date was negotiated with the Voyager Project, the primary flight project user, that would impose the least impact to Voyager data requirements. A low activity period of February-March 1981 was selected. The plan was designed to be completed in two phases. Phase one relocated the minimum equipment required to support network and project processing requirements; phase two relocated the remainder of the equipment.

A commercial moving company, specializing in electronic equipment movement, was contracted to perform the physical move. The Federal Electric Company Digital Maintenance Group prepared equipment under their cognizance for movement by disconnecting, labeling, and coiling all cabling, packing computers and peripherals, and supervising positioning of equipment at the new location. Western Computer Corporation, the contractor responsible for the maintenance of the Sigma 5, performed similar functions on that equipment.

Phase one of the move was completed as scheduled and the minor problems that were encountered served as lessons learned in expediting phase 2. The major problem was movement of the ModComp II double bay computer through doors, hallways, and under lowered ceilings with fire sprinklers protruding. Once these obstacles were overcome, the move proceeded without incident. The natural elements did not go unnoticed as rain fell heavily during phase one; however, the commercial mover supplied the necessary protection. Phase two of the move was also completed on schedule with no major problems. The system was completely operational in its new location on 16 March 1981, one week ahead of schedule (Fig. 2). The actual time that Voyager Project and other users had no computer-generated real-time displays from the NDPA during the relocation period was four days. During these four days, display information was provided to the NDPA users via workaround procedures which included voice interfaces. Computer-generated priority data was restored on the fifth day.

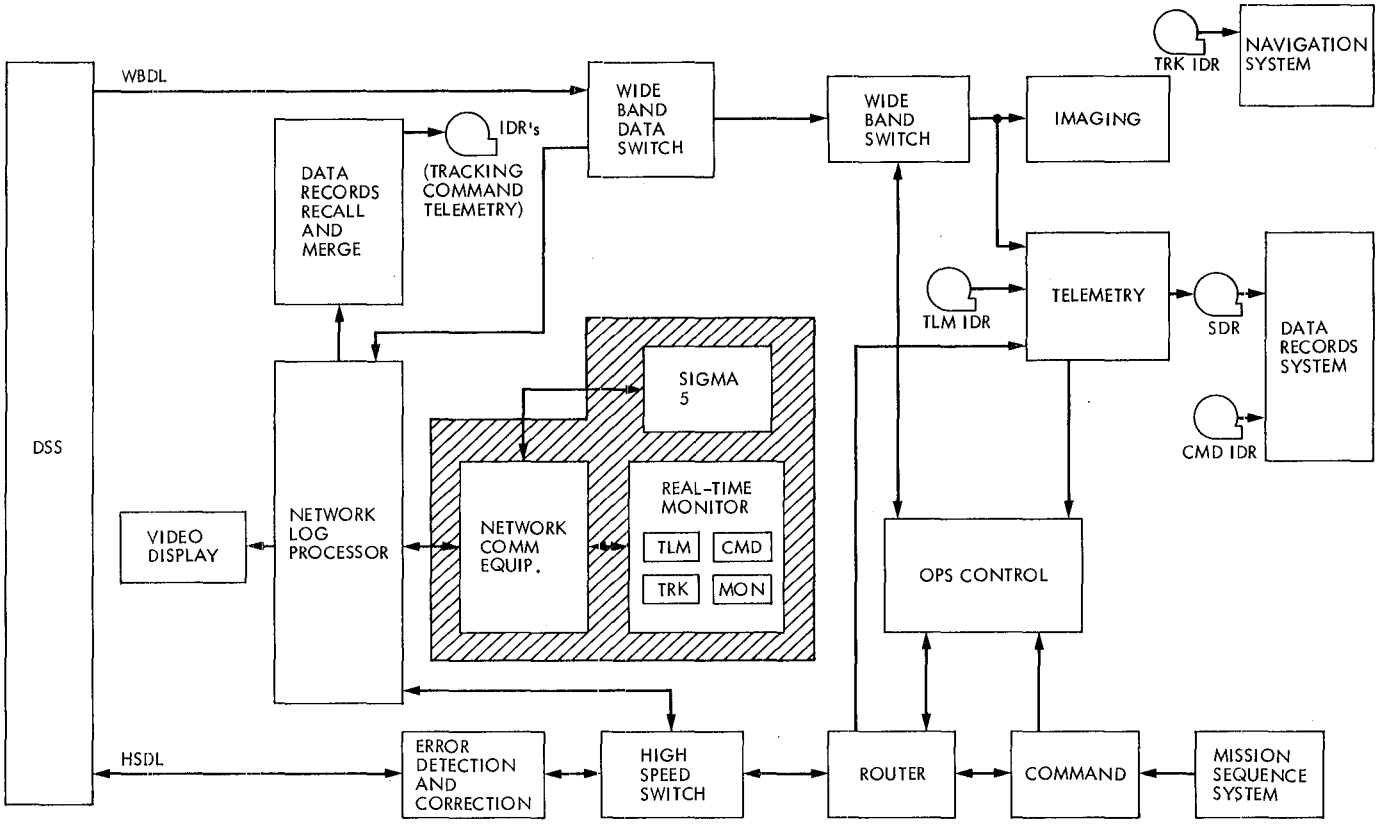

Fig. 1. Data flow functional block diagram

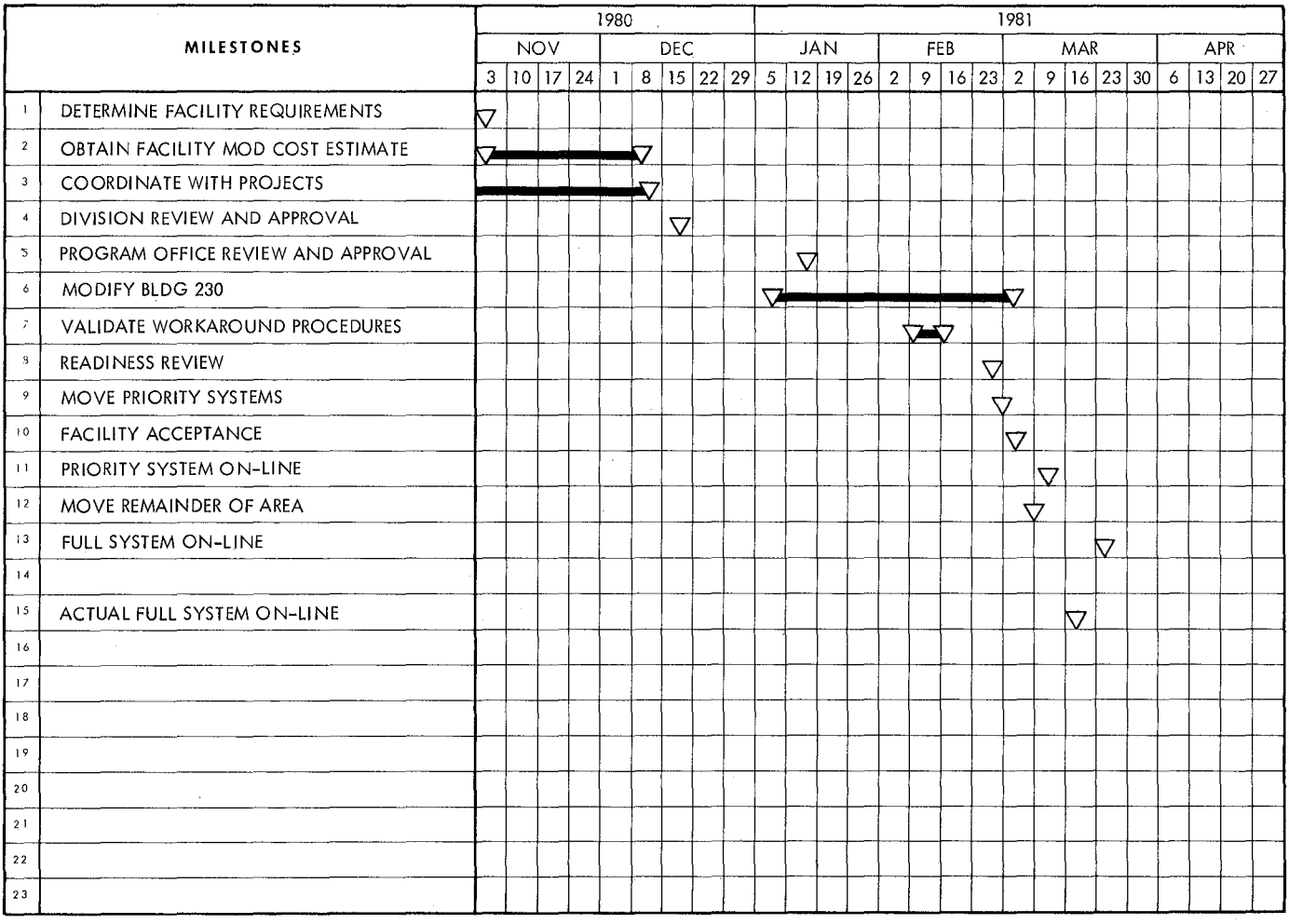

Fig. 2. Implementation schedule

Recycling Used Lubricating Oil at the Deep Space Stations

J. L. Koh
Deep Space Network Support Section

Current practice at the Deep Space Stations (DSSs) is to change the diesel engine lubricating oil after 1000 hours of operation. In 1977, the Canberra, Australia, station (DSS 43) conducted a test to extend engine oil life by recycling the oil through a centrifuge at the 1000-hour periods. Due to massive sludge buildup in the engine, the test was terminated after the oil had been recycled four times. This report provides a comparison on the recycling methods used in the DSS 43 test and the basic requirements which could favor recycling of oil for continuous reuse. The basic conditions for successful recycling were compared to the conditions that exist in the DSN. This comparison shows that to recycle used oil in the DSN would not only be expensive but also nonproductive.

I. Introduction

It is reasonable to assume that each time an engine or equipment lubricating oil change is made at the deep space stations, there is a possibility that the used oil could be recycled for a cost savings and as a conservation measure. The possibility will increase in importance if oil shortages become more acute, while at the same time more stringent environmental controls on the disposal of used oil are effected.

Interest in recycling used oil is not confined to the deep space stations. Large oil consumers, oil filter and purification manufacturers and, in general, environmental conservationists, are also interested in recycling used oil. Understandably, this interest is not shared by lubricating oil manufacturers.

The purpose of this report is to determine whether conditions favor recyling used oil at the deep space stations. The data used in the cost estimates are based on the Commercial Power Feasibility Study for Madrid Tracking Stations, 1980 (Ref. 1), and the DSS 43 Lubricating Oil Recycling report, 1977 (Ref. 2).

II. Methods of Recycling Lubricating Oil

In mid-1976, DSS 43 in Canberra, Australia, conducted a program to extend the life of the lubricating oil used in the four G399 Caterpillar diesel engines used to drive the powerhouse alternators. The method employed was to clean the used oil in situ through a centrifuge after each 1000 hours of engine operation. Cleaning was done with the engine running and the time taken for each cleaning was about 40 hours. Samples were taken after each cleanup and tested at the British Petroleum Oil Company laboratory for suitability and signs of increased wear rates. The results reported by the British Petroleum Oil Company indicated that the oil was still within recommended limits after 4000 hours of use. However, the results obtained were questionable since heavy sludge formation and filtering system damage were detected during the first 5000-hour inspection. The program was therefore terminated and the recommended oil change sequence was resumed.

Compared to commercial or large-scale consumer methods (Ref. 3) of rerefining used lubricating oil, the DSS 43 method was only an extention of continuous partial filtration and cannot be accepted within the context of a recycling process. A typical method of recycling oil is to filter, rerefine, repurify, and test the quality before reuse, as shown schematically in Fig. 1. This process represents a miniature lube blending plant (in terms of equipment and operations) with additional filtration for the feedstock and sludge disposal system. This typical process is the minimum required to ensure that the reclaimed oil can meet the following:

(1) Lubricant and lubrication requirements

(2) Expected quality of good lubricating oil

(3) Disposal of sludge

III. Lubricant and Lubrication Requirements

Whether new or refined, oil is designed and blended to a specification that will fulfill the lubrication functions that the oil is expected to provide. These requirements are summarized as follows:

(1) Lubricate: To function hydrodynamically on all parts, to reduce friction, heat, and wear when introduced as a film between solid surfaces receiving a continuous flow of fluid lubricant. To function as a thin lubricant on parts such as in an oil bath.

(2) Clean: To keep parts and surfaces mechanically clean, thus preventing wear and improving performance.

(3) Seal: To prevent foreign material from entering the parts and surfaces.

(4) Cool: To transfer the heat from the parts to a cooling medium.

(5) Protect: To shield all parts from buildup of foreign material, corrosive attacks and degradation of the lubricant itself.

IV. Expected Quality of Good Lubricating Oil

Virgin lubricating oils extracted from mineral sources, whether straight-run or multiblend, cannot meet all lubrication requirements. Similarly, rerefined oil cannot be expected to retain its original physical properties and function as well as in its original application. Just as natural new lubricating oils are treated as base stocks, the rerefined oil must be considered as base stock, and can be reblended to the required specification. The reblending process might take the sequence of (Ref. 4):

(1) Reblending with other base stocks (including synthetic base oils) to meet viscosity and volatility standards.

(2) Adding of detergents to:

  (a) Prevent gum buildup.

  (b) Clean away dirt and scavenge engine parts of sludge.

  (c) Suspend fine particles.

  (d) Disperse soluble residues and insolubles.

  (e) Prevent sludge formation.

  (f) Neutralize corrosive acids.

  (g) Prevent rust corrosion.

  (h) Ensure adhesion to moving parts.

(3) Adding of chemicals to:

  (a) Reduce rate of wear at critical areas.

  (b) Improve viscosity to improve lubrication strength.

  (c) Improve thermal stability.

  (d) Reduce emulsification.

  (e) Widen margin of applications.

  (f) Improve flexibility.

  (g) Reduce consumption.

(4) Adding inhibitors to:

  (a) Slow down oxidation.

  (b) Reduce metal reaction.

  (c) Increase equipment life.

  (d) Improve performance.

V. Confidence in Using Recycled Oil

No matter how good rerefined oil is, there is at present a negative feeling because it is not new. This lack of confidence stems from the fact that it is impossible to physically or chemically remove all the contaminants that entered the oil when it was originally used. Because of these residual contaminants, it is difficult to maintain the lubrication warranty requirement for the equipment, and the warranty may be invalidated.

Users of rerefined oil will generally downgrade its applications by running on a shorter oil change cycle, or by using it as a topping-up oil. To ensure that such applications can achieve a successful degree of lubrication, a controlled schedule of oil

change and topping must be planned. Table 2 shows such a schedule of an engine's typical oil change cycle and topping-up procedure.

VI. Incentive to Recycle

With proper rerefining processes and careful scheduling in using rerefined oil, the useful life of the oil can be extended indefinitely; hence, potential savings could be realized. As shown in Table 1 for a five-year period, the amount of oil saved is about 52% of the total oil used. As far as the DSN is concerned, the incentive to recycle oil will be the net savings the effort can provide.

At the Madrid Tracking Station, the present operating configuration of the power-house requires two G399, three G398 diesel engine generators, and occasionally others. At a 1000-hour change cycle, these engines will need about eight oil changes per year. G399 requires 420 liters (110 gal) and G398 requires 345 liters (90 gal) of oil per change plus approximately 50% more for topping-up between each change (Appendix A). The total need per year is about 28,350 liters (7500 gal) consisting of:

G399 $2 \times 8 \times 630 =$ 10,080 liters (2670 gal)

G398 $3 \times 8 \times 520 =$ 12,480 liters (3300 gal)

Others 5,790 liters (1530 gal)

28,350

Oil saved per year by rerefining

$0.52 \times 28{,}350 =$ 14,742 liters

Potential dollar savings @ \$0.40/liter

$14{,}742 \times \$0.40 = \$5{,}897$

The above figure (\$5897) does not consider the costs of the recycling process and sludge disposal.

The most desirable way to recycle this used oil would be to have it commercially rerefined and reblended to the original specifications. Since the quantity involved is small, the processors contacted were not interested in performing this service. Alternatively, the used oil could be stored and processed periodically with on-site rerefining equipment. The equipment envisaged will be about a 220 liter-per-hour processing unit fully equipped with storage, blending, and testing facilities. Although such equipment is not readily available, most vendors contacted indicate that the equipment could be built to customers' requirements for about \$40,000, plus \$20,000 for installation, making a total capital cost of about \$60,000.

Based on a large plant (6500 liter/hr), the operating cost per liter for high-level pretreatment (vacuum distillation and solvent extraction) is about \$0.08. With a small unit, the pretreatment costs can be \$0.10 per liter. Additives and other miscellaneous costs add \$0.05 per liter and costs for disposing of sludge at a city sanitation dump add \$0.05 for a total operating cost of about \$0.20 per liter. Based on Madrid data, the operating cost for rerefining the used oil is about \$2,948 per year. The net savings per year is about \$2,949. Since the capital investment is about \$60,000, the savings do not justify rerefining used oil in the DSN under existing circumstances.

VII. Disposal of Sludge

One of the main problems associated with recycling used oil is the disposal of sludge. Since used oil has already been classified as a hazardous waste, the sludge is considered more hazardous and the disposal will have to conform to the conditions stipulated in the Resource Conservation and Recovery Act of 1976, Public Law 94-580 Subtitle C. This act established the standards for treatment, transportation, storage, and disposal of hazardous waste. The act has, in effect, ruled out the common methods of sludge disposal on land or burning in incinerators, and probably increases the problems of sludge disposal beyond the ability of the deep space stations to cope with them. Therefore, the DSN may require outside assistance in the disposal of sludge.

VIII. Alternate Use of Recycled Oil

The above discussions indicate that it would be impractical for the DSN to recycle used oil as a lubricant. If the used oil were to be of any value to the stations, it would have to be used as a fuel mix for the diesel engines. Based on used oil and fuel data from the Madrid stations, the used-oil-to-fuel ratio is about 0.4% by volume (Appendix B). This low percentage of oil-to-fuel ratio will require only simple processes of dilution, mixing and settling to achieve the purpose shown in Fig. 2. A study done by the U.S. Environmental Protection Agency indicated that the technical and environmental factors affecting used oil reuse as a fuel must be considered. These pertinent factors would vary with each situation, but as far as the stations are concerned, they should be reasonably easy to overcome.

IX. Recommendation and Conclusion

The recycling of used lubricating oil is an entirely new technology and current equipment available for small systems for this recycling process is still in the experimental stage. Also, the expertise required to operate such a system would be equivalent to that of a lubricating oil blending plant, and this expertise is not available at the stations. This report shows that there are no incentives at the stations to recycle diesel engine lubricating oil. The simplest method to recover the value of the used oil would be to use it as a fuel mix. Since the quantity involved is small, the pertinent problems normally associated with using the recycled oil as a fuel mix should be reasonably easy to overcome. Further study is continuing.

References

1. "Commercial Power Feasibility Study for Madrid Tracking Stations". Technical Study Report Prepared for DSN Facility in Spain, Sereland Inc., Madrid, 1980.
2. Technical Report – TR 77-2 "DSS 43 Lubricating Oil Recycling" issued by: Network Support Facility, DSS 43, Canberra, Australia, February 1977.
3. Blatz, F. J., and Pedall, R. F., "Rerefined Locomotive Engine Oils and Resource Conservation", Vol 35, pp. 620-621, *ASLE Lubricating Engineering*, November 1977.
4. Lancaster, R., "Description of Lubricating Oil Terms and What They Mean," Presentation paper of Torco Oil Company, Santa Fe Springs, Calif.

Table 1. Average oil savings per year through recycling based on G399 Caterpillar engine (five-year period total 40 oil changes)

Engine hours run	New or recycled oil	Lubrication requirement: Oil change, liters per 1000 hrs	Lubrication requirement: [a]Total top-up liters per 1000 hrs	[b]Oil losses due to recycling liters	Remarks
0	New	420	0	0	First year savings
	Recycled	0	0		Total new oil used = 2688 liters
1000	New	0	210	0	Total re-refined oil used = 2352 liters (oil saved)
	Recycled	0	0		
2000	New	294	0	84	Total quantity of oil used if no recycling = 5040 liters
	Recycled	126	210		
3000	New	294	0	84	Percent oil savings through recycling $= \frac{2352}{5040} \times 100 = 46.7\%$
	Recycled	126	210		
4000	New	294	0	84	Five year savings
	Recycled	126	210		
5000	New	294	0	84	Total new oil used = 12096 liters
	Recycled	126	210		Total re-refined oil used = 13104 liters
6000	New	294	0	84	
	Recycled	126	210		Percent oil savings through recycling $= \frac{13104}{25200} \times 100 = 52\%$
7000	New	294	0	84	
	Recycled	126	210		
8000	New	294	0	84	
	Recycled	126	210		
One-year period	Total new	2478	210	0	
	Total recycled	882	1470	588	
Five-year period	Total new	11886	210	0	
	Total recycled	4914	8190	3276	

[a]Average oil consumed
[b]Assume 80% recovery in recycling

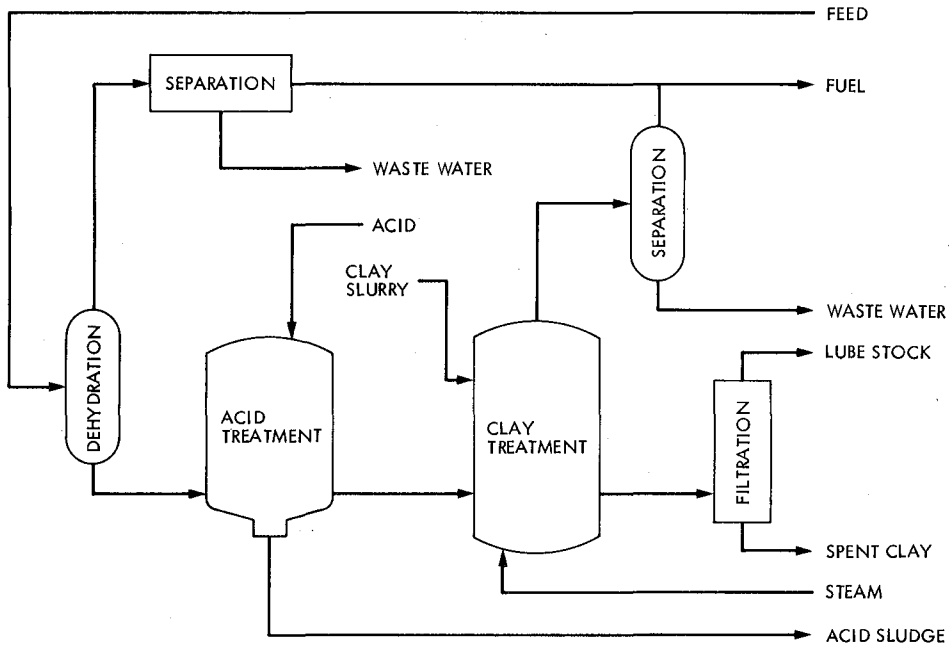

Fig. 1. Rerefining by acid/clay process. Process starts with dehydration to remove any water and solvents from the feed; followed by acid treatment to "break down" contaminants into acid sludge. The acid treated oil passes through a clay bed to remove color bodies and remaining contaminants. The spent clay is removed by filtration, producing a quality base oil product to be blended to specification.

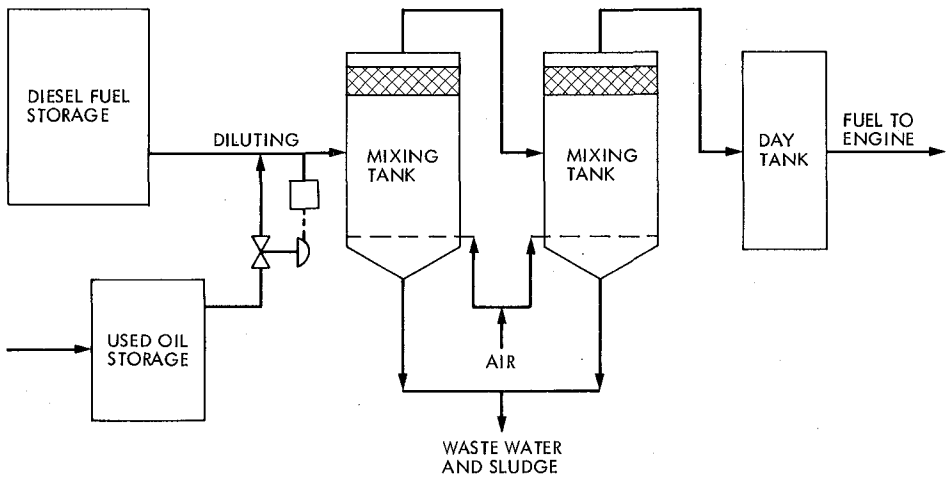

Fig. 2. Fuel and oil mixing process. Process starts with the used oil being diluted with diesel fuel in the appropriate proportion; followed by mixing and settling. Air is used to provide a more homogeneous mixture as well as a means of coalescing water droplets in the mixture. Wire mesh coalescers at the top of the mixing tanks coalesce any water/sludge suspended in the mixture and drop them to the bottom to be drained during settling.

Appendix A

Lube Top-Up Requirements

DSS 14 lubricating oil consumed Jan-Aug 1980 = 2250 liters (595 gal)

Hours engines run same period
Four G399[1] = 3170 hours
Four G398[2] = 1493 hours

Total equivalent G399 engine run $= \left(\frac{500}{750} \times \text{G398 equivalent hours}\right) + 3170 \text{ hours}$

$= \left(\frac{500}{750} \times 1493\right) + 3170 \text{ hours}$

$= 995 + 3170 \text{ hours}$

$= 4165 \text{ hours}$

Equivalent oil consumed per 1000 hours for four G399 $= \frac{2250}{4.165}$

$= 540$ liters (143 gal)

Therefore one G399 consumed $= \frac{540}{4}$ liters

$= 135$ liters (36 gal)

NOTE: 135 liters represents about 32% of a G399 engine oil change under normal operations. With recycling, a 50% quantity is assumed to allow for higher handling losses.

[1] G399 rated at 750 kW.
[2] G398 rated at 500 kW.

Appendix B

Diesel Fuel With Used Oil Mixture

Assumption (Data based on Madrid Tracking Station):

Total lubricating oil usage = 28350 liters/year

Total lubricating oil consumed = 28350 X 0.33

= 9356 liters/year

Used lubricating oil available for fuel = 18994 liters/year

Total fuel oil consumption = 4,722,580 liters/year

Percent oil-to-fuel mixture $= \frac{18994}{(4{,}722{,}580 - 18994)} \times 100\%$

= 0.4%

Computerized Energy Analysis for the Mars Operations Support Building

C. S. Yung
DSN Engineering Section

This article describes a detailed computerized building load simulation of the Operations Support Building at the Mars Deep Space Station, Goldstone, California. Five energy conservation suggestions were investigated prior to implementation. The results showed that cost savings of about 16 percent of present energy costs are possible.

I. Introduction

Energy conservation in the JPL-managed deep space tracking facilities continues to be a major concern in the face of unpredictable and scarce fossil fuel supplies. Energy needed for heating and cooling is increasingly expensive and in short supply. However, heating, ventilating and air conditioning (HVAC) systems are continuously changed by optimizing equipment size and performance and upgrading controls to keep energy consumption at the lowest level.

The Operations Support Building (G-86) at the Mars deep space tracking facility at Goldstone, California, is one of the buildings which has a significant energy consumption. A study was initiated to give a detailed building load analysis, to identify the major energy consumption areas and to investigate the economic benefits of implementing several suggested energy conservation measures. This study is based on the latest building operating mode (BOM) and makes use of an in-house computerized energy consumption program (ECP). The results are described below.

II. Building Configuration

A. Building Description

The Operations Support Building is a two-story building with 1,271 m^2 (13,680 ft^2) total floor area. Figures 1 and 2 illustrate the floor plan for each story. The building is actually composed of 7 air-conditioned zones which are grouped for convenience and modeled by ECP as 6 macrozones. Table 1 lists the location, the conditioned air flow rate to each zone and the number assigned to each zone.

Figure 3 is a sketch of the present HVAC system configuration for the building. The building is air conditioned by three active air handlers (AH1, AH2, and AH3) and a standby unit (AH4). Presently, the heating coils of air handler AH1 are connected to an electric resistance boiler. The coil modulates the air temperature for zone 1 (offices) and zone 3 (control and communication rooms) only.

In the model, the second floor offices are divided into two zones (zones 1 and 4) as indicated in Table 1. Also the com-

mon plenum for both communication and the control rooms is modeled as zone 2 and the comfort area of the communications room as zone 3. The restroom (room 205) is treated as zone 5, and the hydrogen-maser room is identified as zone 6. The first zone receives a total of 3,993 m^3/hr (2,350 cfm) from airhandler No. 1 (AH1). The plenum (zone 2) receives a total of 67,968 m^3/hr (40,000 cfm) of cold air from two air handlers: 28,886.4 m^3/hr (17,000 cfm) from AH1 and 39,081.6 m^3/hr (23,000 cfm) from AH2. The third zone receives a total of 11,010.8 m^3/hr (6,480 cfm) from AH1. The remaining offices (zone 4) and the restroom receive 679.7 m^3/hr (400 cfm) and 212.4 m^3/hr (125 cfm) for AH1, respectively. The maser room is supplied with 3,398.4 m^3/hr (2,000 cfm) from AH3.

The office and the restroom (zones 1, 4, and 5) are modeled as simple zones. The maser room is also treated as a simple zone and is supplied by a separate air handler (AH3) which utilizes the cold air in the plenum for the supply air. A small condensing unit connected to AH3 will operate only when the plenum air temperature is above the AH3 cold deck setpoint. The control room and the comfort area, which are both cooled by the plenum's cold air, are combined into zone 3. Cold air is fed to the plenum and passes through and cools the electronic racks located on the upper level.

B. Structural Data

The structural data of the roof, wall and floor layers for each zone are taken from drawing specifications and field inspection for computing the following heat transmission properties: the overall heat transfer coefficient at steady state U, the amplitude of the heat transfer coefficient for periodic (transient) heat transfer V, and the phase angle (thermal lag) ϕ. Table 2 lists the computed U, V, ϕ values for each zone.

C. Internal Loads

The building internal loads include lighting loads, electrical and mechanical equipment loads, occupancy and thermal loads. The data are taken from current field survey, operating procedure, and equipment specifications.

D. Primary Equipment Data

Air handler AH1, feeding zones 1, 2, 3, 4, and 5, is a multi-zone air handler with double ducts and terminal air mixing boxes. Air handlers AH2 and AH3 are both single-zone air handlers providing cold air only. Zones 2 and 6 are fed by air handlers AH2 and AH3, respectively. The setpoints for AH1 are set at 11.1°C (52°F) for the cold deck and 22.7°C (73°F) for the hot deck. A single setting of 16.7°C (62°F) is assumed for air handler AH2. The setpoint of AH3 is 20.5°C (69°C). There is no outside air economizer on any air handler. The outside air ventilation ratios for AH1 and AH2 are both selected to be 0.05 and AH3 is set at 0.01.

Presently, there are three parallel vapor compression chillers at 98.45 kW(t) (28 tons of refrigeration), each connected to air handler AH2. Two of the chillers are operating and the third is a standby unit. The two parallel chillers were lumped into C1 as a four-stage unit with 49.24 kW(t)/stage (14 tons/stage) capacity. Air handler AH2 is connected to a chiller C2 modeled as a three-stage unit at 49.24 kW(t)/stage (14 tons/stage) capacity. A smaller single-stage unit, C3, is connected to air handler AH3 with 17.58 kW(t) (5 tons) capacity.

III. Result of Analysis at Present Operating Conditions

The result of the computerized analysis of building G-86 indicates that the building at current operating conditions consumes 1,856.9 MWh(e) annually. The annual energy cost is about $112,776 based on the Southern California Edison electric energy cost rate as shown in Fig. 4. Table 3 presents the itemized annual energy consumption of the building. Forty percent of the total energy consumed by the building is due to electrical and electronics equipment such as computers and spacecraft tracking control equipment. Cooling equipment consumes the second largest portion of the total annual energy needs.

The peak cooling loads for chillers C1, C2, and C3 are 142.08, 86.16, and 17.58 kW(t) (40.4, 24.5 and 5 tons of refrigeration), respectively. Hence, the total installed capacity of each of the three chillers is adequate to provide the peak load. The peak annual heating load for heater H1 is given as 2.37 kW(t) (or 8,105 Btu/hr), which if compared to the heater capacity of 60 kW(t) (205,000 Btu/hr) means that the heating demand can be well satisfied.

The computerized model also indicates that the present air flow for zone 1, 13,993 m^3/hr (2,350 cfm), is less than the calculated design air rate of 5,233 m^3/hr (3,080 cfm), which causes the temperature fluctuation in zone 1 during the summer months. However, the present cold draft from the open door connected to zone 3 makes up for the deficiency of air flow in zone 1. Combined air flow rate for zones 2 and 3 is presently 78,979 m^3/hr (46,480 cfm), which is lower than the design rate or 85,884 m^3/hr (50,544 cfm). This difference in air flow rate also results in temperature fluctuations of zones 2 and 3. The present air flow rate for the remaining zones is higher than the computerized design values and is considered adequate.

The required supply air temperature for air handler AH1 was analyzed and was found to range from 10°C (50°F) to

28°C (83°F), which is beyond the setpoints limits of 11.1°C (52°F) to 22.8°C (73°F). However, the difference in supply air temperature can be corrected by increasing the air flow of AH1. The setpoints on air handlers AH2 and AH3 match the required supply air temperature within 1°C(~2°F).

IV. Proposed Modifications

Since the cooling energy represents 25 percent (454,600 kWh(e)) of the total building energy consumption, several suggestions have been made to modify the existing HVAC system to improve performance and reduce energy consumption. The modifications described next are superimposed; i.e., whenever a modification is simulated and found to yield significant energy savings, it is retained as a new base for the next one and so on. Each suggestion was analyzed and the results are presented below.

A. First Modification: Change the Inside Design Temperature to 20°C–25.6°C (68°F–78°F) Range; Install "Dead Band" Thermostat Controls

This modification proposes to change the inside temperature from 22.2°C (72°F) all year round to a variable temperature ranging from a maximum 25.6°C (78°F) to the minimum 20°C (68°F) for zones 1, 4, and 5. For zone 2 (the plenum) the design temperature remains at 17.8°C (64°F). The control room, zone 3, remains at 22.2°C (72°F) all year round.

The annual consumption of the building, after modeling this modification, has dropped to 1,851.7 MWh(e) from the present 1,856.9 MWh(e), resulting in a $310 savings. The annual heating energy has reduced also from 3,784 kWh(e) to 349.5 kWh(e). The peak heating load for heater H1 has dropped by 69 percent from the present condition.

B. Second Modification: Add a Variable Air Volume (VAV) Control for Zone 3 Only

This modification provides a VAV control to zone 3 by installing a motorized damper, the hot duct, closing off the cold duct and bypassing the supply air at unit AH1 whenever there is a decrease of air at zone 3.

The computer results indicated that the total annual consumption dropped from 1,851.7 MWh(e) to 1,849.9 MWh(e), which resulted in a saving of $118 annually. The heating and cooling consumptions are 349.5 kWe(e) and 451.4 MWh(e), respectively. If this modification had been made on the plenum, i.e., installing motorized dampers on the computer racks to regulate warm air flowing into the control room, the saving would have increased. However, the final choice will be made in the final design stage.

C. Third Modification: Rearrange the HVAC System and Change the Piping Network to a Chilled Water System

In this modification, air flows from AH1 to zones 1, 2, and 3 are adjusted to the new flow rates, 5,097.6, 33,984, and 5,904 m^3/hr (3,000, 20,000 and 3,475 cfm), respectively. Compressor C1 is modified to feed both AH1 and AH2. Chiller C2 is disconnected from AH2 and turned off. The air flow of AH2 is reduced from 39,091.6 m^3/hr (23,000 cfm) to 33,984 m^3/hr (20,000 cfm). The piping network will be changed to a chilled water system with the addition of a liquid cooler (LCI).

With this modification, ECP indicated a decrease in energy consumption from 1,850 MWh(e) to 1,757.3 MWh(e) and a decrease in energy cost from $112,348 to $106,740. The cooling energy has decreased from 451.4 MWh(e) to 427.4 MWh(e), and the heating energy has decreased from 0.350 MWh(e) to 0.065 MWh(e). Due to the new air flow, the maximum cooling on chiller C1 has increased to 321 kW(t) (65.7 tons) from the combined C1 and C2 in the previous modification. Also, the peak heating load was reduced significantly to 0.3 kW(t) from 0.8 kW(t) in the previous modification.

D. Fourth Modification: Add Economizer and Automatic Temperature Reset Setpoints to Air Handlers AH2 and AH3

This modification proposes to add economizer and automatic hot and cold deck reset controls to both air handlers AH2 and AH3. Figure 5 illustrates the modified HVAC system configuration with operating economizer for units AH2 and AH3. When the economizer is not in operation, Fig. 6 represents the modified HVAC configuration for that particular situation.

Annual energy consumption has been reduced to 1,604.0 MWh(e) due to the lower cooling energy required (228.0 MWh(e) vs 427.4 MWh(e)). Energy cost was $97,434, a $9,306 saving over the last modification.

E. Fifth Modification: Add a Chilled Water Storage Tank

This modification proposes to install a chilled water tank for load leveling and to minimize the energy waste of the compressor when running at partial loads. A separate computer program (STORAGE) has been developed to estimate the savings. The tank volume was selected to be 37.85 m^3 (10,000 gal) after several size optimization runs.

The computer program (STORAGE) simulates two compressors with each having four stages. Each compressor has a total cooling capacity of 98.5 kW(t) (28 tons of refrigeration)

and each stage represents 25 percent of the total cooling capacity. The minimum cooling capacity of both compressors was assumed to be 0.4 of full capacity. When the compressors are operated in conjunction with the chilled water storage tank, the minimum charging capacity is taken to be 98.5 kW(t) (28 tons) (one compressor capacity). The surplus of the total cooling demand is stored in a chilled water storage tank to be used later in the day. In this model, all losses are neglected. The operating temperature difference of the storage tank is assumed to be 5.6°C (10°F).

Note that the estimated energy and cost savings vary with different modes of operation of the compressor/storage tank system. The projected saving will be about 5.3 MWh(e) or about $2,271.

V. Summary of Modifications

Table 4 summarizes the results of all proposed modifications and the estimated implementation costs. Note that these modifications will not cause any discomfort inside the building because the design conditions are always satisfied. After all the modifications are implemented, the saving will be $17,613, or about 16% of present costs, with a simple payback of 10.5 years.

Table 1. Zone identification for the Operations Support Building

Zone	Zone description	Floor	Zone air flow, M^3/hr (ft^3/min)		ECP Zone
1	Plenum	1	67,968	(40,000)	2
2	Control room, comfort	2	9311.6	(5,480)	3
3	Communication room, comfort	2	1,699.2	(1,000)	3
4	Offices 206, 207, 208, 209, and corridor 202, restrooms 203 and 204	2	3,993	(2,350)	1
5	Offices 210, 211, 212	2	679.7	(400)	4
5	Maser room	1	3,398.4	(2,000)	6
7	Restroom 205	2	212.4	(125)	5

Table 2. Heat transmission properties of the Operations Support Building

Macro-zone	Heat transfer coefficient U, $W/m^{2\circ}C$ (Btu/hr-ft^{2}-°F)			Amplitude of heat transfer coefficient V, $W/m^{2\circ}C$, Btu/hr-ft^{2}-°F			Phase angle, ϕ radians		
	Roof	Wall	Floor	Roof	Wall	Floor	Roof	Wall	Floor
1	0.3877 (0.0683)	0.4382 (0.0772)	2.2707 (0.4000)	0.2520 (0.0444)	0.1113 (0.0196)	2.8384 (0.5000)	1.5844	2.9081	0.3000
2	3.7251 (0.6562)	0.4382 (0.0772)	2.6357 (0.4643)	3.7206 (0.6554)	0.1113 (0.0196)	0.9372 (0.1651)	0.0575	2.9081	1.9946
3	0.3877 (0.0683)	0.4382 (0.0772)	3.7251 (0.6562)	0.2520 (0.0444)	0.1113 (0.0196)	3.7206 (0.6554)	1.5844	2.9081	0.0575
4	0.3877 (0.0683)	0.4382 (0.0772)	2.2707 (0.4000)	0.2520 (0.0444)	0.1113 (0.0196)	2,8384 (0.5000)	1,5844	2.9081	0.3000
5	0.3877 (0.0683)	0.4382 (0.0772)	2.2707 (0.4000)	0.2520 (0.0444)	0.1113 (0.0196)	2.8384 (0.5000)	1.5844	2.9081	0.3000
6	3.7251 (0.6562)	0.4382 (0.0772)	2.6357 (0.4643)	3.7206 (0.6554)	0.1113 (0.0196)	0.9372 (0.1651)	0.0575	2.9081	1.9946

Table 3. Present consumption itemization[a]

Items	Annual consumption, kWh(e), ECP (1980)	Percent of total
Fluorescent lighting	210,900	11
Incandescent lighting	365	0
Cooling equipment	454,600	25
Heating equipment	3,784	0
Electrical/electronics (non HVAC)	749,000	40
Accessories	438,300	24
Total	1,856,949	100

[a]Rounded figures

Table 4. Summary of modifications for the Operations Support Building based on present conditions

Run no.	Modification no.	Description	Annual energy consumption, electrical, MWh(e)	Estimated construction costs, $	Annual costs, $	Annual cost savings, $	Payback period, years
1	–	Present conditions	1856.9	–	112,776	–	–
2	1	Addition of dead band controls	1851.7	2,000	112,466	310	6.45
3	2	Addition of VAV control to zone 3	1849.9	1,500	112,348	118	12.70
4	3	Rearranging HVAC system; addition of CHW system	1757.3	80,000	106,740	5,608	14.30
5	4	Addition of HVAC status panel and ECON and auto reset for AH2 and AH3	1600.6	77,500	97,434	9,306	8.30
	5	Addition of chilled water storage tank	1555.3	25,000	95,163	2,271	11.00
All modifications			1555.3	186,000	95,163	17,613	10.50

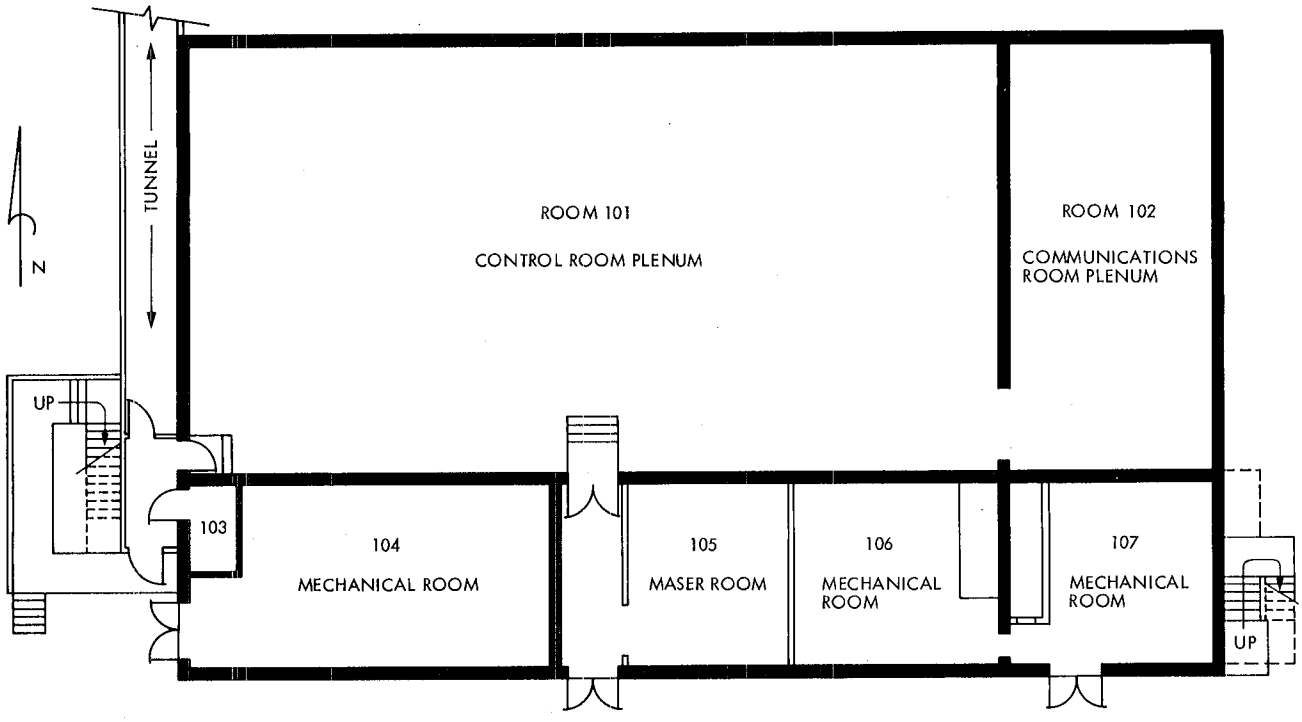

Fig. 1. Floor plan of Operations Support Building (first floor)

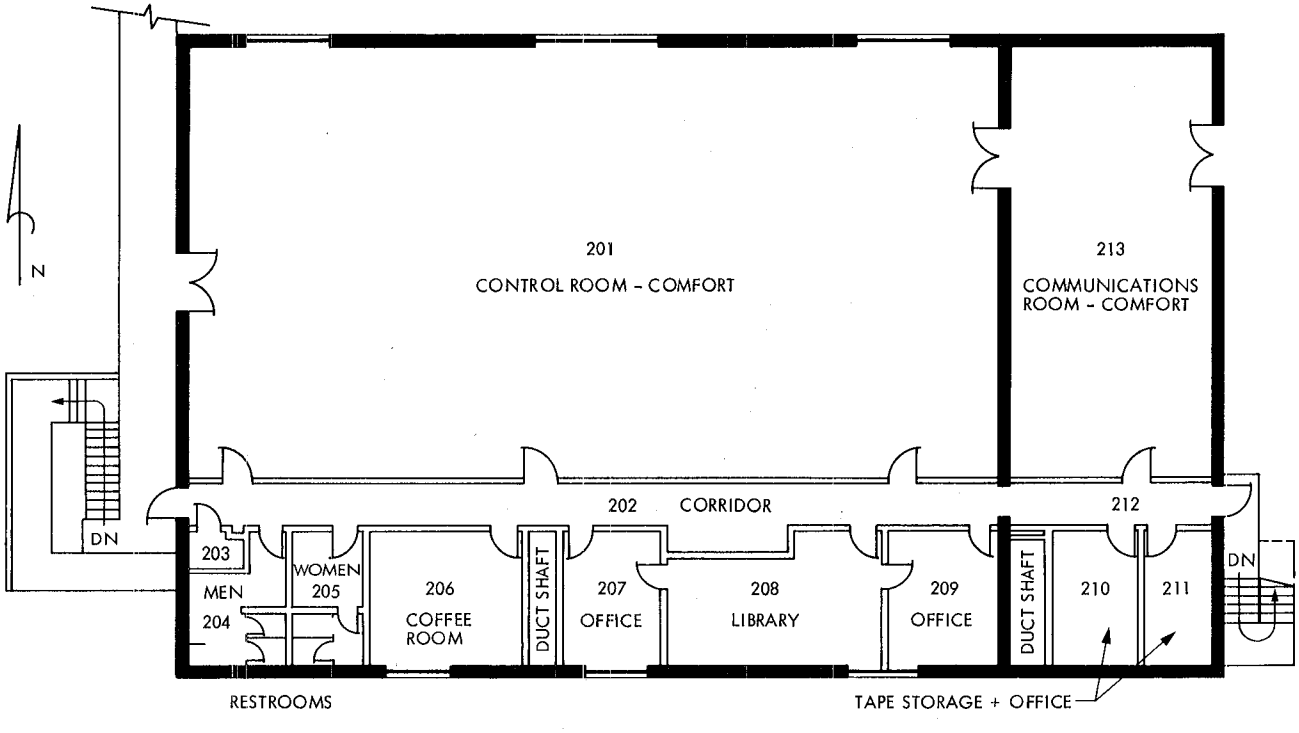

Fig. 2. Floor plan of Operations Support Building (second floor)

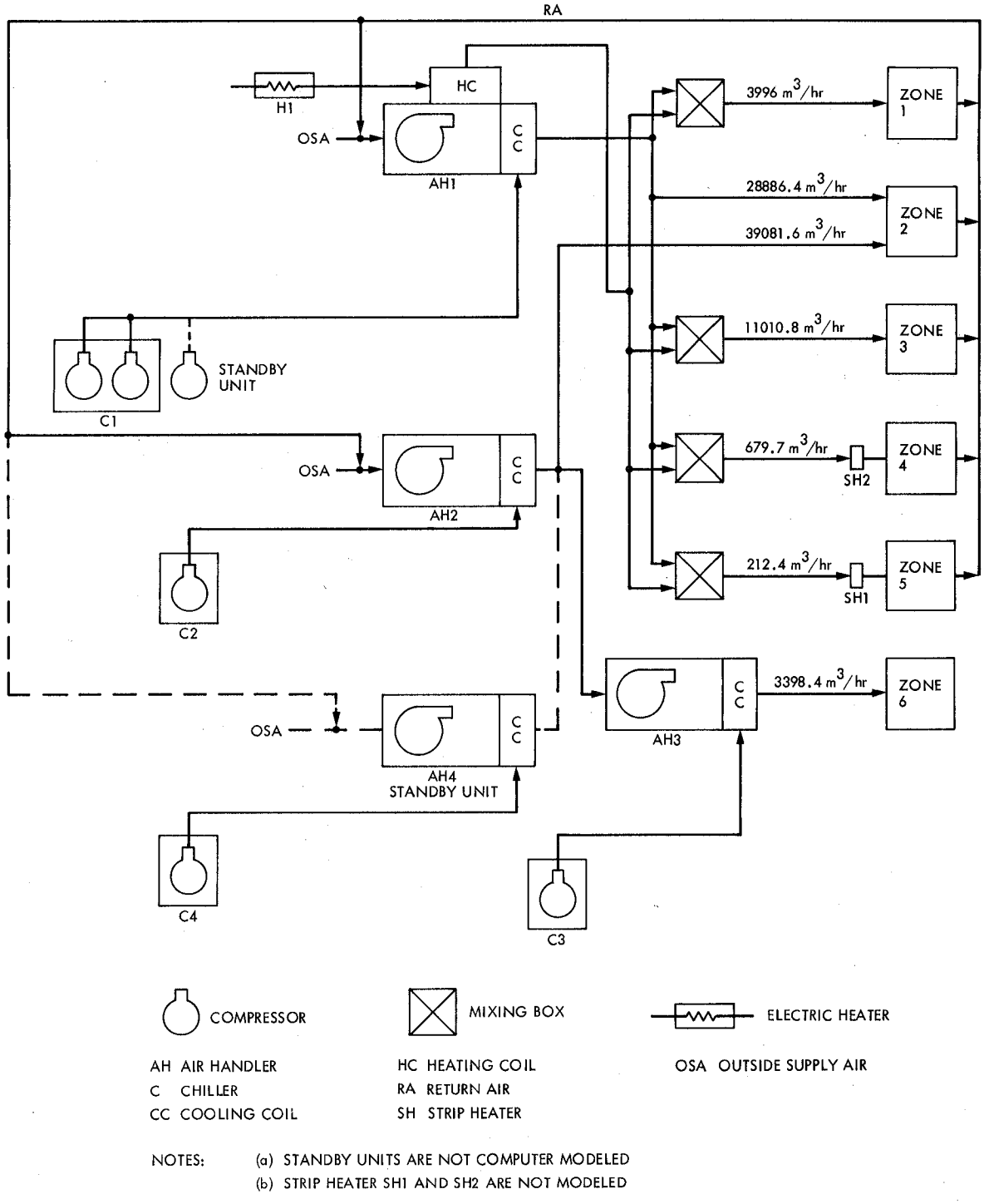

Fig. 3. Present HVAC configuration for the Operations Support Building

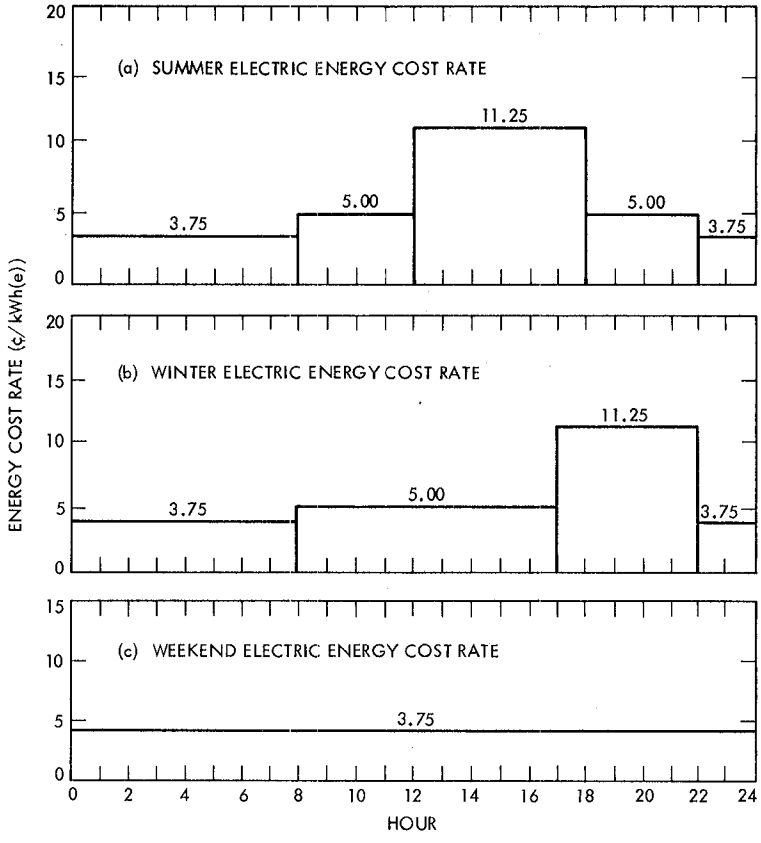

NOTES:

RATES SHOWN IN ABOVE SCHEDULE ARE FROM TOU-8/GENERAL SERVICE-LARGE, SOUTHERN CALIFORNIA EDISON COMPANY DATED JULY 22, 1979, AND INCLUDE A 25% ESCALATION INCREASE, EFFECTIVE OCTOBER 1979

Fig. 4. SCE electric energy cost rates

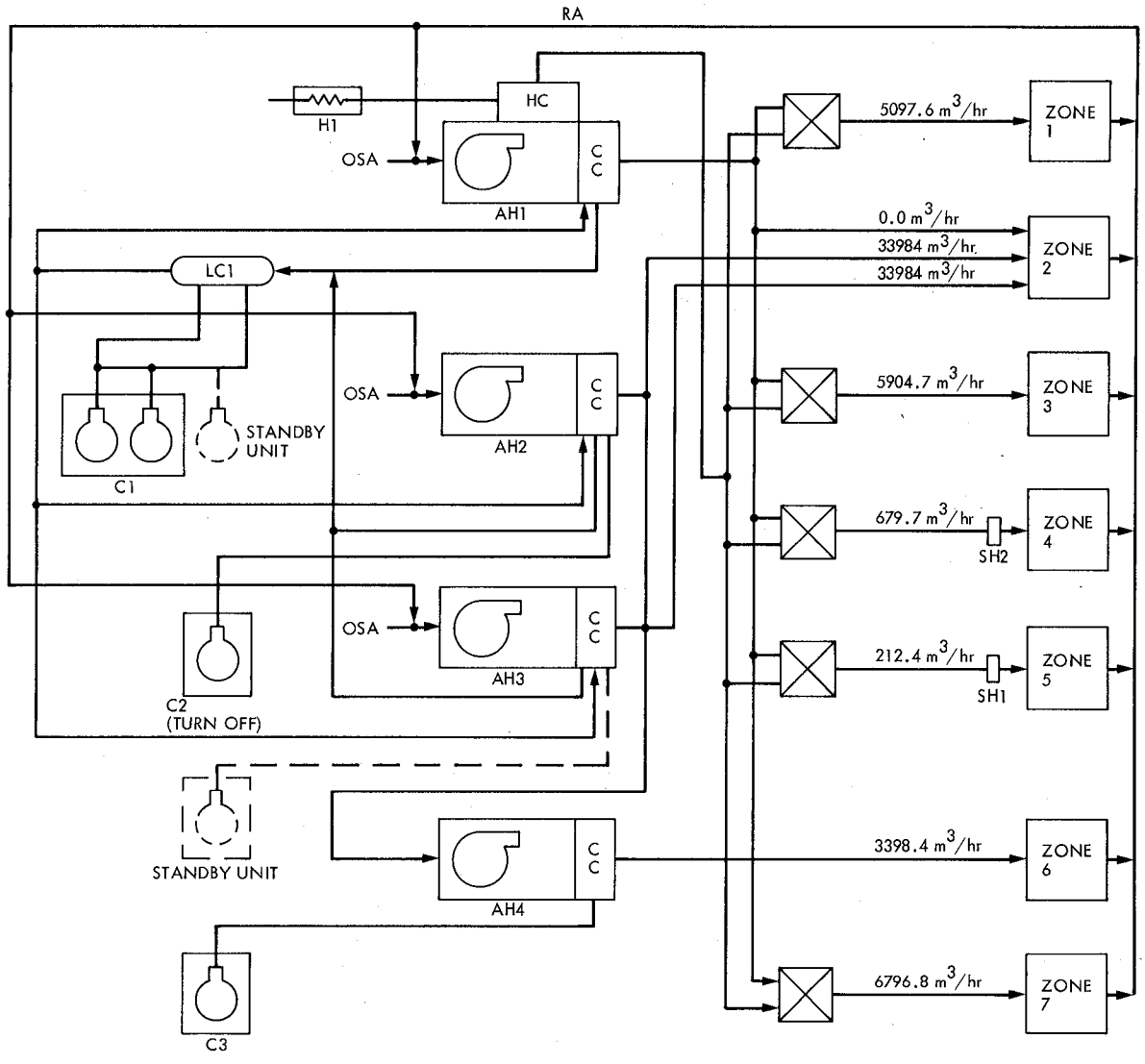

NOTES:
(a) STANDBY UNITS ARE NOT COMPUTER MODELED
(b) STRIP HEATER SH1 AND SH2 ARE NOT MODELED
(c) ZONE 7 (NO LOAD) WAS INTRODUCED IN THE COMPUTER MODEL AS REQUIREMENT FOR UNIT AH1 TO OPERATE IN STABLE PART OF THE FAN CURVE (18691.2 m^3/hr MINIMUM)

Fig. 5. Modified HVAC configuration with operating economizer for units AH1 and AH2

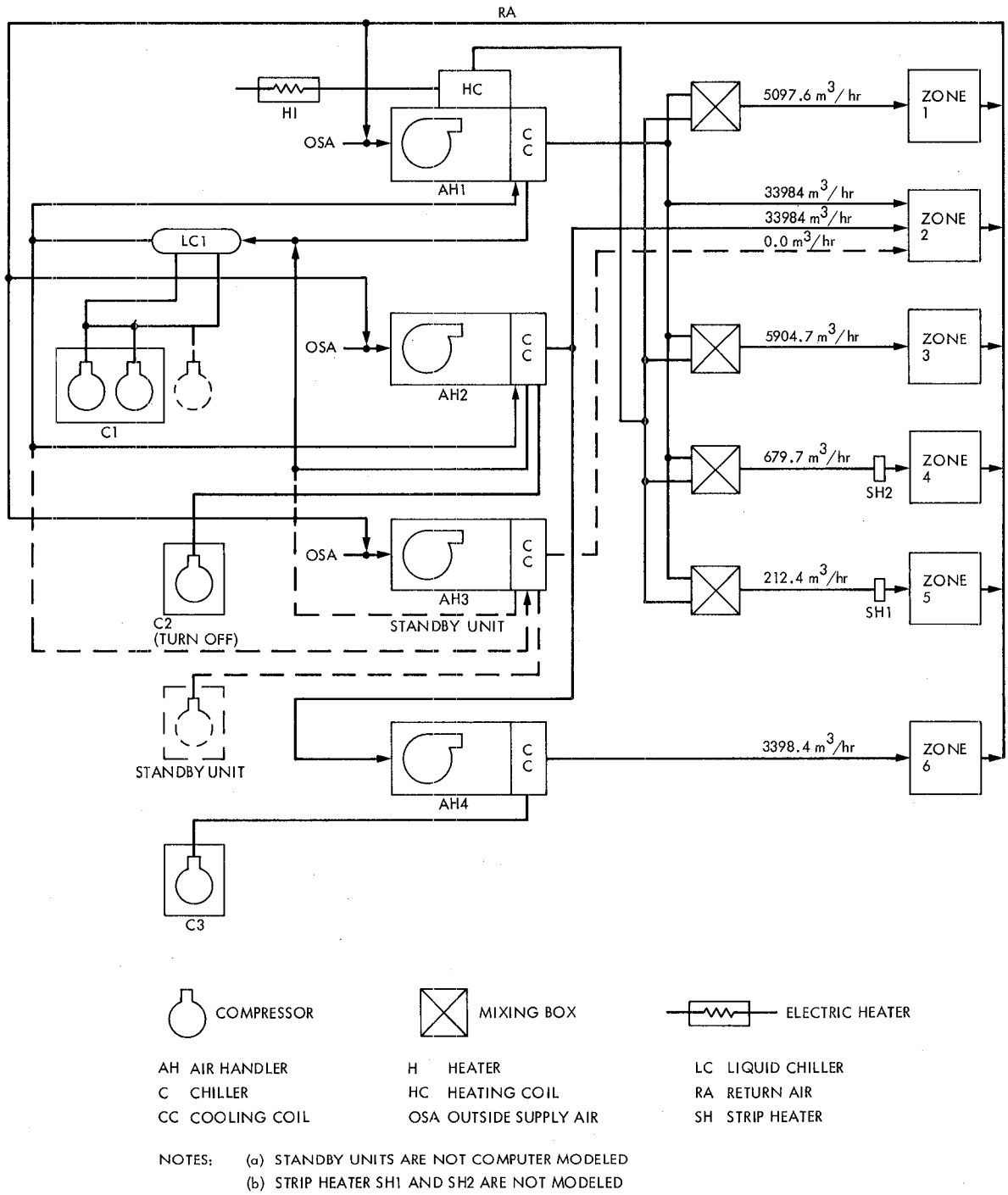

Fig. 6. Modified HVAC configuration with nonoperating economizer for units AH2 and AH3

End of Document